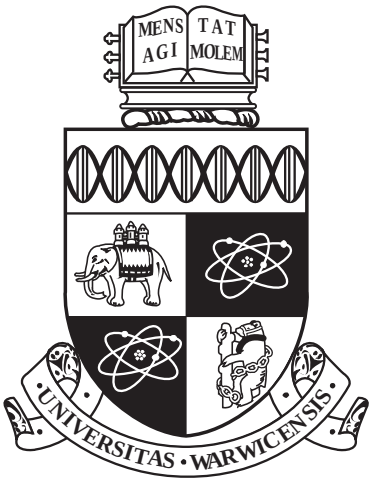

Optical Transients in the WASP Survey

by

George Marshall

Thesis

Submitted to the University of Warwick

for the degree of

Doctor of Philosophy

Department of Physics

September 2010

THE UNIVERSITY OF
WARWICK

Contents

List of Tables

List of Figures

Acknowledgments

I would like to thank my supervisor Dr. Peter Wheatley. His advice, encouragement and support throughout my PhD was invaluable. I would also like to thank Dr. Richard West for his work maintaining the WASP orphans database and developing the means to access the data. Without this any research on transients using WASP would not have been possible. I thank Dr Neil Parley for his work on matching detections to asteroids in the WASP data and, in doing so, reducing what could have been a significant source of false positives. I also thank Lieke van Spaandonk for her help with showing me how to reduce spectra.

I'd like to thank my family for their support and guidance over the years. Finally, I thank my girlfriend, Natalie, for her love, encouragement and making even the most difficult times easier.

Declarations

I declare that the material contained in this thesis is my own work except where collaborations have been stated. I have not used any sections of this text in any previous applications for a higher degree and have not submitted it to any other academic institutions.

There were several small sections that were done in collaboration with others or were based on previously completed work. Chapters 1 and 2 form an introduction to the field and the WASP observatories so are heavily based on the literature. The asteroid matching code described in Section 2.5 was the work Neil Parley and modifications to it described in Section 4.3 were done in collaboration with him. The WASP orphans database is run and maintained by Richard West who developed the clustering program described in Section 2.4.2 to access the data. Later modifications to it described in Section 4.6 were done by myself. The reduction of spectra described in Section 5.2 was done with the help of Lieke van Spaandonk.

The results from Sections 7.1 and 7.2 are intended for publication in the near future.

Abstract

This thesis describes a search for transient phenomena using data from the Wide Angle Search for Planets (WASP) observatories. With images taken of the same region of sky every 15 minutes and a field-of-view of 974 degrees squared, the WASP survey is ideal for identifying both short and long duration transients to a limiting magnitude of 16 in V. A high cadence wide-field survey of this type has not been carried out before so provides a different method of sampling variable populations and has the potential to identify previously unknown phenomena.

An algorithm to carry out a full untargeted search of the database was developed, tested and run on data from 2004, 2006, 2007 and 2008. False positives were rejected based on their proximity to similar magnitude stars, the tightness of the clustering of detections in sky coordinates, the focus of the images and the number of corroborating detections.

Overall, 44 cataclysmic variable candidates, 144 extreme flare candidates, 63 variable star candidates and 57 transients of unknown type were identified. The cataclysmic variable candidates showed similarities to the currently known population although some selection effects were uncovered. Of particular note were two new WZ Sge systems, an eclipsing system with a period of 540 minutes and an object with an M-star spectrum and broad Balmer lines but no visible white dwarf. The flares are some of the largest ever observed on M-type stars. The largest of these released $\sim 10^{35}$erg in the V-band alone. A candidate flare was also identified on a G-type star releasing 1.6×10^{37}erg in the V-band. Alternatively, it may be unrelated to the G-star and could be a gamma ray burst or similar transient without a persistent counterpart. A known supernova and two known novae were also identified.

Abbreviations

2MASS	Two Micron All Sky Survey
AAVSO	American Association of Variable Star Observers
ASAS-3	All Sky Automated Survey
CV	Cataclysmic Variable
GRB	Gamma Ray Burst
LSST	Large Synoptic Survey Telescope
OGLE	Optical Gravitational Lensing Experiment
Pan-STARRS	Panoramic Survey Telescope and Rapid Response System
PTF	Palomar Transient Factory
RAPTOR	Rapid Telescopes for Optical Response experiment
ROTSE-3	Robotic Optical Transient Search Experiment
SDSS	Sloan Digital Sky Survey
USNO	United States Naval Observatory
VLT	Very Large Telescope
VST	VLT Survey Telescope
WASP	Wide Angle Search for Planets

Chapter 1

Introduction

Time-domain astronomy has, for a long time, remained underdeveloped with many important questions still unanswered. While static phenomena can be observed at leisure, transient objects require repeated observations over long time periods. This means immense quantities of data must be analysed which, until recently, was not possible. To further complicate this, transient phenomena can last anything from seconds (gamma ray bursts) to years (novae or supernovae). For these reasons, searching the sky for transient phenomena is a difficult task. However, it is gaining increasing focus with large scale surveys by the Large Synoptic Survey Telescope (LSST) and Pan-STARRS planned over the next decade (see Section 1.3). The aim of this thesis is to carry out a transient survey of this type using the Wide Angle Search for Planets (WASP) observatories.

1.1 The WASP Project

1.1.1 Planet hunting with WASP

As the name suggests, the primary scientific goal of WASP is to identify previously unknown exoplanets. It does this by gathering light curves of large numbers of stars and searching for small dips in luminosity (approximately 1%). These dips in luminosity can be caused by an orbiting planet passing in front of the star and obscuring some of the light. This method for searching for exoplanets is known

Figure 1.1: The WASP South enclosure in South Africa [7]

as the transit method and is used by several other planet hunting projects such as the HATNet project (Hungarian Automated Telescope Network) [14]. The WASP project has shown some considerable success in this field and as of August 2010 has discovered 29 planets.

However, a survey of this type also has many advantages for surveying the sky for transients. Firstly, when hunting for planets, a large number of stars need to be observed. To achieve this, WASP has a very wide field-of-view. This wide field-of-view is ideal for an unbiased survey of transients since, like planets, it is not possible to narrow down the search without introducing selection effects. Secondly, to gather the detailed light curves needed to detect an eclipse, WASP observes the sky with a very high cadence. This is again important for transient surveys as it allows shorter transients to be identified and more detailed light curves can be produced. This is particularly advantageous for observations of cataclysmic variables as it may be possible to measure the superhump or orbital period.

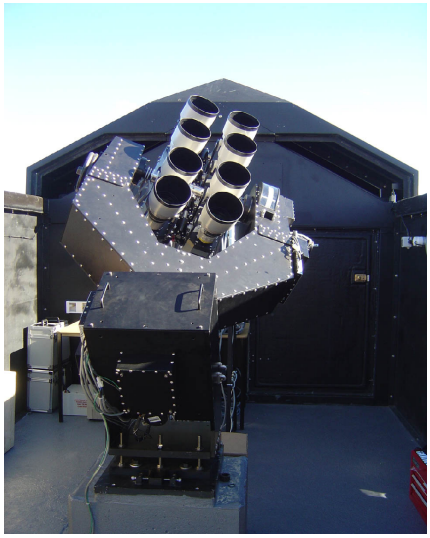

Figure 1.2: The WASP cameras [7]

1.1.2 The WASP observatories

There are two WASP observatory sites, one on La Palma (WASP-north) and one at the South African Astronomical Observatory (SAAO) (WASP-south) (see Figure 1.1). The observatories each consist of an array of 8 wide-field cameras (see Figure 1.2). Each of these cameras have an aperture of 11.1cm and a field-of-view of 7.8 x 7.8 degrees [33]. The cameras are backed by high-quality back-illuminated CCDs with 2048 x 2048 pixels [125]. This means each pixel covers 13.7 x 13.7 arcseconds.

The WASP observatories are able to cover approximately 4 percent of the sky every 15 minutes (although this can vary with different observing strategies). It is possible to detect stars as faint as $\sim$ 16th magnitude although this is dependent on the background flux.

1.1.3 The potential of WASP as an all-sky time domain survey

Many single epoch surveys of the sky have been carried out by projects such as the Sloan Digital Sky Survey (SDSS) [8] and the Two Micron All Sky Survey (2MASS) [36]. These have lead to great steps forward in our understanding of astronomical populations. For example, to date 204 new CVs have been identified using spectral data from SDSS [154], along with a large number of quasars and other phenomena.

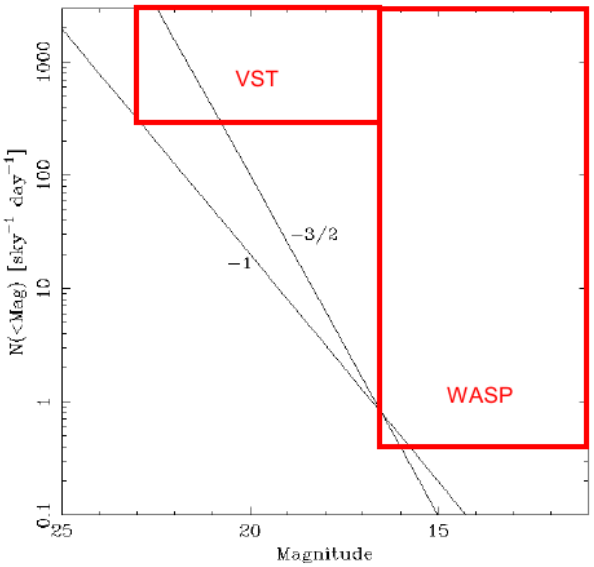

Figure 1.3: A sketch plot representing the observable parameter space for WASP and VST with magnitude on the x-axis and number of events brighter than the x-axis magnitude per sky per night on the y-axis. The plot was taken from [169].

However, most of these surveys have limited or no time domain information. This means that, for at least some classes of transients, unless it is identified independently as a possible variable source, its nature can not be established. While SLOAN has shown considerable success in identifying CVs and quasars, using only this method limits the information available on these objects and risks introducing selection effects to the population. Because of this survey astronomy has increasingly moved towards the time domain to complement the current single epoch surveys.

There are two approaches to achieve this: narrow-deep surveys or wide-shallow surveys (such as WASP). Survey instruments, such as the VLT Survey Telescope (VST), have a relatively narrow field-of-view but can image far deeper than wider field-of-view instruments. These projects tend to carry out deep surveys of smaller regions of sky, often targeted at particular galactic features. Alternatively, there are projects such as WASP which cannot image as deep but cover the whole sky on a nightly basis.

These alternative strategies work in a considerably different parameter space (see Figure 1.3). The figure shows the approximate parameter space covered by

WASP and the VST. The x-axis represents the magnitude of the events being observed and the y-axis represents the number of events occurring in the whole sky every day brighter than a given magnitude.

The diagonal lines represent typical observable populations of isotropically distributed events. The line marked -3/2 shows the theoretical gradient where the number of observable events increase with a fainter magnitude limit as it samples a larger volume of space. The -1 curve may prove to be more realistic though because of the effects of extinction from interstellar dust and the scale height of the galactic disc.

The scale height is the height above the galactic plane at which the density of objects being considered decreases by a factor of $1/e$. At twice the scale height the density would decrease to $1/e^2$ and so forth. This can effect sky distribution and forms an important consideration when surveying more distant galactic objects.

The boxes represent the region of parameter space in which the telescope will identify at least one of these transients a year. While WASP cannot detect anything with a magnitude fainter than approximately 16.5, it covers a large area of sky so only requires a rate of 0.4 events per day per sky to identify at least one event a year. In comparison, while the VST can image as faint as 23rd magnitude, it requires an average of over 300 observable events across the sky to make a detection likely.

While this plot is somewhat simplified and does not account for observing strategy or the distribution of the transients, it does show how wide-field instruments, such as WASP, can still compete effectively with deeper narrower transient surveys. Furthermore, the brighter examples of transient events tend to be more useful as it is easier to gather further information on them. For this reason, most survey projects aimed at identifying asteroids, variable stars or CVs are small wide-field instruments. Generally deeper surveys are aimed towards observing distant, faint events such as micro-lensing from dark matter, novae rates in other galaxies or type Ia supernovae. Some notable examples of these deep time domain surveys include several to detect gravitational lensing (the Deep Lens Survey [20], the Massive Compact Halo Objects (MACHO) project [11] and the Optical Gravita-

tional Lensing Experiment (OGLE) [159]) and general transient surveys (such as the Faint Sky Variability Survey using the Wide Field Camera on the INT [56] and the Subaru/XMM-Newton Deep Survey [107]). Some of the important wide field surveys are discussed below in Section 1.2.

1.2 Wide Field Time Domain Surveys

Northern Sky Variability Survey

The Northern Sky Variability Survey used the ROTSE-1 observatory, when it was not responding to gamma ray burst alerts, to carry out a systematic time-domain survey of the northern sky [174]. The ROTSE-1 observatory, located near Los Alamos in New Mexico, consisted of four Cannon 200mm lenses each with a field-of-view of 8.2 x 8.2 degrees. The cameras had a limiting magnitude of 14.5-15.5 and saturated at 8th magnitude. They exposed in a single unfiltered photometric band similar to the Johnson R band. Over the baseline of a year, 14 million objects were observed with a cadence of 0.5-4 days. The survey has shown particular success in studying the properties of populations of pulsating variable stars such as RR Lyrae variables [79].

ROTSE-3

The ROTSE-3 observatories were designed to detect optical flashes from Gamma Ray Bursts [9]. The project consists of 4 telescopes spread across the world (McDonald observatory in Texas USA, National Observatory in Turkey, near the HESS project in Nambia and Siding Springs Observatory in Australia). Each of the 0.45m telescopes have a 1.85 x 1.85 degree field-of-view. The telescopes patrol the sky taking a pair of 60 second exposures with a limiting magnitude of 18.5. These are followed by another pair taken 30 minutes later. It is also capable of rapidly responding to Swift GRB alerts to gather optical data at the position of the suspected GRB. ROTSE-3 has currently not only successfully detected two GRBs but has also identified several other transients such as cataclysmic variables and flare stars [140].

RAPTOR

The Rapid Telescopes for Optical Response experiment (RAPTOR) [163] consists of a several wide field telescopes monitoring the sky for transients. RAPTOR-A and RAPTOR-B each consist of 4 wide field cameras and a central, more powerful, "fovea" imager. They are separated by 38 kilometers but each view the same 1500 square-degree field. Combined data from the two observatories means it is possible to check for parallax changes indicating a nearby source. RAPTOR's software pipeline is able to identify potential transient events in real time and bring the central "fovea" imager to bear on them for higher quality photometric data. RAPTOR-A and RAPTOR-B are supplemented by RAPTOR-S (a low resolution spectrograph) and RAPTOR-P (a sky patrol telescope with a 60 square-degree field-of-view and limiting magnitude of around 16.5). The RAPTOR observatories have shown success in detecting optical afterglows of GRBs. For example, in 2005 it made 32 detections of GRB 050319 [175].

Catalina Sky Survey

The Catalina Real Time Sky Survey uses the 0.7m Catalina Schmidt Telescope near Tucson Arizona to identify near Earth objects and potentially hazardous asteroids. The telescope has 8 degrees squared field-of-view and typically covers 1200 square degrees of sky a night with four 30 second exposures with a limiting magnitude of 19th to 20th. In searching for asteroids the Catalina sky survey has also shown considerable early success in identifying optical transients. From the first six months of observations 350 optical transients were identified [42] including sixty two supernova candidates and sixty four new cataclysmic variable candidates. Recently the Catalina Sky Survey has expanded to include another observatory near Tucson and at Siding Spring in Australia.

Palomar Transient Factory

The Palomar Transient Factory (PTF) is an experiment to carry out a wide-field transient survey using the 1.26m Samuel Oschin Telescope [131]. The field-of-view

of the wide-field camera is 7.9 $\deg^2$ with a pixel scale of 1 arcsecond per pixel. The project achieved first light in December 2008 with commissioning completed in summer 2009 and is planned to run until the end of 2012. PTF runs several observing strategies the primary two of which are a large area transient survey ($\sim 10,000 deg^2$ per year) observing in the R band with a cadence of five days and a higher cadence survey (1 minute to 3 days) in the g and R band over a smaller area. The PTF survey has shown considerable early success having identified, amongst many other transients, 679 supernovae (as of August 2010) and 3 unusual high amplitude transients from the death throes of massive stars [128].

ASAS-3

The All Sky Automated Survey (ASAS-3) [123] consists of two 0.2m wide field cameras each with a 8.8 x 8.8 degree field-of-view and a more powerful 0.25m telescope with a 2 x 2 degree field-of-view. The wide field instruments survey the whole of the southern sky for transients with an average detection rate of one measurement every two days. The narrow field instrument is designed to rapidly respond to GRB alerts. The limiting magnitudes for the two wide field telescopes and the rapid response telescope are respectively 13.5, 13.2 and 14.8. In 2006 a replica of the ASAS telescopes was built on Hawaii to continue the transient survey in the northern hemisphere. Since the start of the project in 2000 ASAS-3 has discovered 2 comets, 6 novae and 6 dwarf novae [2].

PQ Survey

The Palomar-Quest Digital Synoptic Survey (PQ survey) [40] uses the 1.23m Samuel Oschin telescope at Palomar with a 4 x 4 degree field-of-view. The project uses 45% of the telescope operating time to carry out a time domain survey of a region of sky totalling approximately 15 000 square degrees. A typical field will have between 5 and 10 observations with around 4 hours between observations and a limiting magnitude of approximately 21.5 in r. This comparatively deep survey covering only a fraction of the sky falls somewhere between the deep narrow field surveys

and the other wide field surveys in this section. The primary motivation for the project was to identify over 10 000 quasars in order to discover over 100 strong gravitational lenses.

1.3 The Future of Time Domain Astronomy

The ongoing success of current wide field surveys and an increasing interest in tracking nearby asteroids has led to further investment in large scale wide field survey telescopes capable of not only regularly covering the entire sky but reaching far fainter magnitudes. The main upcoming projects discussed here are SkyMapper which was opened in the middle of 2009, Pan-STARRS which is currently in a prototype phase and the Large Synoptic Survey Telescope (LSST) which is currently under construction and scheduled for full scientific operation by 2017.

SkyMapper

The SkyMapper Telescope is a 1.3m telescope with a 5.7 degrees squared field-of-view located at Siding Spring in Australia [78]. The primary scientific goal of the project is a survey of the southern sky in six colours over multiple epochs (4 hours, 1 day, 1 week, 1 month and 1 year). The telescope will take 110 second exposures with limiting magnitudes varying from 21.5 in u to 20.6 in z. It was officially opened in May 2009.

Pan-STARRS

Pan-STARRS will consist of an array of four 1.8m wide-field telescopes pointing at the same region of sky [75]. Each of these telescopes will have a field-of-view of 7 square degrees and individually be able to detect point sources as faint as 24th magnitude with a 30 second exposure [67]. By combining the data from the telescopes together a magnitude limit of approximately 26th should be achieved. In this mode it will be possible to observe each region of sky once every week. The advantage of using the 4 telescopes in this way is that they can achieve the same

effect as a single, much larger, instrument at a much lower cost.

The primary scientific goal of Pan-STARRS is to identify and track near Earth asteroids to ensure that they pose no risk. However, it also has a wide range of secondary scientific goals. These include identifying Kuipler belt objects, detecting and gathering data on transient events (such as supernovae and gamma ray bursts), identifying new exoplanets around distant stars, mapping out the large scale distribution of galaxies and using gravitational lensing to determine the distribution of dark matter.

Currently a single telescope prototype (PS1) has been constructed on Hawaii as a test before the four telescope array (PS4) is constructed in 2012. In this early prototype phase PS1 has already successfully identified a previously unknown supernova (SN2009kf) [26].

The Large Synoptic Survey Telescope

The Large Synoptic Survey Telescope (LSST) [72] is a 8.36m wide-field telescope currently under construction with first light planned for 2014 and full scientific operation for 2017. The primary mirror of the telescope will be a 5.12m to 8.36m annulus and will have a 9.6 square degree field-of-view. This will allow 10 000 square degrees (approximately a quarter of the sky) to be covered with pairs of 15 second exposures every three nights. For a single visit the limiting magnitude will be approximately 24.5 in r improving to 27.5 if the images are coadded. The primary scientific goals of LSST are to determine the nature of dark energy, identify near Earth objects, discover new transient events, carry out a weak lensing survey for dark matter and map out the structure of our Galaxy.

1.4 WASP in Comparison to Other Wide Field Surveys

The WASP observatories compare well with other current wide-field time-domain surveys and effectively complement future surveys. Table 1.1 shows some of the basic properties of current and future all-sky surveys. The etendue (or grasp) is the

multiple of the light collecting area and the field-of-view. It is used as an indication of how effective a telescope will be for a survey of this nature. While future projects such as Pan-STARRS and the LSST have extremely high etendue values, WASP is shown to be competitive with most current surveys. WASP's limiting magnitude, while not as faint as deeper surveys such as Catalina, PTF or the PQ survey, is fainter than other successful projects such as ASAS-3 and Raptor A+B.

However, the area that WASP stands out in is its extremely large field-of-view. With a total field-of-view across all 16 cameras of 976 square degrees only the RAPTOR A+B observatories are comparable. This allows the WASP data to have a far better cadence than most transient surveys, even including future projects such as Pan-STARRS and SkyMapper. This high cadence makes WASP better suited to identifying short duration transients and allows for more data to be gathered on longer events that are detected.

Project	Aperture (m)	Field of View ($degrees^2$)	Etendue ($m^2 degrees^2$)	Limiting mag.	Pixel size (arcsec/pixel)	Cadence
WASP	0.111	61 (per camera)	9.4	$\sim$ 16	13.7	$\sim$15 min
Northern Sky Variability Survey	0.2	67 (per camera)	8.0	15.5	14.4	0.5-4 days
ROTSE-3	0.45	3.4 (per camera)	2.2	$\sim$ 18.5	3.3	30 min
RAPTOR A+B	0.085 0.4	1500 60	16.1	$\sim$ 12 $\sim$ 16.5	35.1	1 min
Catalina	0.7	8	3	19-20	2.5	30 min
Palomar Transient Factory	1.26	7.8	9.7	21	1.0	5 days
ASAS-3	0.2 0.25	77 (per camera) 4 (per camera)	5.0	$\sim$ 13.5	15.8	2-3 days
PQ Survey	1.23	16	19	$\sim$ 21	1.1	4 hrs
SkyMapper	1.35	5.7	8.2	$\sim$ 23	0.5	4 hrs to 1 year
Pan-STARRS	1.8	7	71	$\sim$ 26	0.3	1 week
LSST	8.36	9.6	329	$\sim$24.5 (27.5 if coadded)	0.2	3 days

Table 1.1: A table comparing the properties of the various wide field time domain surveys

While it may seem that current surveys are going to be overshadowed by future projects, such as Pan-STARRS and LSST, they still have an important role to play. Firstly, discoveries and population analysis results from these projects can help future projects by identifying problems and scientific areas that need further observation. Secondly, these large scale projects are not operating in the same parameter space as smaller telescopes such as WASP. While WASP can only detect events brighter than 15th-16th magnitude, the LSST CCDs will saturate for objects brighter than 16th. This means that any transient identified by WASP would not have been possible to observe using the LSST.

1.5 An Overview of Transient Phenomena

There are a wide variety of both short and long duration transient phenomena that a time domain survey of the sky could potentially identify. These are considered in the sections below with particular attention being paid to the ways that WASP could further our understanding of them.

1.5.1 Flare Stars

Flare stars (or UV Ceti stars) are one of the most common variable objects, comprising ∼10% of stars in the Galaxy [57]. They can appear transient in WASP if the star itself is too faint to detect when not flaring. While flares occur on the Sun, flare stars can show significantly more energetic ones. The majority of flare stars are spectral type M, however large flares can also be seen in earlier spectral types [119] [143] and in brown dwarfs [145]. Furthermore, flares can be found in pre-main sequence T Tauri stars [172] and extreme flares have be seen in RS CVn systems [57].

The mechanism that causes these flares is still not fully understood. Flares are thought to be the result of the reconnection of magnetic loops on the surface of stars so a flare star would be expected to have a significant magnetic field. Current stellar models predict that this magnetic field is created by the differences in

differential rotation between the conductive and convective layers of the star [116] [157]. However, stars of spectral type M3 or later are thought to be fully convective so there might be a significant reduction in the magnetic field for late M or L type stars. However, this has not been seen in population samples of M-stars that were spectroscopically tested for activity. In fact, rates for active stars peaks at around M7 [145] [168]. This suggests instead that the magnetic field for late spectral types must be generated in a different way. The cause of the large flares on RS CVn stars is somewhat different as they are in close binary systems with the brighter of them of spectral type F or G [152] In these systems the flares are believed to be induced by the interaction of the two stars. A similar theory has also been proposed for giant flares on solar type stars with the flares being caused instead by extrasolar planets in close orbits [139].

Extensive work has already been carried out to monitor flare activity on small samples of stars [103] [86] [145]. However, rarer large amplitude flares have been studied far less because of the requirements for long duration coverage over a large region of sky with high cadence. The search carried out in this thesis is not likely to identify the small amplitude events but is well suited to identifying rare extreme flares (although there is a tendency to identify longer duration flares from this class). A candidate for the largest known flare on an M-type star is the photographic discovery of a 7 magnitude flare by Bond in 1976 with an estimated bolometric energy of 4×10^{35}erg [54]. For RS CVn stars it is thought that they may have flares up to 10^{38}erg [57]. The largest known flare on a solar type star was detected in 1899 with 2×10^{38}erg in the V band alone [143]. Detecting the most extreme flares provides a different test for our current models of both late type stars and flares. For example, it may be possible to establish the maximum energy available for flares and whether this maximum energy varies with spectral type.

Furthermore, these large flares have important implications for life on orbiting planets. A sufficiently energetic flare could cause extensive glacial melting and temporarily heat the planet's atmosphere causing mass extinction [143]. The peak energy flares can achieve and their rate would therefore be important for accessing

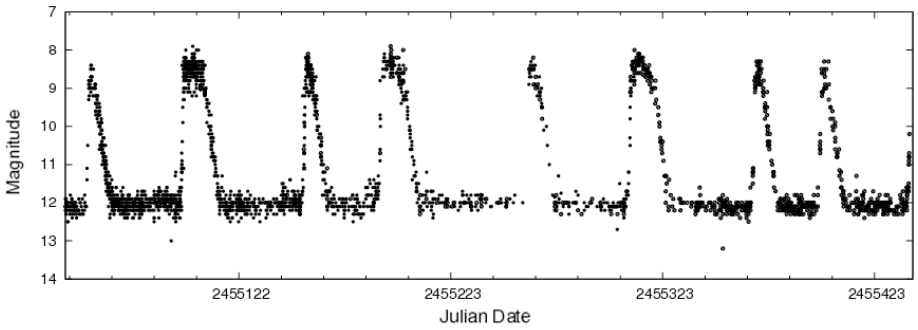

Figure 1.4: A light curve of dwarf nova outbursts from SS Cyg. Data taken from AAVSO [1].

the likelihood of life around other stars.

These extreme amplitude events are also important because they will cause a significant amount of noise in future surveys to optically identify gamma ray bursts [55] [97]. Like gamma ray bursts, flares can be very short and, without detections of the progenitor or observations from other bands, it is difficult to determine what caused the transient. Hence further understanding of large amplitude flares may prove helpful for future attempts to optically identify gamma ray bursts.

1.5.2 Dwarf Novae

Dwarf novae, a subclass of close binary systems known as cataclysmic variables, show short optical outbursts of 2 to 8 magnitudes. Cataclysmic variable systems (CVs) consist of a small but dense white dwarf (the primary) and a larger lower mass companion star (the secondary). The stars orbit each other sufficiently closely that the secondary fills it's Roche lobe causing its outer layers to be stripped away and spiral in towards the primary in an accretion disc. An overview of the properties of these systems is described in this section but a more detailed review of cataclysmic variable models can be found in Brian Warner's book *Cataclysmic Variable Stars* [167].

Dwarf nova outbursts occur if the accretion disc does not deposit its material on the primary rapidly enough as this causes material in the disc to gradually

build up. Once the density reaches a critical point the disc changes to a different equilibrium state. This is because the increase in density causes an increase in the viscous heating. This, in turn, increases the ionisation (and hence opacity) of the disc which causes it to heat up further. This feedback loop continues until the hydrogen in the disc is completely ionised [87]. At this point the opacity stops rising with temperature and a new, high luminosity, equilibrium state is reached. In this state the viscosity is thought to be far higher although the reason for this is not fully understood. This increases the rate of accretion onto the white dwarf and the density decreases until the disc goes back to its original stable state. Outbursts can reoccur on a time scale of weeks, months or even years. A normal outburst typically lasts for several days and can increase the brightness of the system by 2 to 6 magnitudes [110]. An example of a system showing these outbursts is shown in Figure 1.4.

In some systems, known as SU UMas, the disc periodically has a larger outburst (known as a superoutburst). It is believed that these are caused by a gradual increase in the size of the disc over a succession of normal outbursts [109]. The last of these normal outbursts increases the radius of the disc to forty six percent of the separation of the primary and secondary [111]. At this radius the disc is no longer stable and the tidal resonance with the secondary drives the disc to become elliptical triggering a superoutburst. The tidal stresses on the disc are thought to maintain a high accretion rate which, over the period of a week or two, causes the disc to shrink in size again until it is no longer elliptical. Furthermore, the ellipticity of the disc also causes it to process and the interaction of this with the stream of accreted material from the secondary causes a small periodic variation in brightness known as the *superhump period*.

Most studies characterise the CV population by considering the orbital period. For the majority of CVs this is between 78 minutes and 8 hours [69]. The distribution of periods from known outbursting systems in the Ritter and Kolb catalogue [136] is shown in Figure 1.5. There are two features that stand out in this figure; the lack of CVs with orbital periods between 2 and 3 hours and the abrupt

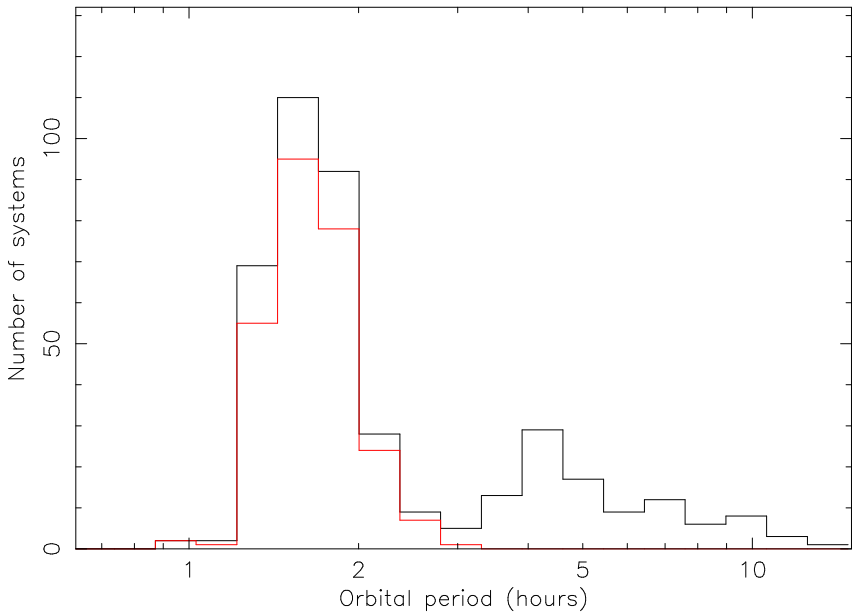

Figure 1.5: A histogram show the orbital periods of systems in the Ritter and Kolb catalogue [136] known to have dwarf nova. SU UMa systems are shown in the red histogram.

lower limit of 77 minutes.

The 2-3 hour feature is known as the period gap and is thought to be caused by a change in the way the companion star loses angular momentum during this period of its evolution [69]. The period minimum is an expected feature of the population. However, models predict that it should be at 65 minutes rather than the observed period of 77 minutes [17]. There have been several attempts to match the models to the observed properties but none have so far shown much success [83] [80]. It can also be seen from Figure 1.5 that almost all CVs below the period gap are of SU UMa type (shown in red) but almost none above the gap are. Systems below the period gap have older, and hence lower mass, secondaries. This means that only these systems are likely to have a sufficiently extreme mass ratio (<0.33) to cause superoutbursts.

To understand this period distribution is to understand the evolution of CVs. A graphical representation of this is shown in Figure 1.6. It is thought that the majority of systems begin accreting with orbital periods in excess of 3 hours after a

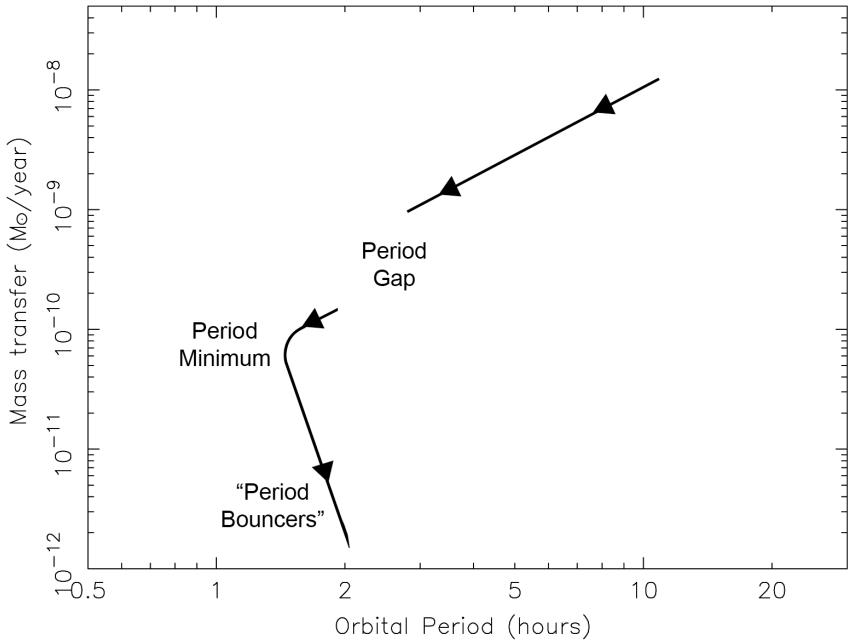

Figure 1.6: A plot showing the changes in orbital period and accretion rates as cataclysmic variables evolve. The plot was taken from [63].

common envelope phase [135]. At this stage in their evolution the secondary primarily loses angular momentum by magnetic braking [130] which causes the orbital period to gradually decrease. During this process the mass loss from the secondary star makes it become thermally bloated (lower mass for its radius than would be expected on the main sequence) as there is not sufficient time for it to settle back into equilibrium. However, when the orbital period reaches 3 hours the star is believed to become fully convective which is thought to cause a dramatic reduction in magnetic breaking and hence in the angular momentum loss rate. This allows the secondary star to settle again into equilibrium by shrinking to a normal size. This reduction in radius causes the secondary to disconnect and stops the mass transfer, converting the system into a detached binary. Mass transfer restarts once the orbital period reaches 2 hours as the star is once again filling its Roche lobe. The few CVs that are found in the period gap represent systems that originally started mass transfer at an orbital period between 2-3 hours. These systems would not have gone through the change of state at 3 hours so would not disconnect. While details of this are not

very well understood, in principle this model does appear to explain the period gap [69].

Below the period gap it is believed that CVs primarily lose angular momentum by gravitational radiation [44] [114] instead of magnetic breaking. The systems will then continue to lose angular momentum until they reach the period minimum (65 minutes by theory, 77 minutes observationally [17]). At the period minimum the secondary star becomes degenerate which means further mass loss causes it to expand rather than shrink. The effect of this is to cause the orbital period to start increasing to longer periods. These systems are known as period bouncers and are thought to have very low accretion rates with large but infrequent outbursts (although it is possible that their accretion rates are so low that they never outburst at all [83]). It is predicted that these period bouncers should make up a large proportion of the CV population ($\sim$70 percent [82]) and should be seen as a sharp peak at the orbital period minimum in Figure 1.5. Until recently though, no systems were confirmed to be of this type and this peak at low periods was missing from the discovered population suggesting the current model may be wrong [127]. It was theorised that the low accretion rate, high outburst amplitude WZ Sge systems may represent some of these period bouncers [70]. However, none of these were confirmed to be of this type and they are not known in sufficient numbers to account for the discrepancy between the predicted population and what has been observed. However, recently the Sloan Digital Sky Survey has shown some promising results with several confirmed period bounce systems [91] [92]. Furthermore, by identifying CV candidates by their spectra rather than observing outbursts, it appears that the missing period spike has at last been found [48] although their outburst rates and properties are still not known.

Dwarf Novae are ideal candidates for an all-sky transient survey by WASP. The systems are relatively common and have fairly frequent large outbursts. Systematic surveys to identify these systems in the past (such as the Sloan Digital Sky Survey) have largely identified them based on their characteristic colours and spectra. An optical transient survey based on outburst detections would comple-

ment this well. For example, extremely low accretion rate systems, such as period bouncers, may appear similar to detached binaries from their spectra so detections of outbursts may be the only way to identify them. Unlike WASP, current optical transient surveys (such as the Catalina real-time transient survey [42]) have a comparatively low cadence so have not been able to identify the orbital (or superhump) periods from their data which is the most important piece of information in classifying a CV.

Using the WASP survey it may be possible to estimate the space density of dwarf nova outbursts and, using the detected periods, understand the distribution of the population and hence the evolution. While the WASP sample will still be incomplete (see analysis of completeness in Section 6.2) and contain selection effects, they will be different to those of spectral searches for CVs and will be better constrained than the currently known population (listed in Ritter and Kolb's catalogue [136]). The known population is based on many different surveys so selection effects are extremely complicated [47]. In contrast the WASP data provides the opportunity for a consistent survey which means selection effects can be more clearly defined.

This is important because discrepancies between CV population models and observations have presented a significant issue through out CV research. Numerous attempts have been made to create CV population models that explain the known sample with limited success [70] [80] [69] [17]. However, as the selection effects on the known population are unclear the significance of this is uncertain. Some research has suggested the population models are fundamentally wrong [127] while other work has suggested that the selection effects can explain the current inconsistencies [83]. A large sample of CVs discovered by a consistent method could help resolve these issues as it would be easier to determine whether the sample matched with what would be expected from the model.

1.5.3 Novae

Novae outbursts have been observed for over 2000 years. However, it was not until the 1920s that it was realised that classical novae represented a different phenomena

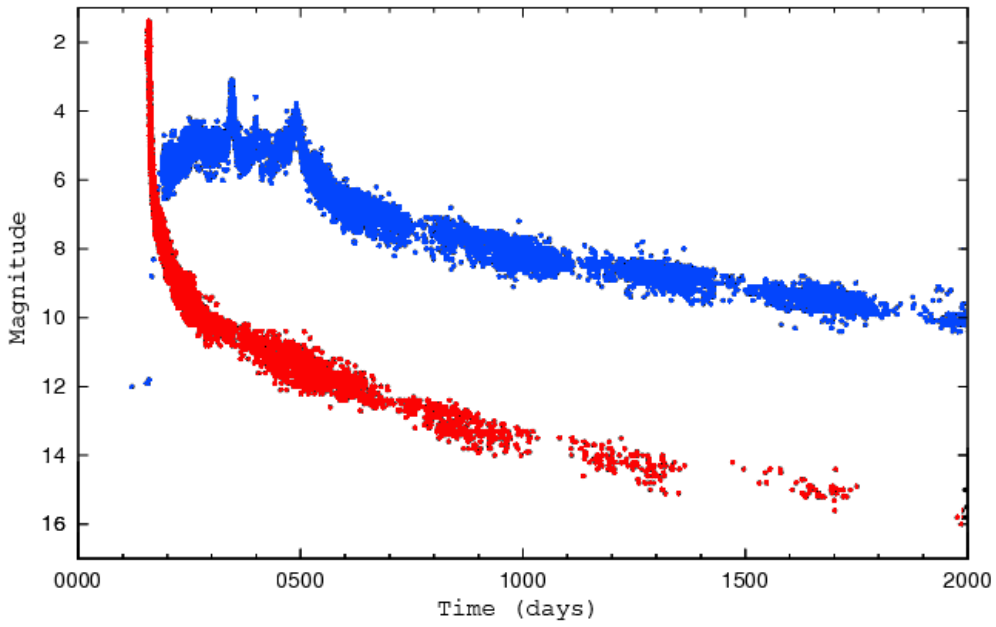

Figure 1.7: Light curves of the fast nova V1500 Cyg in red and slow nova HR Del in blue. The data was taken from AAVSO [1].

to supernovae [24]. Like dwarf novae, novae occur in cataclysmic variable systems and are a consequence of the accretion onto the white dwarf. Material striped from the secondary star forms an accretion disc which gradually deposits the material onto the primary (see above). Over time this layer of accreted hydrogen builds up putting the lower layers under increasing pressure. Eventually this become sufficiently great to initiate thermonuclear burning [150] which leads to a rapid runaway reaction causing the entire accreted layer to burn or be ejected as an expanding nova shell. This greatly increases the luminosity of the system, typically by 8-15 magnitudes [63]. The exact properties of the nova are determined by the white dwarf mass, the white dwarf temperature and the mass accretion rate [176]. Once the nova eruption is complete the system returns to its accreting state indicting that no long term change has occurred to the system as a whole. This process and the physics behind it is again well reviewed in Brian Warner's book *Cataclysmic Variable Stars* [167].

There are several different classifications of novae based on their photometric

and spectral properties [24]. Systems that are only known to have had one nova eruption are known as classical novae. The duration of these eruptions can vary dramatically. V1500 Cyg only took 3.6 days to decrease 3 magnitudes from peak outburst while HR Del took 230 days to do the same. A plot showing the light curves of a slow nova (in blue) and a fast nova (in red) is shown in Figure 1.7. As can be seen from this plot, fast novae can resemble WZ Sge systems around peak outburst which is an important consideration when classifying transient candidates.

Novae that are seen to erupt multiple times are classified as recurrent novae. Typically recurrent novae have recurrence times of decades and often have large orbital periods with giant secondaries [152]. These short recurrence times also require a high mass primary (often close to the Chandrasekhar limit) and comparatively high accretion rates [149]. Currently only 10 recurrent novae are known in our Galaxy with several others identified in neighbouring galaxies [24].

Observations of novae are scientifically useful for several reasons. Firstly, using detections of the peak apparent magnitude and the shape of the decline it is possible to use novae as distance indicators [38]. There are also several significant unanswered questions in our understanding of novae themselves [24]. For example, the role of novae in CV evolution is still poorly understood. It is thought that there may be a link with recurrent novae and supernovae of type Ia. In classical novae heavy elements are often detected in the nova shell suggesting that the nova eruption blasted off more than just the accreted material causing a net reduction in the white dwarf mass. However, in recurrent nova it is thought that the white dwarf mass (already near the Chandrasekhar limit) may be increasing [148]. The natural conclusion for this would be a type Ia supernova as described in Section 1.5.4. Secondly it is not understood whether classical nova and recurrent nova really represent the same population (with all novae being recurrent and our current recurrent nova population being those that repeat on the shortest time scales).

The potential for a survey using the WASP observatories to address these questions is somewhat limited. The current discovery rate for galactic novae is $\sim 8 \mathrm{yr}^{-1}$ [120]. The overall estimated rate in the Galaxy is $\sim 34 \mathrm{yr}^{-1}$ [38] with $\sim 12 \mathrm{yr}^{-1}$

predicted to be brighter than 11th magnitude in V [90]. This low rate of galactic novae means that they are normally discovered in the galactic plane. Fast novae in particular are confined to within 100 pc of the plane (although slow novae can reach up to 1000 pc) [24]. The WASP observatories do not observe in the galactic plane because of the problem of stars blending together (see Section 2.1). While it is possible for WASP to detect nova in other galaxies (such as M31), only the brightest examples could be found and only in ideal observing conditions.

An alternative source of detectable novae could be *tramp novae* which are thought to be stripped out of galaxies during galactic collisions [146]. Measurements of the positions and rates of these could provide a way to estimate the quantity and distribution of stars in intergalactic regions. From this it may also be possible to establish the proportion of mass in the universe that is found as these intergalactic stars. Novae are one of the best ways to measure intergalactic populations because they can be used as standard candles to accurately estimate their distance.

Overall, while WASP is not well suited to identifying novae in the galactic plane, it may be possible to detect intergalactic or halo novae. These could be used to estimate the distribution and quantity of stars in these regions. Novae also form an important consideration when classifying WZ Sge candidates because of the similarities in their light curves.

1.5.4 Supernovae

Supernovae were first identified as being different from novae in the 1930s [13]. Since then, extensive study has lead to them being subdivided into several different types although it now appears that there are only two causes for them [59]. A theory for type Ia supernovae is that they occur in close binary systems (similar to those described above). In these systems the accreted material builds up on the surface of the white dwarf until it reaches the Chandrasekhar limit. This causes the white dwarf to explode creating a highly luminous transient. The mechanism for this is not fully understood but, as described in Section 1.5.3, it is thought to occur in recurrent nova systems [148]. An alternative theory is that type Ia supernovae are caused by

two white dwarfs merging [65]. From this model it is difficult to understand the lack of variation in absolute magnitude but it may explain a subset of cases.

In contrast types Ib, Ic, II and IIdw are thought to be caused by the core collapse of a giant star. In these cases the core of the star runs out of fuel, again causing a highly luminous event as the core collapses to a dense remnant and the outer layers are ejected. Type II make up approximately 45% of core collapse supernovae [59]. They are caused by massive progenitors with hydrogen rich envelopes and can be identified by strong spectral Balmer lines. Type IIdw are similar to Type II but interact with the remains of a dense wind left by the progenitor. This interaction can be detected in radio waves [31] [32]. These make up approximately 30% of core collapse supernovae [59].

Finally types Ib and Ic are distinguished by a lack of hydrogen lines in their spectra (with Ic also lacking helium lines). These are believed to be caused by the core collapse of stars that have previously lost their outer layers and comprise approximately 25% of core collapse supernova [59]. A further subdivision of type I supernovae, called hypernovae, has also recently been identified. Several of these extremely large supernovae have been discovered and appear to correspond to long duration gamma ray bursts [46] [66] [99].

Optical light curves for supernovae appear as very bright transients that fade slowly over hundreds of days. After the initial event, the light curve is due to the radioactive decay of Nickel-56 and Cobalt-56. Type Ia supernova light curves tend to be quite consistent although there is far more variation in core collapse systems [152]. Early observations of supernovae are rare since they occur largely without warning. However, this early data is important for identifying the properties of the progenitor. Specifically detection of the shock breakout can be used to constrain the radius of the progenitor as was done for SN1993J [177] and SN2008D [102]. These events are particularly bright in UV and X-ray and have been detected several times such as in the UV for SNLS-04D2dc [144] and in the optical for SN1993J [89]. These early optical observations of SN1993J are shown in Figure 1.8. Durations of shock breakouts can vary from a few hundred seconds for a blue super giant progenitor to

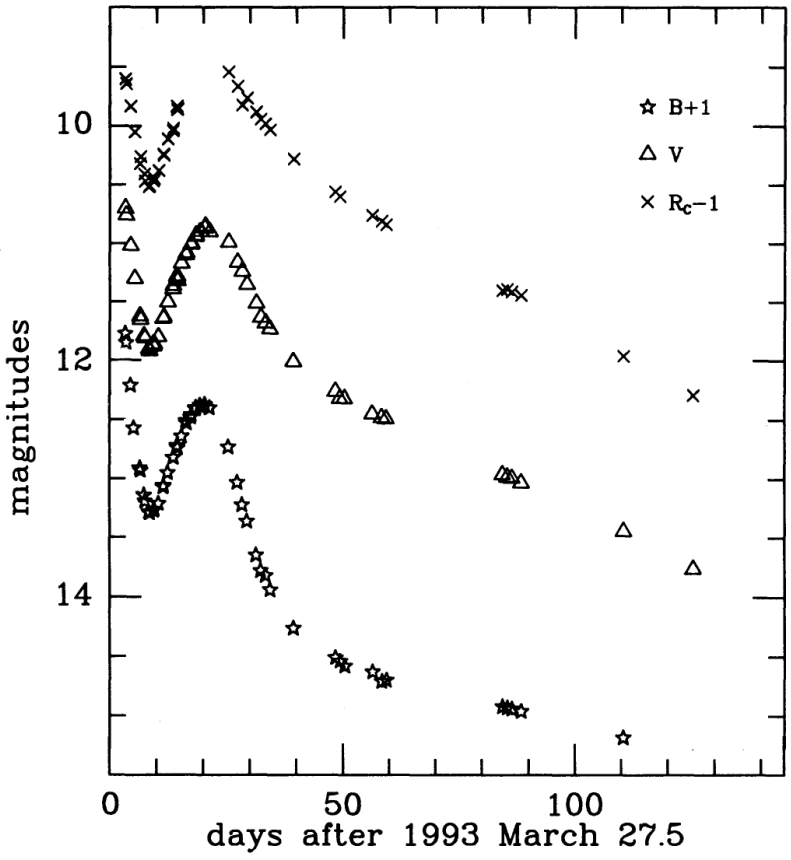

Figure 1.8: Optical light curve of SN1993J. The plot was taken from [89].

1-2 days for a red super giant progenitor [43].

While not as luminous in the optical it is still possible for this shock breakout to be detected. From the early optical detections of SN1993J [89] it appears that the breakout was ~ 0.6 magnitudes brighter than the later peak in the B band and ~ 0.2 magnitudes in the V band. For the longer duration cases of red supergiants and to a depth of 24th magnitude, there is an estimated upper limit of 1 detectable shock breakout event every 200 square degrees per year [29]. This is equivalent to an upper limit of 0.93 across the whole sky per year to a depth of 15th magnitude (the approximate magnitude limit of WASP).

Deeper surveys, such as Pan-STARRS and Catalina, are likely to detect more supernovae than WASP. However, the higher cadence of WASP means that it is able to measure the shock breakout. A detection of this could prove useful for constraining the radius of the progenitor and hence the theoretical models for supernovae and maybe even their connection to gamma ray bursts (discussed further below).

1.5.5 Gamma Ray Bursts

Gamma-ray bursts (GRBs) are short-duration bursts of gamma-rays from the distant universe. They were first detected on July the 2nd 1967 by the United States military Vela satellite systems that had been built to monitor the nuclear test ban treaty [81]. Over subsequent years these have been studied in more detail with substantial progress being made first with the launch of BeppoSAX [25] and then with Swift [49] [76]. GRBs have been found to occur at extreme distances with the furthest currently being GRB 090423 at a red shift of 8.3 [155]. This large distance implies that they must have been caused by extremely energetic beamed events.

The causes of GRBs is not certain although it appears that there may be two different types; long GRBs with durations of greater than ~ 2 seconds and short GRBs with durations of less than ~ 2 seconds [84]. Long GRBs are far better studied and are believed to be caused by relativistic jets formed during the supernova eruption of massive stars [122] [73] [171]. Short bursts are more of a mystery with

current theories favouring compact object merger or accretion onto a black hole [21] [88] [101].

Along with these burst of gamma rays, GRBs are accompanied by a bright optical afterglow which is caused by the interaction of the jet with surrounding matter. A plot showing the magnitudes reached by previously-observed optical afterglows is shown in Figure 1.9. As can be seen from this it is possible that a survey, such as WASP, with a depth of 15th magnitude could detect the brighter of these events. The brightest of these, GRB080319B, could even be seen with the naked-eye [129].

Independent observation of these could help further increase our understanding of GRBs. For example, if simultaneous X-ray observations were taken, the ratio to the detected visible light can be used to estimate the properties of the region the event occurred in and potentially establish whether it was in a galaxy. The really important scientific observations though could be the identification of a GRB without gamma-ray emission. These orphan afterglows are expected to be caused by a wider beaming angle in the optical than in the gamma-rays. Studies of this could help to constrain the beaming angle which it has not been possible to measure with current observations [53] [121]. WASP discoveries of GRBs could be particularly useful as they would represent some of the brightest events and hence easiest to carry out detailed follow-up observations of.

However, constraining the beaming angle in this way is difficult (this is discussed by Neal Dalal [37]). Perhaps most significantly, without the gamma-ray detections, it may prove difficult to confirm that an optical transient was caused by a GRB [55]. This is one of the major difficulties facing both current wide-field surveys (such as WASP) and deeper future projects such as Pan-STARRS and LSST (see Section 1.3) in contributing to this field.

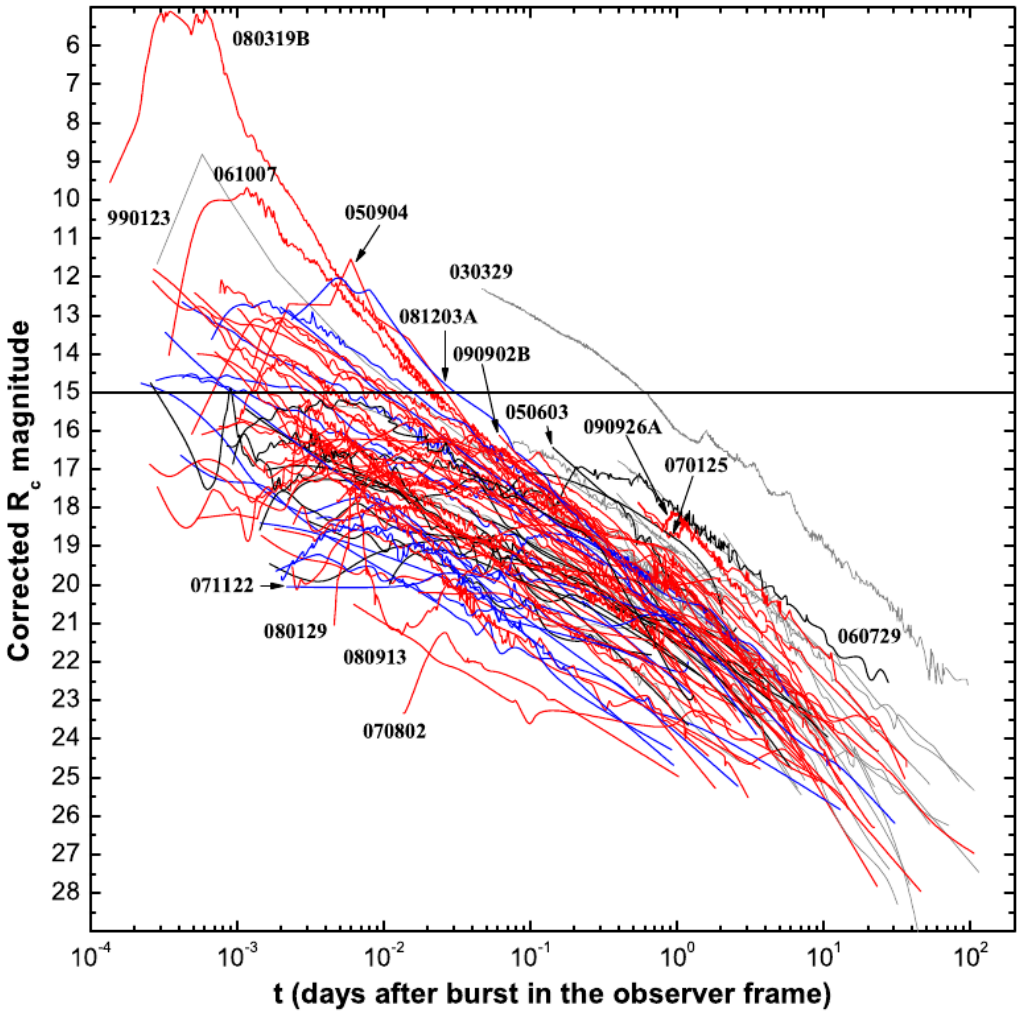

Figure 1.9: Optical light curves of all GRBs discovered before the end of April 2009. Magnitudes are corrected for Galactic extinction. Swift GRBs are shown in red and blue and pre-swift GRBs are shown in grey. The plot was taken from [76].

1.5.6 Pulsating Variable Stars

There are many different types of pulsating variable stars with a wide range of amplitudes and periods. While they are not normally transient, they can appear so in the WASP data if the star is too faint to detect at minimum but but bright enough at maximum. They are interesting not only because of their role in stellar evolution but many can also be used for distance estimates (such as in globular clusters [34]). As will be discussed in later chapters, the transient survey carried out in this thesis is primarily sensitive to high amplitude events as they are clearly distinct from the host star (see Section 4.7). Several high amplitude pulsating variables are discussed in this section as they may form a component of the final candidate transient population.

Mira variable stars

Miras are pulsating red giant stars that show regular periodic oscillations of over 2.5 magnitudes in the V band with periods of 80 to 1000 days [152]. The are thought to represent one of the final stages of stellar evolution and are found at the end of the asymptotic giant branch in the H-R diagram. Example light curves from several of these systems are shown in Figure 1.10. The stars themselves are red giants and expand and contract with these changes in luminosity. By measuring the period of Mira stars they can be used as distance indicators [52] to, for example, probe the structure of the galactic halo. Furthermore, the period can also be used as indication of stellar metallicity in the region [45].

Semi-regular variables

Semi-regular variables consist of giants and supergiants which show variability on a similar time scale to Miras. Indeed at least some are believed to be precursors to Miras [93] and have similar period-metallicity relations [45]. However, unlike Miras the amplitudes of these oscillations can be, and often are, less than 2.5 magnitudes in V and the oscillation itself can appear far less regular.

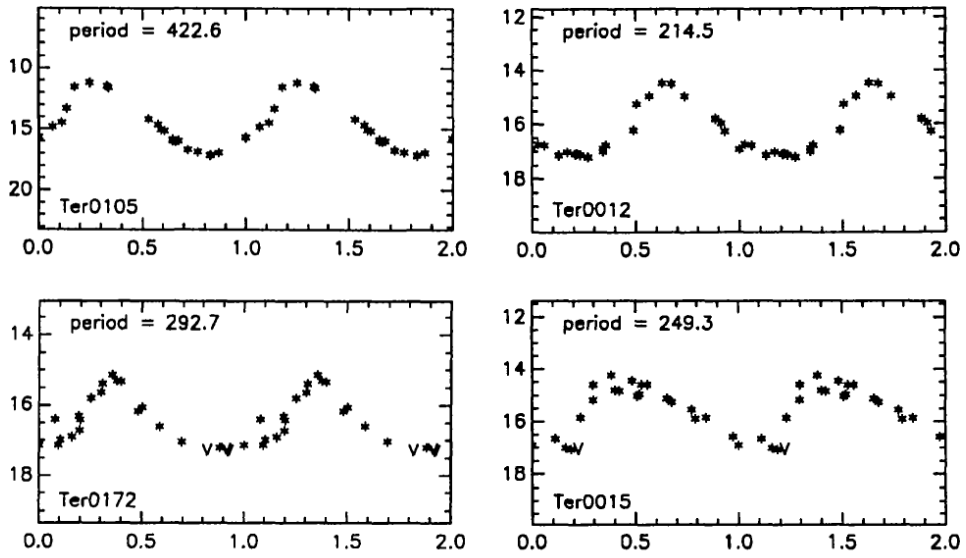

Figure 1.10: Folded light curves of 4 known Mira stars. These plots were taken from [10].

RV Tau variables

RV Tau stars are supergiants that show irregular luminosity and spectral oscillations where the star alternates between shallow and deep dips in luminosity. For some systems these alternations occur in turn but in others it can only be seen as a statistical effect over long durations. Periods between deep dips in luminosity vary from 30 to 150 days and amplitudes are normally between one and two magnitudes [152]. During these oscillations the spectral type of the system can change from F or G at maximum to G or K at minimum. RV Tau stars are often mistaken for semi-regular variables. However, more detailed analysis reveals them to be a separate class of object [126].

1.5.7 FU Ori Stars

FU Ori stars are young, pre-main sequence stars, that show large amplitude outbursts. During outburst the star can be seen to increase in brightness by $\sim$4 magnitudes and can take decades to return to quiescence [62]. Example light curves of FU Ori systems V1057 Cyg and FU Ori are shown in Figure 1.11. The current model

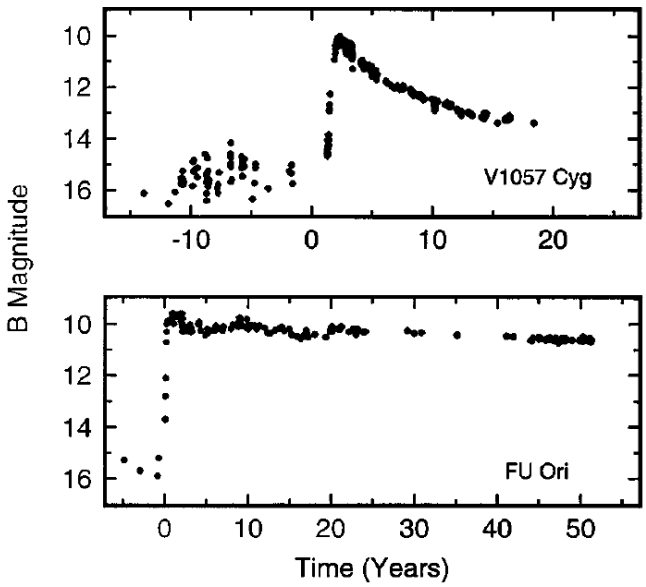

Figure 1.11: Light curves of V1057 Cyg and FU Ori. These plots were taken from [62].

predicts that these stars are surrounded by an accretion disc and these increases in brightness, as with dwarf novae, are caused by thermal-viscous instabilities in the disc [61]. These events cause the accretion rate onto the star to increase dramatically and in a single outburst up to $0.01M_{sun}$ can fall onto the surface of the star [62]. It is thought that these outbursts cause no dramatic long term alteration to the system and they will undergo at least ten of these before evolving onto the main sequence [64] [62]. Detections of these systems could help further increase the known population and hence further test the current models.

1.5.8 Gravitational Microlensing

If a high-mass foreground object passes in front of a distant light source it can cause an apparent distortion in the light seen from the distant source where multiple images of it are visible and even elongated into rings. The cause of this is gravitational bending of light around the foreground source due to Einstein's theory of relativity. This effect is known as strong gravitational lensing but, because of the huge

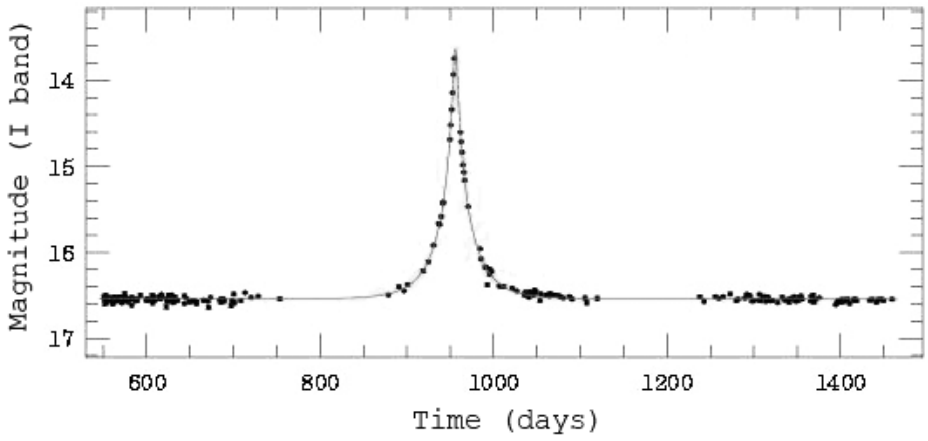

Figure 1.12: An example light curve of a microlensing event. Data taken from the OGLE project [173].

distances involved, seems static on our time scale.

However, a similar effect can also be seen if a lower mass object in our Galaxy, such as a brown dwarf or a stellar mass black hole, passes in front of a more distant star [112]. While the image distortion cannot be resolved this causes a transient increase in the brightness of the distant star. This increase in brightness can be several magnitudes and last for anything from days to years depending on the mass of the foreground object. An example light curve of this is shown in Figure 1.12.

Gravitational microlensing events are useful as they can be used as a probe of objects too faint to normally be detected. For example, they have been used to measure the dark matter content of the halo (such as with the MACHO [11] and OGLE [158] projects). It is also possible to identify extrasolar planets by searching for small changes in the shape of the light curve. Unlike discovering planets by the transit method, microlensing is most sensitive to planets at slightly larger separations of 1 to 5AU. This technique has successfully been used by the OGLE project [19].

Every year 500-600 candidate microlensing events are detected [5] although most are detected around the galactic bulge, where WASP does not observe, or are too low amplitude for WASP to identify. However, it is possible that WASP could detect higher amplitude examples and, if a microlensing event were detected,

WASP would be well suited to identifying any extrasolar planets because of the high cadence of the coverage.

1.5.9 Tidal Disruption of a Star by a Supermassive Black Hole

There is considerable evidence that there are supermassive black holes at the centre of all, or at least most, galaxies including our own. For example, comparing the movements of high proper-motion stars near the centre of our Galaxy to mass distribution models reveals the presence of a large amount of mass in a comparatively small central region [51]. Accretion onto these is thought to drive the extreme fluxes seen in active galactic nuclei. However, even if the galaxy is not active it is thought that the black hole remains. A star drifting too close to a galaxy's central black hole could be tidally disrupted by the large gradient in gravitational forces across it. The disrupted remnants of the star would then form an accretion disc around the black hole causing a significant increase in luminosity [132].

In the past it was theorised that these disruption events may be frequent enough to explain how active galactic nuclei are powered. However, current estimates of their frequency are far lower suggesting instead that the associated increase in brightness is transient. The frequency of tidal disruptions is dependent on the properties of the galaxy as a low star density would mean a chance encounter is less likely and too large a supermassive black hole would cause smaller stars to be swallowed whole without first being disrupted. In a less luminous galaxy it is estimated that a tidal disruption event occurs approximately once every 10^4 years [98]. This is equivalent to around once a year in the Virgo cluster [132].

The duration of one of these events is dependent on the size of the black hole and the star that is disrupted. For a typical main sequence star it is calculated that the transient event should last for 0.1-0.2 years [153] with a luminosity of no less than $10^{-3} - 10^{-2}$ of its Eddington luminosity in the U and V bands [160]. For a red giant the accretion of the star would be fainter but last far longer with the black hole being illuminated to 1/30th of its Eddington luminosity for up to a thousand years [153].

A number of claims have been made of observations of these events although confirmation of them has proved difficult. For example, a faint ultraviolet flare lasting for approximately a year was detected at the centre of NGC 4552 [133]. In 1986 an anomalous increase in optical brightness in the galaxy NGC 5548 was observed [118]. However, as it was an optically variable Seyfert galaxy it was not possible to be sure that the increase in brightness was due to a tidal disruption event. High-luminosity soft X-rays were detected by ROSAT coming from three galaxies with no past evidence of Seyfert activity. Chandra observations of these a decade later showed that these X-rays were no longer being detected and confirmed that two of the galaxies were not active [58]. More recently, two UV/optical flares were observed in apparently inactive galaxies [50]. Light curves taken of these events matched well with theoretical tidal disruption models.

With so few of these events detected any new discoveries made by transient surveys could help to further constrain theoretical models and rates of these events. A detection of a tidal disruption would also indicate the presence of a supermassive black hole which could be used to establish what types of galaxies contain them. Furthermore, the luminosity of the tidal disruption flare is dependent on the mass of the black hole so could be used to estimate it [98].

1.5.10 New Phenomena

It is also possible that new transient phenomena could be discovered by a high cadence survey such as is being carried out by WASP. For example, in 2006 an unexplained transient peaking at 21st magnitude in i and z and lasting for $\sim$100 days was found using the Hubble Space Telescope [16]. While it seems unlikely that a new type of bright, long duration transient could have remained undiscovered for so long, shorter duration phenomena lasting only tens of minutes or hours could easily have been missed. For this reason an open mind must be kept when looking at candidate transients with no obvious cause.

1.6 The Sensitivity of WASP to Transient Phenomena

The sensitivity of WASP to the transient phenomena discussed in Section 1.5 is dependent on several parameters. Primarily these are the amplitude of the outburst and the decay time. Due to the requirement to remove non-variable stars from the orphans data (as described in Section 4.7) the search carried out in this thesis is insensitive to low amplitude (less than 1-2 magnitude) variability. Furthermore, while WASP's cadence is extremely high compared to other surveys, it is still insensitive to transient events that are detectable for less than 15 minutes.

Figure 1.13 shows a sketch plot where WASP's sensitivity is shown as a black line. The dashed section marks where WASP will not be able to detect a decline of two magnitudes in a single season of observing. In the cases of gamma ray bursts and supernovae the amplitude is determined from the host galaxy rather than the progenitor as, in most cases, WASP will be unable to resolve the galaxy.

The plot indicates that WASP is sensitive to cataclysmic variables, novae, FU Ori stars, high amplitude pulsating variables such as Miras and some higher amplitude microlensing events. WASP should also be able to identify longer duration gamma ray bursts and stellar flares although in many cases they will fade too quickly to be identified. Low amplitude events such as supernovae and tidal disruptions of stars (compared to the normal brightness of the host galaxy) are less likely to be identified as they are difficult to distinguish from their host.

Figure 1.13 also indicates several potential difficulties in classifying new transient candidates. Extremely high amplitude dwarf nova outbursts could be difficult to distinguish from low amplitude novae. Longer duration events are particularly difficult to classify as Miras, semi-regular variables, microlensing events and supernovae all occupy overlapping regions of parameter space. Microlensing and pulsating variables will both show a gradual rise and decline with pulsating variables showing further rises and declines. The shock breakout from a supernova could be confused with a lower amplitude stellar flares although the colours (when available) or the presence of a galaxy should indicate a likely classification.

The problems identified here are further complicated when gaps in observing

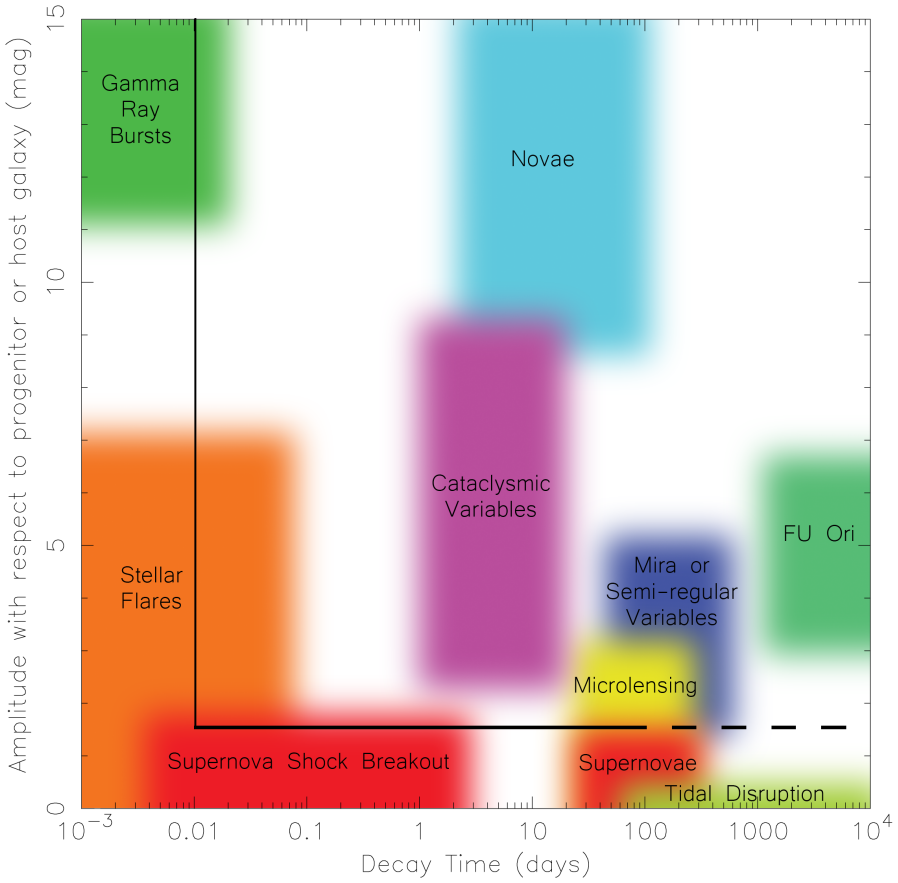

Figure 1.13: A plot showing the approximate parameter space occupied by various variable objects. Amplitude represents the maximum amplitude from peak outburst to quiescence (or in the case of gamma ray bursts or supernovae to the brightness of the host galaxy as these will not be resolved by WASP). The decay time represents the number of days for the outburst to decline by two magnitudes (or to quiescence for low amplitude events).

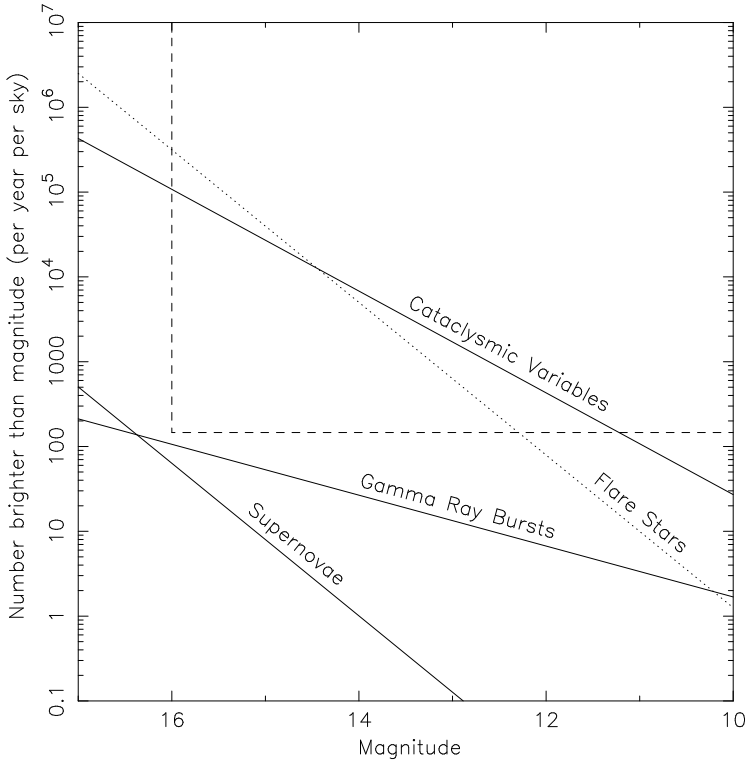

Figure 1.14: A plot representing the observable parameter space for WASP with magnitude on the x-axis and number of outbursts brighter than the x-axis magnitude per sky per year on the y-axis. Labelled lines show the estimated numbers of outbursts for cataclysmic variables, flare stars, gamma ray bursts and supernovae. The dashed box represents the region in parameter space where WASP would be expected to detect at least one event per year.

and the sky background are considered. A long duration event that is close to the limit of how faint WASP can observe may only be detected for a few nights making classification of it extremely difficult.

Another important consideration is the number of events that occur each year that are detectable by WASP. Figure 1.14 shows the number of events peaking at brighter than a given magnitude occurring across the whole sky each year (this is similar to Figure 1.3 discussed in Section 1.1.3 but with estimates of the rates of several types of transients). The boxed area represents the parameter space for which WASP would be expected to identify at least one event in an observing season.

The line for cataclysmic variables was determined by calculating the approximate number of outbursts brighter than 10th magnitude from the Ritter and Kolb

catalogue [136] which should be almost complete at this brightness. The gradient was chosen to be -1 rather than the theoretical -3/2 because of the effects of scale height reducing the numbers of fainter cataclysmic variables (see Section 1.1.3).

There is little knowledge of extreme stellar flares so it was not possible to position the flare star line accurately. However, the gradient was chosen as -3/2 because flare stars will typically be far closer than cataclysmic variables so extinction and scale height should not play as significant a role.

The rate for supernovae was determined by using the average number of discovered supernovae brighter than 15th magnitude over the last 10 years with a gradient of -3/2. The rate of gamma ray bursts was calculated by considering the number of SWIFT GRBs with peak brightness greater than 15th magnitude (see Figure 1.9). A gradient of -1/2 was found to fit the SWIFT GRB data. This shallow gradient is likely to be because of the finite extent of the universe.

FU Ori stars and tidal disruption events are not included as their rates are expected to be extremely low and uncertain. Microlensing events and pulsating variable stars are more common but, due to their low amplitudes, the numbers detectable by WASP would be significantly lower than any estimated rate. For novae most examples that would be bright enough to detect would be found in the galactic plane which WASP does not observe.

From this it is clear that the transients WASP discovers will be dominated by cataclysmic variables (not including pulsating variable stars) with possible large numbers of flare stars. Gamma ray bursts could also be detected with a strong possibility of a supernova being detected over several years. However, this is likely to be an overestimate of the number of gamma ray bursts and supernova since (as is shown in Figure 1.13) many of these that occur will not be in a parameter space WASP is sensitive to.

Chapter 2

The WASP Orphans

2.1 WASP Observing Strategy

As was shown in Section 1.4, WASP has the potential to compete with other notable transient surveys. However, the observing strategy of the telescopes also plays an important role in establishing what types of transients WASP is sensitive to.

To create a systematic strategy the sky has been divided into fields. Each field represents a region of sky that fills the field-of-view of one of the WASP cameras. Repeat observations of these fields can then be compared to create a light curve for the sources inside them. The field names (SW(aaaa)±(bbbb)_(ccc)) are determined by the right ascension (aaaa) and declination (bbbb) of the centre of the field and the camera the field was observed with (ccc).

In normal operation, during the night each WASP camera moves between 8 fields. Each field is observed for 1 to 2 minutes (depending on whether 1 or 2 exposures are taken). Each exposure takes 30 seconds, read-out is 4 seconds and acquiring the field takes just under 30 seconds. Once a field has been observed the camera moves on to the next and the process is repeated. Once all 8 fields have been observed, the camera moves back to the original field and proceeds to cycle through them again. Throughout the night as each field sets it is replaced in the cycle by a new field that is rising. On average this observing strategy provides over 6 hours of coverage on six fields (∼50 images) and a further 4 hours coverage on 10

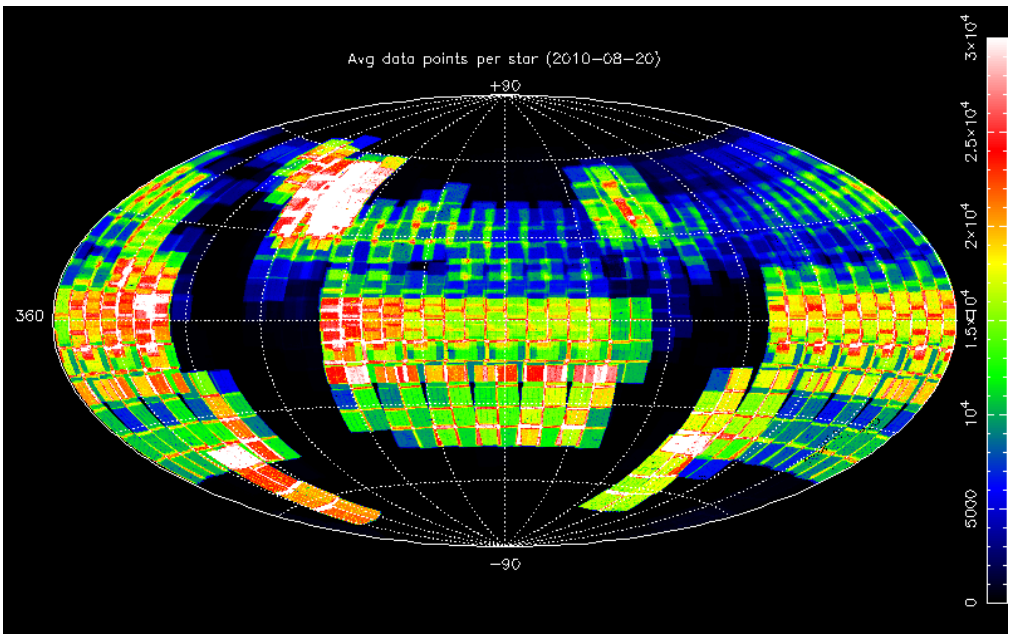

Figure 2.1: A plot of the sky coverage for WASP planet fields in right ascension and declination as of August 2010. The colours represent the average number of observations for that region of sky with a key for this on the right. [6]

fields (∼35 images) per night per camera.

These fields are known as the *planet fields* and are processed by the planet hunting software. To avoid the fields becoming too overcrowded the galactic plane is avoided. Fields passing too close to the moon are also omitted as the high background light levels would make accurate flux measurements very difficult. The sky coverage of the planet fields, as of August 2010, is shown in Figure 2.1.

Each night two consecutive images are also taken for all visible fields. Data from fields observed in this manner are called the *all-sky data*. This produces data over a far larger region than the standard observations but with a far lower cadence. Besides these observations bias frames, thermal dark-current exposures and twilight-sky flat field exposures are also taken each night at dusk and dawn.

2.2 An Overview of the WASP Pipeline

The WASP pipeline is described in detail in Pollacco's 2006 paper [125]. However, the following sections contain an overview of the various steps that are carried out.

2.2.1 Reduction of images

Bias, dark and flat-field frames are taken at dusk and dawn each night. The ten to twenty calibration frames of each type are tested statistically to remove outliers before combining them to make master bias, dark and flat-field frames. The master bias is then subtracted from all dark, flat-field and science frames. A correction for temporal drift is applied using the mean counts in the overscan region. Following this, the master thermal dark frame, scaled for exposure time, is subtracted from all flat-field and science frames. The sky-flats are taken in a set of fifteen exposures with durations from 1 to 30 seconds and peaking at ∼28000ADU in the centre of the image. Corrections are applied for the travel time of the shutter and vignetting and then the science frames are divided by the master flat-field for that night.

2.2.2 Astrometric solution

These reduced images are searched using the Starlink EXTRACTOR package [22] to identify detections. The threshold for doing this is set at 4 sigma or greater. A subset of the TYCHO-2 catalogue [68] covering a region slightly larger than the expected field position is then used to establish a preliminary astrometric solution. The 100 brightest stars from this sub-catalogue are automatically compared to the brightest WASP detections to match patterns and hence identify stars. This is refined by matching further stars and correcting for barrel distortions and the location of the optical axis. The rms scatter from the TYCHO-2 positions is typically around 0.2 pixels (2.7 arcseconds).

2.2.3 Identification of orphan detections

Once an astrometric solution has been established the EXTRACTOR detections are matched with catalogued known stars. The catalogue used is a subset of USNO-B1.0 [106] again chosen to cover a region slightly larger than the expected field position and only for stars with r2 magnitude brighter than 15th. Any unmatched EXTRACTOR detections or detections with substantially different magnitudes to what's expected from the catalogue are classified as *orphan detections*.

2.2.4 Flux measurement

Stars from the USNO-B catalogue with r2 magnitude brighter than 15 and any identified orphan detections are used to create a photometric input catalogue. To account for gradients in the sky background an exclusion mask is created consisting of all pixels within a magnitude-dependent radius of any objects on the photometric input catalogue. A quadratic surface is then fitted to the remaining pixels. This quadratic fit is then subtracted from the image. Images with large numbers of significant deviations from this fit are rejected as they are likely to have been effected by cloud cover.

Aperture photometry is carried out at the positions of all objects in the photometric input catalogue with radii of 2.5, 3.5 and 4.5 pixels. The sky background for each object is calculated from an annulus of of radius 13 to 17 pixels. The raw fluxes from this aperture photometry are then calibrated using an algorithm called PPWASP. This corrects for primary and secondary extinction, instrumental colour response and the system zero-point. The WASP flux (f_{wasp}) corresponds to micro-vegas and can be converted into a WASP magnitude (m_{wasp}) using the formula:

$m_{wasp} = -2.5 \times log_{10}(\frac{f_{wasp}}{1{,}000{,}000})$

These fluxes have a precision of less than one percent for magnitudes brighter than 12th.

In 2004 only WASP north was operating and only with 5 cameras for 6 months. However, from this period alone light curves for ~ 6.7 million objects were produced with over 12.9 billion data points in total.

2.3 The Orphans Database

The orphan detections are not useful for planet hunting so are stored separately in an orphans database. They can represent many different thing such as faint stars detected in good conditions, spurious detections on the chip and transient phenomena. The number of orphans detected in a given image can vary significantly depending on the features of the field and observing conditions (see Section 4.1). For a good image it is typical for there to be a few hundred orphans detected. As of September 2010, the orphans database contains 2.5 billion detections from the planet fields and 64 million detections from the all-sky fields. The various values recorded for each orphan are listed in Table 2.1.

As the orphans database is likely to contain most of the transient objects detected by WASP the majority of this thesis is focused on automatically identifying these phenomena from other unwanted features.

Data	Description	Cone search	Field search
tstart	The start time of the observation	x	
tmid	The middle time of the observation in seconds after JD 2453005.5	x	x
ra	The right ascension of the detection	x	x
declination	The declination of the detection	x	x
flux	The measured WASP flux of the detection	x	x
flux_err	The error on the WASP flux	x	x
rawflux	The raw flux in counts per image	x	x
rawflux_err	The error in the raw flux	x	x
skybkg	The measured sky background around the detection	x	x
ccdx	The CCD coordinates in the x-axis	x	x
ccdy	The CCD coordinates in the y-axis	x	x
image_id	The image identification code	x	x
night	The date the observation was taken on	x	x
field	The field the observation was in	x	x
camera_id	The identification code of the camera	x	x
az	Azimuth of the detection		x
el	The elevation of the detection		x
FWHM_major	Full width half maximum along major axis		x
FWHM_minor	Full width half maximum along minor axis		x

Table 2.1: The data recorded for each WASP orphan detection. The third and fourth columns mark which values are retrieved by the cone and field searches respectively.

2.4 Accessing the Database

There are two pieces of software available to search the orphans database. Either all detections around a chosen position can be retrieved (see Section 2.4.1) or all data can be extracted for a given year, field and camera (see Section 2.4.2).

2.4.1 The cone search algorithm

To search the orphans database, Richard West at Leicester University developed a piece of software to carry out a cone search at a user specified position returning all orphans across all years and fields within a chosen radius. The data returned includes information on positions (both in terms of sky position and CCD coordinates), flux values (including unprocessed values and errors), times of observation, the camera used, the field the detection was found in and a unique identification code for the image. These data outputs from the cone search are marked in Table 2.1. This method of accessing the data is used in Chapter 3.

2.4.2 Accessing the data by field and the clustering algorithm

An alternative method to search the database uses a C+ program, called worphget, to access the orphans data marked in Table 2.1. This retrieves all orphans from a chosen field, season and camera.

When accessing the data by this method it is necessary to be able to group related detections together. This would allow orphans caused by the same feature to be identified as a single object. An algorithm (worphbin) that had been developed by Richard West was used to do this (private communication).

The algorithm divides the observed sky from an individual WASP field into a grid of bins each 30 arcseconds across. Any orphans in a bin are clustered together. If one of the neighbouring eight bins contains any orphans these are also added to the cluster. These connected bins are treated in the same way so are in turn connected to any other neighbouring bins containing orphans. This is shown graphically in Figure 2.2. Once this process has been carried out across the whole field, the connected

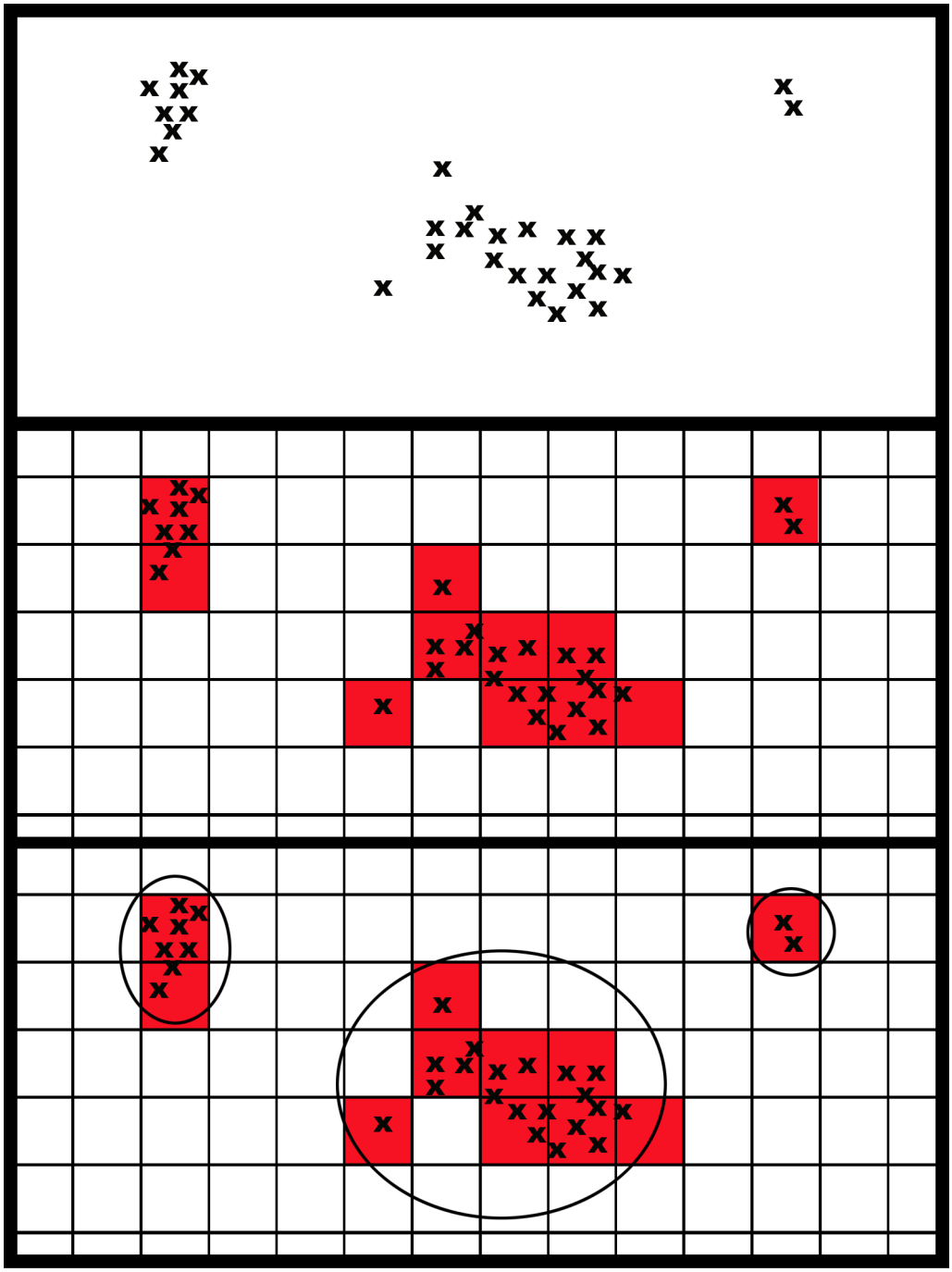

Figure 2.2: Graphical representation of the clustering algorithm. The top box shows the positions of a number of individual WASP orphans. The field is then divided into bins as shown shown in the second box. Bins containing WASP orphans are then connected to adjacent bins containing orphans. These groups of connected bins are then identified as clusters (circled in the final box).

Data	Description
ra	Median right ascension of the cluster
dec	Median declination of the cluster
xcent	Median x-axis CCD coordinates
ycent	Median y-axis CCD coordinates
xmin	Minimum x-axis CCD coordinates
xmax	Maximum x-axis CCD coordinates
ymin	Minimum y-axis CCD coordinates
ymax	Maximum y-axis CCD coordinates
area	Area of cluster (number of bins)
numpoints	Number of orphans in cluster
flux mean	Mean flux of orphans in cluster
flux chisq	Chi-square of flux of orphans in cluster
flux skew	Skew of flux of orphans in cluster
flux kurtosis	Kurtosis of flux of orphans in cluster
az	Median azimuth of the cluster
el	Median elevation of the cluster

Table 2.2: The data calculated and recorded for each WASP orphan cluster

orphans can then be analysed as clusters rather than individually. The position of the cluster is determined as the average position of the detections that it contains.

The algorithm not only groups the orphans together but also calculates several properties of these clusters. These are listed in Table 2.2.

2.5 Asteroid Identification

Neil Parley has independently been working on the identification of known asteroids in the orphans database. To achieve this he cross-correlated the positions of catalogued asteroids with the WASP data. An orphan was considered a positive detection if it was within two camera pixels (27.4 arcseconds) of an asteroid position, if the flux matched what was expected and if the detection was not blended with a nearby star. Once an orphan was identified as originating from an asteroid the detection was flagged and not included in results from future queries of the database. A more detailed description of this can be found in his paper [117].

2.6 The USNO-B Catalogue

The USNO-B1.0 catalogue [106] is used both by the WASP pipeline (see Section 2.2) and in later chapters as part of an automated search algorithm (see Section 4.7). The USNO-B catalogue is an all-sky catalogue with three colour, two epoch coverage and is complete to $V \sim 21$. The measurements were collected from various photographic plate surveys from 1949 to 2002 and then digitised by the Precision Measuring Machine at the US Naval Observatory Flagstaff Station.

The catalogue is used, both in the WASP pipeline and as part of the search algorithm in Chapter 4, because of its completeness to faint magnitudes and its all-sky coverage. However, the photographic nature of the survey limits its precision. The astrometric precision is 0.2" although in some cases systematic offsets of 0.25" were found. Photometric accuracy is 0.3 magnitudes. However, the accuracy for faint magnitudes is dependent on the photometric standards available (only 44 percent of fields have faint calibrators on the same plate). This means that the accuracy in some regions can be far better or worse than this.

Due to the data being taken from photographic plates, measurements near the edge of a plate can be erroneous. Errors can also occur if the object being observed is resolved as no contingency was included to photometrically calibrate resolved objects.

2.7 Data Quality Issues

There are various data quality issues that exist in the WASP data that have to be considered when searching for transients. In the case of blurred images the detections are often still usable whereas with more severe problems (as listed in Section 2.7.3) the data from effected images may need to be discarded in its entirety.

2.7.1 Regions not cross-correlated with the USNO-B catalogue

The WASP cameras were found to slowly drift in right ascension and declination during the season. This resulted in the area of the sky observed for each field being

far larger than expected. In the majority of fields this meant that some regions near the edge were not cross-correlated with the USNO-B catalogue in the pipeline phase and thus all detections were included in the orphans database. An example of this can be seen in Figure 2.4 along the top and on the left. This issue does not effect the scientific value of the data and is not a problem directly. However, it is an important consideration when attempting to characterise the data to identify other issues such as are discussed in the following sections.

2.7.2 Blurring in images

The WASP telescopes have temperature dependent focus problems. As the CCDs are not parallel to the lenses, this means that parts of some images are not in focus. An example of this is shown in Figure 2.3. The severe blurring in the lower corner can cause erroneous detections of orphans. The extent of this problem can be seen in Figure 2.4 where the positions of detected orphans are plotted for the same field. The blurred corner in Figure 2.3 corresponds to the corner with the far more dense distribution of orphans. While this example is a particularly severe case, this problem can be seen to a lesser extent in many of the WASP fields.

Blurred images or regions of images can be identified by analysing the full width half maximum of the data. The full width half maximum is the distance (in pixels) between points on the opposite sides of the detection which are determined to have half the maximum flux value. In the WASP pipeline this is calculated automatically both along a major axis (the direction in which the detection is most extended) and a minor axis (the perpendicular direction).

The image on the left of Figure 2.5 shows the average full width half maximum of orphans (along the major axis) in the field shown in Figure 2.4. From this it can be seen that the full width half maximum is larger in regions with severe blurring. The image on the right of Figure 2.5 shows the average elongation of the detections (the full width half maximum along the major axis divided by the full width half maximum along the minor axis). For this the dependence on focus is far less prominent especially if the heavily populated regions that were not

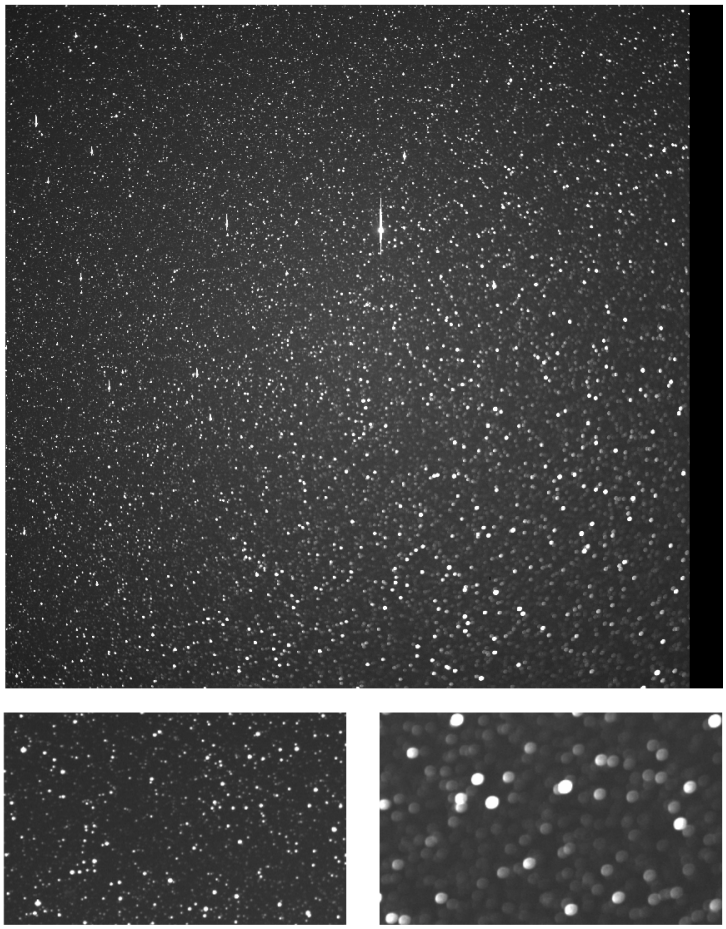

Figure 2.3: An example of a severely blurred WASP image with zoomed in images from regions with and without blurring.

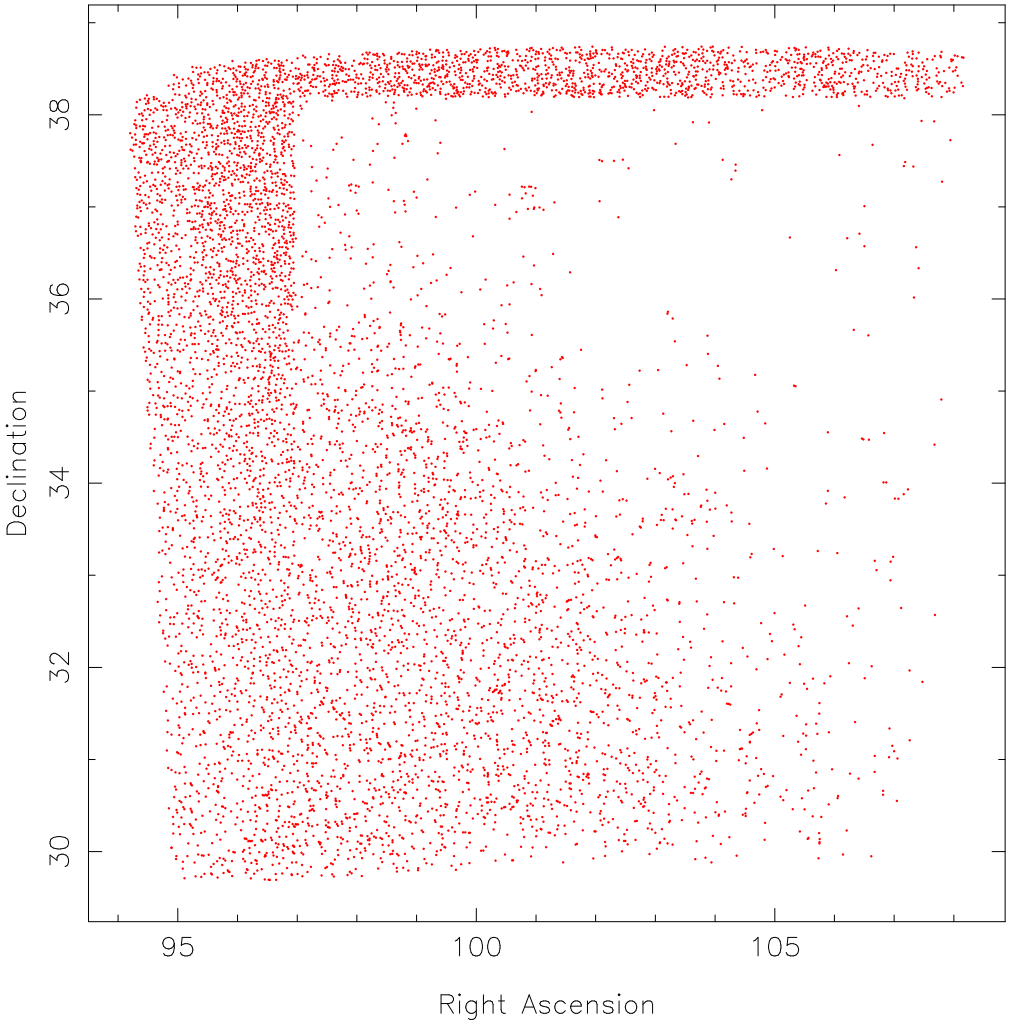

Figure 2.4: WASP orphans from a field with severe blurring problems. The band of detections along the top and left of the plot were caused by the catalogue matching error. The dense region of orphans in the lower left corner was caused by poor focus.

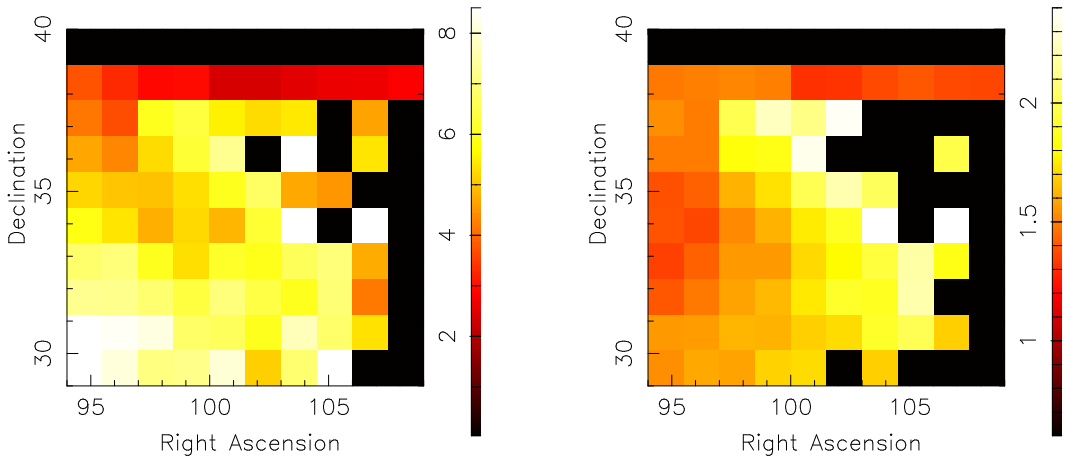

Figure 2.5: An example field showing variations in full width half maximum with focus. The plot on the left shows the average full width half maximum (major axis) in different regions of the field. The plot on the right shows the average elongation of detections.

cross-correlated with USNO-B are considered.

Only in severe cases are blurred images sufficiently badly effected to require data to be discarded. In the cases where it is necessary the full width half maximum can be used to identify the problem (see Section 4.8). However, poor focus can causes other issues, for instance with cross-correlation with catalogues (see Section 4.7.2).

2.7.3 Bad images

In a small proportion of images the pipeline fails to carry out a reliable analysis and a large number of orphan detections are found. These are referred to as *bad images*. They can occur if there is a problem with measuring the background which could cause the number of chance detections of the random background noise to dramatically increase. Another error that can occur is that when the images are read from the CCD they can become misaligned. An example of this is shown in Figure 2.6. What seems to have happened is that the top part of the image is at the bottom and the bottom part of the next image is at the top. In these cases the USNO-B cross-correlation fails for at least part of the image creating a large number of orphans that are not in the correct part of the sky. If a similar problem occurs on a series of images this can create large numbers of candidate transients

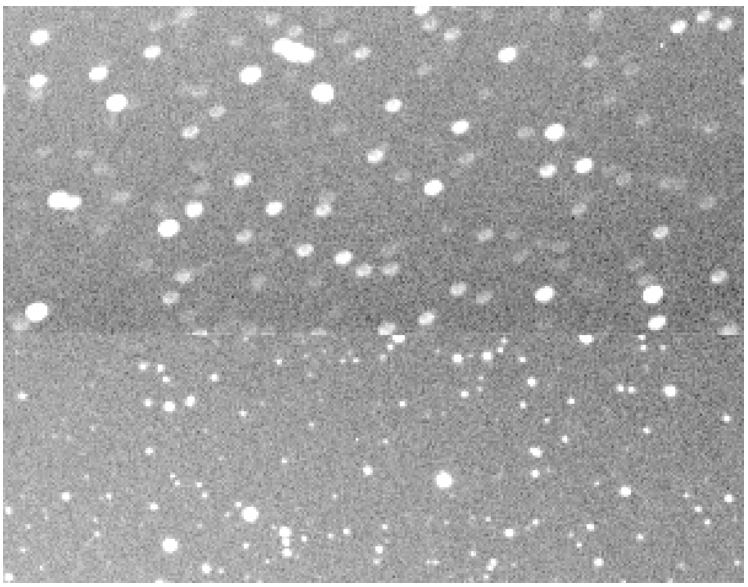

Figure 2.6: A misaligned section from a WASP image where the top of one image has been joined to the bottom of another.

on a given night. A third type of error was found in the targeted search for gamma ray bursts (see Section 3.6). The camera moved during an exposure causing every star to be detected twice at a slight offset (see Figure 3.16).

These various problems can be characterised by unusually large numbers of orphan detections in the images. Cumulative histograms of the number of orphans per images are shown for two fields in Figure 2.7. The field shown in green has good focus and no regions where the USNO-B catalogue was not matched with the data. The field shown in red has both poor focus and extensive regions where the USNO-B catalogue was not cross-correlated with the data (this field is plotted in Figure 2.4). From this it can be seen that the typical number of orphans per image can vary depending on the focus and the extent of any regions that were not cross-correlated with USNO-B. However, in each field in less than one percent of images the number of orphans is drastically higher. These correspond to bad images where a serious error has occurred in the WASP pipeline. This property of bad images can be used to filter them out (see Section 4.4).

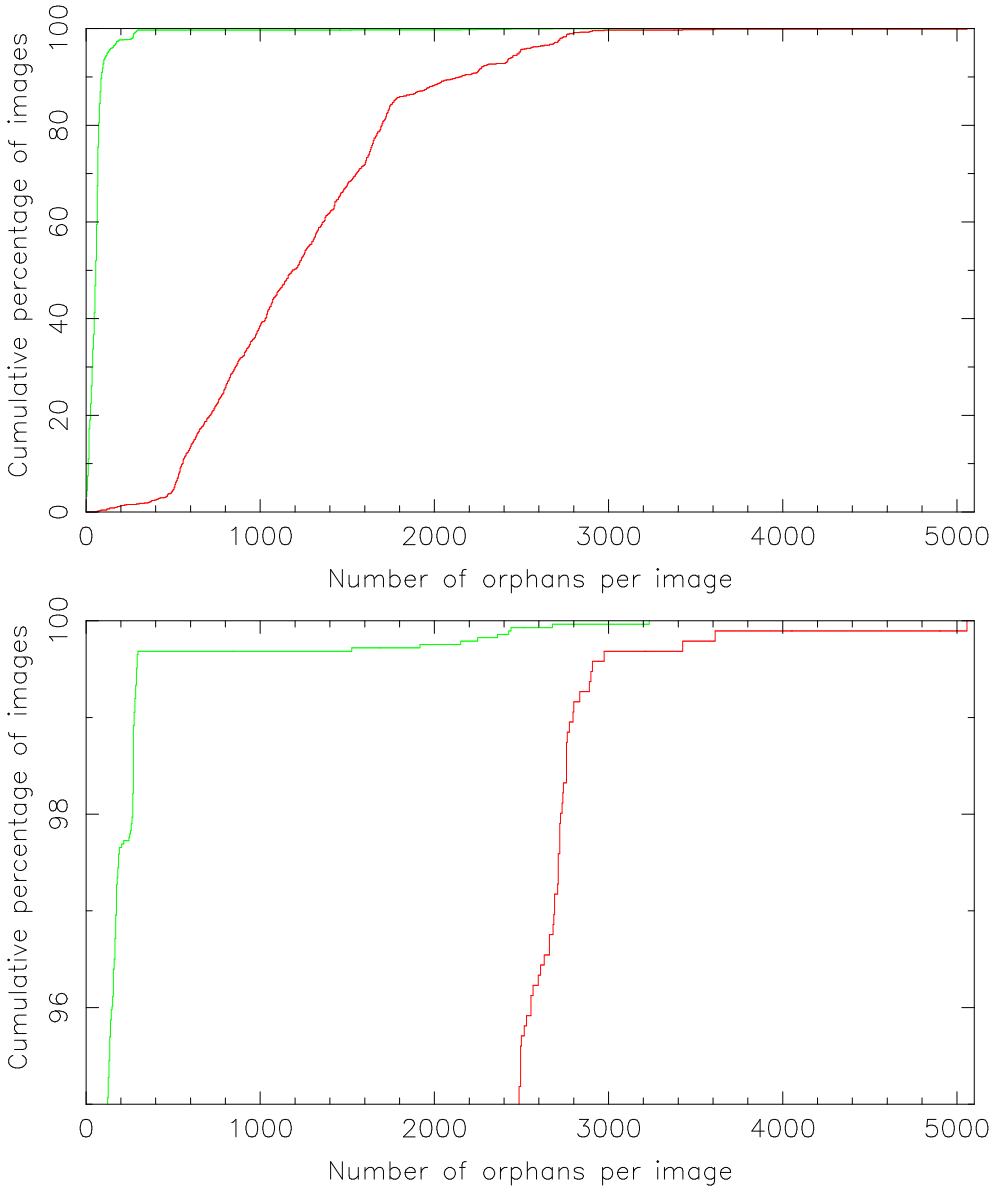

Figure 2.7: A cumulative histogram of the number of orphans per image. The field shown in red has severe focus problems and extensive regions not matched with USNO-B. In contrast the field shown in green does not have these issues. The lower plot shows the same data but only for the five percent of images with the most orphans.

Chapter 3

A Targeted Search for Transient Phenomena

3.1 Motivation

Besides any new transients detected by WASP, the orphans database also contains a large number of known transient phenomena. These are of interest for several reasons. Firstly the number detected and the quality of the data provides a useful indication of the effectiveness of WASP in surveying transients. Secondly the sample found in the data will be a useful test set that can be used to calibrate automatic transient searches (see Chapter 4). Finally, it is also possible that the WASP data may contain useful information on some of these phenomena. For example, the high cadence coverage of dwarf novae means it is possible to measure the superhump period which may have been missed in previous detections. Also there is the potential to detect the shock breakout from a supernova which normally occurs before observers become aware of it (see section 1.5.4). For Gamma Ray Bursts there is a chance of detecting an optical counterpart (see section 1.5.5). For these reasons the WASP orphans database was searched at the locations of known cataclysmic variables, supernovae and gamma ray bursts.

Furthermore, using a similar targeted search method it may be possible to confirm new transient phenomena from a list of candidate positions. This is at-

tempted in Section 3.7 by searching the database at the positions of known X-ray sources.

3.2 General Method

The method used to carry out these targeted searches was to first establish a list of candidate positions, either from known transient phenomena in Sections 3.4, 3.5 and 3.6 or from positions of candidate transients in Section 3.7. The cone search algorithm (see Section 2.4.1) was then used to search at each of these positions with the search radius chosen based on the astrometric precision of WASP (see Section 3.3) and the precision of the catalogue being used. Depending on the size of the candidate list and the nature of the transients being searched for, various automatic selection criteria were then applied before each was examined individually.

3.3 Astrometric Precision of WASP

To determine the astrometric precision of the WASP data, the orphans were searched at the positions of known Ritter and Kolb cataclysmic variables [136] as described in Section 3.4. For the purposes of establishing the precision a search radius of 60 arcseconds was used. The offsets from each detected dwarf nova in right ascension and declination are shown in Figure 3.1. The precision of the Ritter and Kolb catalogue is better than 1 arcsecond for the dwarf novae used here.

From this it can be seen that all detections associated with the dwarf nova appear to be within 30 arcseconds of the catalogued position with most within 20 arcseconds. The features outside of this radius represent chance alignments with other detected stars for individual positions. A histogram of the offsets of each detection is shown in Figure 3.2. If 30 arcseconds is taken to be the upper limit, 95% of detections fall within 13.4 arcseconds of the catalogued position. This is shown as a red line on the plot. The documented precision of WASP is a rms scatter of 2.7 arcseconds (see Section 2.2). This coincides with the peak in Figure 3.2 where most of the detections are found.

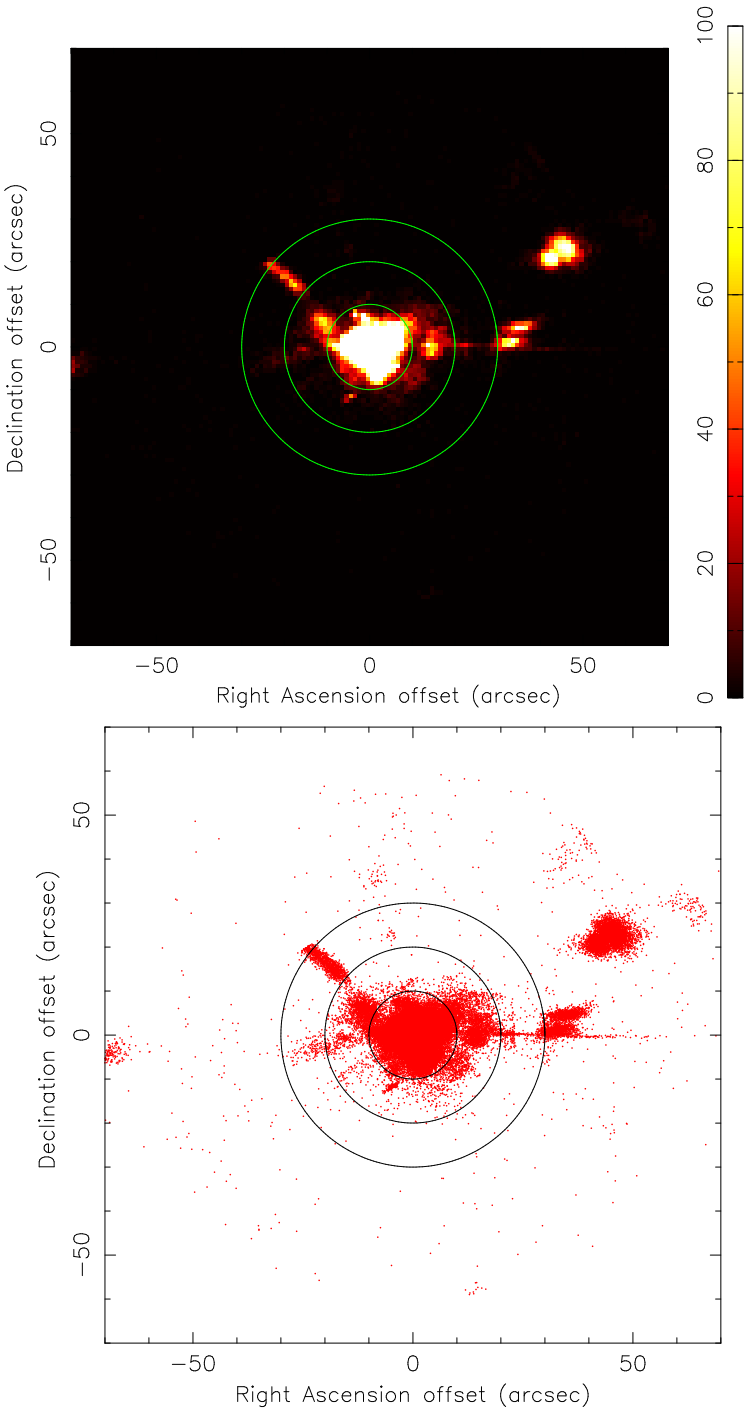

Figure 3.1: The offset in position of WASP detections of known Ritter and Kolb CVs. The three circles have radii of 10, 20 and 30 arcseconds. The detections within the 20 arcsecond radius are associated with dwarf nova outbursts from the Ritter and Kolb CVs whereas the features outside this radius are caused by chance alignments with individual targets.

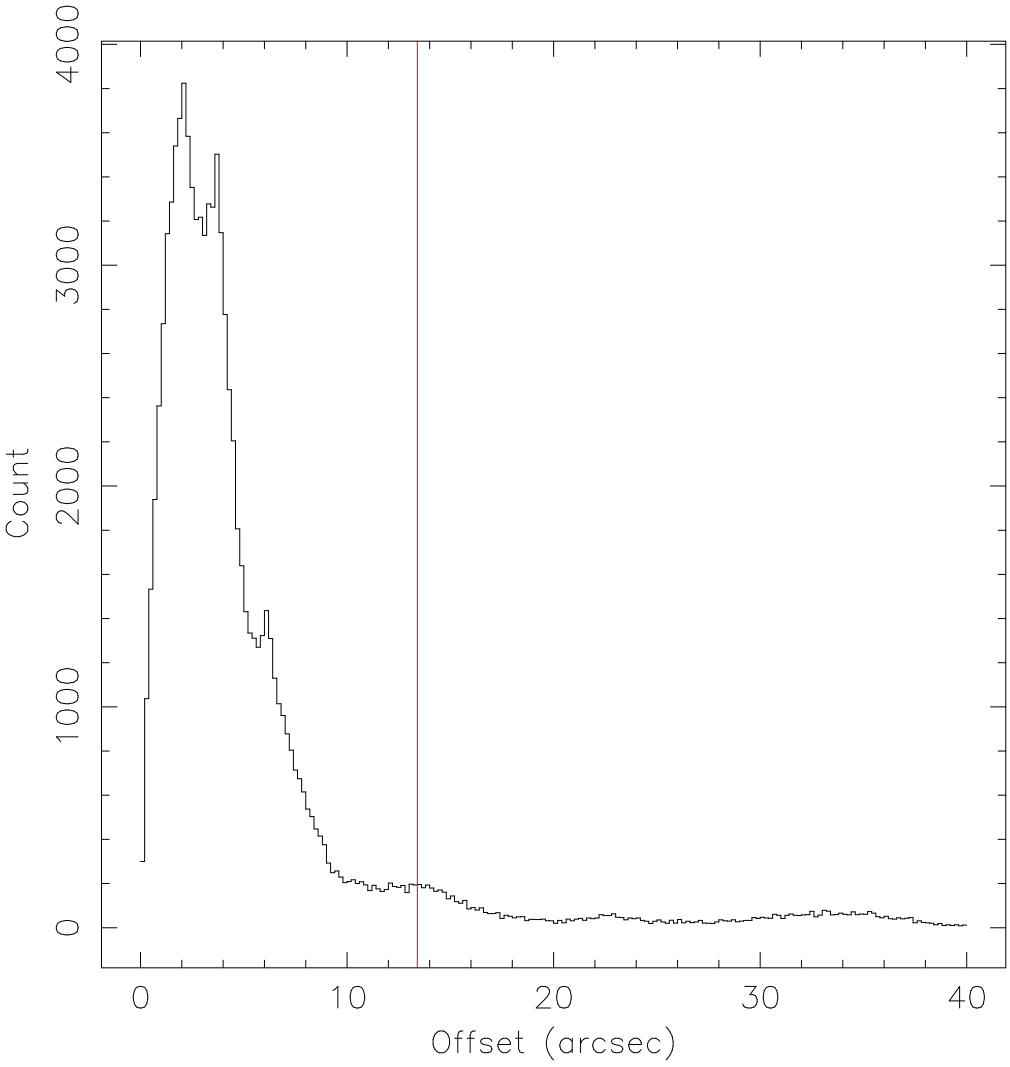

Figure 3.2: A histogram of the offsets of detections of Ritter and Kolb dwarf novae from their catalogued positions. The red line marks the radius where 95% of detections are within it.

3.4 Cataclysmic Variable Stars

3.4.1 Method for searching for known cataclysmic variable stars

The sample of CVs chosen were from the Ritter and Kolb catalogue [136]. This consisted of 835 Cataclysmic Variables all with known orbital periods. The WASP orphans database was searched at the positions of each of these with a radius of 60 arcseconds up to the end of the 2008 observing season. Systems where there were more than 3 detections within 30 arcseconds were then looked at by hand. As is discussed in Section 3.3, this 30 arcsecond search radius can be seen to be justified by Figure 3.1 which shows the right ascension and declination offsets of all detections found within 60 arcseconds of a CV's known position. All the detections associated with the central object are within 30 arcseconds (2.2 pixels) of it.

Once a candidate list was established, several steps were taken to determine whether an outburst from the cataclysmic variable was indeed detected:

- The detected flux values were compared to known outburst magnitudes from the Ritter and Kolb catalogue.
- The right ascension and declination of the detections was considered with respect to the position of the cataclysmic variable and how tightly clustered the orphans were.
- The shape of the light curve was compared to known dwarf nova light curves.
- Raw images were examined to see if a transient was visible.
- The time and magnitude of the outburst was compared to known outbursts observed by AAVSO.

3.4.2 Results of search

From 835 Ritter and Kolb CVs, 107 were found to have detections in WASP. Of these 82 were dwarf nova outbursts, 21 were nova-like systems, 1 was a nova outburst and 3 were nova systems that were not observed in outburst. As is shown in Section

Ritter and Kolb classification	Total No. of systems in Ritter and Kolb	No. of systems detected by WASP
U Gem	54	18 (33%)
SU Uma	266	51 (19%)
Z Cam	28	4 (14%)
WZ Sge	42	5 (12%)

Table 3.1: A table of the ratio of types of CVs found from the Ritter and Kolb sample.

6.2.1, 316 out of 436 dwarf nova systems in Ritter and Kolb (72%) were observed more than 500 times each. In 25% of these systems an outburst was detected and recorded in the orphans database.

The light curve of the nova V2467 Cyg is shown in Figure 3.3. The nova originally occurred 73 days before our coverage began so our detections are of its decline [108]. Figure 3.4 shows an example light curve of one of the detected nova-like systems. As expected these systems do not appear to show outbursts in the WASP data and any with USNO-B r2 magnitudes brighter than 15th will have been included in the main WASP archive. However, in some cases the USNO-B r2 magnitude might be erroneously faint or the USNO observations may have been taken during a low-state of the system allowing the detections to be included in the orphans database. The light curves of detected dwarf nova outbursts found in WASP are shown in Appendix A Figure A.1. They are ordered, as in Ritter and Kolb, by orbital period. Of particular note is the outburst from HS 0218+3229 which was originally identified spectroscopically and was found to have an orbital period of 428 minutes [138] but has never been seen in outburst before.

The ratios of the types of CVs observed are shown in Table 3.1. It appears from this that WASP is most sensitive to U Gem systems with over a third of the known systems detected by WASP. In contrast only 19% of SU Uma systems and 12% of WZ Sge systems are observed. The primary reason for this is likely to be that WZ Sge systems in particular tend to have far less frequent outbursts than U Gems so the chance of observing one during an outburst is far lower. Conversely though it may be expected that for the same reason a larger proportion of WZ Sge

systems remain undiscovered compared to U Gems (and may even dominate the population if they represent the predicted 'period bounce' systems).

Precursor outbursts

In QZ Vir, AQ Eri and PU CMa it appears that we have detections of a precursor outburst as well as the main superoutburst (see Figure 3.5). In each of these cases the small normal outburst occurs within four day of the superoutburst, declining only the night before the superoutburst begins to rise.

Observations of these precursor outbursts are unusual but have been made in other systems such as T Leo [77]. However, they are predicted to occur before all, or at least most, superoutbursts [161]. The theory is that the expansion of the disc during outburst allows the gravitational influence of the secondary to drive the disc to become elliptical, provided the disc is sufficiently large, and trigger a superoutburst.

The lack of optical observations is because it can be difficult or even impossible to distinguish between the normal outburst and the subsequent superoutburst[162]. For example, Voyager 2 UV observations of a superoutburst from VW Hyi found only a 1.8 day gap between the peaks of the superoutburst and its precursor [124]. In the optical the two outbursts were indistinguishable. While WASP may be unable to provide light curves for precursor outbursts that are optically indistinguishable from their superoutburst, the detailed early observations of superoutbursts should allow WASP to identify any more distinct precursors. A systematic survey of early outburst properties of dwarf nova, such as in this thesis, has not been carried out before.

CVs observed in quiescence

In three of the systems shown in Figure A.1 (LX And, V893 Sco and PU CMa) we appear to detect the system in quiescence as well as in outburst. This is because while the quiescent system is too faint to be included in the main WASP database, it not so faint that it can not be detected in good conditions. A light curve including

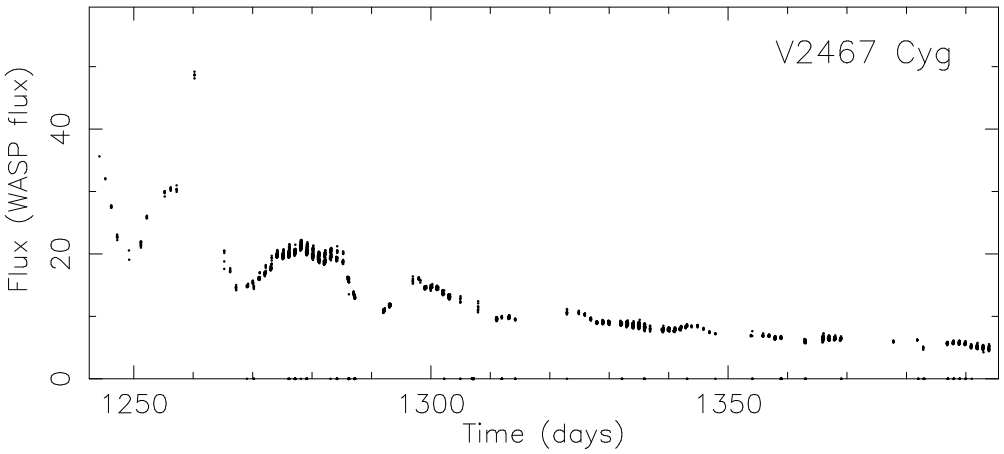

Figure 3.3: Light curve of WASP detections of the nova eruption from V2467 Cyg. Time is in days after JD 2453005.5.

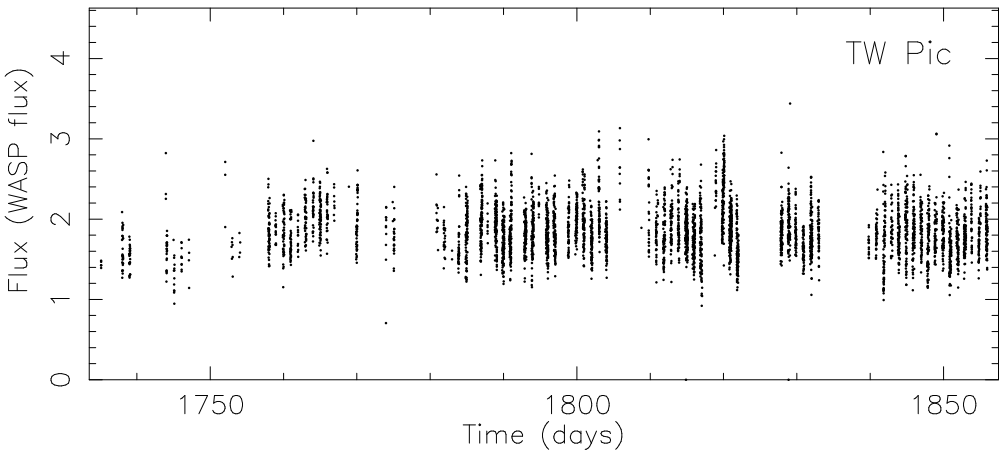

Figure 3.4: Light curve of WASP detections of novalike system TW Pic. Time is in days after JD 2453005.5.

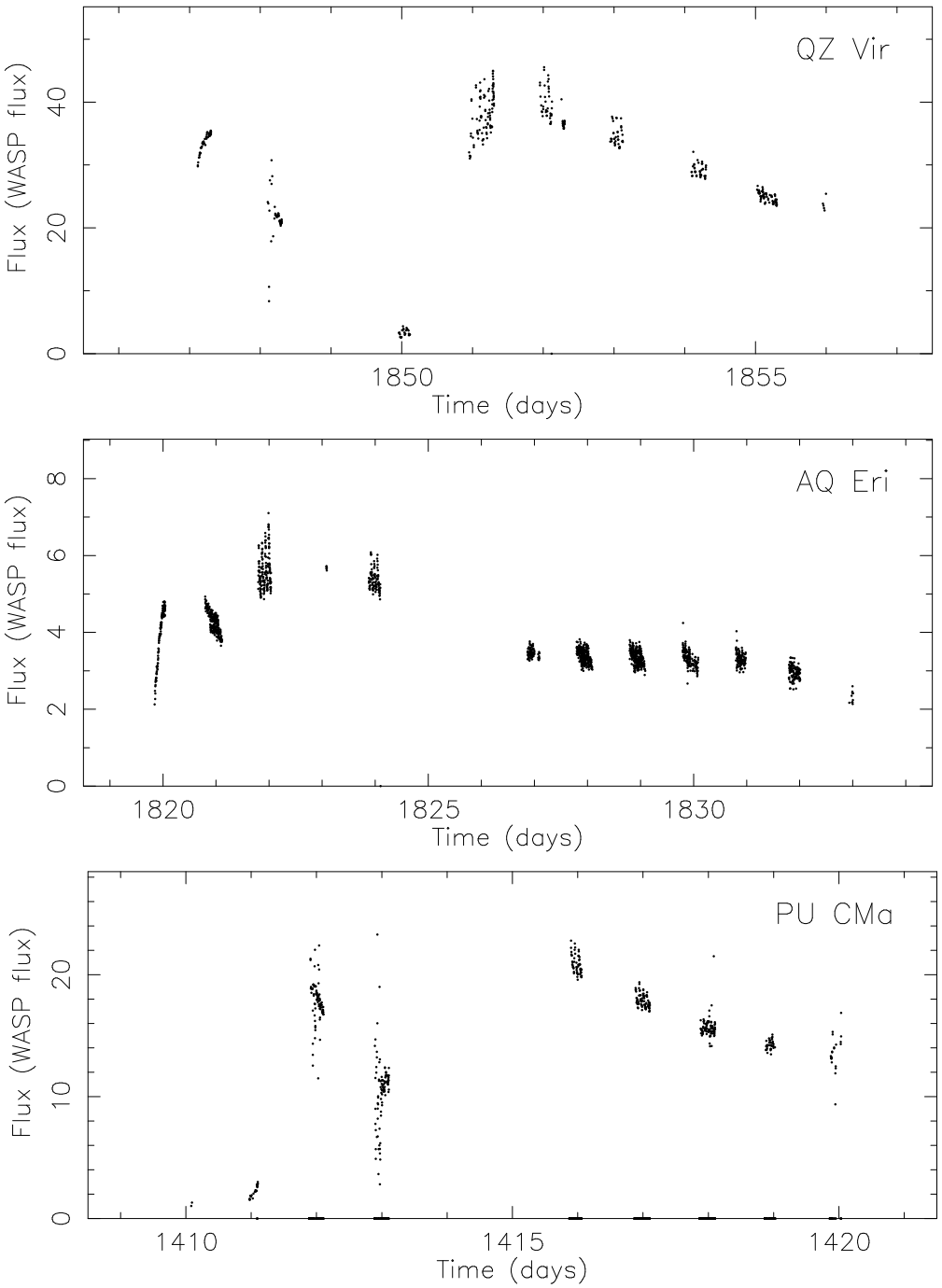

Figure 3.5: Light curves of WASP detections of precursor outbursts in systems QZ Vir, AQ Eri and PU CMa. Time is in days after JD 2453005.5.

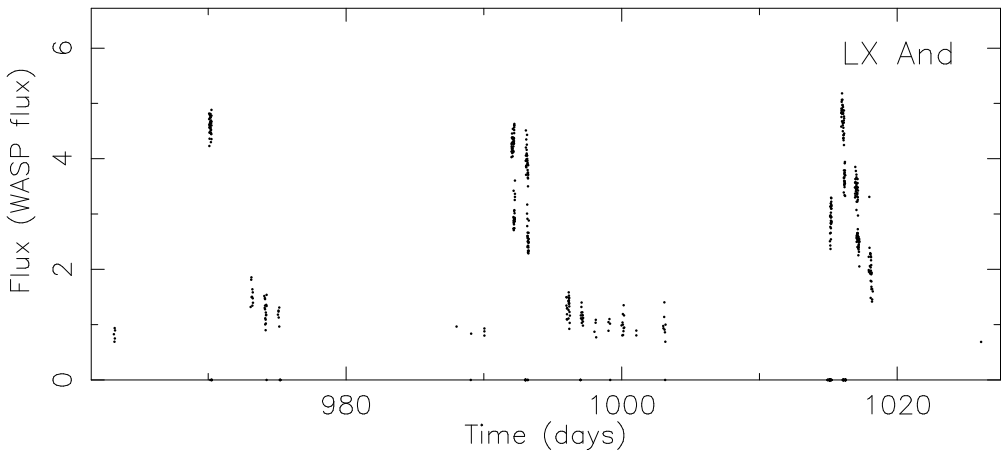

Figure 3.6: Light curve of WASP detections of LX And including quiescent detections. Time is in days after JD 2453005.5.

quiescent detections of LX And is shown in Figure 3.6. V803 Cen appears to be similar, however, the quiescent magnitudes of the system are too faint to be detected even in good conditions. It is believed in this case that what is being observed between outburst is likely to be several nearby stars that when combined are bright enough to detect.

WZ Sge systems

It has been theorised that along with infrequent large amplitude superoutbursts, WZ Sge systems may have more frequent shorter outburst. There have been some claimed detections of these shorter outbursts [170] [71] but these have not been confirmed. The WASP observations should be a good test of this as our extensive coverage of some WZ Sge systems should mean we are in a good position to detect outbursts of this nature.

WASP should be able to identify outbursts as short as an hour, however, none of these theorised short outbursts are detected. Out of the 42 WZ Sge systems in Ritter and Kolb only 5 have detections in WASP. In these systems the only outbursts observed are the expected large amplitude super outbursts or small echo outbursts following these. A full light curve of 1RXS J0232-3718 with these echo outbursts is shown in Figure 3.7.

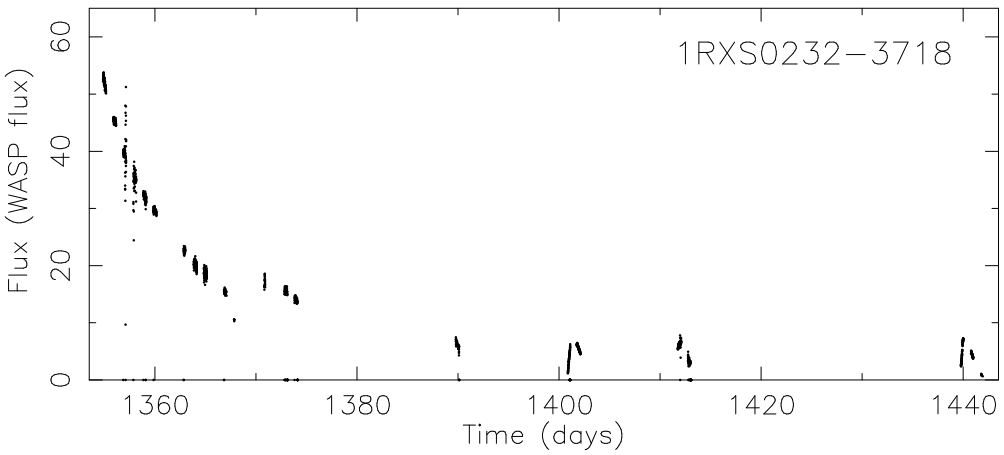

Figure 3.7: Light curve of superoutburst and echo outbursts from 1RXS J0232-3718. Time is in days after JD 2453005.5.

The fact that several supposedly less frequent superoutbursts are observed but no normal outbursts suggests one of three possibilities. Firstly the small outbursts might be too faint to be observed by WASP. In 1RXS J0232-3718 echo outbursts were observed and reached 13th magnitude. This means that any normal outbursts would need to be 2-3 magnitudes fainter than the echo outbursts to be missed. Secondly the normal outbursts may be extremely infrequent. Given that 5 superoutbursts were identified this would imply that normal outburst must be at least five times less frequent (although these are small number statistics and the longer, brighter superoutburst are far less likely to be missed by any breaks in the WASP coverage). Thirdly these smaller outburst may not be a typical behaviour of WZ Sge systems.

3.4.3 Analysis of light curves

With the high cadence coverage and high photometric accuracy of the WASP data it should be possible to detect short period variability in these light curves (such as the superhump or orbital periods). A zoomed in plot of one night's data from CSS J1631+1031 is shown in Figure 3.8 where periodic oscillation do indeed appear to present.

To measure periodic oscillations, such as this, the light curves for the CVs

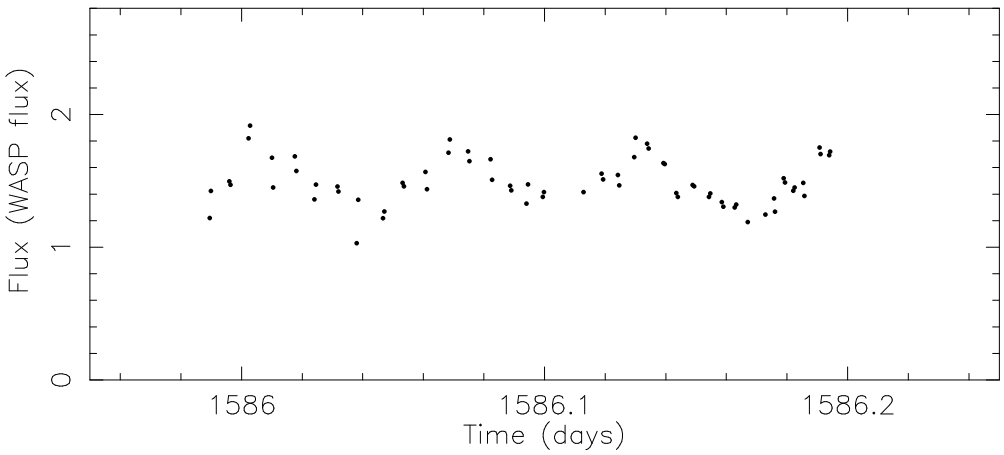

Figure 3.8: WASP light curve of one night of detections from an outburst of CSS J1631+1031.

were analysed with Lomb Scargle periodograms on various subsets of the data. If a dominant peak was found a sine wave and first harmonic was then fitted to the data. From this the period and asymptotic standard errors could be calculated. The flux values had the average flux for the night subtracted to negate any long periods from the data associated with the shape of outburst light curve itself. An example of the periodogram from TT Boo is shown in Figure 3.9. Not only is the superhump period detected, 112.5 minutes (marked in blue), but it is even possible to distinguish it from the known orbital period, 108.9 minutes (marked in red). The WASP measured period of 112.2 minutes is just 0.3% offset from the correct value.

The overall results for the observed CVs are shown in Table 3.2. Example folded light curves for some of these are also shown in Figure 3.10.

From the 82 Ritter and Kolb CVs with detected dwarf nova outbursts, periodic oscillations were detected in 29 of them. Out of these, only GY Cnc was a U Gem system. The oscillations resulted from eclipses but as only two were detected on different nights it could only be shown to be consistent with the recorded orbital period (see Figure 3.11). A further 27 appear to have detections of the superhump period. SDSS J1656+2121 was of unknown type but also appears to show superhumps suggesting it may be an SU UMa. For each of these the percentage offset from the known orbital period was calculated. These offsets are shown in Figure

Name	Type	Known Orbital Period (minutes)	Known Superhump Period (minutes)	Period Detected by WASP (minutes)
SDSS1627+12	SU UMa	149.8	158.4	158.4±0.8
YZ Cnc	SU UMa	125.0	130.0	131.1±0.9
TU Crt	SU UMa	118.2	122.8	123.0±0.1
CTCV0549-49	SU UMa	115.5	122.4	116.7±1.7
2QZ0219-30	SU UMa	113.0	116.9	114.2±1.7
TT Boo	SU UMa	108.9	112.5	112.2±0.1
VW CrB	SU UMa	102.1	105.0	105.0±0.1
V699 Oph	SU UMa	98.5	101.1	94.8±0.3
TY Psc	SU UMa	98.4	101.4	102.0±0.1
SDSS1100+13	SU UMa	95.0	97.3	97.0±0.2
1RXS0232-37	WZ Sge	93.2	95.3	96.1±0.1
ER UMa	SU UMa	91.7	94.6	88.3±1.4
SDSS1656+21	DN	90.9		93.8±0.1
VY Aqr	WZ Sge	90.9	93.1	92.8±0.1
CSS1631+10	SU UMa	90.4	92.3	92.0±0.1
HO Del	SU UMa	90.3	92.7	93.8±1.0
SY Cap	SU UMa	90.0	91.9	92.6±0.8
AQ Eri	SU UMa	87.8	89.7	89.6±0.1
HS2219+1824	SU UMa	86.3	89.0	88.1±0.1
SDSS1502+33	SU UMa	84.8	86.8	87.0±1.4
QZ Vir	SU UMa	84.7	87.0	86.2±0.4
RZ LMi	SU UMa	84.1	85.5	84.5±1.8
PU CMa	SU UMa	81.6	83.5	83.2±0.1
V455 And	WZ Sge	81.1	82.4	81.7±0.5
V844 Her	SU UMa	78.7	80.5	78.2±1.8
GW Lib	WZ Sge	76.8	77.9	80.2±0.6
V485 Cen	SU UMa	59.0	60.8	61.1±0.1
V803 Cen	SU UMa	26.6	26.9	26.9±0.1

Table 3.2: A table of the detected periods from Ritter and Kolb CVs.

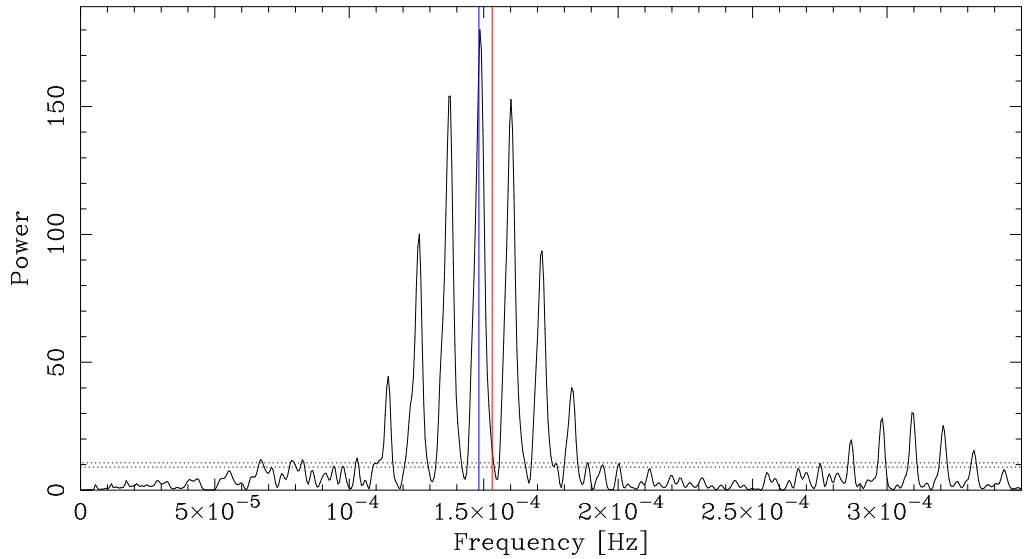

Figure 3.9: A Lomb Scargle periodogram for TT Boo. The orbital period is marked with a red line and the superhump period with a blue line.

3.12. From this figure it can be seen that the offsets tend to increase with longer periods. This is not surprising as longer periods would tend to mean fewer cycles would be observed.

From the 51 systems without detected periods in the WASP data, 24 of them are above the period gap (compared to only 1 with a detected period). This is probably because these systems will not be of SU UMa type so will not show superhumps. Orbital periods can be more difficult to identify unless the system is eclipsing as with GY Cnc. This is especially problematic with the longer periods of systems above the period gap as fewer complete cycles will have been observed. Below the period gap 27 systems did not have a detected period. The reasons for this could be either lack of data or only normal outbursts being detected.

The results of this analysis does not show anything unexpected although a period for SDSS J1656+2121 was detected which may represent a superhump period. What the results do demonstrate is that WASP is capable of producing scientifically valuable period analysis measurements for detected transients which is something that many other competing transient surveys (such as Catalina Sky Survey [42]) are lacking.

TT Boo

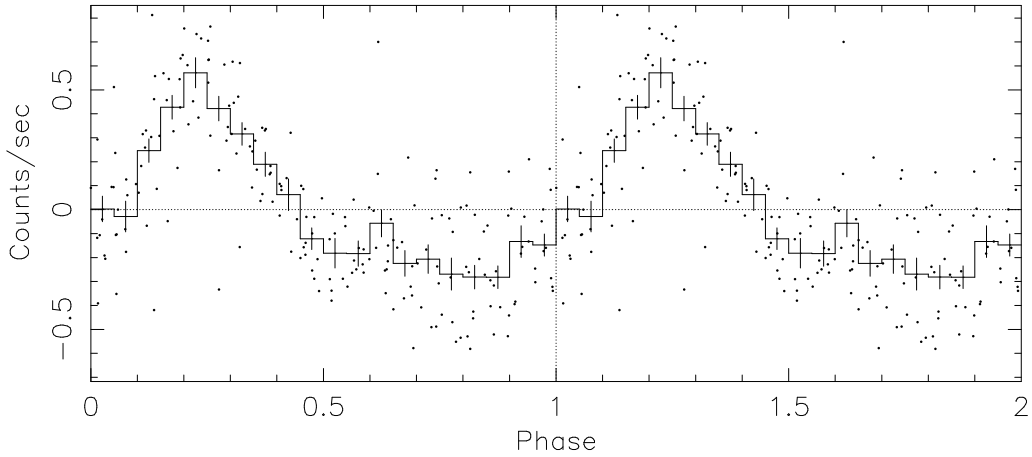

V844 Her

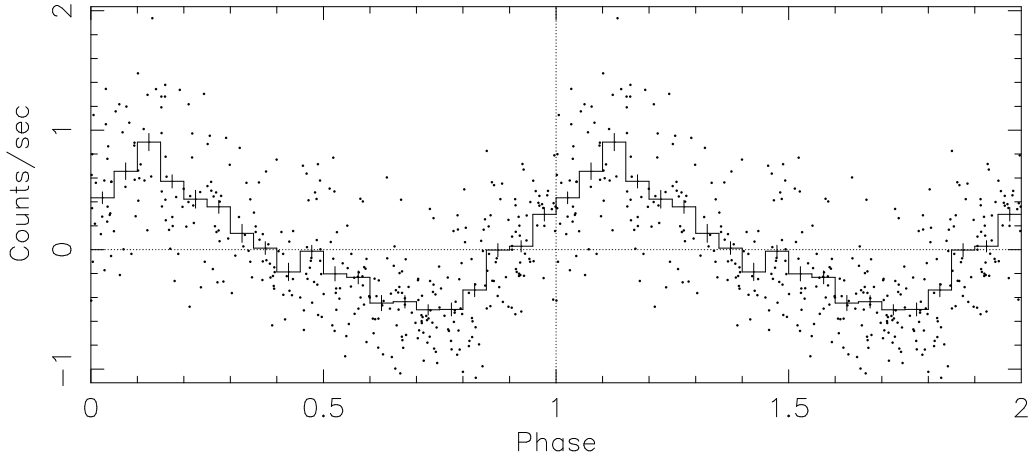

SDSS J1627+1204

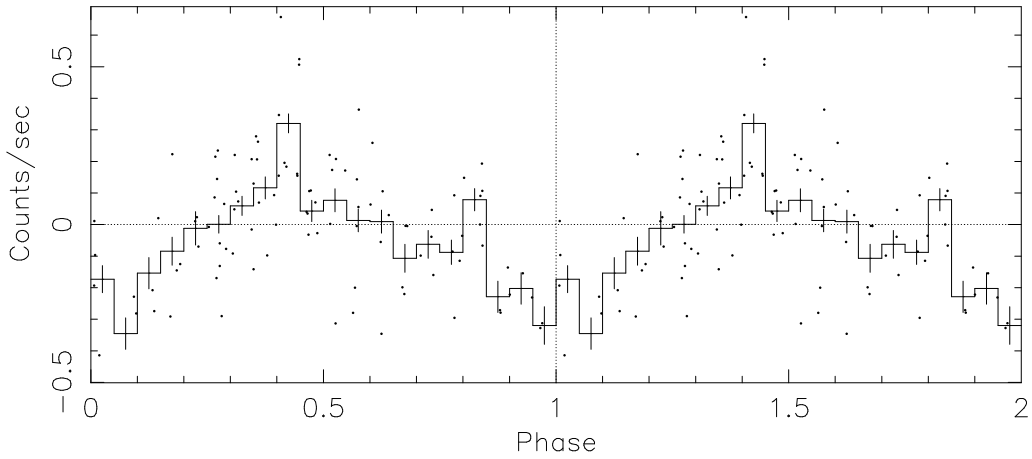

Figure 3.10: Folded light curves showing the superhump oscillations for TT Boo, V844 Her and SDSS J1627+1204.

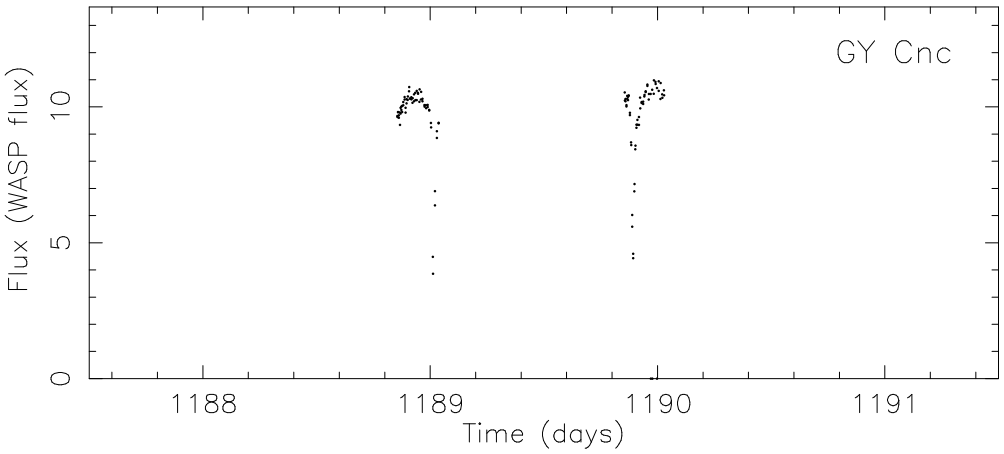

Figure 3.11: Light curve of WASP detections of GY Cnc showing two eclipses. Time is in days after JD 2453005.5.

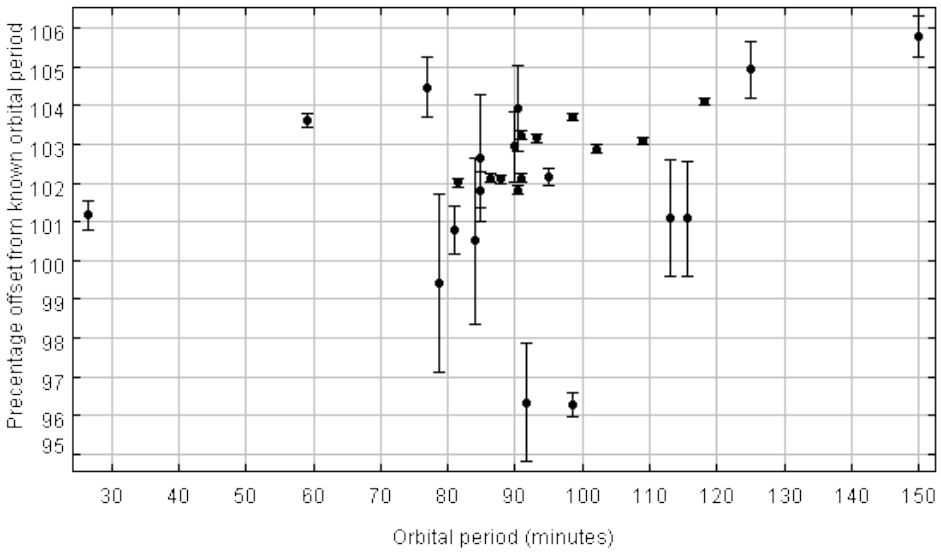

Figure 3.12: Scatter plot of the percentage offset of the measured WASP period from the orbital period against the orbital period in the Ritter and Kolb catalogue.

3.5 Supernovae

3.5.1 Method for searching for optical detections of known supernovae

As with the search for known cataclysmic variable detections described in Section 3.4, the method used was to carry out cone searches at the positions of known events. The catalogue used was the Harvard list of Supernova [3]. Cone searches were carried out with a radius of 70 arcseconds although to be considered as a candidate at least one of the detections must be within 30 arcseconds. Furthermore, at least one of the detections was required to be within 180 days (approximately 6 months) of the discovery date of the supernova.

The WASP data was searched for detections in the years 2004, 2006, 2007 and 2008. From the Harvard catalogue this gave 1916 prospective supernova to search for although only 133 had peak magnitudes brighter than 16th.

3.5.2 Results of search

The cone searches produced 222 candidates which were looked at by hand. For each of these candidates plots were made of the right ascension and declination of the detections and of the light curve of these detections. Digital Sky Survey and WASP images were also compared to help to understand their cause.

This analysis established that none of these candidates were caused by a supernova. 178 of them were detections of the host galaxy, 6 more were chance alignments with stars, 36 were chance alignments with spurious WASP detections and 2 were caused by errors associated with the CCDs.

From considering the WASP coverage at the discovery date of the supernova it appears that it was reasonable to expect WASP to be able to detect some of the supernovae with concurrent WASP observations. Two of these, SN 2006be and SN 2007ap, are considered in more detail to understand why WASP failed to identify them. SN 2006be had a peak observed magnitude of 15.4 and WASP observations were concurrent with this. SN 2007ap had a peak observed magnitude of 15.5 with

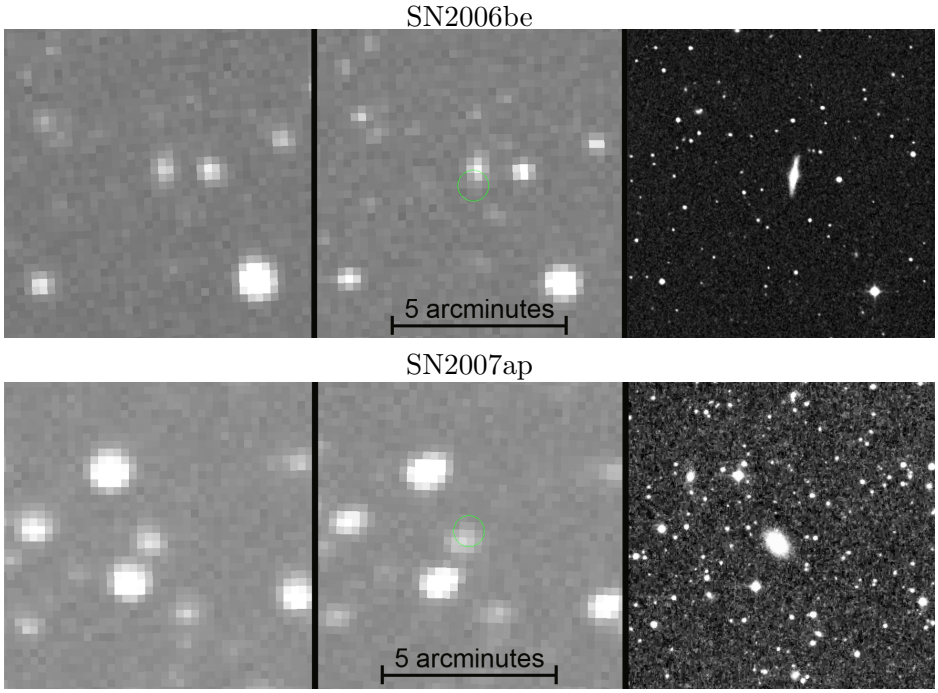

Figure 3.13: Each row contains two WASP images (the first being before the supernova and the second during it) and a DSS image of the host galaxy.

observations occurring within 24 hours of the discovery date. Figure 3.13 shows WASP images of these systems before and during the supernova along with a Digital Sky Survey image on the same scale.

It appears from these that the galaxies themselves were too bright to observe the comparatively faint supernovae. The galaxies, which are resolved in the DSS images, appear as point sources in WASP. It seems that for WASP to detect a supernova not only must the supernova reach a peak magnitude brighter than 15th-16th but the host galaxy must also be comparatively faint.

3.5.3 Supernova detected in the all-sky data

While carrying out a test search of the all-sky data, a known type II supernova (SN 2007od) was found to have detections in WASP. It was missed in the targeted search as, since the all-sky data had not been fully processed, it was not included in the cone search.

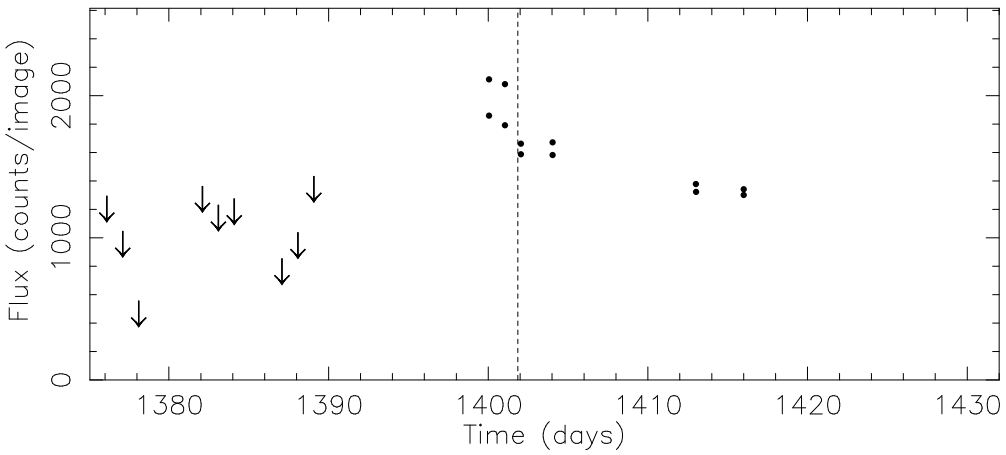

Figure 3.14: WASP light curve of the supernova SN 2007od. WASP detections are shown as black circles with limits for non-detections as arrows. The dotted line marks the discovery date for the supernova. Time is plotted in days after JD 2453005.5.

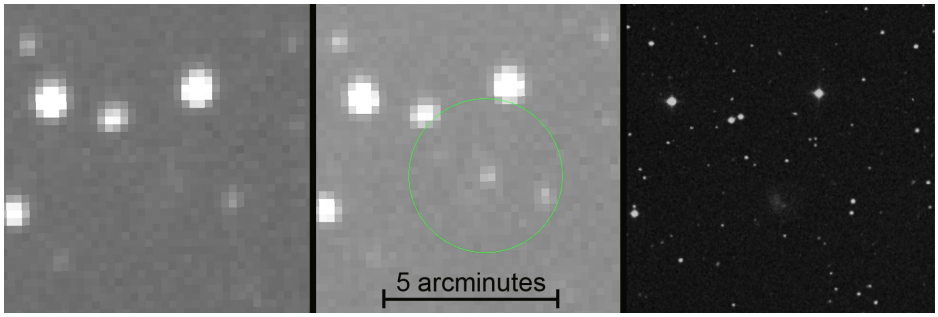

Figure 3.15: Two WASP images (the first before the supernova and the second during) and a DSS image at the location of the supernova.

The light curve for the supernova is shown in Figure 3.14. The WASP data actually predates the discovery date of the system (shown on the plot as dotted line) by a few days. The supernova itself is believed to have occurred about a week before this which is unfortunately during a period with no WASP observations. There are no further detections after the last one shown on the plot as that was the last observation of this field during this observing season.

Figure 3.15 shows WASP images of the system both before and during the outburst as well a DSS image of the same region of sky. Unlike the images shown in Figure 3.13, the galaxy is far fainter and does not appear to be detectable in the

WASP data. This meant that unlike in SN 2006be or SN 2007ap the supernova was not masked by its host galaxy.

3.6 Gamma Ray Bursts

3.6.1 Method for searching for optical detections on known gamma ray bursts

The WASP orphans database was searched at the positions of known outbursts which had been observed with Swift's X-ray Telescope (XRT). XRT observations were required because, unlike most gamma ray burst detectors, the XRT gives extremely precise measurements of position with errors of less than 5 arcseconds [28]. As a positive detection of a GRB could be a single detection point, too wide an error radius would make it very difficult to distinguish between a genuine detection and an error in the WASP pipeline. Considering GRBs up to the end of 2009 produced a list of 373 targets. The WASP database was searched at these positions with a radius of 30 arcseconds ($\sim$ 2 pixels). Any remaining candidates with detections within a week of the recorded outburst were then investigated in more detail.

3.6.2 Results of search

Out of the 373 GRBs, 68 had at least one orphan detection within 30 arcseconds. Only 3 of these had detections within a week none of which appear to have been caused by an optical flash from a GRB. The identification of these 3 candidates is shown in Table 3.3. The brightest recorded gamma ray burst, GRB 080319B [129], while bright enough to detect, was not in the footprint of WASP during 2008.

The chances of observing an optical outburst from a GRB were always low because of their often faint magnitudes and extremely short duration so the results, while disappointing, are not surprising. However, the test is relatively simple to carry out and the results, if successful, could be very informative so it seems worth while to rerun tests like this on WASP data as it comes in.

GRB	Separation (arcsec)	Time offset (hours)	Cause of detection
GRB080310	17.0	27.1	Detections caused by nearby bright star
GRB080307	12.1	158.8	Camera moved during exposure causing double images (see Fig 3.16)
GRB070419A	13.9	11.6	Faint star detected intermittently at position of GRB

Table 3.3: A table of the properties and causes of the 3 best GRB candidates

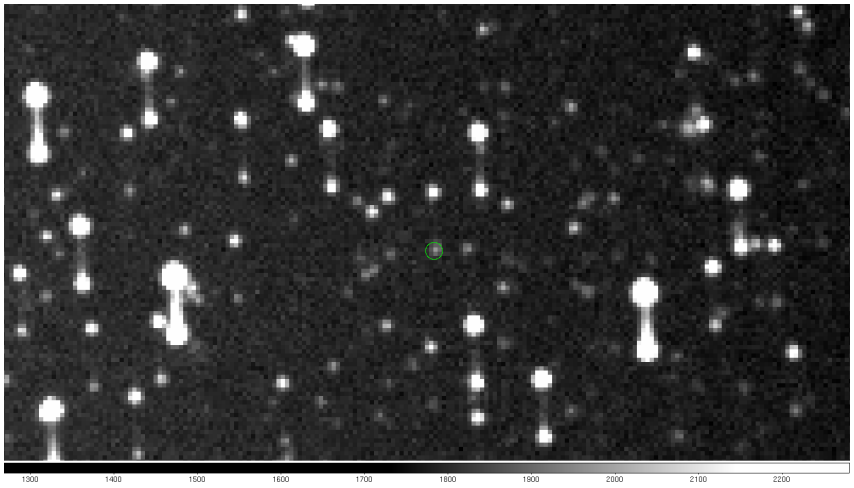

Figure 3.16: The WASP image for a spurious detection near GRB080307

3.7 Targeted Search for New Transients in the WASP data

3.7.1 Motivation

A full untargeted search of the database for transient phenomena is extremely challenging. However, a simpler intermediate step is to search at the positions of likely transients based on a target list. As cataclysmic variable stars can be relatively bright in X-rays we used two X-ray catalogues, the ROSAT bright source catalogue [164] and the ROSAT faint source catalogue [165], as target lists. This search not only identified several transient candidates but in the process of finding them several techniques for automatically filtering out spurious detections were developed. These techniques were then used for a full untargeted search as is described in the following chapters.

3.7.2 Method

Cone searches were carried out at the positions of X-ray sources in selected regions of the ROSAT faint source catalogue (between right ascensions of 0-135 and 150-360 in the northern hemisphere) and at all positions in the ROSAT bright source catalogue. These right ascensions were chosen to correspond with two observing opportunities at the William Herschel Telescope in La Palma in June and September 2008. The cone searches had radii of 140 arcseconds which was far larger than any of the offset tests described below. This ensured that any relevant detections were identified. The positions with detections were then analysed by the following three tests.

Offset from the target position

A simple test that was carried out on the candidates was to consider the offset of the WASP data from the catalogue position. The offsets of WASP detections from the position of the transient are relatively small (13.4 arcseconds as is shown in Section 3.3). Unfortunately the uncertainties in the ROSAT catalogues can be quite large so this restriction in offset from the X-ray position could not be too

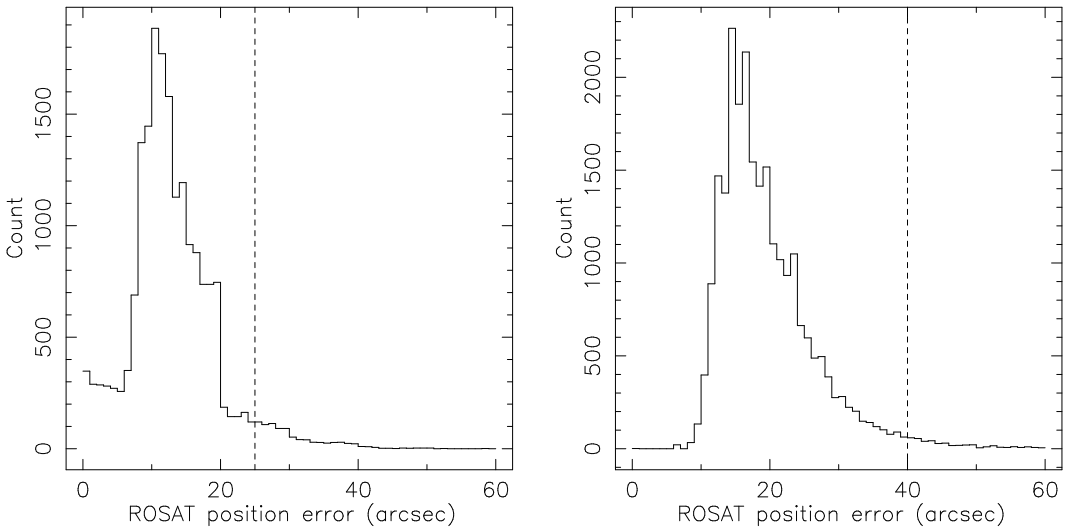

Figure 3.17: Histograms showing the distribution of errors in position from the ROSAT bright source catalogue (left) and ROSAT faint source catalogue (right). The data to make these plots is from the whole of the sky for the bright source catalogue and from the northern hemisphere with right ascensions of 150-300 for the faint source catalogue.

tight. A histogram showing the range of these errors in both catalogues is shown in Figure 3.17. From this a limit of 25 arcseconds was chosen for the ROSAT bright source catalogue and 40 arcseconds for the ROSAT faint source catalogue. This was implemented such that any candidate must have at least one detection within this radius to be considered further. The following tests were than carried out on the detections inside this radius.

Multiple detections on one night

A test was introduced that required at least three detections on one of the nights the candidate was detected. This test was designed to remove any candidates caused by chance alignments with spurious detections. These could be caused by errors in the WASP pipeline (especially near the edge of the CCD) or satellites. Since it is unlikely that an individual candidate would have 3 or more of these chance alignments on one night it would only pass the test if there were detections of a genuine feature. This could lead to very short duration transients, such as short duration flares or gamma ray bursts, being rejected. However, longer duration events lasting for more than

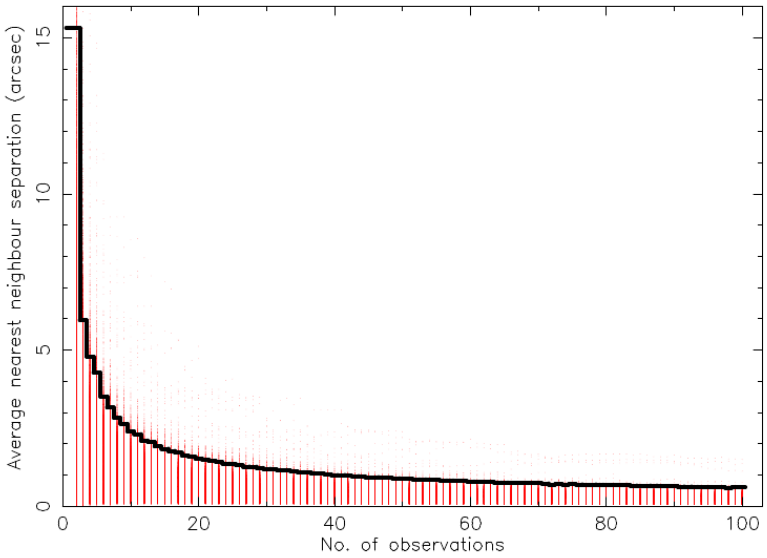

Figure 3.18: A scatter plot of the average nearest neighbour separation against the number of detections for a test sample of constant stars. The 99th percentile is marked with a black line and is the cut used for testing transient candidates. Objects with larger separations than this are likely to be internal reflections in the WASP cameras, fast moving objects or faults with the CCD.

$\sim$ 30 minutes, such as dwarf novae, novae and supernovae, should not be affected by this test.

Nearest neighbour test

To identify candidates caused by erroneous diffuse features a test was introduced to analyse how tightly clustered the detections were. Problems such as ghost images (internal reflections of bright stars in the WASP cameras), fast moving objects (such as satellites or asteroids) and faults on the CCD could be found using this technique. To achieve this, the median distance to the nearest other orphan detection was calculated for each candidate. This statistic was expected to vary with the number of detections. To find how this should vary for detections of a genuine object a test sample of 20000 USNO-B stars with r1 magnitudes between 15.00 and 15.01 was identified. These magnitudes were chosen as they were too faint to be included in the main WASP database but still bright enough to expect detections in the orphans

database. The WASP orphans database was then searched at the positions of these stars. Between 2 and 100 detections were then taken from each star to act as a test sample for establishing the properties of a genuine object. The median nearest neighbour distance was calculated for each of them and the results of this are shown in Figure 3.18. A limit was determined to reject anything with a worse average nearest neighbour separation than the 99th percentile for each value of number of orphans per star. For candidates with more than 100 orphans the limit for 100 was used.

3.7.3 Results of search

The results from the automated tests are summarised in Table 3.4. The remaining candidates were then each individually examined to establish which were likely transient candidates. This was done in several ways. Firstly, the light curves for each of these candidates were compared to the surrounding USNO-B stars to establish whether they were detections of non-variable nearby stars. Furthermore, in some cases, the shape of the light curve itself suggested a transient source. Secondly the distribution of detections in right ascension and declination and in CCD coordinates was considered to confirm it resembled a genuine non-moving object. Finally, raw images were examined to confirm that there were no obvious issues.

A reduced list of likely transient candidates is shown in Table 3.5. Each candidate is given a unique identifier to keep track of it, WTC (WASP transient candidate) followed by a number. Light curves for these candidates are shown in Figure A.2 in Appendix A. From the light curves, WTC001, WTC007 and WTC034 standout as being clear dwarf nova candidates and WTC017, WTC019, WTC021, WTC026, WTC029, WTC030 and WTC031 appear to be flare star candidates. Low resolution optical spectra were taken of several of these using the William Herschel Telescope (see Section 5.2). From this WTC017 and WTC019 were confirmed to be flare stars and WTC001, WTC006 and WTC028 were confirmed to be CVs. These spectra are discussed in more detail in Section 7.1.3.

The unclassified candidates could represent cataclysmic variables which have

	ROSAT bright source catalogue	ROSAT faint source catalogue
Number of positions	18,806	40,682
Number of positions with orphan detections within 140 arcseconds	5,407	22,831
Number that passed offset test	2,942	8,125
Number that passed three detections on one night test	1,298	3,423
Number that passed average nearest neighbour test	1,726	3,445
Number of candidates	1,149	2,740

Table 3.4: A table showing the number candidates that passed the various automatic tests.

less distinctive light curves, pulsating variable stars such as Miras, long duration flares or non-physical false detections. Three of these candidates have matching stars in 2MASS [147]. For WTC025 the j-k colour of 1.63 supports the possible classification as a pulsating variable star whereas for WTC005 and WTC010 the j-k colours of 0.60 and 1.14 are less conclusive.

3.7.4 Summary

From this targeted search for new transient phenomena 5 new cataclysmic variable candidates were identified (3 later confirmed spectroscopically) along with 7 new flare star candidates (2 later confirmed spectroscopically) and 11 new transient candidates of unknown type.

Perhaps even more importantly than these candidates, the large data sets meant it was necessary to develop methods to identify candidate transients from spurious detections. These methods are essential for carrying out an untargeted search because of the large number of spurious detections. In particular, a modified version of the average nearest neighbour test developed in Section 3.7.2 was used later in the untargeted search algorithm (see Section 4.9).

WASP name	Right Ascension	Declination	ROSAT catalogue	Transient type
WTC001	00 15 38	+26 36 57	faint	CV*
WTC005	01 26 17	+30 27 52	faint	Unknown
WTC006	01 33 09	+38 32 18	faint	CV*
WTC007	02 32 38	-37 17 55	bright	CV
WTC008	04 25 38	+32 44 51	faint	Unknown
WTC010	05 10 20	+27 14 03	bright	Unknown
WTC011	07 04 02	+37 35 14	faint	Unknown
WTC013	10 59 38	+20 58 20	faint	Unknown
WTC017	13 23 54	+26 51 20	faint	Flare*
WTC019	14 29 03	+46 45 38	faint	Flare*
WTC020	14 33 00	+17 04 23	faint	Unknown
WTC021	15 08 05	+39 58 54	faint	Flare
WTC022	15 10 18	+33 22 04	faint	Unknown
WTC025	17 15 28	+54 25 09	bright	Unknown
WTC026	17 35 30	+34 32 13	faint	Flare
WTC027	17 42 43	+21 37 31	bright	Unknown
WTC028	17 48 28	+50 50 40	faint	CV*
WTC029	17 55 04	+24 00 43	faint	Flare
WTC030	17 55 31	+54 11 25	faint	Flare
WTC031	18 02 05	+39 34 49	faint	Flare
WTC032	18 04 02	+54 10 14	faint	Spurious
WTC033	18 10 06	+34 29 55	faint	Unknown
WTC034	20 56 52	-30 14 39	bright	CV
WTC036	22 15 31	-28 32 03	bright	Unknown

Table 3.5: A table showing the candidates identified by the targeted searches at the positions of ROSAT bright source and ROSAT faint source catalogue positions. Transient types marked with a * have been confirmed spectroscopically.

Chapter 4

An Untargeted Search for Transient Phenomena

The next step to find transient events in the WASP data is to use a search algorithm to identify candidates without an initial target list. The primary difficulty this presents is that the algorithm must filter out the various types of spurious detections (see Sections 4.1). As the vast majority of detections in the orphans are spurious or detections of unwanted non-variable objects, developing an algorithm to remove these but identify the comparatively small number of genuine detections is extremely challenging. The algorithm developed to achieve this is described in Section 4.2.

4.1 Origin of False Positives

There are a wide variety of sources of unwanted orphan detections. These include genuine detections of non transient phenomena, such as constant stars and asteroids, and failures of the cameras or pipeline, such as detections caused by features on the CCD and internal reflections of bright stars causing ghost images. Some of the more general data quality issues are highlighted in Section 2.7.

4.1.1 Constant stars appearing as transients

A large proportion of the orphan clusters appear to be *constant stars* (non-variable stars detected in the orphans database). Constant star detections should be matched with the USNO-B catalogue in the WASP pipeline so ideally should not be detected as orphans. However, there are several ways that a constant star could be identified as an orphan. In some cases their catalogued value may be erroneously faint and hence they were detected but not identified. When the WASP data is cross-correlated with the USNO-B catalogue it matches stars with r2 magnitudes brighter than 15th. This means that if the USNO-B r2 magnitude is incorrect, or indeed if that magnitude is missing, the detections will not be matched and will be identified as orphans.

Constant stars that are slightly fainter than 15th magnitude may also be detected when observing conditions are good and again these will appear as orphans. In a large number of the WASP fields there was also a pipeline error where some areas of the WASP field were not cross-correlated with the correct region of the USNO-B catalogue. This meant that all detections of constant stars in these regions were considered orphans.

Constant stars could also be included in the orphans database if the focus were sufficiently poor. In these cases the detections could overspill the aperture used to measure the flux from a catalogued stars. This would allow some of the detections to be sufficiently far from the star's catalogued location for them to be identified as orphans.

These constant stars can pose a further problem if they are on the threshold of detection as the phase of the moon changes the background light levels and hence they may not be detected around full moon (see Figure 4.1). This 28 day variability can make their light curves appear transient. This effect can also occur if a star is near the edge of a field. This is because the pointing of the cameras can change significantly over an observing season which moves stars out of the field-of-view.

Clusters caused in these ways can be difficult to identify. They are genuine detections so are in many ways similar to a candidate transient and, as described

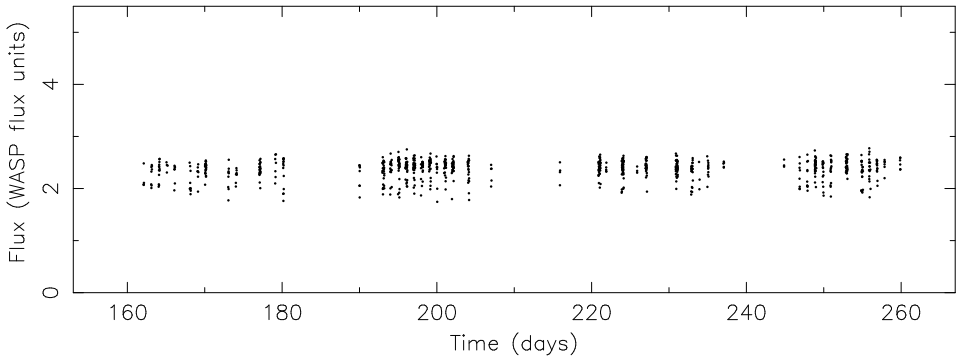

Figure 4.1: Light curve of a faint star detected as orphans by WASP when the moon is not full. Time is in days after JD 2453005.5.

above, can appear to have transient properties. Therefore to identify them it is necessary to compare the positions of the orphans to catalogues of known stars. An automatic system to do this is described in Section 4.7.

4.1.2 Asteroids

Asteroids can also be found in the orphans database. On an individual night the detections appear to move across the sky producing an elongated cluster of orphans (see Figure 4.2). Over longer periods the path of the asteroids across the field can be seen as a trail of these clusters. These should be removed by the search algorithm developed by Neil Parley (see Section 2.5) so should not effect transient searches.

4.1.3 Satellites

Satellites are regularly detected by WASP and can cause problems with both large numbers of single, uncorroborated detections and genuine detected objects gaining extra, high flux detections. An example of a satellite trail observed by WASP can be seen in Figure 4.3. A satellite is normally only observed in one image but in that image can be detected many times. These detections can occur when the satellite passes in front of a faint source, with statistical variations in flux or when the satellite gets brighter, if it is rotating. As satellites move quickly it is unlikely to form a cluster of detections since each individual detection is normally at a large

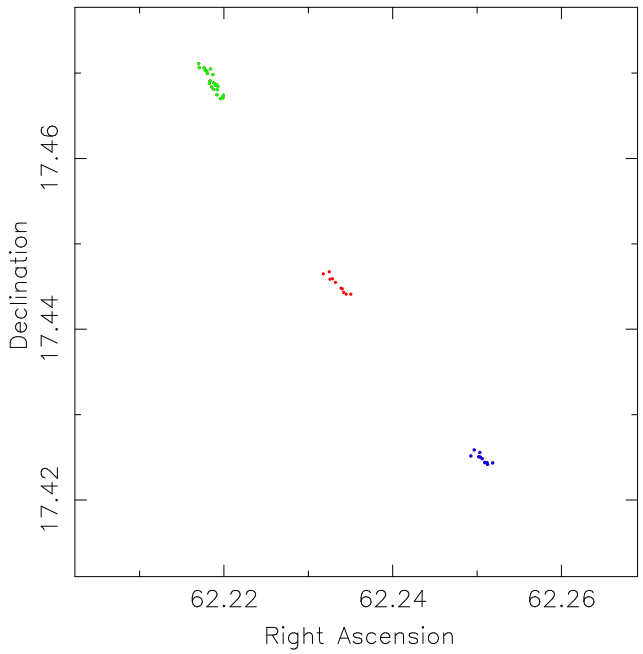

Figure 4.2: Right ascension and declination scatter plot of an asteroid detected by WASP over three nights. Each cluster is shown in a different colour.

distance from the previous one. The other problem caused by satellites, high flux single detections in existing clusters, can be addressed by simply ensuring that any tests done on the clusters are robust with respect to outliers without confirmation from a second detection.

4.1.4 Ghost images

Internal reflections in the WASP lenses can cause light from bright objects to be reflected back onto the wrong part of the CCD. The pointing of the WASP telescope changes slightly during the night which causes this reflection to move. This means that, when looking at WASP images, the stars can be seen to move in one direction across the CCD and the ghost image can be seen to move in the other. This can be seen in Figure 4.4 which shows two WASP images taken on the same night. The ghost image (circled in red) has moved in the opposite direction to the background stars relative to a bad pixel (a fixed point on the CCD). This large movement each night means an individual ghost image produces a very large diffuse cluster.

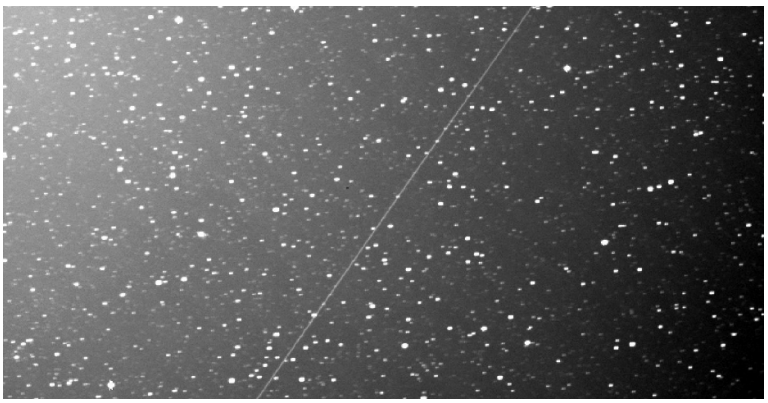

Figure 4.3: A satellite in a WASP image.

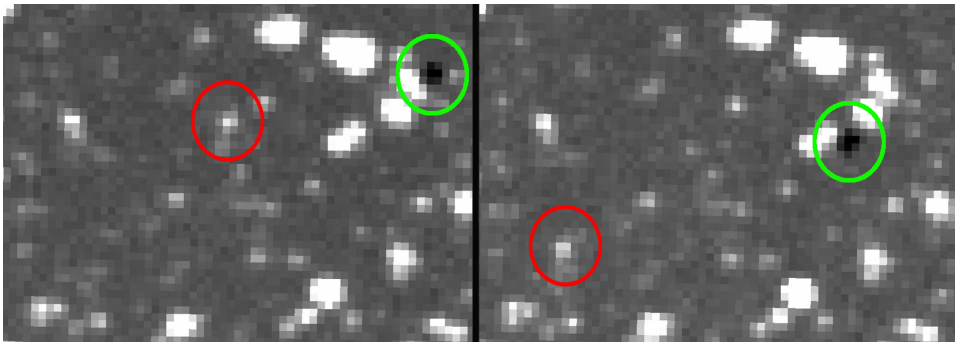

Figure 4.4: Two WASP images taken on the same night containing a bad pixel (circled in green) and a ghost image (circle in red).

An example of this is shown in Figure 4.5. Because of their extreme nature these clusters are comparatively easy to identify either by their high separation between detections or by their large size. A test to automatically remove the diffuse clusters caused by ghost images is described in Section 4.9.

4.1.5 Statistical fluctuations of the background

Statistical fluctuations in the background can cause single spurious detections. These, and other sources of uncorroborated detections, form a significant part of the orphans database, as shown in Figure 4.6. As can be seen from the cumulative histogram on the right, over 80% of clusters contain only one, uncorroborated, orphan. This large proportion of single orphan clusters means that it important that an orphan is confirmed by a second or third detection before it can believed.

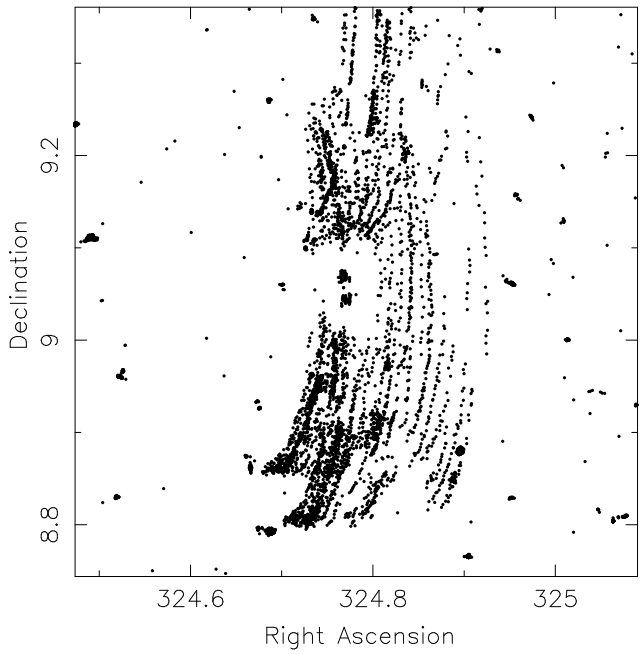

Figure 4.5: Right ascension and declination scatter plot of orphans caused by a ghost image.

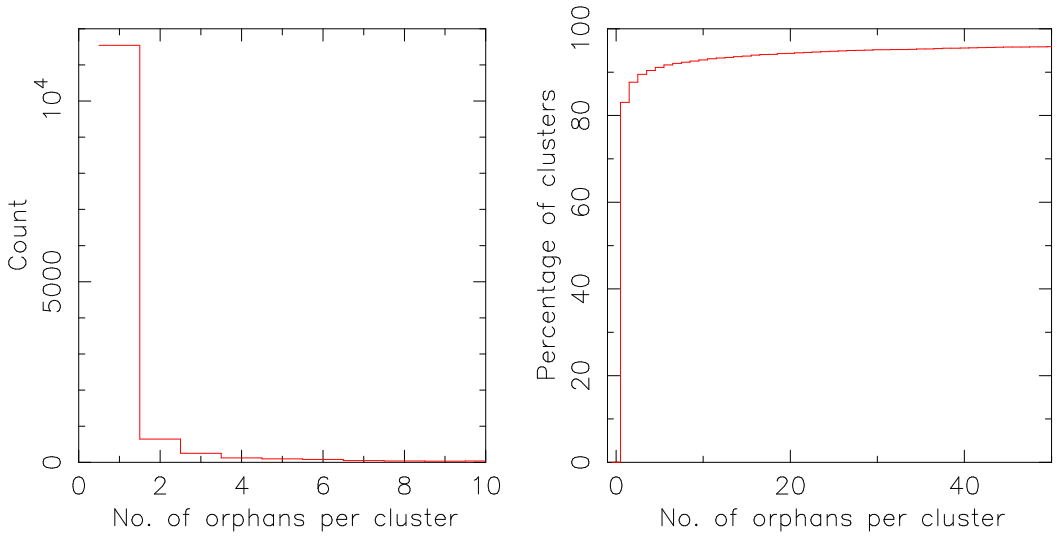

Figure 4.6: The left plot shows a histogram of the number of orphans per cluster for a typical field. The right plot is the same data shown on a cumulative histogram.

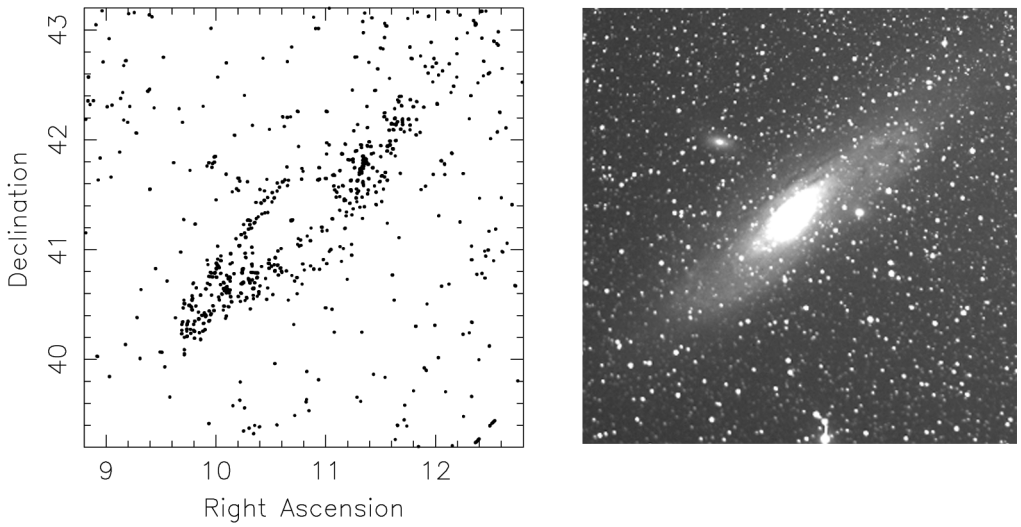

Figure 4.7: On the left is a right ascension and declination scatter plot of orphan detections of the Andromeda Galaxy. On the right is a WASP image of the corresponding region of sky.

4.1.6 CCD features

Faults on individual pixels on the CCD or errors in readout can produce either false detections or non-detections of real objects. Non detections are cased by bad pixels on the CCDs (such as in Figure 4.4). These are a relatively minor problem as, like ghost images, the drift of the observed field in sky coordinates means that that the pixel will not cover the same object for more than one or two images. In contrast hot pixels can cause false detections. In these cases the right ascension and declination can be seen to change while the CCD coordinates stay the same.

4.1.7 Extended objects

The WASP pipeline was not designed to analyse extended objects so large, nearby galaxies are often not matched with catalogues and appear in the orphans database. They can produce large regions of orphan detections as the pipeline identifies brighter parts of their structure as point detections and these can change with focus and background light levels. An example of one of these is shown in Figure 4.7.

Galaxies that are not resolved by WASP can also cause problems as again their USNO-B magnitudes (where they are resolved) may not match what is de-

tected by WASP. This can cause clusters similar to what would be expected from a catalogue error as described in Section 4.1.1.

4.2 An Overview of the Automated Search Algorithm

In order to identify candidate transient events it was necessary to develop a search algorithm capable of dealing with orphans caused by each of the problems described in Section 4.1. The semi-targeted search (described in Section 3.7) was a useful test of some of the subroutines that were required. However, as it was no longer possible to search at known positions, other methods of testing the data had to be developed and the algorithm had to produce far fewer false positives.

An flow diagram of the search algorithm is shown in Figure 4.8. The asteroid matching and *preclustering tests* are carried out on the individual orphans. They are described in more detail in Sections 4.3, 4.4 and 4.5. The orphans are then clustered using the clustering algorithm described in Section 2.4.2 with some modifications described in Section 4.6. In the *post-clustering section*, these clusters are in turn tested for with respect to known nearby bright stars in USNO-B, the full width half maximum of the detections and the tightness of clustering. These tests are described in more detail in Sections 4.7, 4.8 and 4.9. Finally, tests are applied to remove any cases where the search algorithm has failed and an anomalously large number of candidates have been found (see Section 4.10). The algorithm then outputs a list of candidates that have passed all of these tests.

4.3 Remaining Asteroids

As described in Section 2.5, detections of asteroids should have already been removed. However, a test search of the orphans database revealed that not all moving objects were removed. By cross-correlating with Harvard's catalogue of known asteroids it was found that these corresponded to bright known asteroids. An example of these detections can be seen in Figure 4.9 where detections associated with asteroids are shown in green and other orphan detections are shown in red.

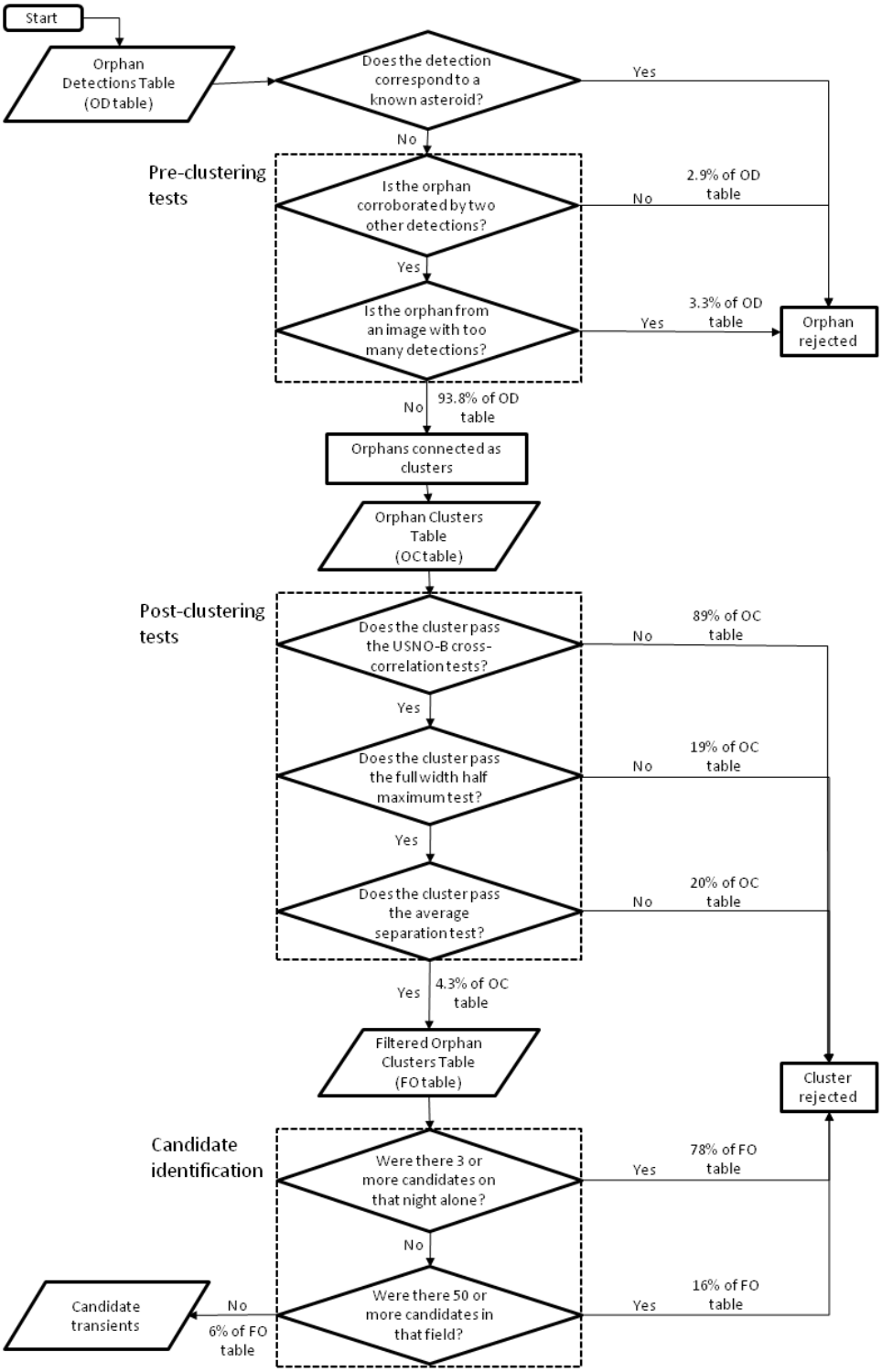

Figure 4.8: A flow chart for the automated search algorithm. The percentages rejected at each stage were calculated from the search results in Section 4.13.

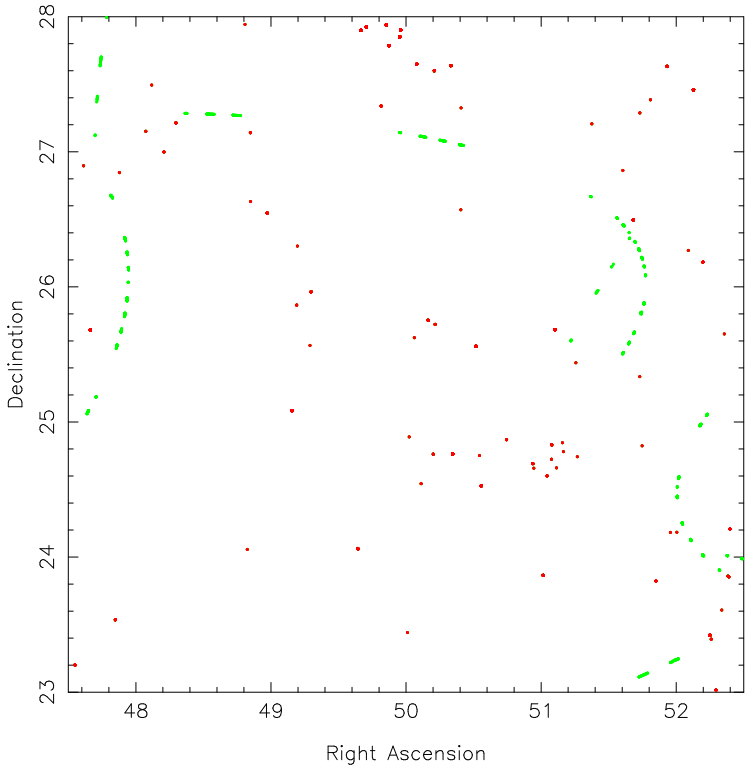

Figure 4.9: Right ascension and declination of detections in a large region of sky. Detections caused by asteroids are in green with other detections in red.

In investigating this, a bug was found in the orphans archive where some asteroid detections were not being matched with the corresponding orphans. While most of the asteroid detections were removed by this correction a proportion from 2006 and 2007 still remained. The reason for these remaining, and the lack of asteroids in the 2004 data, was that the asteroid matching code had used a 60 arcsecond search radius in 2004 but was then reduced to 30 arcseconds for later years. While errors in the WASP data are normally smaller than this, errors in the positions of the known asteroids meant some detections were over 30 arcseconds from their catalogued position. To account for this Neil Parley increased the asteroid search radius to 45 arcseconds.

4.4 Removal of Bad Images

Bad images can be identified by an anomalously high number of orphans (see Section 2.7). However, a simple cut of rejecting images with more than a set number of orphans in them is not flexible enough to deal with data from different fields and different years. The reason for this is that, due to a known bug in the WASP pipeline, regions of some fields are not matched with the USNO-B catalogue. This typically occurs at the edge of the field and is due to the observed area being larger than expected because the camera drifted across the sky over the season. This results in all detections in these regions being classed as orphans. An example of this can be seen in Figure 4.10.

When this issue occurs the number of detections classed as orphans in any image is increased enormously. This means that in fields where there are large regions with this problem a significant number of images are rejected for having too many orphans. While the USNO-B matching may have failed in the WASP pipeline, the detections themselves should still be accurate so should not be rejected. Increasing the cut to accommodate for this problem would result in a lack of sensitivity for bad images when this issue did not occur.

To solve this and make the cut value sensitive to the features of the field,

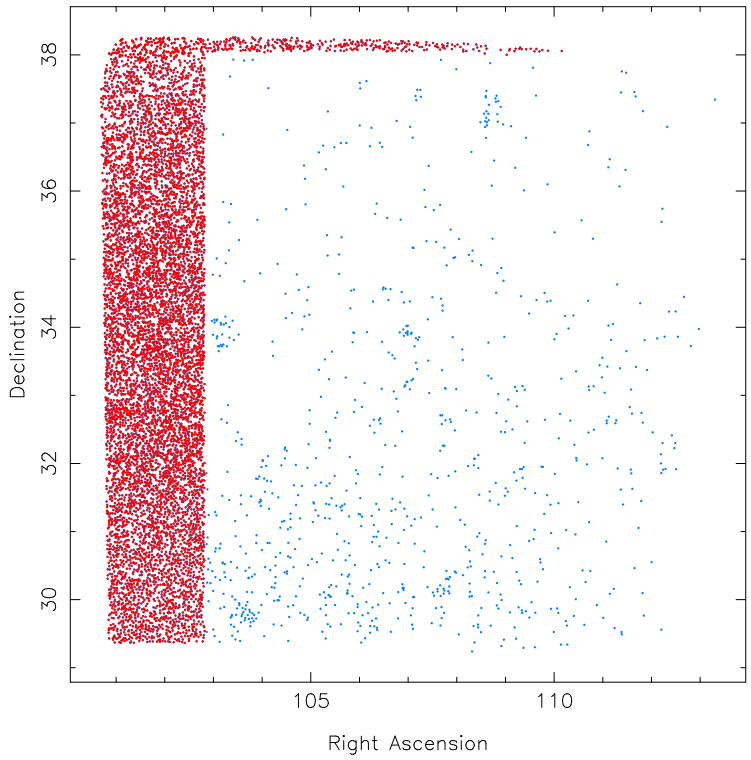

Figure 4.10: Scatter plot of the right ascension and declination of orphan detections for one field. Regions cross-correlated with USNO-B are highlighted in blue and unmatched regions in red.

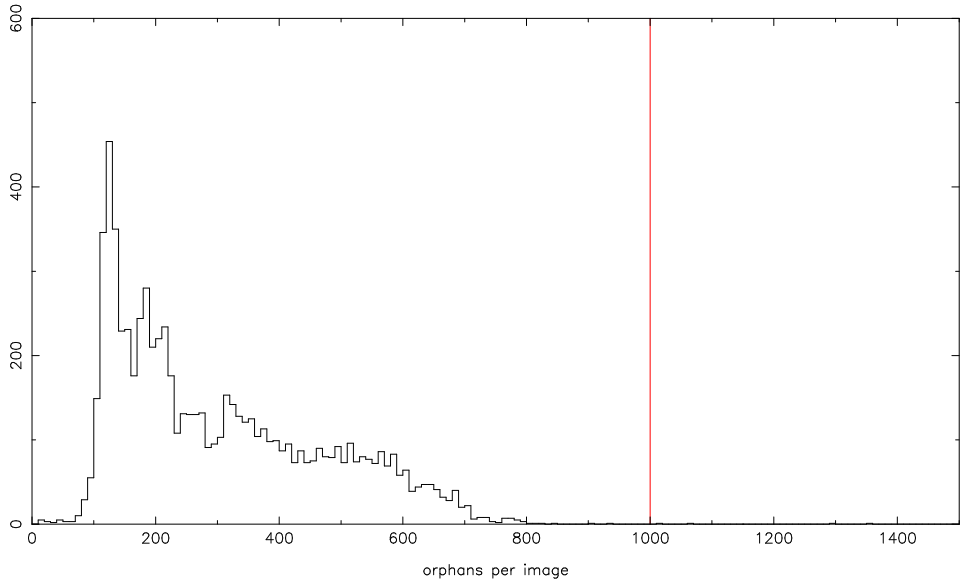

Figure 4.11: Histogram of the number of orphans per image for a field without any cross-correlation errors.

the cut is set so that the top one percent of images from each field are rejected. This will avoid any fields losing large numbers of images unnecessarily while still rejecting data from outlier images. This cut will only be applied when an image has more than 1000 orphans. This minimum value was determined by looking at the number of orphans per image in fields where the catalogue matching problem did not occur. The results from one of these fields is shown in Figure 4.11. Only images to the right of the red line will be considered for rejection. From this it is clear that the vast majority of images should not be affected by the cut.

4.5 Auto-correlation Test

To remove single erroneous orphans caused by problems such as satellites and background errors, a test was added to ensure that each orphan was corroborated before being considered further. Any real transient object lasting for longer than about an hour should be detected several times (depending on the cadence of the field) at the same position in orphans database. An orphan was judged to be at the same position as another if it was within 15 arcseconds of it. This value was chosen as it

was the maximum offset for two orphans in the same cluster determined in Section 3.7.2 and slightly larger than the astrometric precision determined in Section 3.3. Any orphan that was not corroborated in this way by two other orphans from the same night's data was rejected.

4.6 Clustering of the Orphans

The orphan detections that passed the above tests were clustered using Richard West's clustering algorithm described in Section 2.4.2. However, some modifications were made to avoid over clustering.

This can occur if two sources of orphan detections are too close to each other as they are then combined as one object in the clustering stage of the search algorithm. This can cause problems as the tests described below can be ineffective in dealing with clusters that comprise of more than one source. For example, two constant stars at large separations from each other may not be identified by the constant star tests if they are grouped as one cluster. In cases like this the cluster position can be offset from the catalogued star positions meaning that they are not matched. While some over clustering is inevitable, it is desirable to keep it to a minimum to reduce the number of erroneous candidates.

The default bin size of the clustering program was set to 30 arcseconds. This was reduced for the search algorithm to 15 arcseconds to match the orphan corroboration test described in Section 4.5. This means that only detections close enough to corroborate each other are guaranteed to be clustered together.

4.7 USNO-B Cross-correlation Test

The majority of clusters from the orphans database are caused by non-varying constant stars (see Section 4.1.1). There are several ways that detections of these stars can be included in the orphans database. Erroneous magnitudes (specifically the r2 magnitude) in the USNO-B catalogue can lead to the WASP pipeline failing to identify the star, faint stars near WASP's threshold of detection can be seen in good

observing conditions, very bright stars can cause detections at large offsets and stars that are too close on the WASP CCDs can merge together. Any test for removing these must be robust enough to remove almost all clusters caused by any of these effects.

4.7.1 Flux-magnitude relation for detected USNO-B stars

The most obvious orphan property that is likely to be related to the magnitude of a corresponding constant star is the measured flux. In considering this it was possible to utilise the non-USNO matched regions to produce a sample of clusters caused by stars with USNO-B magnitudes brighter than 15th. Figure 4.12 shows a scatter plot of the mean WASP flux of a cluster against the USNO-B magnitudes for stars within 60 arcseconds. There is a clear linear feature in each of the plots where the cluster's mean flux decreases for fainter magnitudes. This feature represents detections in WASP of constant stars and hence indicates the flux-magnitude relation in WASP data. Also noticeable in the bottom left plot (the r2 magnitude plot) is a particularly dense region of detections on this feature between 15th and 16th magnitudes. This represents the stars that were too faint to be included in the WASP catalogue but bright enough to be detected. The green line shows the revised cut that varies with the flux of the cluster. Orphan detections to the left of the line are considered to be associated with a constant star. The gradient of the green line was determined as -0.4 to correspond with the flux-magnitude relation:

$$log_{10}F \propto -\frac{2}{5}m$$

Where F is the detected flux and m is the apparent magnitude.

The position of the line was chosen such that all detections that appear to be associated with the linear feature were to the left of the line and hence in the rejection region.

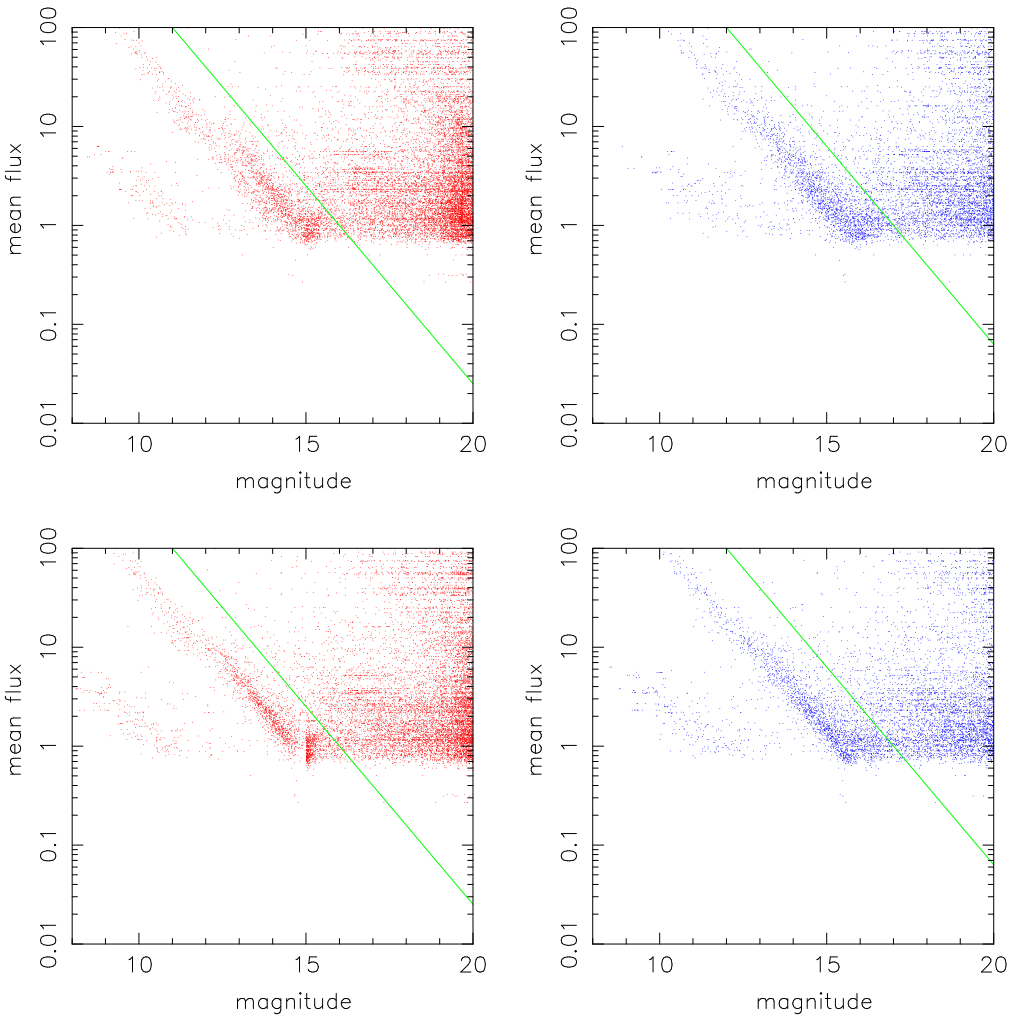

Figure 4.12: Scatter plots of measured WASP flux against USNO-B magnitude. The four plots each correspond to a different USNO-B magnitude (r1 in the top left, r2 bottom left, b1 top right and b2 bottom right). The green line marks the new rejection criteria.

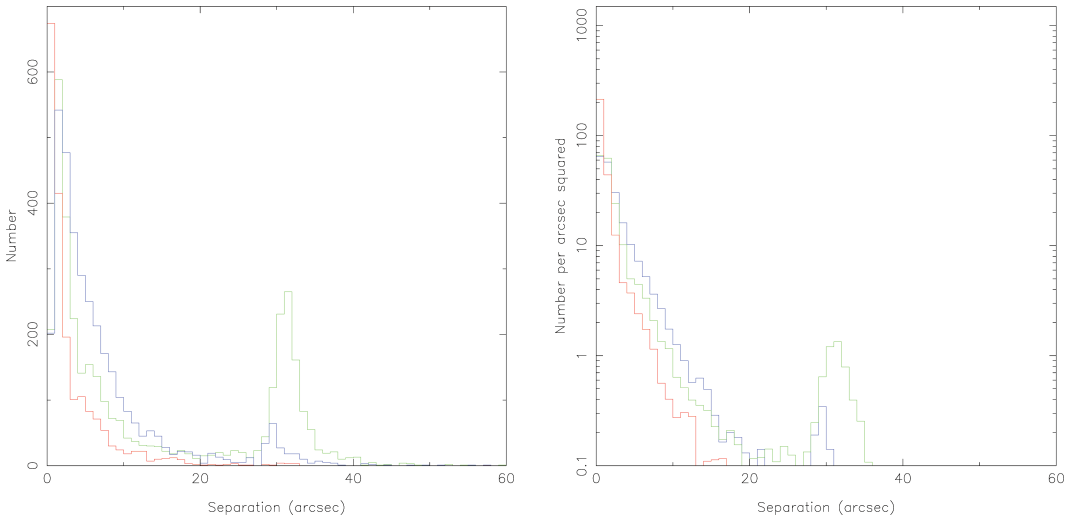

Figure 4.13: A histogram of the separation of constant stars from their corresponding clusters. SW0933+4730_143 is shown in red, SW1522+3000_144 in green and SW2215+1711_142 in blue. The histogram on the right has been adjusted to account for the changing area at different radii and put on a log scale.

4.7.2 WASP offsets from USNO-B positions

With this flux-magnitude relation established it was important to determine the radius around a cluster for which this cut needs to be applied. Figure 4.13 shows histograms of the number of associated constant stars at different radii for three example fields known to have catalogue matching problems. A constant star was considered to be associated with the cluster if it's mean flux was in the rejection region of the flux-magnitude plot (as shown in Figure 4.12) and if it was the closest star to the cluster to do this (up to a maximum separation of 60 arcseconds). There are two sources of noise in this plot. Firstly, chance alignments can occur through errors in USNO-B or for particularly faint constant stars. Secondly, the histogram favours matches at higher radii due to the area for chance alignments to occur being far larger. This second source of noise is corrected for in the second histogram in Figure 4.13 by scaling the counts to adjust for this increased area.

From these histograms it can be seen that there is a clear peak of matches centered at a separation of 0 arcseconds with a tail decreasing into the noise at approximately 20 arcseconds. In fields SW1522+3000_144 and SW2215+1711_142

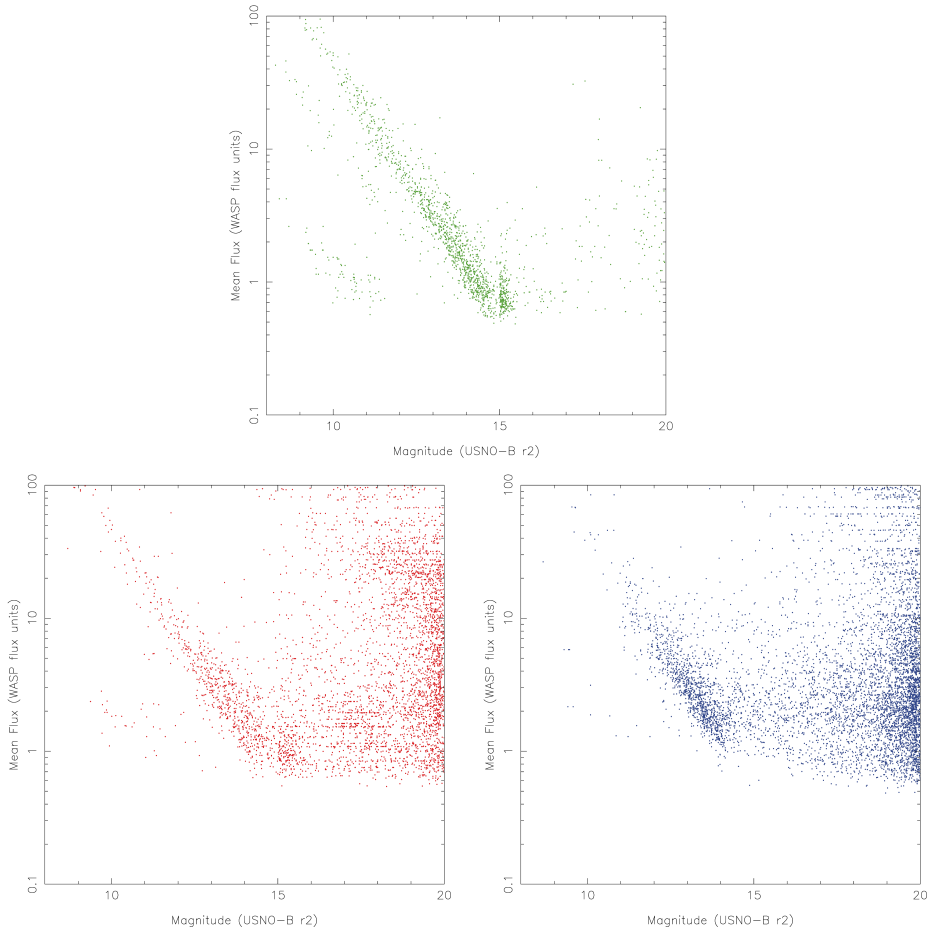

Figure 4.14: Scatter plots of the measured WASP flux against the USNO-B r2 magnitude. The plot in green is for stars within 5 arcseconds of the cluster, red for stars between 5 and 20 arcseconds and blue for stars between 25 and 40 arcseconds.

there also appears to be a "bump" at around 30 arcseconds. This is considered further below.

To establish whether the peak, tail or bump occupy different areas of the flux-magnitude plot this was replotted with these different features shown in different colours (see Figure 4.14). The plot shows that while the linear flux-magnitude feature becomes less prominent at large radii compared to the noise (the detections to the right of the plot), there is no fundamental change in this relationship. However, there do not appear to be any stars in the bump fainter than 15th magnitude.

From Figure 4.13 it appears that the majority of detections of constant stars

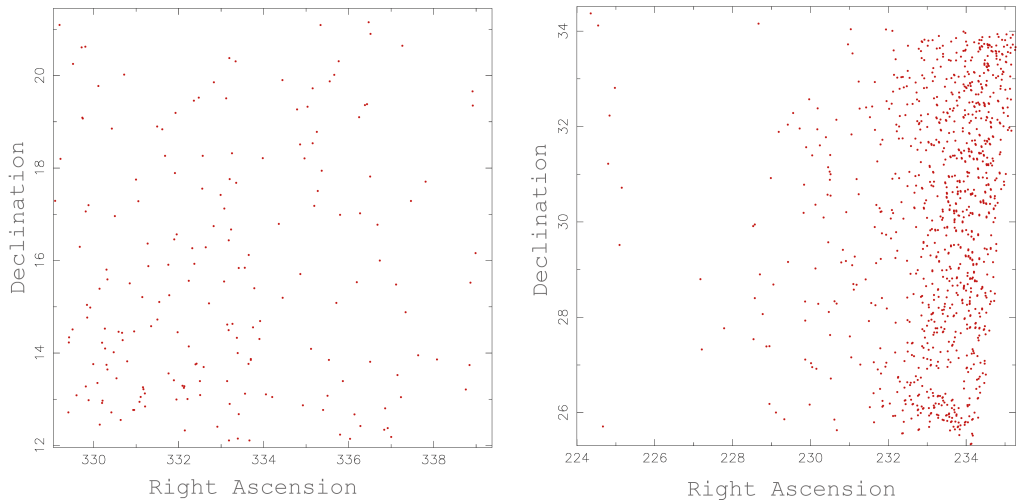

Figure 4.15: Scatter plot of the position of the orphans that make up the 30 arcsecond feature. The left plot corresponds to the field SW2215+1711_142 and the right corresponds to SW1522+3000_144.

match closely with their known positions. The main peak and its tail can be encompassed by a 20 arcsecond search radius. However, the increase in the number of matches at around 30 arcseconds in fields SW1522+3000_144 and SW2215+1711_142 does not appear to correspond with this.

To further complicate this, Figures 4.15, 4.16 and 4.17 indicate that the 30 arcsecond bumps in different fields do not have consistent properties. Figure 4.15 shows the right ascension and declination of the matches in the 30 arcsecond bump for each field. The matches in field SW2215+1711_142 seem to be spread evenly across it whereas in SW1522+3000_144 they are concentrated to one side.

A vector plot of the average offsets for these fields is shown in Figure 4.16. There is no clear systematic offset in SW2215+1711_142 but there is in SW1522+3000_144 (in the area affected by the 30 arcsecond feature). Lastly, Figure 4.17 shows scatter plots of the mean full width half maximum from the WASP images against the mean detected flux. In this plot detections of clusters matching USNO-B stars within 20 arcseconds are shown in red and clusters from the 30 arcsecond feature are shown in green. From field SW2215+1711_142 the 30 arcsecond bump seems to correspond to clusters with extremely large full width half maximum values whereas in

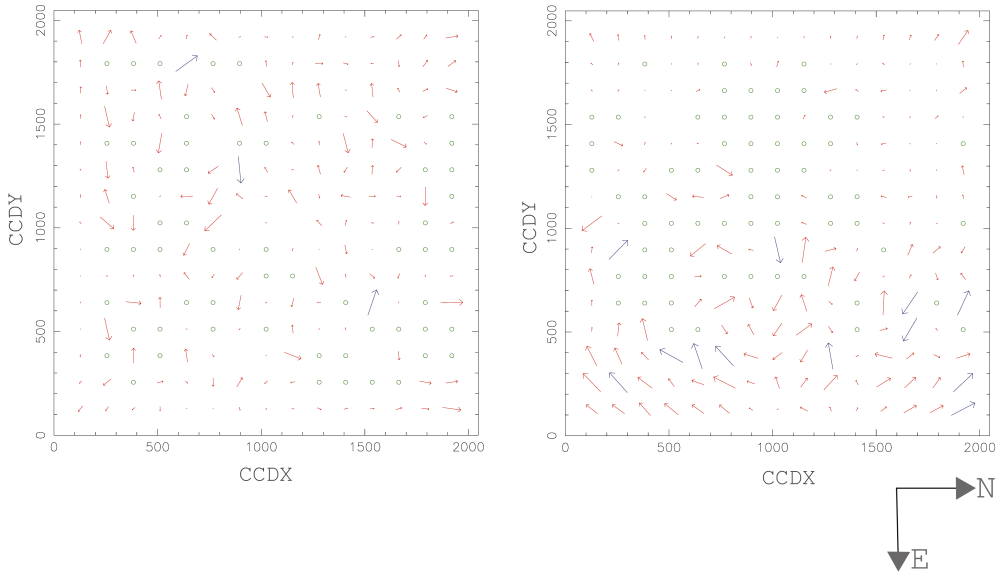

Figure 4.16: Vector plots of the offsets of the orphan clusters with their corresponding USNO-B stars. The green circles indicate where there were too few clusters to determine an average vector. The blue arrows correspond to when the length of the vector has exceeded the maximum being plotted. The left plot is from the field SW2215+1711_142 and the right plot SW1522+3000_144.

SW1522+3000_144 there is a far less clear distinction.

This suggests that in fields such as SW2215+1711_142 detections in the 30 arcsecond bump occur in blurred images. Blurring alone though would be expected to produce a broader central peak rather than a secondary peak at 30 arcseconds. However, if the star is brighter than 15th magnitude then it would have been included in the main WASP archive. This would mean that detections within 30 arcseconds of it will be in the main archive and not in the orphans. The only measurements classified as orphans would be a small number that had overspilled the 30 arcsecond search cone forming one or two clusters in a circle around the star. An example of this is shown in Figure 4.18.

From examining the raw images it can be seen that a similar effect is also occurring in SW1522+3000_144 (see Figure 4.19). The image is extremely badly blurred with the orphans being detected in a brighter region on the edge of the doughnut. It appears that the pipeline only identified part of the doughnut as the

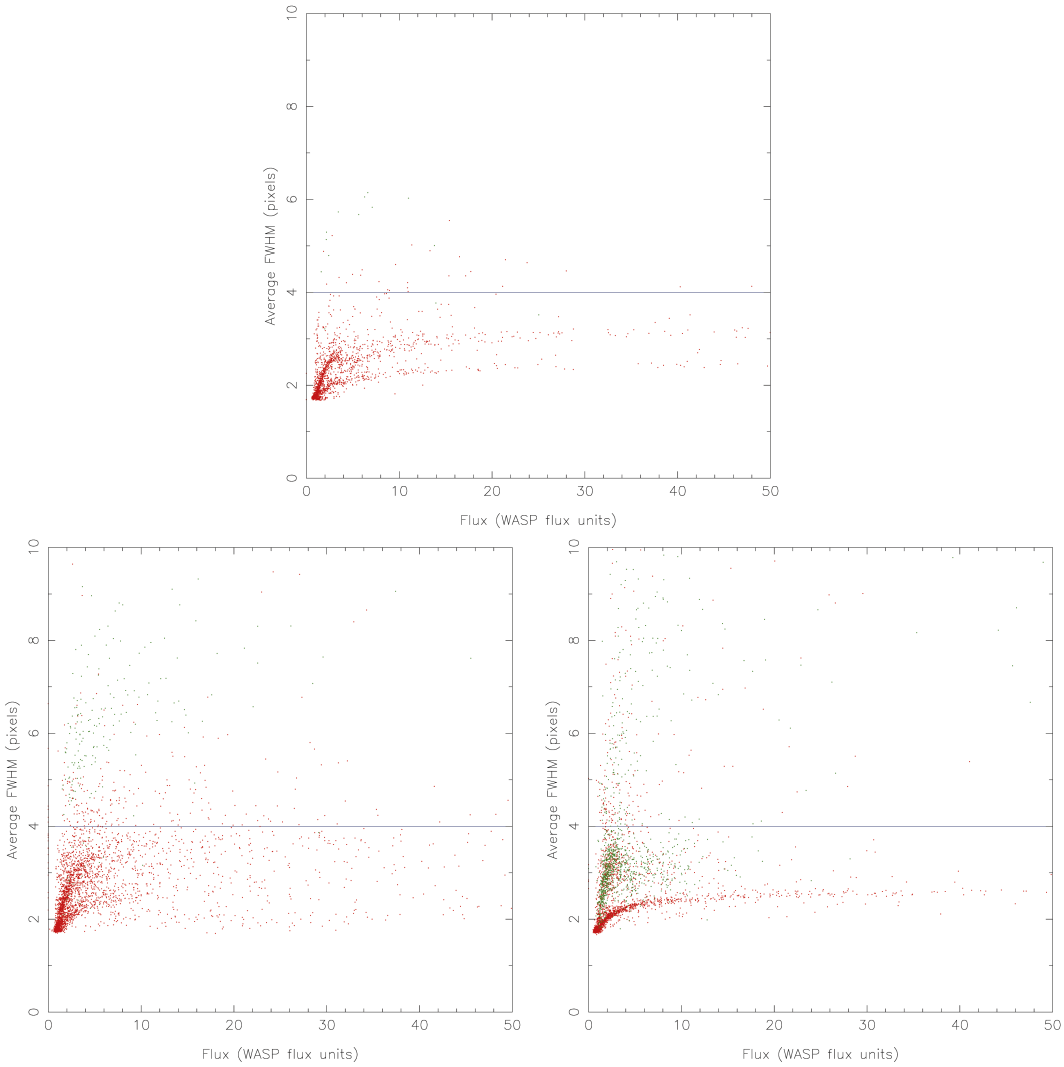

Figure 4.17: Scatter plot of measured full width half maximum against measured flux for the three example fields (SW0933+4730_143 at the top, on the left SW2215+1711_142 and on the right SW1522+3000_144). The green points highlight clusters from the 30 arcsecond feature.

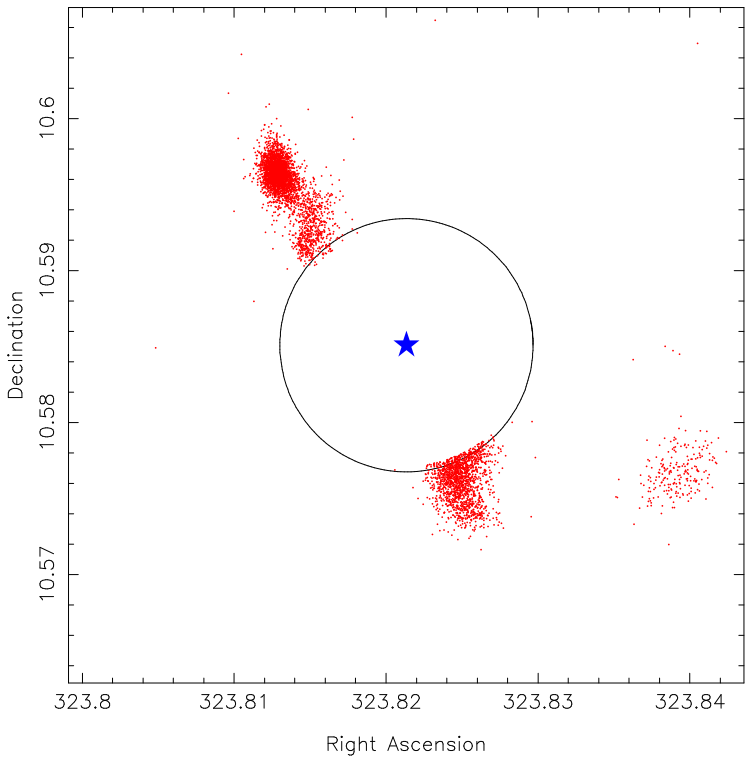

Figure 4.18: Right ascension and declination of orphan detections (in red) caused by a blurred bright star (marked by a blue star) overspilling from the main catalogue. The central circle has a radius of 30 arcseconds.

Figure 4.19: An image from a WASP camera with severe focus problems.

object so the full width half maximum remained relatively small despite the severe blurring.

Combining this information from these and other fields a new cut for rejecting candidates associated with detectable USNO-B stars was introduced. In the new cut any candidate with a USNO-B star within 20 arcseconds that fails the flux-magnitude limit (determined in section 4.7.1) for half or more of the USNO-B magnitudes available, will be rejected. Furthermore, the cluster will also be rejected if a star that fails the flux-magnitude limit with an r2 magnitude brighter than 15th is within 40 arcseconds of the cluster. The USNO-B r2 magnitude of 15th was chosen as this was the cut-off that was used to determine whether a star would be included in the main WASP archive.

4.7.3 Merged detections of multiple USNO-B stars

By examining some of the remaining transient candidates it was discovered that in some cases constant stars were still causing unwanted detections. This occurred when two stars approximately 40 arcseconds apart were being detected as a merged single cluster directly between them. An example of this is shown in Figure 4.20. Their offsets from the center of the detections are larger than 20 arcseconds so the

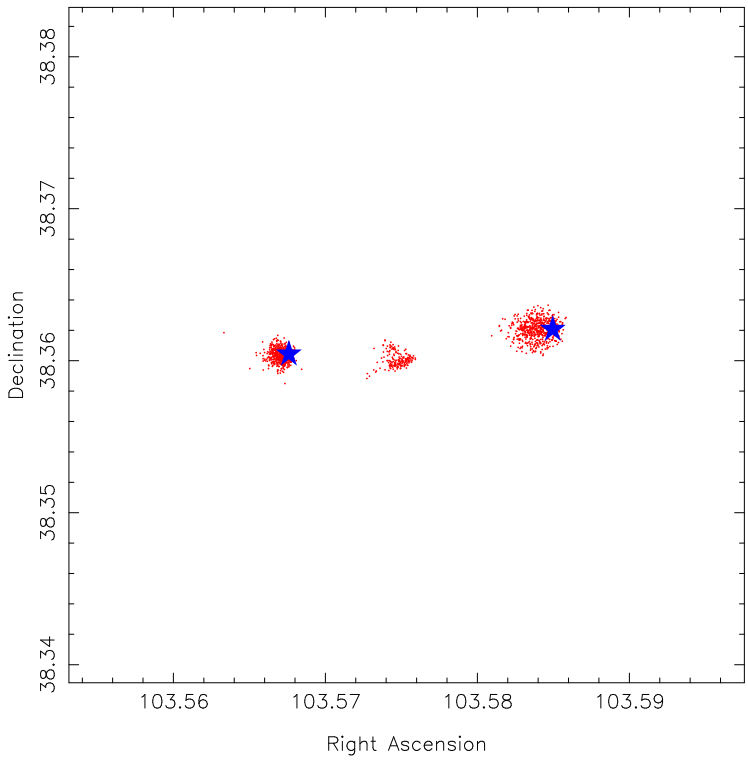

Figure 4.20: A plot of orphan detection positions (in red) in relation to the position of two detectable constant stars (marked by blue stars)

20 arcsecond cut fails to remove them and their USNO-B r2 magnitudes are fainter than 15th so the 40 arcsecond cut also fails to reject them.

From a test sample the star's offsets from the cluster center was found to be between 20 and 27 arcseconds. To remove these false positives a new cut was added to reject clusters with two stars between 20 and 30 arcseconds of the cluster position. Again these stars would be required to fail the magnitude limits described in Section 4.7.1.

4.8 Full Width Half Maximum Test

In cases where the images are extremely badly blurred false transients can be detected. These can be caused by bright stars being identified at the wrong position or by pipeline errors caused by trying to measure what are effectively resolved objects. Even when genuine transient events are detected, the poor image quality and

unreliable positions make it extremely difficult to confirm the source position and whether it was genuine on not. This makes candidates identified from extremely blurred images both unreliable and difficult to follow up. The full width half maximum data provides a means of identifying candidates with this problem (see Section 2.7).

Constant stars identified by the method in Section 4.7.1 were used as a test set for the properties of the full width half maximum of genuine detections. From Figure 4.17 it can be seen that the average full width half maximum of detected constant stars increases with flux up to a limit that is dependent on the properties of the field. However, in none of the cases (or in other tested fields) does the constant star feature rise above a full width half maximum of 4 pixels. This indicates that this value could be used as a limit where sources with a larger median full width half maximum could be rejected for having too blurred images.

4.9 Nearest Neighbour Test

The average nearest neighbour test in the targeted search (see Section 3.7.2) proved to be an effective means of rejecting diffuse clusters. However, the choice of sample in determining the values for the limit was susceptible to noise from chance alignments and the limit itself became ineffective in cases where there were more than 100 detections.

To improve on this a new sample was found by again considering the clusters that were matched with stars using the 20 arcsecond test described in Section 4.7. These were plotted on a log-log plot of number of detections against median nearest neighbour distance. These points are shown in red in Figure 4.21 for an example field. Also shown on the plot is a blue line marking out the original limit, blue crosses showing candidate transients in the field (determined by using the USNO-B cross-correlation tests from Section 4.7 only) and red stars marking the positions of detections of known CVs in the WASP orphans database. This plot indicates that genuine detections fall largely in a diffuse diagonal feature. This feature appears to

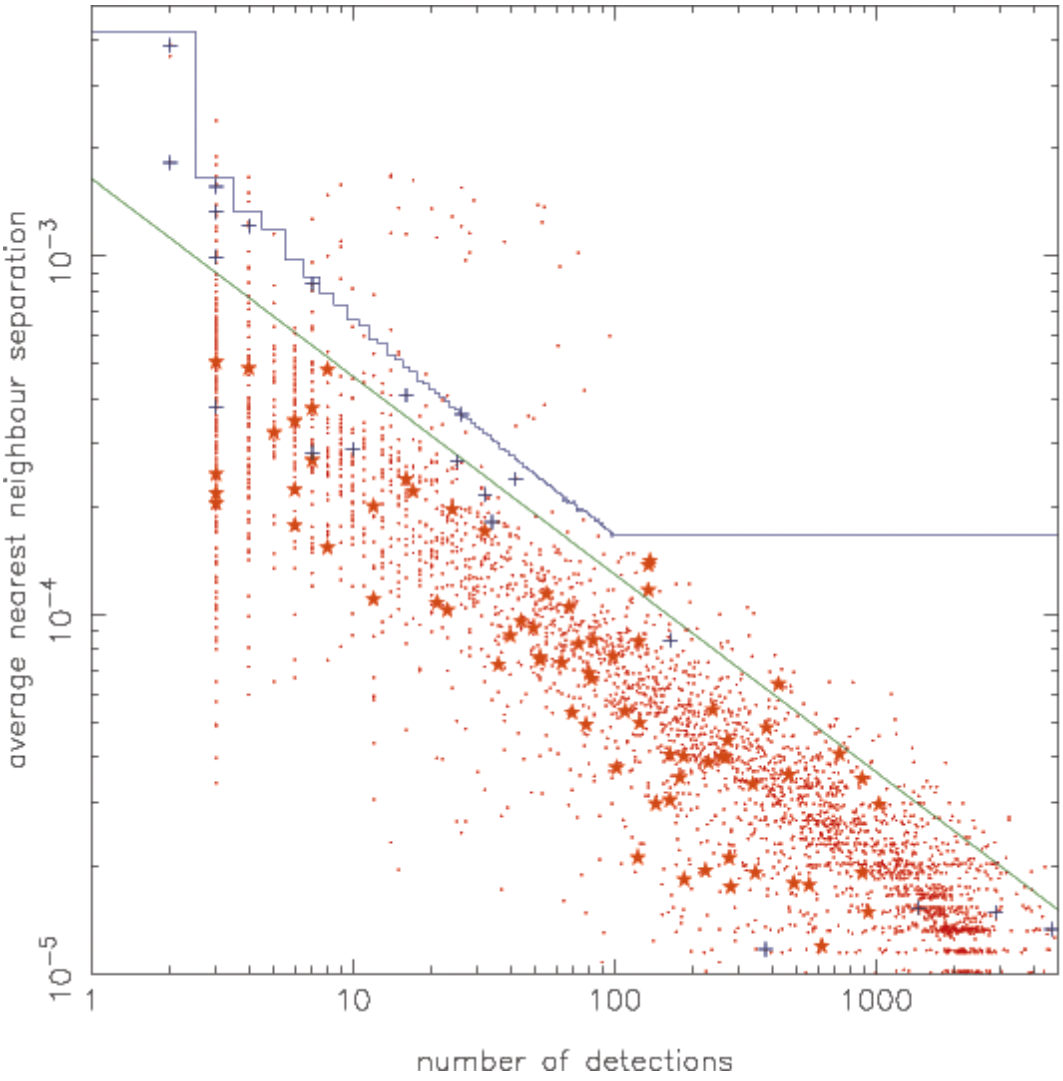

Figure 4.21: Scatter plot of the average nearest neighbour separation against the number of detections of an object. The red dots represent detections of constant stars, the stars mark positions of known CVs detected in WASP and the blue crosses are candidate transient events. The blue line marks the original rejection criteria whereas the green line represents the improved version.

be linear in the log-log plot and shows an inverse relationship between number of detections and median nearest neighbour separation.

From this a new limit was determined following the green line marked on the plot. The gradient and position of the line were chosen to be parallel to the diagonal constant star feature and to allow any clusters that were in this feature to pass the test. While a few of the known CVs are still rejected by this, the number of candidates transients in the rejection area is disproportionately high. This increased ratio between candidates and confirmed transients suggests that while it is possible for genuine detections to fall in the rejection zone the likelihood of false candidates is far higher.

Overall, this new cut causes the rejection of 6 out of 72 clusters caused by known dwarf novae (8%). However, this small reduction of the completeness of the WASP sample is offset by the large reduction in the number of candidates identified by the search algorithm. Out of the 27 candidates identified in the example field by the USNO-B cross-correlation tests (marked as blue crosses on Figure 4.21), 14 (52%) are rejected by the nearest neighbour test.

4.10 Multiple Candidates on One Night

In some cases errors in the WASP data can cause large numbers of false detections on individual nights. These detections are normally removed by the 'bad image' test described in Section 4.4. However, erroneous candidates can still survive this test in several ways. Firstly, if the problem occurs in too many images (more than one percent) then only the worst will be removed. Secondly, if in some images the problem of the data not being matched with the USNO-B catalogue is unusually severe, the images with false detections may not be in the top one percent and therefore may not be rejected. Finally, if the false detections are isolated to a small region of the chip its effects may not be noticeable when considering the entire image.

To deal with candidates caused by errors of this nature, a test was added to

the algorithm to count the number of single night candidates (candidates that only have detections on that night) for each night of observations. If on any given night there are four or more single night candidates then they are all rejected as false. Due to the large number of nights of observations in a given field and the comparatively small number of candidates, it is unlikely that that many genuine candidates would fall on the same night. The choice of placing the cut at four candidates was based on this number being far larger than would be expected to be on one night by chance.

In some cases more serious problems can occur in an individual field leading to these false candidates appearing on more than one night. From a test sample of typical fields these cases seemed unusual and since this would cast into doubt any candidates from theses fields it was decided to not use any where this had occurred. A cut-off of 50 candidates was determined by these samples to be reasonable as it was far larger than a typical field without any systematic problems. Fields with more candidates than this were rejected in their entirety.

4.11 Summary of the Search Algorithm

Based on the work described in this chapter the final cuts for the search algorithm were set as follows.

Pre-clustering

1. Orphans with less than two other corroborating detections within 15 arcseconds on the same night are flagged out and not included in the clustering stage.

2. All orphans from the top one percent of images with the most orphans are rejected unless the number of detections in the image is less than 1000.

Clustering

1. The observed sky is divided into 15 arcsecond bins in right ascension and declination.

2. Neighbouring bins containing detections are connected.

3. Orphans in connected bins are grouped as a cluster.

Post-clustering

1. Clusters within 20 arcseconds of a detectable USNO-B star are rejected. A star is determined to be detectable if the median observed flux (f) is faint enough to obey the relation shown below for half or more of the available USNO-B magnitudes. If the USNO-B magnitude (m) is a red magnitude c=16 and if it is a blue magnitude c=17.

$$f < 10^{0.4*(c-m)}$$

2. Clusters with two detectable USNO-B catalogued stars between 20 and 30 arcseconds of the cluster position are rejected.

3. Clusters within 40 arcseconds of a detectable USNO-B star with R2 magnitude brighter than 15th are rejected.

4. If the median full width half maximum of a cluster is greater than 4 pixels it is rejected.

5. A cluster is rejected if it's average nearest neighbour distance (A) is greater than a limit determined by the number of detections (N):

$$A > 10^{-2.7825-0.5519*log_{10}N}$$

Candidate identification

1. Nights with 4 or more single night candidates were rejected.

2. Fields with 50 or more candidates were rejected.

4.12 Method for Eyeballing Automatically Identified Candidates

Each of the automatically identified candidates was examined individually to establish whether it appeared to represent a detection of a real transient event and, in other cases, establish the source of the detections. For each candidate there were several steps that could be taken to achieve this.

Firstly the light curve, sky coordinates and CCD coordinates were examined. The light curve could indicate a strong transient candidate if a clear rise and decline could be seen over several nights. Failing that it indicated whether the cluster represented a persistent detection of many nights or whether it occurred on a far shorter time scale. Scattered detections from the cluster and around it in sky coordinates indicated a ghost image (these often also had a distinctive shape in CCD coordinates) or an error with the background subtraction in that image. A relatively large scatter with an unusually high full width half maximum (greater than 3.25 pixels) indicated a blurred image. The cluster was expected to move each night with respect to the CCD coordinates so any unusual movement compared to other stars on the chip could indicate a feature on the CCD.

Secondly the cluster was cross-correlated with numerous catalogues including USNO-A [105], USNO-B [106], 2MASS [147], the Ritter and Kolb cataclysmic variables catalogue [136], the Downes cataclysmic variable catalogue [41], AAVSO [1] and the SIMBAD catalogue. A match with a known transient clearly indicated a genuine detection. By comparing USNO-A, USNO-B and 2MASS it was possible to establish if the USNO-B magnitudes were erroneous causing the USNO-B matching section of the search algorithm to fail. An extremely bright star nearby or a crowded field could also cause detections.

Finally, a selection of WASP images were examined for each remaining candidate. These could be used to identify asteroids, blurred images or more unusual problems such as those described in Section 2.7.3. Each candidate was then given a classification based on the results of this analysis.

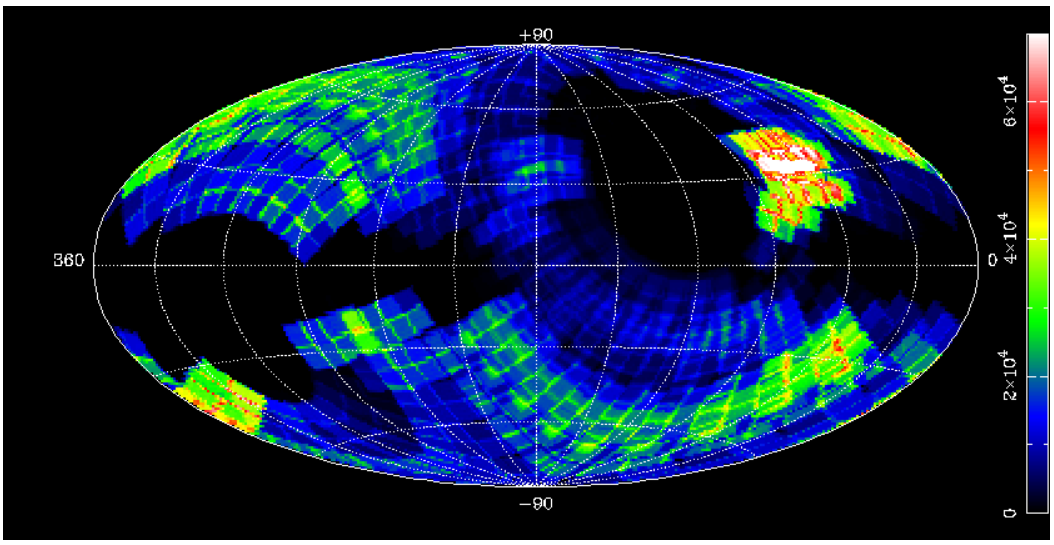

Figure 4.22: A plot of the sky coverage of the WASP planet fields in galactic coordinates as of March 2011. The colours represent the average number of observations for that region of sky with a key for this on the right.

4.13 Search Algorithm Output Results

The search algorithm was run on all planet field data from both WASP north and WASP south for the years 2004, 2006, 2007 and 2008. For a field to be searched it was required that it had at least 500 observations. In 2004 only WASP north was operational and with only five cameras. The results of the search algorithm and eyeballing for WASP north are in Section 4.13.1 and for WASP south are in Section 4.13.2.

Figures 4.23, 4.24, 4.25 and 4.26 show the sky coverage of the WASP observatories each year for WASP north and WASP south. Figure 4.22 shows the sky coverage of WASP in galactic coordinates. It can be seen from these plots that the galactic plane has very little coverage. As described in Chapter 2, this is because of overcrowding in these fields. It can also be seen that there is only limited overlap between the footprints of WASP north and WASP south. The only overlap is due to the northern hemisphere observations of WASP south in 2006. This means that only a small number of transients are expected to be independently identified by both WASP north and WASP south.

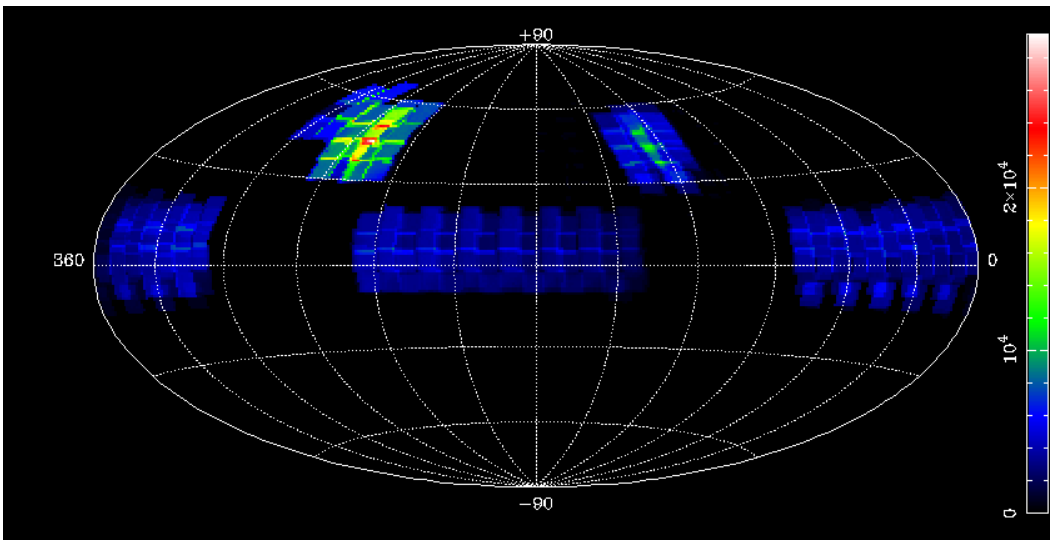

Figure 4.23: A plot of the sky coverage for WASP planet fields in right ascension and declination for the 2004 season. The colours represent the average number of observations for that region of sky with a key for this on the right.

4.13.1 Results from the northern hemisphere planet fields

The results of the search algorithm for the 2004, 2006, 2007 and 2008 planet fields observed by WASP north are shown in Table 4.1. A breakdown of the results of a manual examination of the candidates produced by the search algorithm is shown in Table 4.2. WASP north was only operating in a limited capacity in a prototype phase in 2004 so there are some differences in the numbers of results from that year.

Other than this there are several points to note from the tables. Firstly it appears that the 2006 data contains a comparatively large number of clusters that fail the average nearest neighbour test (described in Section 4.9). In 2006 43.3% of clusters failed this test compared to 16.4%, 10.9% and 20.1% in 2004, 2007 and 2008 respectively.

It also appears that, from 2006, the number of clusters that are automatically identified as candidates increases each year (0.1%, 0.2% and 0.3% successively). However, this increase does not appear to correspond to an increase in transients detected suggesting instead that changes in the observing strategy (such as observing different areas of sky or taking double images at each pointing) may have made the

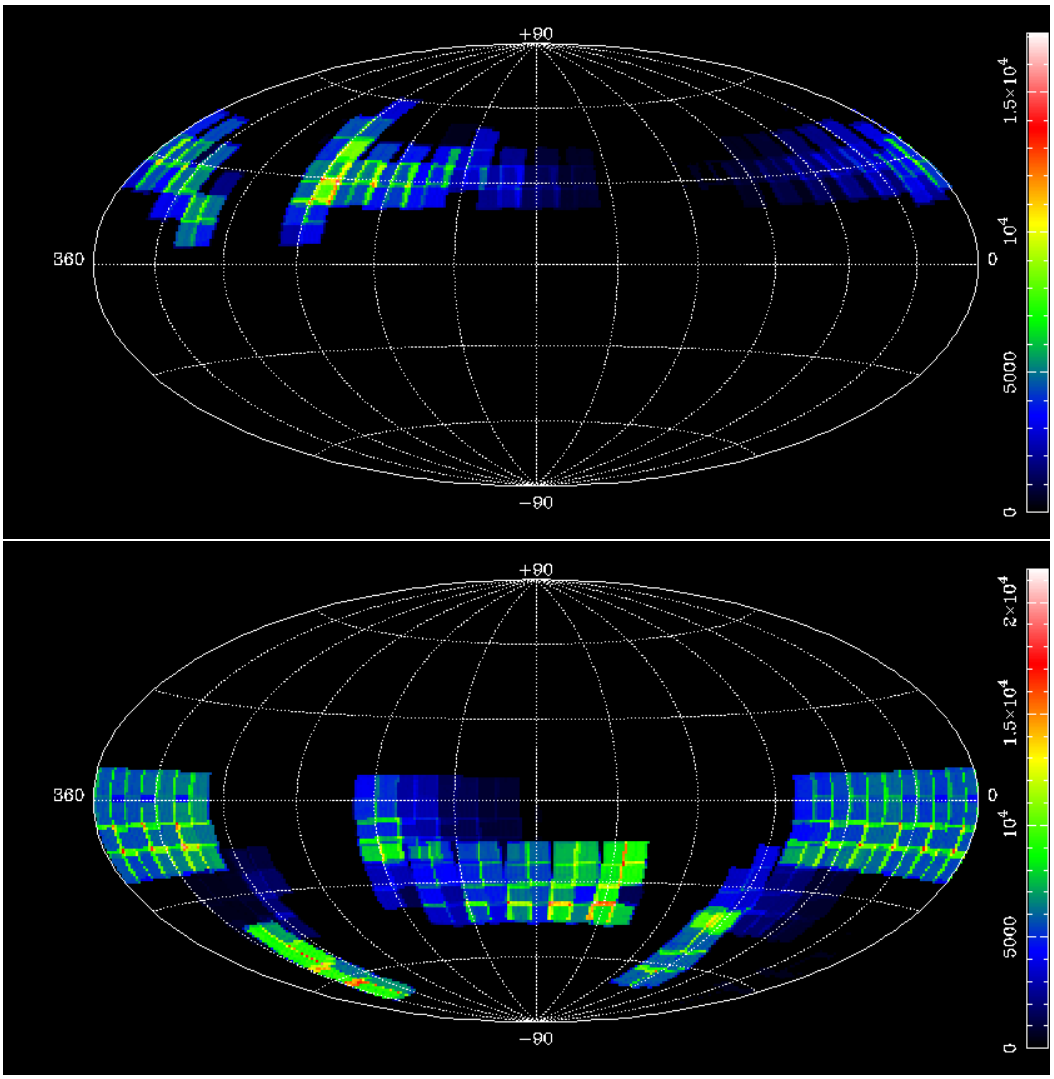

Figure 4.24: Plots of the sky coverage for WASP planet fields in right ascension and declination for the 2006 season. The top plot shows the sky coverage of WASP north and the bottom plot shows the sky coverage of WASP south. The colours represent the average number of observations for that region of sky with a key for this on the right.

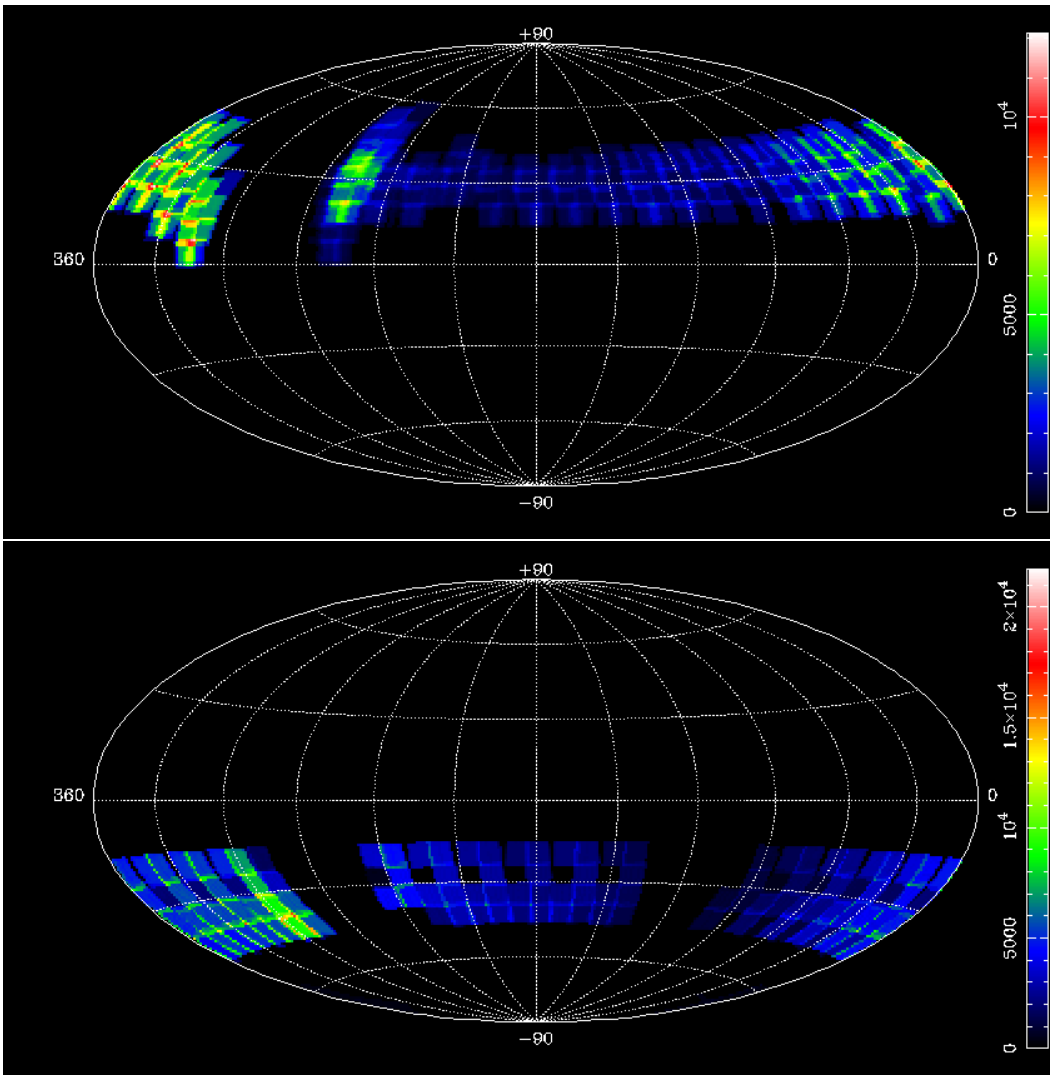

Figure 4.25: Plots of the sky coverage for WASP planet fields in right ascension and declination for the 2007 season. The top plot shows the sky coverage of WASP north and the bottom plot shows the sky coverage of WASP south. The colours represent the average number of observations for that region of sky with a key for this on the right.

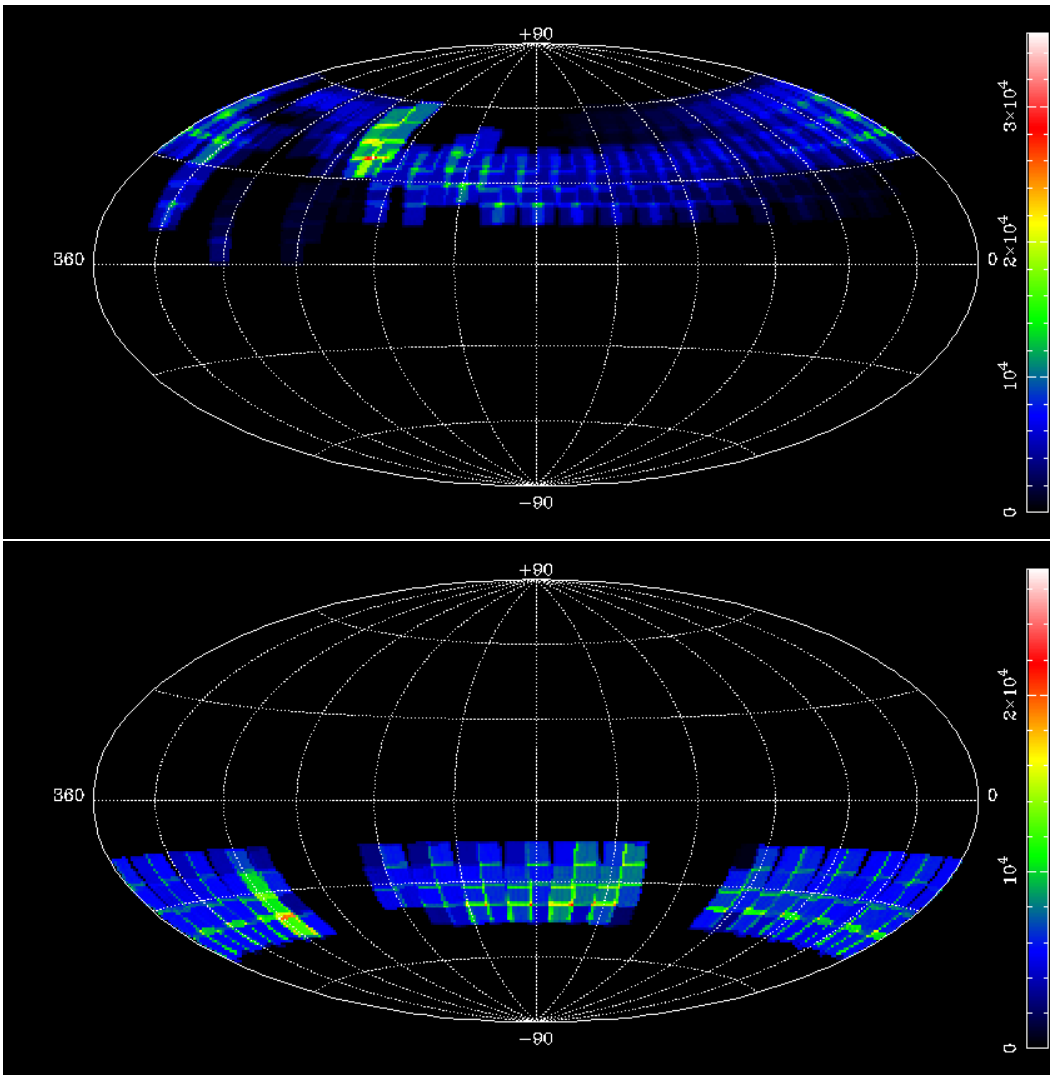

Figure 4.26: Plots of the sky coverage for WASP planet fields in right ascension and declination for the 2008 season. The top plot shows the sky coverage of WASP north and the bottom plot shows the sky coverage of WASP south. The colours represent the average number of observations for that region of sky with a key for this on the right.

search algorithm slightly less effective in later years.

The majority of false positives were caused by a four distinct sources. 30.76% were large or diffuse clusters in right ascension and declination. The majority of these were likely to be ghost images although some may have been associated with poor focus or a moving object. 17.14% were caused by erroneous magnitudes in USNO-B causing the cross-correlation test described in Section 4.7 to fail. 16.4% were caused by a cluster of closely grouped faint stars appearing as a single source in the WASP images. Finally 10.01% were false detections associated with severe blurring in the WASP images.

9.11% of the automatically identified candidates were found to either be known optical transients or strong candidate detections.

	2004n	2006n	2007n	2008n	Total
No. of orphans	69,178,208	157,694,023	461,552,403	469,204,206	1,157,628,840
No. of images	315,800	336,344	846,871	697,448	2,196,463
No. of bad images	643	2,162	7,103	5,745	15,653
No.of orphans from bad images	1,149,420	4,883,261	27,035,452	15,993,514	49,061,647
No. not corroborated	4,564,366	8,173,567	12,456,354	11,086,218	36,280,505
No.of orphans that pass the tests	63,464,422	144,637,195	422,060,597	442,124,474	1,072,286,688
No. of clusters	162,974	814,790	1,448,481	928,629	3,354,874
Rejected by average nearest neighour test	26,726	352,514	158,596	186,658	724,494
Rejected by FWHM test	50,741	123,749	291,923	190,155	656,568
Rejected by 40arcsec USNO test	104,089	430,289	1,335,794	784,349	2,654,521
Rejected by 30arcsec USNO test	6,812	17,220	62,956	21,555	108,543
Rejected by 20arcsec USNO test	109,902	420,176	1,217,665	688,154	2,435,897
Rejected for too many candidates on one night	169	30,171	549	24,486	55,375
No. of field with too many candidates	3	3	13	14	33
No. of clusters rejected for too many candidates in field	206	240	1,372	2,757	4,575
No. of candidates	1,042	1,097	2,488	2,347	6,974

Table 4.1: A table showing the numbers of orphans and clusters from northern hemisphere fields and their reasons for rejection by the automated search algorithm.

Classification	2004n	2006n	2007n	2008n	Total
New transient candidate	22 (2.11%)	20 (1.82%)	29 (1.17%)	40 (1.7%)	111 (1.59%) [98]
Known cataclysmic variable	11 (1.06%)	13 (1.19%)	28 (1.13%)	20 (0.85%)	72 (1.03%) [47]
Known pulsating variable	131 (12.57%)	69 (6.29%)	179 (7.19%)	67 (2.85%)	446 (6.40%) [282]
Other known transient	2 (0.19%)	0 (0%)	2 (0.08%)	2 (0.09%)	6 (0.09%) [5]
Subtotal	166 (15.93%)	102 (9.30%)	238 (9.57%)	129 (5.49%)	635 (9.11%) [432]
USNO-B catalogue error	144 (13.82%)	272 (24.79%)	535 (21.5%)	244 (10.4%)	1195 (17.14%)
Faint star detected in good conditions	89 (8.54%)	1 (0.09%)	10 (0.4%)	2 (0.09%)	102 (1.46%)
Group of stars	188 (18.04%)	199 (18.14%)	606 (24.36%)	151 (6.43%)	1144 (16.4%)
Nearby bright star	41 (3.93%)	5 (0.46%)	33 (1.33%)	69 (2.94%)	148 (2.12%)
High proper motion star	5 (0.48%)	0 (0%)	0 (0%)	3 (0.13%)	8 (0.11%)
Blurred images	26 (2.5%)	55 (5.01%)	309 (12.42%)	308 (13.12%)	698 (10.01%)
Two bright stars at opposite sides of cluster	74 (7.1%)	16 (1.46%)	80 (3.22%)	107 (4.56%)	277 (3.97%)
Asteroid	13 (1.25%)	31 (2.83%)	120 (4.82%)	100 (4.26%)	264 (3.79%)
Galaxies or clusters	3 (0.29%)	2 (0.18%)	2 (0.08%)	5 (0.21%)	12 (0.17%)
Error on CCD	0 (0%)	11 (1%)	0 (0%)	1 (0.04%)	12 (0.17%)
Edge of CCD	27 (2.59%)	8 (0.73%)	27 (1.09%)	14 (0.6%)	76 (1.09%)
Large diffuse cluster	214 (20.54%)	213 (19.42%)	519 (20.86%)	1199 (51.09%)	2145 (30.76%)
Other	52 (4.99%)	182 (16.59%)	9 (0.36%)	15 (0.64%)	258 (3.7%)
Subtotal	876 (84.07%)	995 (90.7%)	2250 (90.43%)	2218 (94.51%)	6339 (90.89%)
Total	1042	1097	2488	2347	6974

Table 4.2: A table showing the results of manual analysis of the automatically identified candidates from WASP north fields. Each candidate is assigned to one of the sources/reasons for rejection listed on the left. Numbers in square brackets represent the unique total of phenomena identified.

4.13.2 Results from the southern hemisphere planet fields

The results of the search algorithm for the 2006, 2007 and 2008 planet fields observed by WASP south are shown in Table 4.3. A breakdown of the results of a manual examination of the 3937 candidates produced by the search algorithm is shown in Table 4.4.

The data from WASP south shows some significantly different properties to WASP north. WASP north seems to have more of a problem with bad images. 0.7% of images are rejected in the north because of this compared to only 0.2% in the south. This results in more orphans passing to the clustering stage in the south (95.9%) compared to the north (92.6%). It also appears that more clusters are rejected by the 40 arcsecond USNO-B cut (Section 4.7) in the north (79.1%) than in the south (58.5%). In contrast though the southern data has more of a problem with too many candidates on a given night and in a given field (8.5% and 2.4% compared to 1.7% and 0.1% respectively). More clusters are automatically identified as candidates in the south (0.4% compared to 0.2%) but no individual year has a higher percentage than the 2004 test year with 0.6%.

	2006	2007	2008	Total
No. of fields	122	126	195	443
No. of orphans	101,864,755	240,562,906	327,188,363	669,616,024
No. of images	462,975	837,255	1,037,417	2,337,647
No. of bad images	447	1,745	2,674	4,866
No. of orphans from bad images	1,146,866	4,620,841	4,776,316	10,544,023
No. not corroborated	3,497,924	5,448,362	7,922,904	16,869,190
No. of orphans that pass the tests	97,219,965	230,493,703	314,489,143	642,202,811
No. of clusters	234,150	431,881	439,517	1,105,548
Rejected by average nearest neighbour test	22,334	112,468	54,332	189,134
Rejected by FWHM test	54,199	107,859	77,432	239,490
Rejected by 40arcsec USNO test	146,114	231,754	268,348	646,216
Rejected by 30arcsec USNO test	8,855	16,232	18,670	43,757
Rejected by 20arcsec USNO test	144,831	192,312	332,874	670,017
Rejected for too many candidates on one night	20,689	53,357	20,278	94,324
No. of fields with too many candidates	12	27	8	47
No. of clusters rejected for too many candidates in field	11,592	14,022	1,045	26,659
No. of candidates	830	1,130	1,977	3,937

Table 4.3: A table showing the numbers of orphans and clusters from southern hemisphere fields and their reasons for rejection by the automated search algorithm.

Classification	2006s	2007s	2008s	Total
New transient candidate	35 (4.22%)	65 (5.75%)	114 (5.77%)	214 (5.44%) [171]
Known cataclysmic variable	2 (0.24%)	5 (0.44%)	16 (0.81%)	23 (0.58%) [20]
Known pulsating variable	94 (11.33%)	106 (9.38%)	151 (7.64%)	351 (8.92%) [208]
Other known transient	3 (0.36%)	5 (0.44%)	3 (0.15%)	11 (0.28%) [7]
Subtotal	134 (16.15%)	181 (16.01%)	284 (14.37%)	599 (15.22%) [406]
USNO-B catalogue error	167 (20.12%)	192 (16.99%)	478 (24.18%)	837 (21.26%)
Faint star detected in good conditions	0 (0%)	3 (0.27%)	6 (0.3%)	9 (0.23%)
Group of stars	169 (20.36%)	248 (21.95%)	399 (20.18%)	816 (20.73%)
Nearby bright star	49 (5.9%)	61 (5.4%)	111 (5.61%)	221 (5.61%)
High proper motion star	0 (0%)	2 (0.18%)	9 (0.46%)	11 (0.28%)
Blurred images	76 (9.16%)	90 (7.96%)	56 (2.83%)	222 (5.64%)
Two bright stars at opposite sides of cluster	8 (0.96%)	28 (2.48%)	31 (1.57%)	67 (1.7%)
Asteroid	61 (7.35%)	117 (10.35%)	206 (10.42%)	384 (9.75%)
Galaxies or clusters	0 (0%)	2 (0.18%)	6 (0.3%)	8 (0.2%)
Error on CCD	4 (0.48%)	4 (0.35%)	0 (0%)	8 (0.2%)
Edge of CCD	3 (0.36%)	4 (0.35%)	7 (0.35%)	14 (0.36%)
Large diffuse cluster	146 (17.59%)	142 (12.57%)	383 (19.37%)	671 (17.04%)
Other	13 (1.57%)	56 (4.96%)	1 (0.05%)	70 (1.78%)
Subtotal	696 (83.85%)	949 (83.99%)	1693 (85.63%)	3338 (84.78%)
Total	830	1130	1977	3937

Table 4.4: A table showing the results of manual analysis of the automatically identified candidates from WASP south fields. Each candidate is assigned to one of the sources/reasons for rejection listed on the left. Numbers in square brackets represent the unique total of phenomena identified.

Chapter 5

Transient Classification

From the search described in Chapter 4, 1234 clusters were classified as candidate transients. Counting only the unique candidates (see Tables 4.2 and 4.4) and allowing for the small region of overlap between WASP north and WASP south, this corresponded to 810 separate objects. 545 of these corresponded to known astronomical phenomena. Section 5.1 describes the methods used to classify the remaining 265 transient candidates. The nature of a number of these were confirmed with spectroscopic observations described in Section 5.2. An overview of the results of the classification is described in Section 5.3 with a more detailed analysis carried out in Chapter 7.

5.1 Method for Classification of Transient Candidates

The new candidate transients were classified as cataclysmic variables, stellar flares or pulsating variables by considering the properties of their light curves (duration and shape), the magnitudes of any matching USNO-B [106] or 2MASS [147] stars and the properties of any corresponding phenomena in SIMBAD. Candidates that did not clearly fall into one of these categories are listed as unknown transients (see Section 5.1.4). The possibility that one of the candidate transients represents a rarer phenomena such as a nova or a gamma ray burst is discussed in Sections 7.4 to 7.8.

5.1.1 Cataclysmic Variable Candidates

For a transient candidate to be classified as a cataclysmic variable it was required that the outburst should be visible in the WASP images for at least two nights but no more than fifty. The amplitude of the outburst was required to be more than approximately 1.5 magnitudes although anything larger than 10 magnitudes would strongly suggest a nova. This corresponds to the parameter space shown in Figure 1.13. With the exception of faint outbursts at the limit of detection, it was required that after a short rise the outburst was seen to be declining in brightness. Where more complete data was available the shape of the decline was checked to be consistent with a dwarf nova outburst. In some cases superhumps were detected which were used to confirm the nature of the candidate.

5.1.2 Flare Star Candidates

A candidate was classified a flare star candidate if the outburst duration was less than two hours and if an optical counterpart was present in 2MASS and USNO-B. In some cases the field had shorter coverage than this or a change of pointing moved the candidate out of the field of view. In these cases the candidate was classified as unknown as it was not possible to confirm the duration of the outburst.

5.1.3 Pulsating Variable Candidates

Candidates were classified as pulsating variable candidates if their light curves were consistent with slow, smooth oscillations in brightness and if there was a corresponding bright star in USNO-B. In some cases the detections were recorded in the main WASP archive as well as the orphans so this was checked when considering possible pulsating variable candidates.

5.1.4 Candidates of Unknown Classification

For some candidates there was not sufficiently strong evidence to identify them as any of these candidates. A large proportion of these are transients that appear

throughout one night of coverage but don't appear either in the data or in the raw images on subsequent nights. Many of these may be short dwarf nova outbursts. However, it is also possible that some may represent stellar flares where the coverage during the night was too short to observe the decline. The longer duration candidates could be pulsating variables with insufficient coverage. Finally, several candidates appear from their detections to be short transients without counterparts. However, the raw image data was not available meaning asteroids or pipeline failures could not be ruled out.

5.2 Spectral Observations of Transient Candidates

Spectra of transient candidates were taken using the ISIS instrument on the William Herschel Telescope in La Palma in June and September 2008. The gratings used in the two arms of the spectrograph were R316R and R300B with central wavelengths of 6450 Å and 4253 Å and a 2x2 binning. Before observing approximately 20 bias frames and 20 flat field exposures were taken for each arm. Arc line exposures were taken between targets. A further 20 bias frames and 20 flat field exposures were taken for each arm at the end of the night weather permitting.

To reduce the spectra the STARLINK package FIGARO was used to calculate the average nightly bias and flat-field frames. The spectra were then extracted using the PAMELA software [100]. Copper-argon arc lamp exposures were used to establish the wavelength scale. Finally, the spectra were normalised to the continuum level by using a spline fit.

A list of the observations taken can be found in Tables 5.1 and 5.2. The targets selected for observation were found from the targeted X-ray search (see Section 3.7) and by using a prototype version of the untargeted search algorithm (see Chapter 4). They were chosen to represent the best transient candidates visible during the observing period.

The targets observed in June 2008 (listed in Table 5.1) were found using the targeted method described in Section 3.7. As this process was less refined than for

Date	Identification	UT	Exp. time (s)	Spectra
04/06/2008	WTC014i	21:46	1800	Featureless star
	WTC015i	22:34	1800	Featureless star
	WTC017i	23:19	1800	Flare star
	WTC019i	00:08	900	Flare star
	WTC019i	00:23	900	
	WTC023i	00:45	1800	Featureless star
	WTC028i	01:37	1800	Cataclysmic variable
	WTC041i	02:25	1800	Cataclysmic variable
	WTC041i	02:55	1800	
	WTC041i	03:29	1800	
	WTC030i	04:07	1800	Too faint
	WTC027i	04:45	1800	Featureless star

Table 5.1: A list of observations taken in June 2008. After the name of the object in column two the roman numeral indicates which matching USNO-B star was observed. The numbering is in ascending order from nearest to furthest.

transient searches in later chapters, the false positive rate can be seen to be relatively high with 4 targets showing no signs of variability from their spectra. The targets observed in September 2008 (listed in Table 5.2) were found using the untargeted search described in Chapter 4 and had only two false positives over the three nights of observations.

Date	Identification	UT	Exp. time (s)	Spectra
28/09/2008	WTC065i	22:59	900	Cataclysmic variable
	WTC065i	23:15	900	
	WTC068i	00:36	300	Possible cataclysmic variable
	WTC068i	00:41	300	
	WTC068i	00:48	900	
	WTC068ii	01:10	900	Featureless star
	WTC039i	01:33	1800	Cataclysmic variable
	WTC001i	02:42	600	Cataclysmic variable
	WTC001i	02:53	600	
	WTC041i	03:11	1800	Cataclysmic variable
	WTC041i	03:41	1800	
	WTC048i	04:21	1800	Cataclysmic variable
	WTC051i	05:12	1800	Flare star
	WTC058i	05:52	600	Pulsating variable
	WTC058i	06:07	60	
	WTC061i	06:10	300	Pulsating variable
	WTC061i	06:20	30	
29/09/2008	WTC045i	03:19	60	Flare star
	WTC045i	03:20	300	
	WTC045i	03:26	600	
	WTC050i	03:46	240	Flare star
	WTC057i	04:01	600	Flare star
	WTC057iii	04:17	600	Featureless star
	WTC006i	04:33	1800	Cataclysmic variable
	WTC054i	05:13	889	Observations incomplete
30/09/2008	WTC067ii	20:27	900	Featureless star
	WTC067i	20:50	440	Featureless star
	WTC067iii	21:01	300	Featureless star
	WTC067iv	21:10	240	Featureless star
	WTC069i	21:51	1800	Featureless star
	WTC038i	22:43	300	Observations incomplete

Table 5.2: A list of observations taken in September 2008. After the name of the object in column two the roman numeral indicates which matching USNO-B star was observed. The numbering is in ascending order from nearest to furthest.

5.3 Classification of Candidate Transients Identified by Search Algorithm

Of the 810 unique candidate transient identified, 545 correspond to known astronomical phenomena. Of these, 61 are known cataclysmic variable stars, 2 are known flare stars, 472 are known variable stars and 10 are other known transients (including nova eruptions from V2467 Cyg and N LMC 2009 which are discussed in more detail in Section 7.4).

The remaining 265 objects represent new transient candidates. As described in Section 5.1, these candidates were given provisional classifications of the type of object they are likely to represent. They were divided into 3 types; cataclysmic variable systems (38 candidates), flare stars (136 candidates) and pulsating variable stars (60 candidates) with the classification of the remaining 31 systems unknown. These three distinct populations of transients can be seen in the reduced proper motion-colour plot shown in Figure 5.1. Known systems are marked with circles and new candidates with crosses. Pulsating variable stars are shown in blue, flare stars in yellow, cataclysmic variables in red and transients of uncertain type in green. The reduced proper motion (H) can be calculated from the proper motion in arcseconds per year (μ) and the apparent magnitude (m) using the formula:

$$H = m + 5 + 5log(\mu)$$

The proper motion was taken from the matching star in the USNO-B catalogue. Errors on this were typically less than $\sim$30 marcsec. The reduced proper motion is approximately proportional to absolute magnitude so can be used as a proxy for it when distances (and hence absolute magnitudes) are not available [141]. Hence the reduced proper motion against colour plots shown in Figure 5.1 separates the different types of stars in a similar way to the Hertzsprung-Russell diagram.

Coordinates and WASP identifiers of the new transient candidates can be found in Appendix B along with a measurement of the superhump/orbital period (when available) for cataclysmic variable candidates. Positions are typically accurate to within 13.4 arcseconds (see Section 3.3). The results from each of these transient

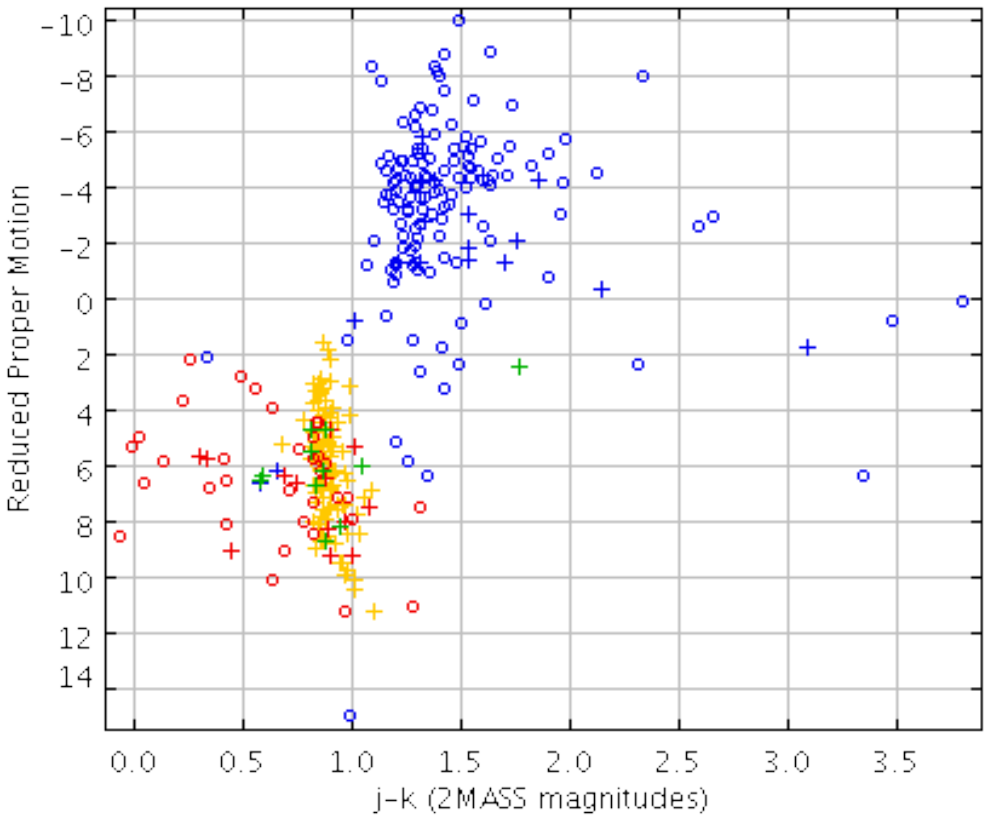

Figure 5.1: Reduced proper motion scatter plot of transients observed with WASP. CVs are marked in red, flare stars in yellow, pulsating variable stars in blue and undetermined transients in green. Known systems observed by WASP are marked with a circle and new discoveries are marked with a cross. The reduced proper motion and colour values are calculated from matching stars in the 2MASS catalogue.

types, along with the possibility of detections of rarer phenomena, is considered in more detail in Chapter 7.

Plots showing the candidates which were not given a provisional classification are shown in Figure C.4 with their positions listed in Table B.4. All of these systems appear from their light curves at least roughly consistent with one of the three classifications considered above so a rarer transient type is unlikely. This is reenforced by their positions on Figure 5.1 where the majority of unknown transients appear to be nearby M-dwarfs from their colours. This would indicate either a long duration flare or a short dwarf nova outburst.

Figure 5.2 shows the position on the sky of the unknown transient candidates. These can be compared to Figures 7.13 and 7.14 for the dwarf nova sky distribution, Figure 7.22 for the flare star distribution and Figure 7.35 for the pulsating variables. The sky coverage of WASP is shown in Figures 4.23, 4.24, 4.25 and 4.26.The unknown transient candidates appear relatively evenly distributed across the sky suggesting the majority are from either a nearby or extragalactic source. This would again be consistent with flare stars and dwarf nova causing a large number of them.

A further considerations is that many are not classified because of issues in the data suggesting instead that there may be a significantly higher false positive rate amongst this class of transient candidate than the others.

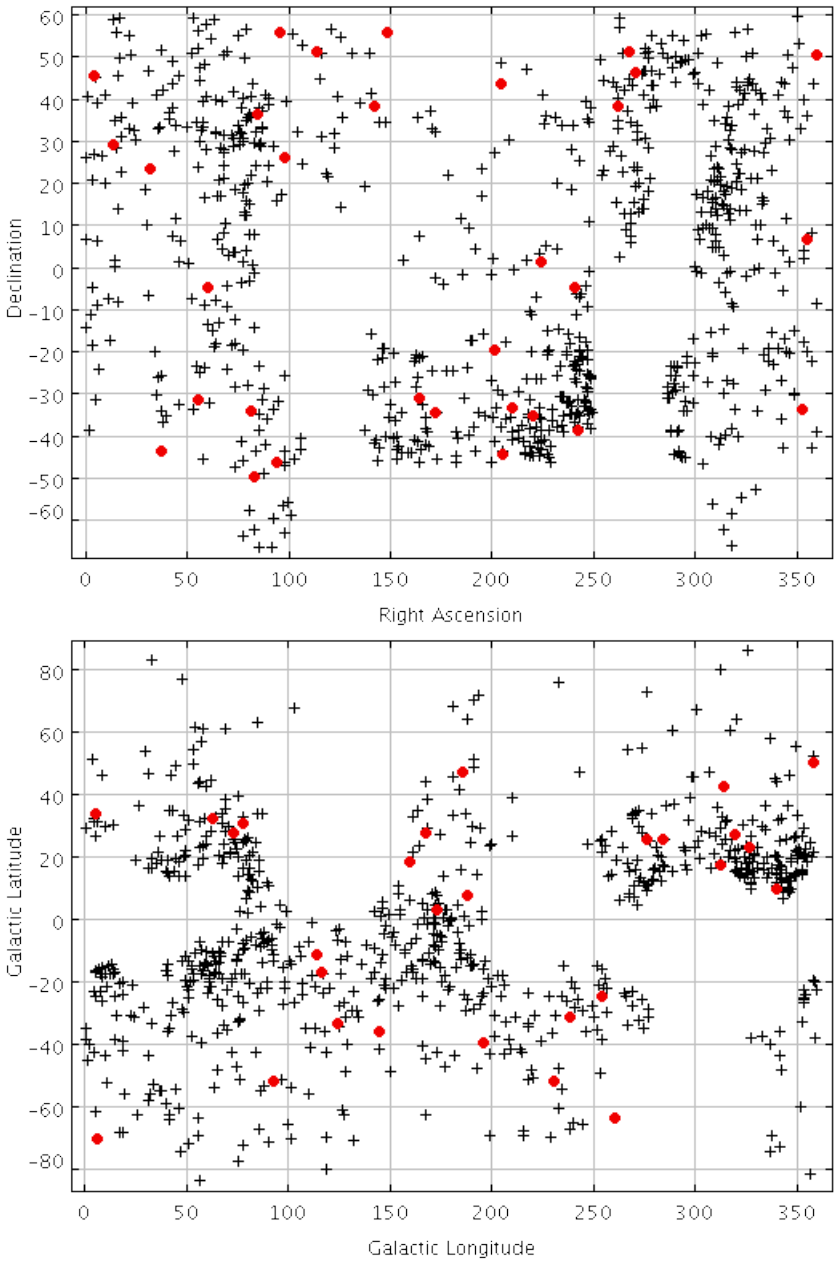

Figure 5.2: Plots of the sky distribution of unknown transient events in right ascension and declination and galactic coordinates. New transient candidates of unknown type are marked with red circles. All other detected transients are marked with black crosses.

Chapter 6

Efficiency and Completeness of the WASP Survey

In a large scale automated search, such as described in this thesis, it is inevitable that a proportion of the candidates produced will be false positives and that some of the genuine transients will be rejected. In determining the types of tests and the strictness of the cuts described in Chapter 4 a balance had to be found between ensuring that enough false positives were rejected (the *efficiency*) and that as many genuine transients as possible were identified (the *completeness*). In this Chapter the efficiency and completeness of the untargeted search algorithm is analysed and discussed.

6.1 Efficiency

The search of the WASP orphans data for the years 2004, 2006, 2007 and 2008 (see Section 4.13) produced 1,827,244,864 orphans. The initial pre-clustering tests rejected 6.2% of these detections leaving 1,714,489,499 to be clustered. This produced 4,460,422 separate clusters. The post-clustering tests rejected 99.76% of these leaving 10,911 to be examined by hand.

As is discussed in Section 4.13, the majority of these automatically identified candidates were spurious or unwanted, non-transient detections. However, 909 of

these clusters (8.3%) were found to correspond to known variable sources. The majority of these known variable sources were pulsating variable stars (797 clusters) such as Miras and semi-regular variables. 95 of the clusters were caused by known cataclysmic variables and 17 were caused by other known variable sources such as novae.

Of the remaining clusters identified by the search algorithm 325 (3.0%) were, on closer examination, found to be candidate discoveries of new transients. A detailed description of this can be found in Sections 4.12 and 5.1. From the spectral follow-up observations described in Section 5.2 it appears that the vast majority of candidates identified by this method are genuine transient phenomena.

If the known transient detections are combined with the new candidate detections it implies that the automated search algorithm has an efficiency of 11.3%. While this may seem low it should be viewed in the context of the fact that 99.76% of clusters were rejected by the algorithm. The false positives are caused by a wide variety sources (see Section 4.13) so any further tests would risk significantly reducing the completeness of the sample.

6.2 Completeness

6.2.1 Ritter and Kolb Dwarf Novae

The completeness of the sample of dwarf novae detected by WASP can be considered in several ways. Firstly, what proportion of systems in regions of the sky observed by WASP were actually detected in outburst. Secondly, of these systems, what proportion would be identified by the untargeted search algorithm.

To test this the sample of Ritter and Kolb dwarf novae identified in Section 3.4 was used. The Ritter and Kolb catalogue [136] contains 436 systems thought to show dwarf nova outbursts. By carrying out cone searches at the positions of these systems (see Sections 3.4.1) orphan detections of outbursts from 82 systems were found.

To establish the number of observations taken at the position of each cata-

No. of observations	No. of CVs	No. of CVs detected
0	66	0 (0%)
1 - 500	54	4 (7%)
500 - 10,000	138	28 (20%)
>10,000	178	50 (28%)

Table 6.1: A table showing the proportion of cataclysmic variables detected in outburst by WASP for various amounts of coverage.

clysmic variable the main WASP archive was searched with a radius of 0.1 degrees. The nearest seven detected stars were then taken and the median number of observations was used as an indication of the coverage for that region of sky. A region of sky was considered to be in the footprint of WASP if there were 500 observations or more before the end of the 2008 observing season. This was chosen to correspond to the requirement for a field to be observed 500 times for it to be searched with the untargeted search algorithm (see Section 4.13).

The numbers of CVs identified with a given number of observations are listed in Table 6.1. If the results for all systems with more than 500 observations are combined it is found that 78 of the 316 systems are detected (25%).

This calculation does not account for differences between the Ritter and Kolb sample and the sample of new CVs that WASP has discovered. For example, it is likely that the newly discovered systems will, on average, outburst less frequently hence making them more difficult to find and explaining why they were not already included in Ritter and Kolb. This would make the actual ratio of systems detected lower.

The second consideration for the completeness of the dwarf nova sample discovered by WASP is the number of systems identified by the search algorithm. The post-clustering cuts described in Section 4.11 were tested on a sample of the Ritter and Kolb CVs which were known to have outbursts that had been detected by WASP. Out of 72 clusters in this test sample the search algorithm successfully identified 40 as transient candidates (equivalent to 56%). A breakdown of the results is shown in Table 6.2.

While the number of rejections from this sample is high this is in part because

Failed 20 arcsecond test for constant stars	20 out of 72
Failed 30 arcsecond test for pairs of constant stars	0 out of 72
Failed 40 arcsecond test for constant stars	8 out of 72
Failed full width half-maximum test	3 out of 72
Failed average separation from nearest neighbour test	6 out of 72
Number of clusters identified as candidates	**40**

Table 6.2: A table showing the number of clusters caused by confirmed CV outbursts rejected by each test.

there are several brighter systems where the CV itself causes the rejection. Under good conditions these could be detected in quiescence so the rejection is correct. Types of systems like this are unlikely to be undiscovered so represent little loss in terms of discovering new transients. These account for 4 of the rejected clusters.

A further 15 clusters have been rejected because the USNO-B catalogued magnitudes were too bright. A likely cause of this would be if the system were in outburst when the USNO-B magnitudes were measured. Again, systems like this are likely to have already been discovered since for USNO-B and WASP to have detected them in outburst it is probable that they outburst quite frequently.

If these cases are discounted the search algorithm is found to successfully identify 76% of the remaining clusters caused by known CVs. The remaining 24%, although clustered, failed one or more of the post-clustering tests. As can be seen from Figure 4.21, four of the CVs failed the average nearest neighbour test and the majority of the remaining clusters were rejected because of chance alignments with bright stars (particularly with the 40 arcsecond USNO cross-correlation test).

6.2.2 Classification of Known Transients

A further consideration is what proportion of dwarf novae detected as transients are correctly classified as dwarf novae and what proportion are classified as being from an uncertain source. To test this the 94 detected clusters associated with known cataclysmic variable systems were classified according to the criteria described in Section 5.1.

From examining the light curves and corresponding USNO-B stars 78 of the

clusters were classified as dwarf nova candidates. Another 4 single night candidates were classified as dwarf novae when the raw images were examined. A further 3 single night outbursts matched other dwarf nova candidates so could also be classified as such. This left 9 clusters caused by known dwarf novae that would have been classified as unknown transient candidates.

This implies that the classification system catagorises 90% of clusters caused by dwarf novae correctly. If actual candidates rather than clusters are considered, 53 out of 62 would be identified (85%).

6.2.3 Previously Identified Candidates

The X-ray targeted search (described in Section 3.7) discovered five dwarf nova candidates. All of these were identified as candidate transients by the automated untargeted search algorithm (described in Chapter 4). However, the subsequent classification of them was different. One was again identified as a dwarf nova candidate, another was identified as a candidate of uncertain type and three more were subsequently found by other surveys (such as the Catalina Sky Survey) so were classified as known dwarf novae.

Four cataclysmic variable candidates were identified by a prototype of the untargeted search (WTC039, WTC041, WTC065 and WTC068). Of these three were identified as dwarf novae by the final search algorithm but one failed two of the tests so was not identified (the nearest neighbour separation test described in Section 4.9 and the USNO-B cross-correlation test described in Section 4.7).

6.2.4 Completeness for Other Phenomena

The completeness for other transient types is far less certain since a large test sample of detections (similar to Ritter and Kolb for dwarf novae) is not available. Most of the transient candidates that are not dwarf novae are likely to be stellar flares or pulsating variables. The completeness for these is expected to be extremely low. As is discussed in Section 1.6, the relatively low amplitude of variability for most pulsating variables and the high probability of the USNO-B observations being

taken during a high state means that most would not be expected to pass the USNO cross-correlation test described in Section 4.7.

Low amplitude flares could also fail to be identified for this reason. The typically very short duration is likely to exacerbate this as WASP is unlikely to get the required three detections. Of the seven flares identified by the X-ray targeted search for candidate transients (see Section 3.7) only two were identified by the untargeted search algorithm which further highlights how incomplete the identified sample is.

For rarer phenomena such as gamma ray bursts, novae and supernovae the lack of or very small test sample of detected known outbursts and the complicated selection effects mean that it is very difficult to establish the completeness of the WASP sample.

Chapter 7

Discussion

7.1 Cataclysmic Variables

7.1.1 Candidate cataclysmic variable stars identified

From the final untargeted search of the WASP orphans database 54 transients believed to be associated with new cataclysmic variables were identified. These corresponded to 38 separate systems which are listed in Table B.1. Also included in this table are periods that were identified in the WASP data. The method used to do this was the same as in Section 3.4.3. Of the 38 new cataclysmic variable candidates 14 were found to have periods in the WASP data with most of the remaining systems having insufficient data on individual nights to confidently establish a period.

7.1.2 Analysis of light curves

The light curves for the new cataclysmic variable candidates identified in the WASP data are shown in Figure C.1 in Appendix C. Of particular note are the extremely long outbursts seen in WTC126 and WTC150. From Figure 7.4, which shows a histogram of the duration of outbursts observed in WASP, these two can clearly be seen to be outliers with WTC126 lasting longer than any outburst of a known CV detected by WASP. It is possible that outbursts with light curves such as these are caused by fast or recurrent nova (see Section 7.4). However, the detection of

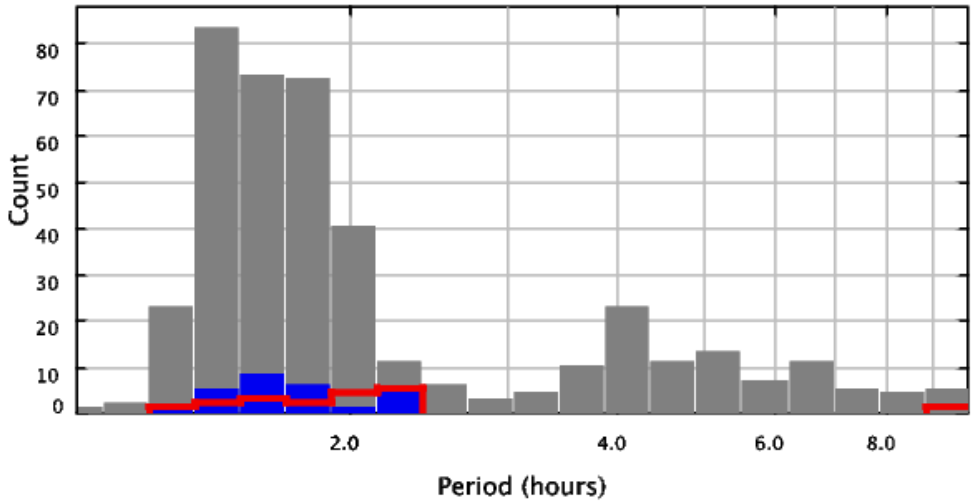

Figure 7.1: A histogram showing the period distribution of cataclysmic variable systems that display dwarf nova outbursts. Known periods of Ritter and Kolb CVs [136] are shown in grey. WASP measurements of known CVs are shown in blue. WASP measurements of new CV candidates are shown as a red outline.

a period of 88 minutes in WTC126 suggests instead that this system is of WZ Sge type which can also have extremely large outbursts.

WTC179 should also be highlighted as interesting. From the WASP data the system was found to have an orbital period of 540 minutes and, unusually, was found to be eclipsing. This system is discussed more in Section 7.1.5.

A histogram showing the distribution of detected periods in both known and unknown systems is shown in Figure 7.1. Known orbital periods of dwarf novae from the Ritter and Kolb catalogue [136] are plotted in grey. WASP measurement of the periods in known systems are shown in blue. Periods from new cataclysmic variable candidates are shown as a red outline. A caveat that should be noted is that for the periods measured by WASP it was not known whether these were orbital or superhump periods. However, this is unlikely to make a difference of more than a few percent.

With the small number of new systems with measured periods it is difficult to draw any strong conclusions about the period distribution we are detecting. What can be seen is that all but one of the new cataclysmic variables and all of the known

systems with periods in WASP are below the period gap. This is not surprising and is likely to be due to a selection effect in finding the period. CVs below the gap are likely to display superoutburst with superhump periods that are easier to detect. Furthermore CVs above the gap can have periods longer than a night of WASP coverage making the period far more difficult to identify. WTC179 is the exception because it is an eclipsing system making the orbital period far more pronounced.

From the even distribution of periods below the gap the data suggests that the sample of CVs being discovered by WASP is not radically different to what has already been found. Significantly there seems to be no evidence of a spike of rarely outbursting systems at the period minimum which is predicted by current theories [83] and was found by SDSS [48]. This is perhaps not very surprising as the majority of known systems were, as with the WASP sample, identified by the detection of an outburst. However, unlike current outburst selected samples, such as the Ritter and Kolb catalogue [136], WASP has identified a uniformly selected sample of dwarf novae. This makes the WASP sample useful for testing population models and space density estimates.

7.1.3 Spectra of candidate systems

Spectra were taken of cataclysmic variable star candidates identified by the targeted search described in Section 3.7 and the untargeted search described in Section 4.2. Naturally this had some overlap with the candidates identified by the final version of the search algorithm (specifically WTC039, WTC041 and WTC068). As described in Section 5.2, the spectra were taken using the ISIS instrument on the William Herschel Telescope in La Palma in June and September 2008. The gratings used in the two arms of the spectrograph were R316R and R300B with central wavelengths of 6450 Å and 4253 Å. Bias and flat field corrections were applied to the data. The spectra from five untargeted systems are shown in Figure 7.2 and from three X-ray selected candidates (see Section 3.7) in Figure 7.3.

The Balmer emission lines in each of these spectra suggests that their identification as cataclysmic variables was correct. There appears to be broad absorption

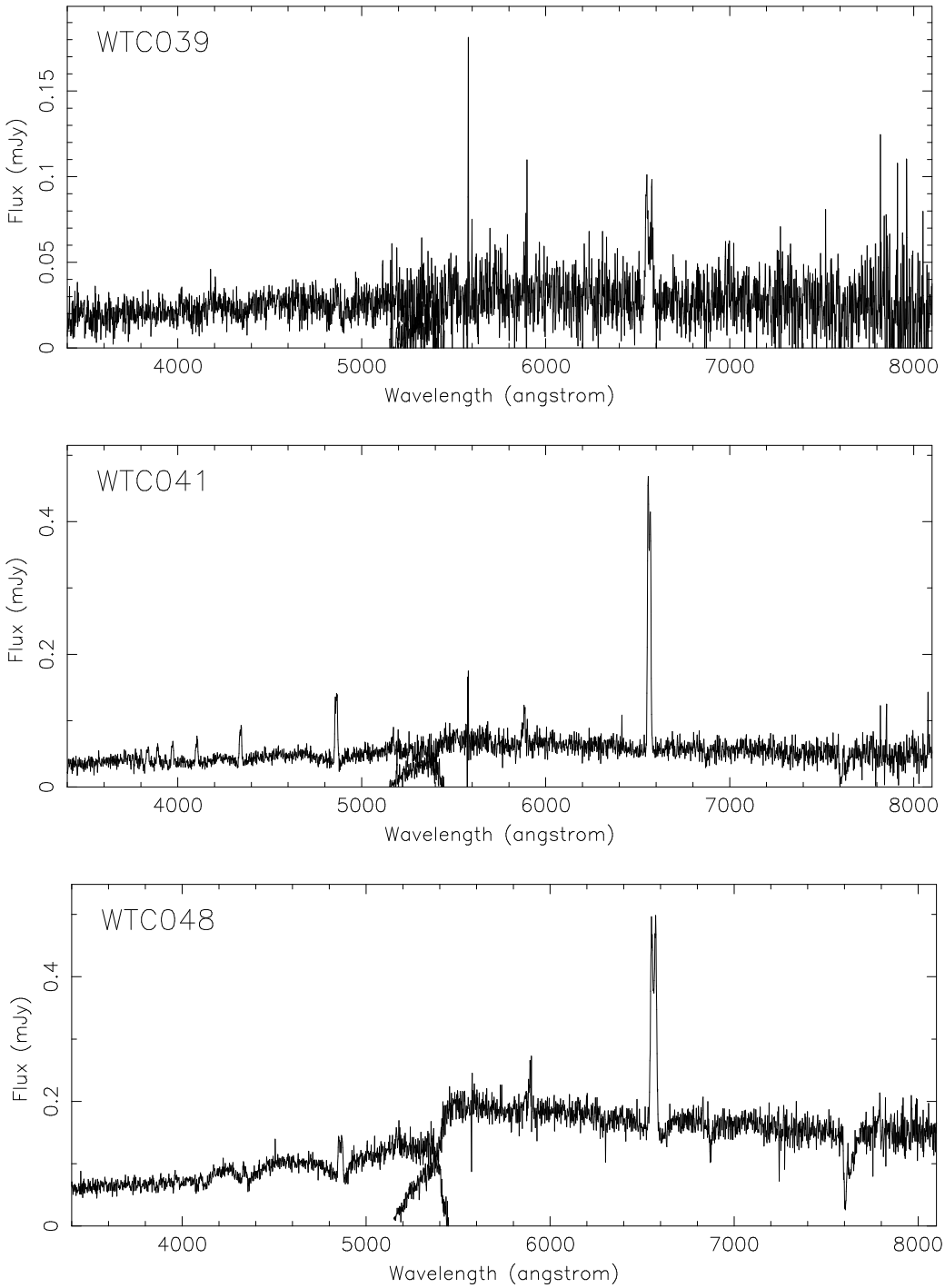

Figure 7.2: Spectra taken at the William Herschel Telescope of new cataclysmic variable candidates during quiescence. Candidates were identified by a prototype version of the untargeted search algorithm (see Chapter 4).

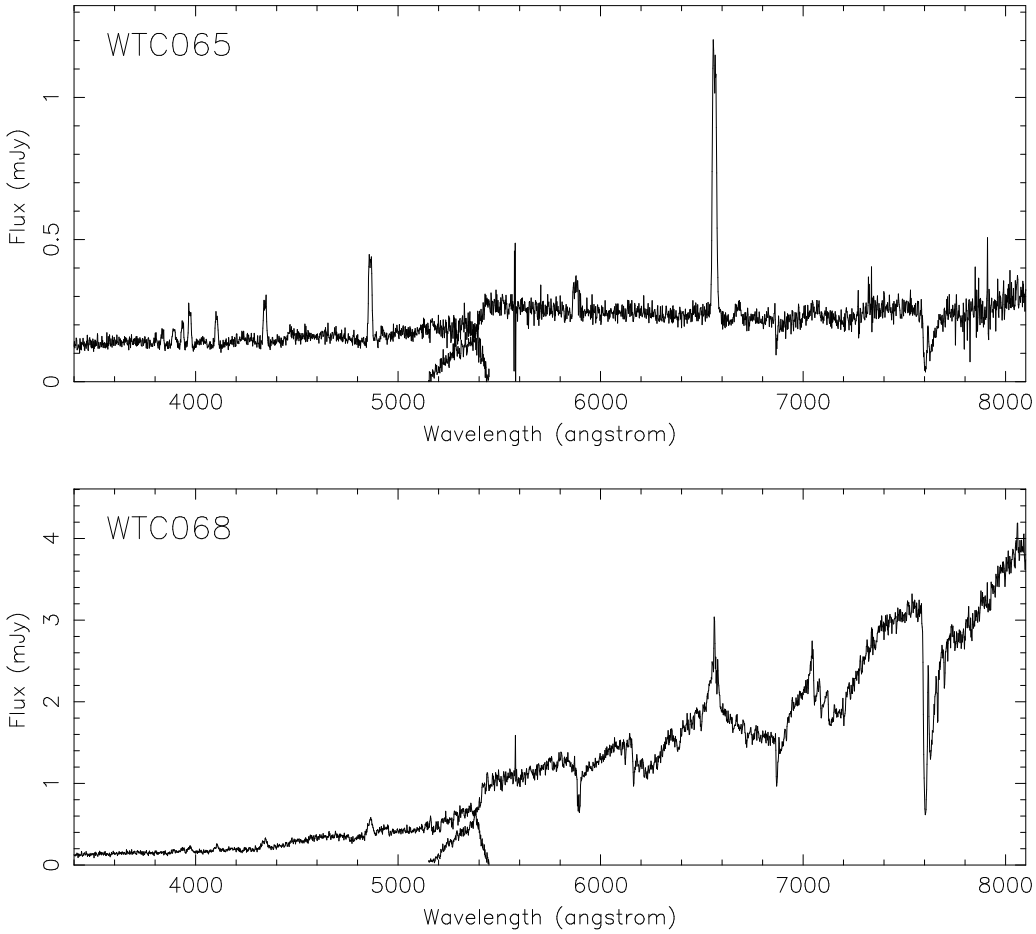

Figure 7.2 continued: Spectra taken at the William Herschel Telescope of new cataclysmic variable candidates during quiescence. Candidates were identified by a prototype version of the untargeted search algorithm (see Chapter 4).

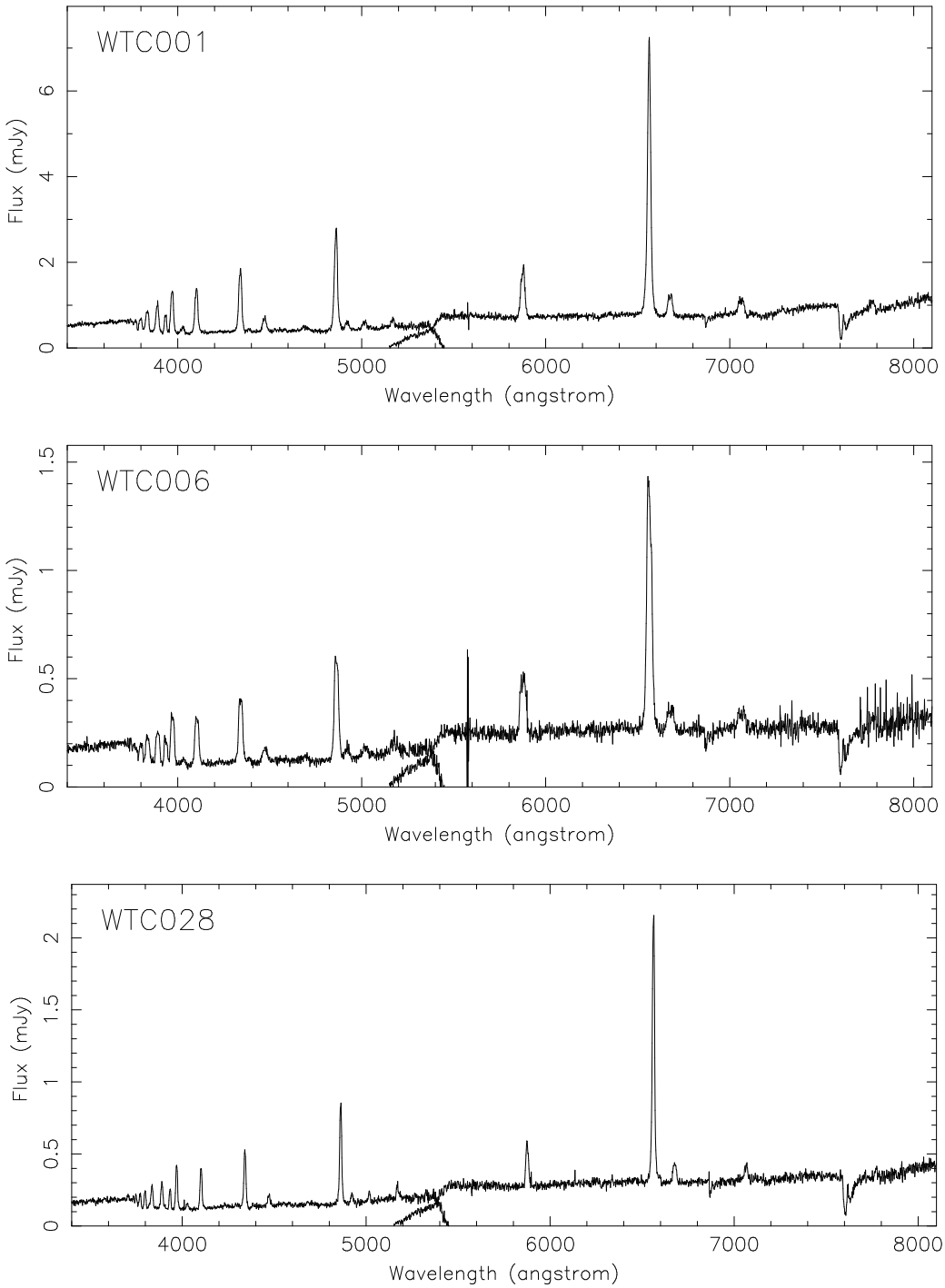

Figure 7.3: Spectra taken at the William Herschel Telescope of new cataclysmic variable candidates during quiescence. Candidates were identified by searching at the positions of known X-ray sources (see Section 3.7).

lines around some of the emission lines in WTC041 and WTC065 which would represent a detection of the white dwarf indicating the disc does not dominate the spectra. The observed period for WTC065 of 111 minutes is consistent with this. In WTC048 the absorption lines are far more pronounced suggesting that this could be a low accretion rate system with a period close to the minimum. It can be seen that none of the X-ray selected systems (shown in Figure 7.3) display any indication of the white dwarf suggesting a higher accretion rate. This is not surprising as to be a strong X-ray source, it is likely the system would have a higher accretion rate. The double peaked Hα lines in WTC039 and WTC048 suggest they are relatively high inclination systems.

WTC068 should be singled out in particular as its spectrum is significantly different to the others. It looks like a late type star but there is no indication of the white dwarf at the blue end of the spectrum. This is discussed more in Section 7.1.5.

7.1.4 Outburst properties of cataclysmic variable candidates

A histogram comparing the observed outburst durations of known cataclysmic variable systems detected in WASP to new candidates is shown in Figure 7.4. Known systems are shown in grey, candidate cataclysmic variables as a red outline and unclassified new candidate transients as a green outline. The two longest duration candidate cataclysmic variables appear to be outliers from the main population. These are discussed in more detail in Section 7.1.2 and are considered as possible nova candidates in Section 7.4. The long duration known system is PY Per and is a Z Cam system that appears to have been detected in standstill. The long duration unknown transient is likely to be a variable star although the WASP coverage is not complete enough to be certain.

The two populations of known and new cataclysmic variable stars appear quite similar in this plot. However, there is a lack of new cataclysmic variable systems with short outbursts when compared to the known systems. This is likely to be due to a selection effect rather than the new candidates representing a different

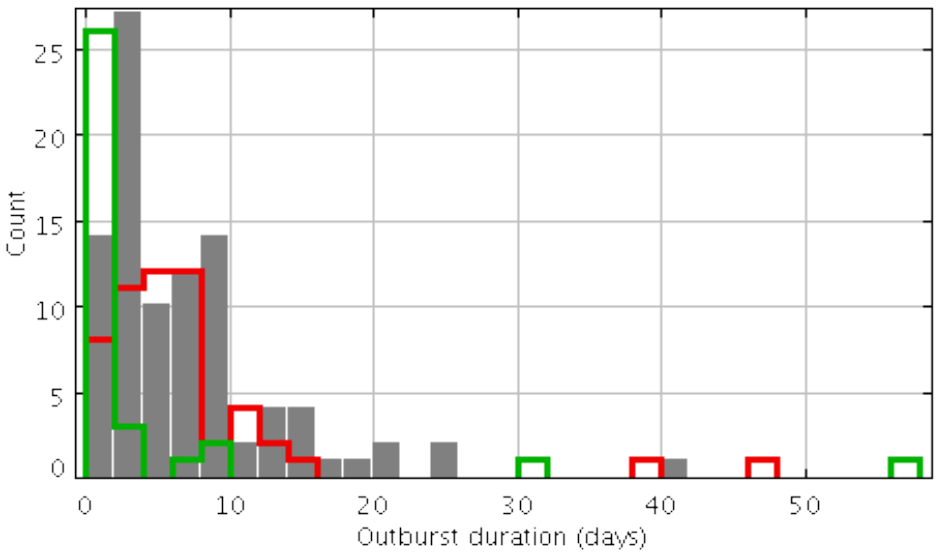

Figure 7.4: A histogram of the duration of the longest observed outburst for each object in the WASP data. The grey shows known dwarf novae, the red new candidate dwarf novae and the green undetermined new transients.

sample of the CV population. When classifying the transients with a type it was difficult to do this with any certainty if there was only one night's worth of data meaning a large number of these would be classified as unknown. This would not only explain the lack of new short duration dwarf nova outbursts but also, at least partially, account for the large number of unknown transients with outbursts lasting for two days or less as many will be CVs.

A histogram showing the ratio of time each object is detected in outburst against the number of nights observed (an estimate of the duty cycle) is shown in Figure 7.5. As before known CVs are shown in grey, new candidate CVs as a red outline and new unclassified candidates as a green outline. The most noticeable feature of this is that there appear to be more known CVs in outburst for 5% -10% of the time they are observed when compared to the new candidates. If this is analysed with a Kolmogorov-Smirnov test it gives a probability of less than 0.001 that these two samples are consistent. This is likely to represent a selection effect in the currently known population as CVs that regularly go into outburst are far more likely to have already been discovered. While WASP is also somewhat susceptible to

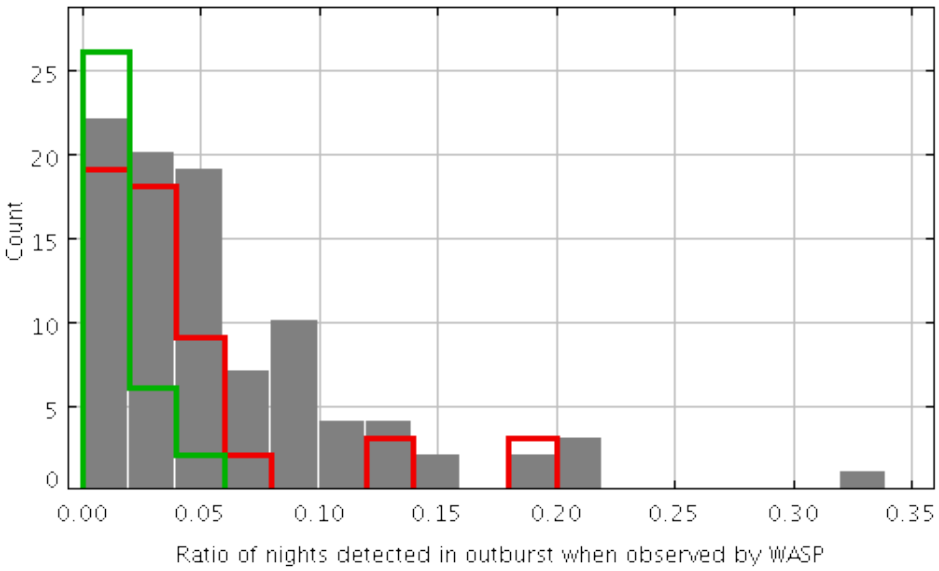

Figure 7.5: A histogram of the ratio of the time detected compared to when the region of sky was observed by WASP. Known CVs are shown in grey, new candidate CVs are shown in red and new undetermined transients are shown in green.

this selection effect it still appears to be more complete than the current population sample.

Figure 7.6 shows the amplitude of observed dwarf nova outbursts with respect to the corresponding USNO-A r magnitude (in red) and USNO-A b magnitude (in blue). The peak magnitudes were calibrated using the known peak magnitudes of dwarf novae in the Ritter and Kolb catalogue [136]. This was done by converting the peak WASP flux values (f) to magnitudes (m) using the formula:

$$m = -2.5 \times log_{10}(\frac{f}{1{,}000{,}000})$$

The average offset from the Ritter and Kolb peak V-band apparent magnitude of outburst was then calculated and this correction was applied to the calculated magnitudes of all dwarf nova outbursts detected by WASP. The advantage of this method is that, by comparing the WASP magnitudes to magnitudes from known dwarf novae, the calculated V-band magnitude should be correct despite the WASP cameras spanning several different colour bands.

The two largest outbursts from known CVs were caused by a superoutburst from the WZ Sge system V455 And and an error in the WASP pipeline causing

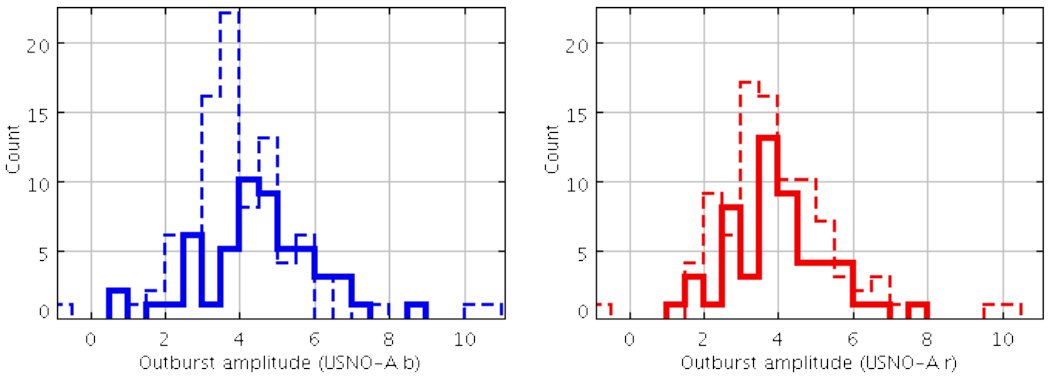

Figure 7.6: Histograms showing the amplitude of the dwarf nova outbursts observed by WASP. The left is with respect to USNO-A b magnitude, the right is with respect to USNO-A r magnitude. The dotted lines mark known systems and the solid line new outbursts from new candidate systems.

detections of an outburst in SS Cyg to be given flux values that were too large. If a Kolmogorov-Smirnov test is carried out to compare the blue amplitudes of the known cataclysmic variables with those of the new candidate systems it is found that there is only a probability of 0.001 that two samples could be consistent. As both the known and new sample were found by the WASP search algorithm, it does not seem possible for a selection effect in WASP to cause this discrepancy. This therefore suggests that the new cataclysmic variable systems that WASP is discovering form a sample of systems with larger amplitude outbursts that have previously been missed.

7.1.5 Exceptional cataclysmic variable candidates

WTC126

WTC126 is the largest amplitude dwarf nova candidate found in the WASP data (8.6 magnitudes relative to USNO-A b). This is within the limits of a fast or recurrent nova however the measured superhump period of 88 minutes suggests that it is a WZ Sge system. Using this measurement of the superhump period (P_{sh}) the orbital period (P_{orb}) can be estimated using the formula [48]:

$$P_{orb} = 0.9162 * P_{sh} + 5.39$$

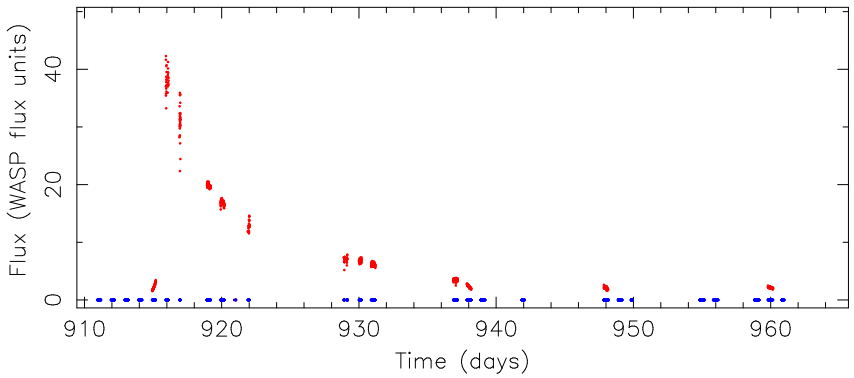

Figure 7.7: Light curve of cataclysmic variable candidate WTC126. Time in days after JD 2453005.5 is plotted on the x-axis. Flux is plotted on the y-axis in WASP flux units. Red dots mark detections and blue dots at zero flux mark observations.

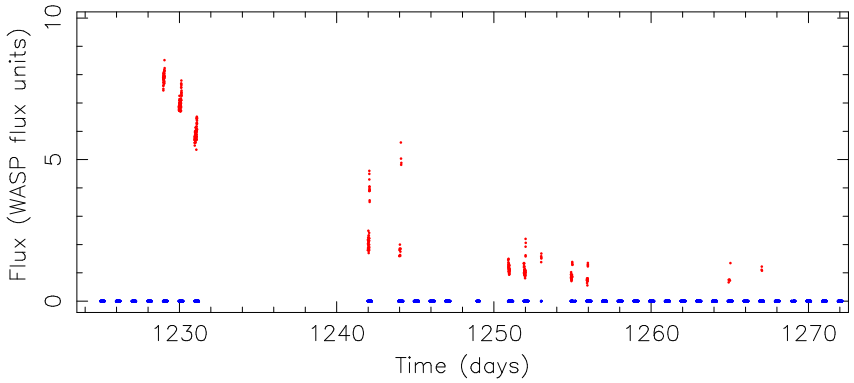

Figure 7.8: Light curve of cataclysmic variable candidate WTC150. Time in days after JD 2453005.5 is plotted on the x-axis. Flux is plotted on the y-axis in WASP flux units. Red dots mark detections and blue dots at zero flux mark observations.

This gives an orbital period of 86 minutes indicating that the candidate is either a low accretion rate system about to hit the period minimum or is a period bounce system.

The light curve shown in Figure 7.7 is interesting as after the huge superoutburst it appears that a series of echo outbursts are also detected. These were also found on the known dwarf nova 1RXS J0232-3718 (see Section 3.4.2).

WTC150

Like WTC126, WTC150 show an unusually long duration and large amplitude outburst (6.9 magnitudes relative to USNO-A b). Unlike WTC126 a superhump period

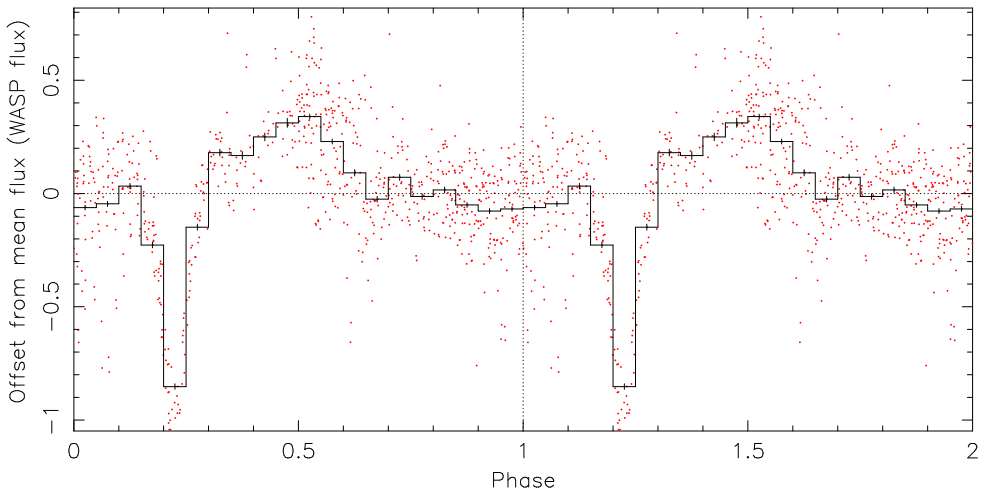

Figure 7.9: A folded light curve for WTC179. Flux on the y-axis represents the offset from the average flux for that night.

was not found. The nightly coverage for WTC150 was shorter than WTC126 although a strong short period should still have been identified. However, a nova would have to have an unusually small amplitude to account for WTC150 suggesting that a superoutburst from a dwarf nova is still likely to be the source. The light curve of WTC150 is shown in Figure 7.8. On nights 1242 and 1244 there are several detections significantly brighter than expected. These appear to be caused by an error in the WASP pipeline at the end of the night.

WTC179

WTC179 is unusual as it appears to be an extremely long period eclipsing CV (540 minutes). A folded light curve of the WASP data is shown in Figure 7.9, a periodogram is shown in Figure 7.11 and the light curves from each night aligned in phase are shown in Figure 7.10. WTC179 has one of the longest periods known in an eclipsing dwarf nova system. The only ones known with longer orbital periods are CXOGlb J0024-7204 with a period of 1597 minutes and V1129 Cen with a period of 1286 minutes (although the classification of V1129 Cen has not been confirmed). Other than GY Hya with a period of 500 minutes no other eclipsing CVs with confirmed dwarf nova outbursts are known to have an orbital period of more than

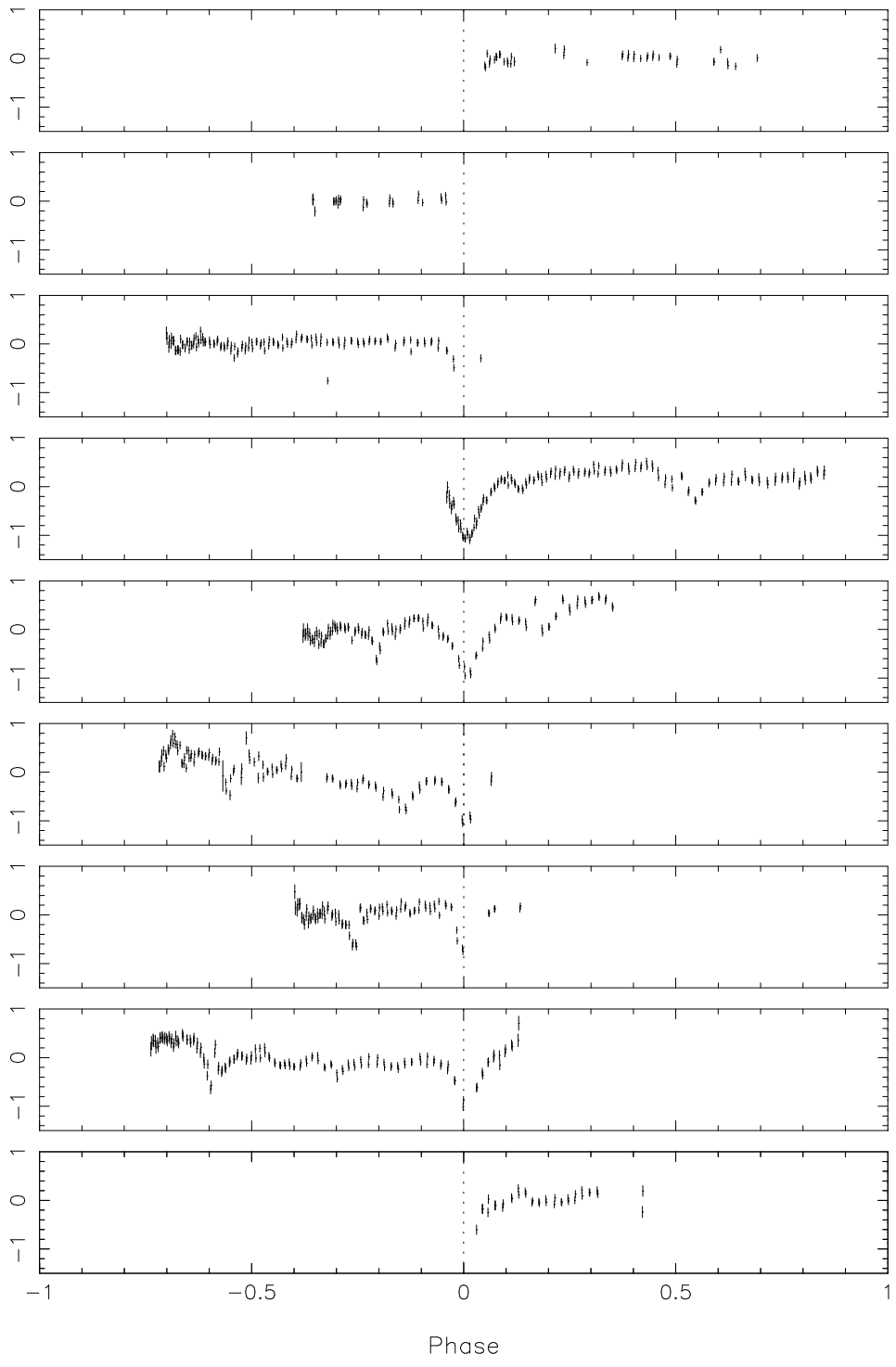

Figure 7.10: Light curves from each night of observation of WTC179. The phase of the measured period is shown on the x-axis and the offset of the flux from the nightly average is shown on the y-axis.

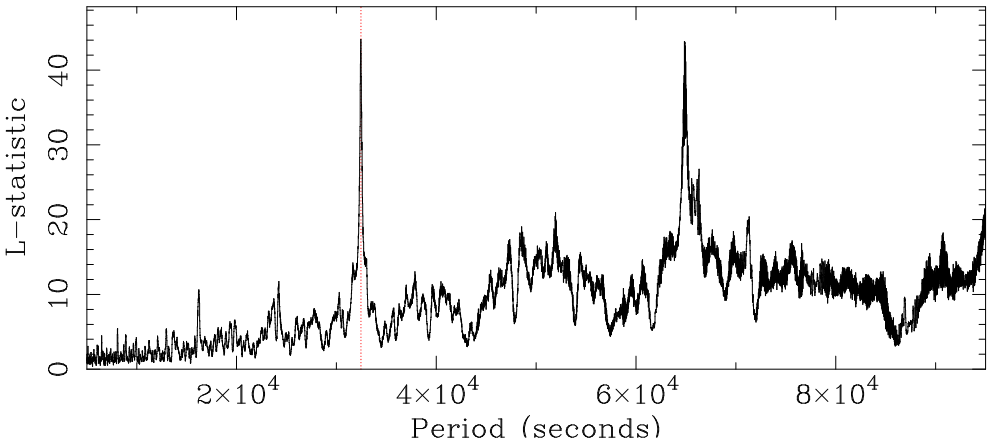

Figure 7.11: A periodogram of L-statistic [39] against period for WTC179 with the period 540 minutes marked in red

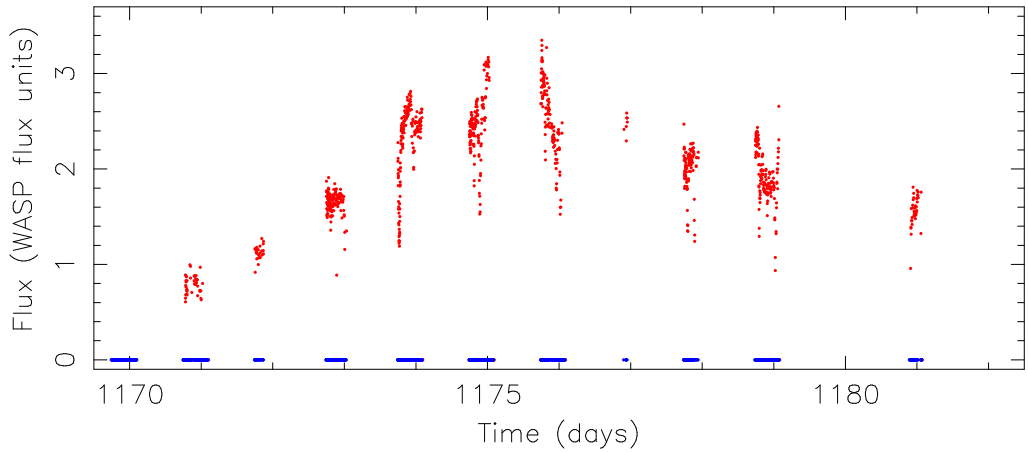

Figure 7.12: Light curve of cataclysmic variable candidate WTC179. Time in days after JD 2453005.5 is plotted on the x-axis. Flux is plotted on the y-axis in WASP flux units. Red dots mark detections and blue dots at zero flux mark observations.

7 hours [136].

Follow up observations will be required to establish more detailed properties of the system as the eclipses that were measured were during outburst. Radial velocity measurements could be used to establish the mass ratio and detailed observations of the eclipses could be used to measure the radius of the white dwarf. Using *eclipse mapping* it may even be possible to establish the temperature of different parts of the disc.

WTC179 is also unusual for its slow rising light curve (see Figure 7.12). This combined with it being an eclipsing system with an extremely long period makes it a high priority candidate for follow-up observations to confirm its nature.

WTC068

From the light curve (a 5 day outburst with a 3.6 magnitude amplitude) WTC068 appears to be a cataclysmic variable candidate. The broad H-alpha lines in the spectrum (see Figure 5.1) appear to supports this. However, no white dwarf features are visible. While these could be masked by a red giant (if it were a symbiotic star for example), the measured reduced proper motion of 6.4 and 2MASS J-K value of 0.68 implies that the M-star must be a dwarf (see Figure 5.1) which eliminates the possibility of it being a symbiotic system. The broad H-alpha lines are difficult to explain without an accretion disc which leaves several remaining possibilities.

Firstly it could be a dwarf nova with an extremely cool, and hence faint, white dwarf. This would account for the lack of white dwarf features in the spectrum. However, the system would need to be in an extremely unusual state for the white dwarf to have become so cool. This could only happen if accretion had only recently started after a very extended period of detached evolution.

Alternatively, the system could be a black hole or neutron star binary. However, outbursts from these are normally longer and would have made the system extremely bright in the X-rays so should have been detected.

Another possibility is that the star is a young T Tauri and the outburst represents an accretion disc instability. Although these stars can be brighter than

older M-stars, and hence further away, the observed proper motion is still consistent. Disc outbursts have been observed in young FU Ori systems (see Section 1.5.7) although these last for decades rather than days. However, only a relatively small number of FU Ori stars are known and, as they are discovered by their outburst, they have rarely been monitored in quiescence so it is far from certain that they do not have shorter outbursts that have been missed.

Further observations of this system will be required to fully understand its nature. Radial velocity measurements should be able to determine which of these possibilities is consistent. No radial velocity would support the non-binary T Tauri possibility whereas detection of a radial velocity could indicate a dwarf nova or black hole binary if it is large enough.

7.1.6 Sky distribution of cataclysmic variable candidates

The right ascension and declination distribution of the CV candidates is shown in Figure 7.13. New candidates are shown in red (circles on the scatter plot), known CVs found in the WASP data are shown in blue (squares on the scatter plot) and all dwarf novae in the Ritter and Kolb catalogue [136] are shown as a grey background in the histograms and green crosses in the scatter plot. These can be compared to the WASP sky coverage plots shown in Figures 4.23, 4.24, 4.25 and 4.26. While there does not appear to be any difference in right ascension, there is a clear discrepancy in declination. 69% of known systems are in the northern hemisphere. This difference is not just seen in the systems observed by WASP but is also in all of the known dwarf nova systems (67% of Ritter and Kolb dwarf nova systems are in the northern hemisphere). This suggests that our knowledge of the CV population is significantly more complete in the northern hemisphere. This is re-enforced by the fact that far more new dwarf novae were discovered in the southern hemisphere.

A scatter plot of the galactic coordinates of the candidates is shown in Figure 7.14. The WASP sky coverage in galactic coordinates is shown in Figure 4.22. There appears to be some difference in galactic longitude. However, this is likely to be an artifact of the less complete sample of CVs in the southern hemisphere. This

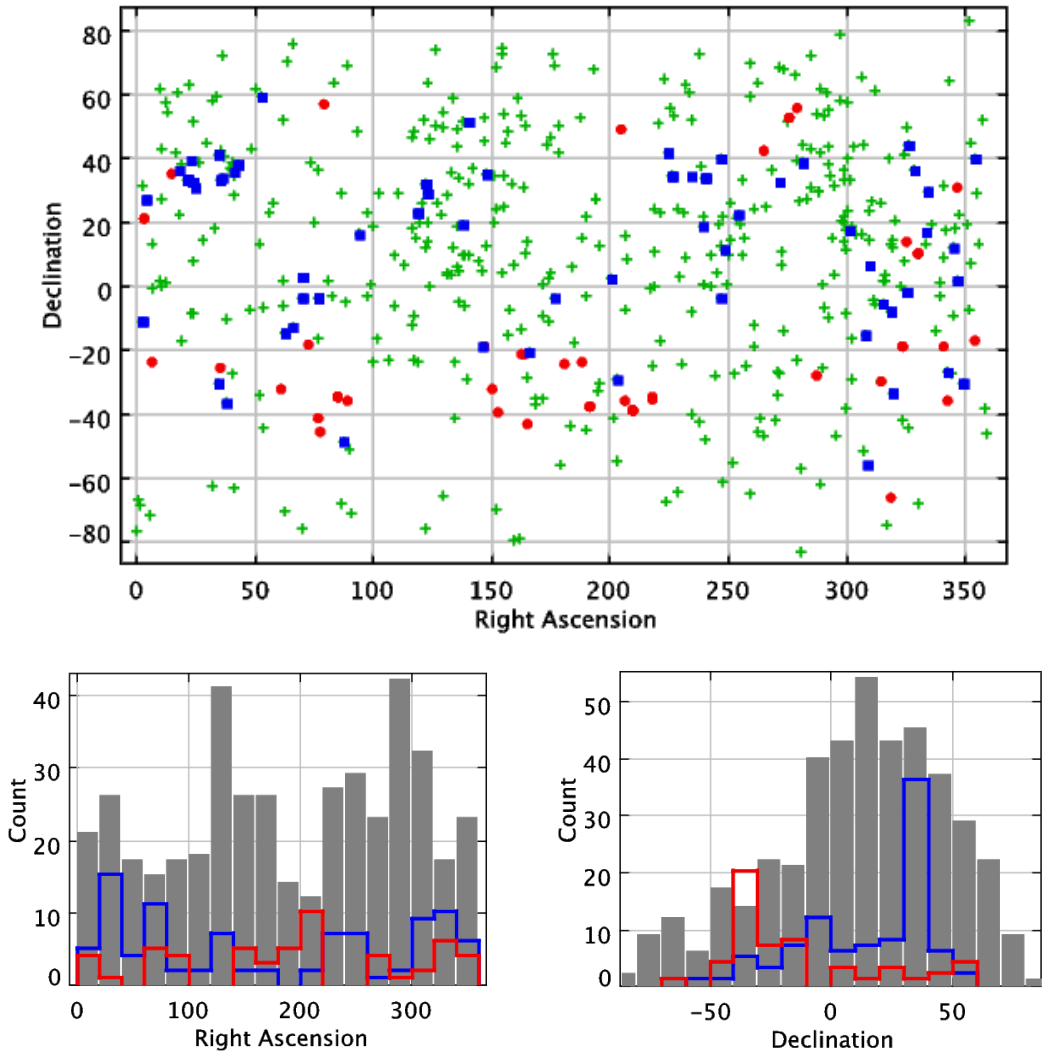

Figure 7.13: The top plot shows the distribution of CVs in right ascension and declination. New candidates are shown in red, known systems detected by WASP are shown in blue and all dwarf novae in the Ritter and Kolb catalogue [136] are shown as green crosses. The bottom two histograms show the right ascension and declination distributions of these systems. In these plots the Ritter and Kolb dwarf novae are shown in grey.

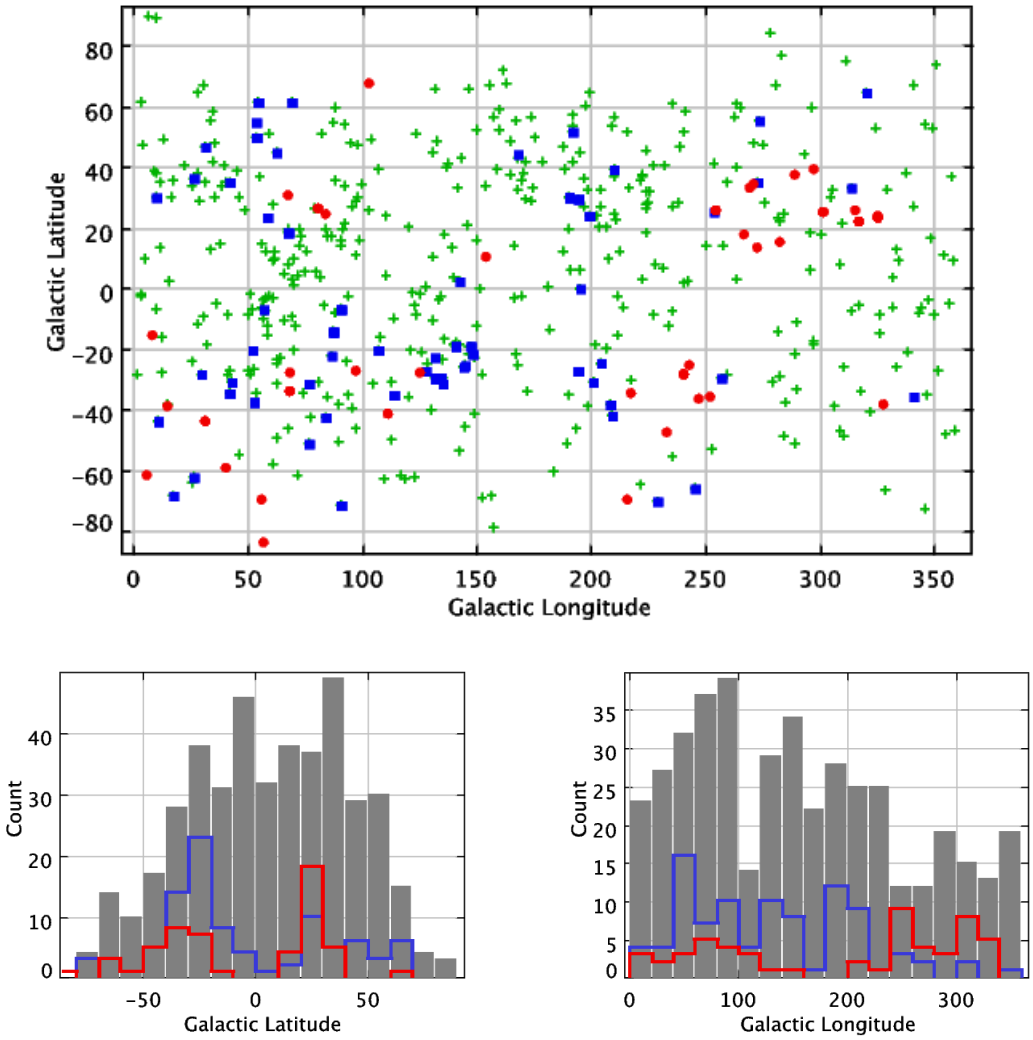

Figure 7.14: The top plot shows the distribution of CVs in galactic coordinates. New candidates are shown in red, known systems detected by WASP are shown in blue and all dwarf novae in the Ritter and Kolb catalogue [136] are shown as green crosses. The bottom two histograms show the galactic latitude and longitude distributions of theses systems. In these plots the Ritter and Kolb dwarf novae are shown in grey.

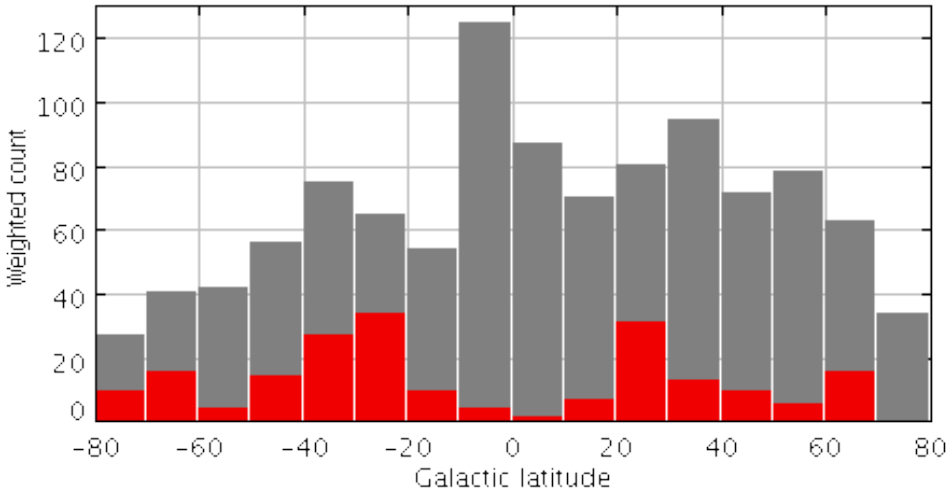

Figure 7.15: A weighted histogram of the number of dwarf novae at each galactic latitude. The weighting accounts for the changing sky area with latitude. Known dwarf novae from the Ritter and Kolb catalogue [136] are shown in grey and dwarf nova detected by WASP are shown in red.

appears to be confirmed if both the known and new systems observed by WASP are considered as the combined distribution is more even. In galactic latitude there is a peak in the Ritter and Kolb population at zero. This is likely to indicate that these systems are being found at distances similar to or further than the scale height of the galactic disc. This is not seen in the systems observed by WASP with peaks at either side of it instead. This is because WASP does not observe in the plane so can not discover systems with those galactic latitudes. However, the two small peaks represent the remnants of this feature as they are as close to the galactic plane as possible before the WASP coverage becomes too incomplete. A weighted version of this plot to account for changing area at different galactic latitudes in shown in Figure 7.15.

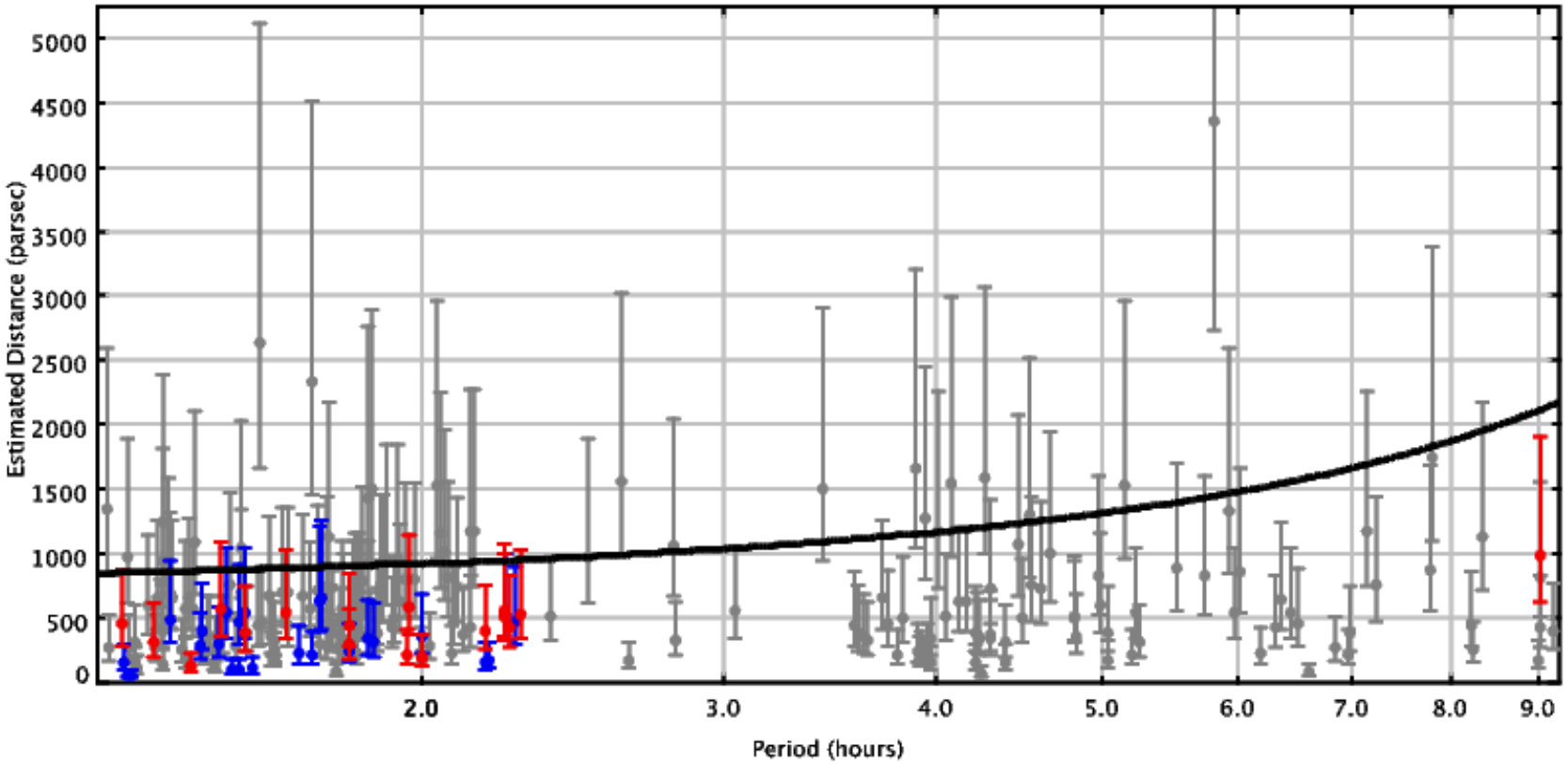

Figure 7.16: A plot showing the estimated distances of CVs. New candidates are shown in red, known systems with measured periods are shown in blue and dwarf novae from the Ritter and Kolb catalogue [136] are shown in grey. The errors are set at a one sigma level for variations in inclination of the systems. The black line represents the threshold for how far WASP is able to detect outbursts from these systems.

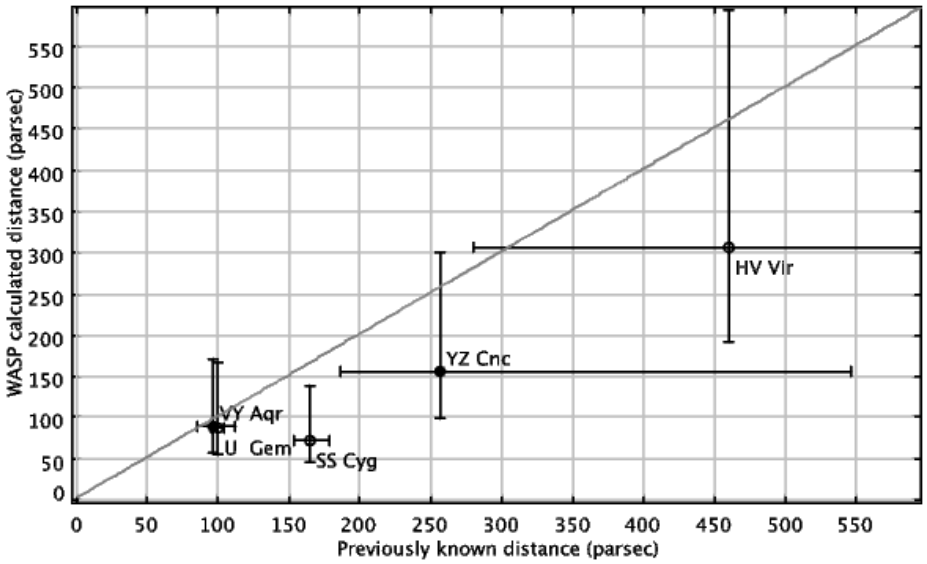

Figure 7.17: Distances to VY Aqr, Yz Cnc and HV Vir were from [156] and to U Gem and SS Cyg were from [60].

7.1.7 Distance estimates to cataclysmic variable candidates

For the CVs with observed orbital periods it was possible to use a relation between orbital period and peak absolute magnitude of outbursts to estimate the distance to the system [113]. This relation is:

$$M_{max} = 5.74 - 0.259 P_{orb}$$

The orbital period (P_{orb}) is in hours and the peak absolute magnitude in the V-band (M_{max}) is for a system in normal outburst. To convert this into a distance the apparent magnitude observed can be used in the following equation:

$$m_{max} = M_{max} + 5(log_{10}(d) - 1)$$

Apparent magnitude (m_{max}) is calculated from the peak WASP flux values (which were calibrated using outbursts from known systems). Distance (d) is in parsecs. In order to correct for the inclination of the system (i) a correction is needed for the absolute magnitude [166]:

$$\Delta M = -2.5log((1 + \tfrac{3}{2}cos(i))cos(i))$$

As the orbital inclination is not known for the new systems an average inclination of 57 degrees was assumed. The errors were determined purely on the

uncertainty of the inclination and were set to include 68% of systems with a random orientation. The results of this are listed in Table 7.1 and plotted in Figure 7.16. New candidates are shown in red, known systems with observed periods are shown in blue and all Ritter and Kolb dwarf novae are shown in grey with their orbital period and peak outburst magnitude taken from catalogued values [136]. The black line is for a 15th magnitude outburst and represents the limit for what WASP would be expected to detect. It can be seen that all the new CVs are within about 600 parsecs apart from WTC179 at ∼1000 parsecs. This shows that, at high galactic latitudes, WASP should detect outbursts form most dwarf novae in the galactic disc if the sky is observed for long enough.

There are several reasons for uncertainty in the calculated distance. Firstly, as already discussed, the orbital inclination is not known (the errors on the plot are based entirely on this uncertainty). Secondly, it is not always known whether the outburst observed was from a normal outburst or superoutburst. However, from Figure 7.17 it appears that the WASP distances are representative of the actual values. The plot compares the known distances of several systems from parallax measurements to the WASP values. As before the WASP errors are based on the orbital inclination alone. Ideally the systems would fall on the one to one line shown in grey but, while this is not the case, it is encouraging to see that in all cases, with the exception of SS Cyg, the known value is within the estimated WASP errors.

Using the galactic latitude of the systems and the estimated distance it was possible to calculate the height of the system above the galactic plane. The results of this are shown in Figure 7.18. As before new candidate systems are shown in red, known systems observed by WASP are shown in blue and Ritter and Kolb dwarf novae are shown in grey. From this it appears that all the newly discovered systems seem to lie within about 500 parsecs of the galactic plane which is also true for most known systems. This can be seen more clearly in Figure 7.19 which shows a histogram of the height above the galactic plane with a clear spike at low separations. In this plot dwarf novae from the Ritter and Kolb catalogue are shown in grey and all dwarf novae identified in the WASP data are shown in red.

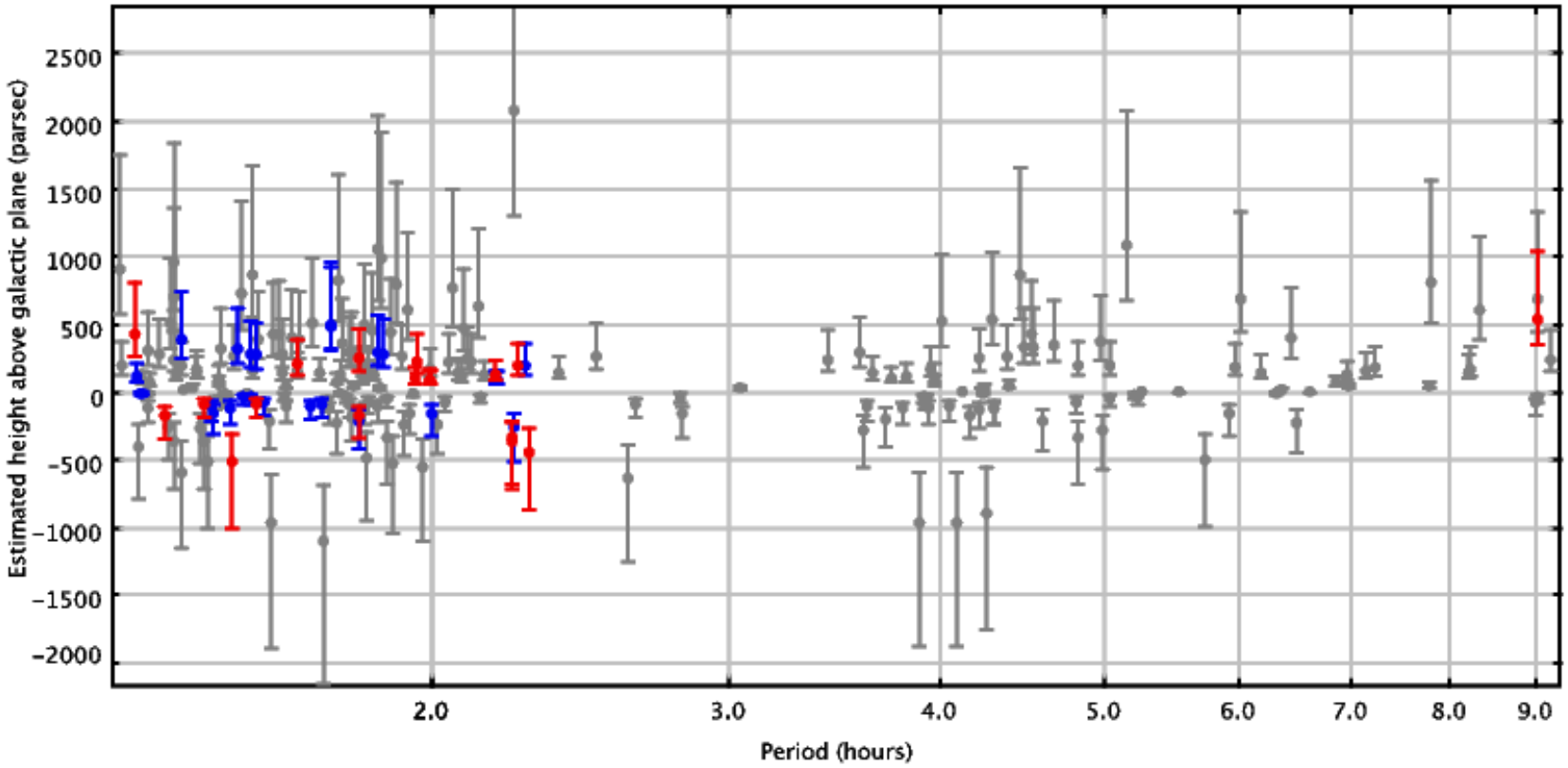

Figure 7.18: A plot showing the estimated offsets of CVs from the galactic plane. New candidates are shown in red, known systems with measured periods are shown in blue and dwarf novae from the Ritter and Kolb catalogue [136] are shown in grey. The errors are set at a one sigma level for variations in inclination of the systems.

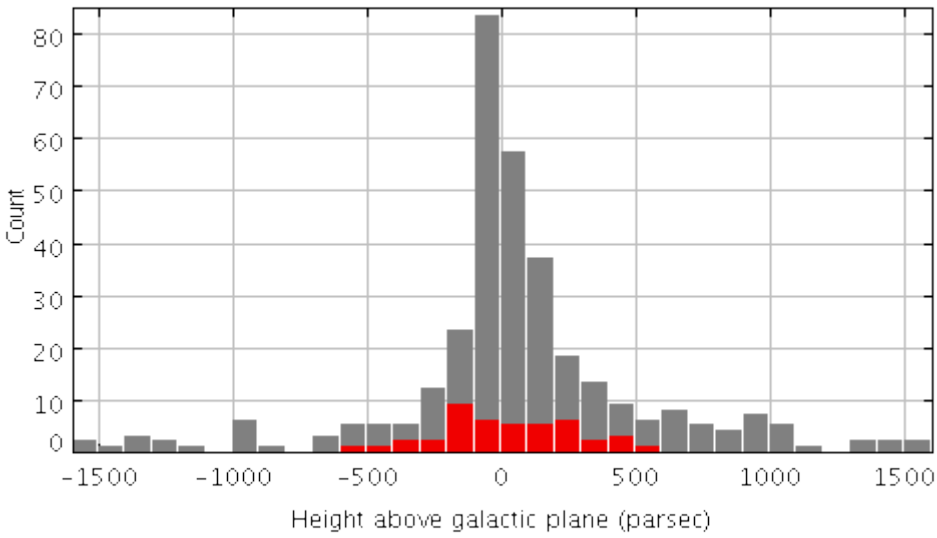

Figure 7.19: A histogram of the estimated offset from the galactic plane for known dwarf nova systems (shown in grey) and dwarf novae identified by WASP (shown in red).

By using these measured heights the space density of dwarf novae identified by the search algorithm was estimated. Galactic latitudes of less than 20°were not included as these regions had poor WASP coverage. The volumes of space being observed by WASP at different heights were estimated by calculating the volume of a cone directed toward a galactic latitude of 90°and limited by a galactic latitude of 20°. For a chosen range of heights above the galactic plane, the number of dwarf novae contained in this range and at higher galactic latitudes than 20°was determined. The volume of space being searched was calculated by subtracting the volume of a cone with an axis of the lower limit of the height above the plane from the volume of a cone with an axis of the upper limit. The number of detected dwarf novae was then divided by this volume to get the observed space density. The results are this are shown in Figure 7.20.

WASP name	Period (min)	Distance (pc)	Height above the galactic plane (pc)
WTC009	83.4±0.1	310	-185
WTC034	108.9±0.1	288	-181
WTC109	101.2±0.3	527	196
WTC125	136.3±0.3	525	-453
WTC126	87.7±0.1	112	-99
WTC144	80.0±0.1	448	413
WTC151	134.6±0.1	424	183
WTC158	90.5±0.4	556	-522
WTC175	131.2±0.2	387	117
WTC179	539.7±0.6	978	531
WTC182	120.1±0.7	188	78
	119.9±0.1	183	76
	119.0±1.3	208	87
WTC198	95.0±0.2	378	-102
WTC313	134.6±0.1	546	-379
	134.5±0.1	508	-352
WTC322	107.7±0.1	431	239

Table 7.1: A table of the estimated distances of new candidate cataclysmic variables discovered by WASP.

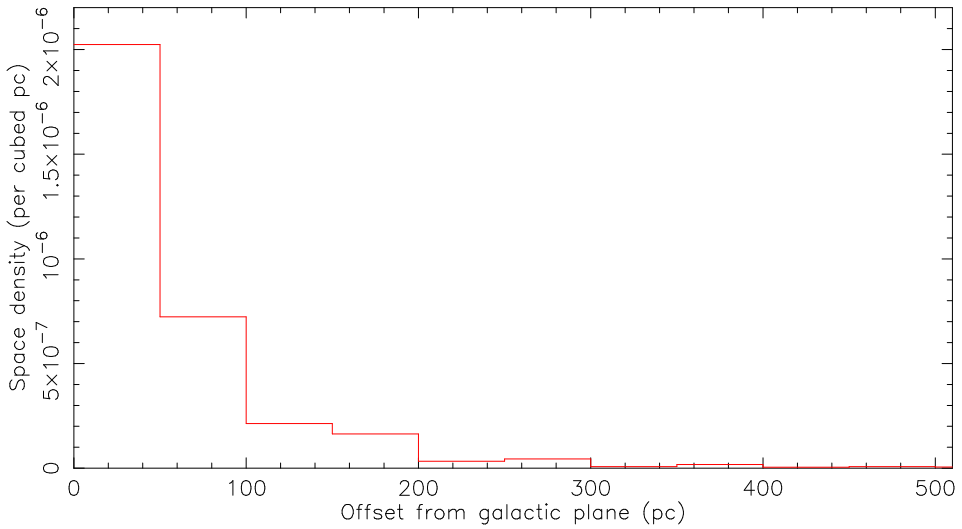

Figure 7.20: A histogram showing the space density of dwarf novae detected by WASP at different heights above the galactic plane. Areas with a galactic latitude of less than 20°were not included as the WASP coverage was too infrequent.

7.1.8 The cataclysmic variable population

From these results it appears that in most respects the new candidates discovered are similar to the population already known. However, selection effects in the known population in sky distribution (see Section 7.1.6) and duty cycle (see Section 7.1.4) were uncovered. This suggests that, in these respects at least, the WASP sample is more complete. A slightly larger amplitude of outburst was also found (see Section 7.1.4) which suggests that WASP may be sensitive to lower accretion rate systems. These tend to have larger, less frequent outbursts and because of their longer recurrence times can easily be missed by non-systematic surveys. However we, like many other surveys, do not detect the spike in systems at the period minimum. As was discussed in Section 1.5.2, this may be because these systems only have extremely rare outbursts if they have any at all [83].

If a project such as this is run over a longer period it may be possible to get a far clearer understanding of the population of cataclysmic variables. From the four years of data we only detected 12% of known WZ Sge systems compared to 19% of SU Umas and 35% of U Gems (see Section 3.4). Over a longer period of observations outbursts would be expected from almost all of these systems allowing for a far less biased sample of CVs and, if WZ Sge or similar rare outbursting systems do make up part of the period bounce population, the spike at minimum periods may become visible. A wide-field survey, such as WASP, is ideally suited to do this. Furthermore, Section 7.1.7 demonstrates that the depth WASP reaches is ideal for discovering CVs by their outburst alone. The scale heights of the galactic thin and thick discs are 300pc and 900pc respectively [74]. Given this and the distance estimates in this section, it is apparent that WASP is already detecting CVs up to twice the scale height above the galactic plane.

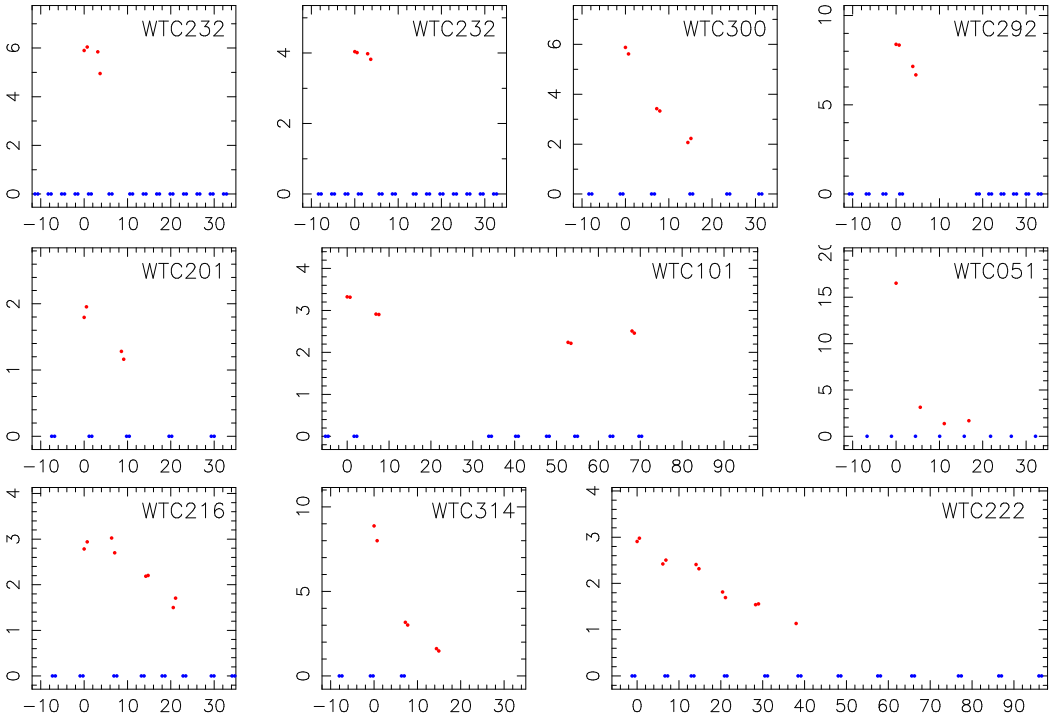

Figure 7.21: Example light curves of candidate flares detected in WASP. Time in minutes after the start of the flare is plotted on the x-axis. Flux is plotted on the y-axis in WASP flux units. Detections are marked with red dots and observations are marked with blue dots at zero flux.

7.2 Flare Stars

7.2.1 Candidate flare stars identified

136 new candidate flare stars were identified from 150 clusters in the WASP orphans database. These are listed in Table B.3 in Appendix B and their light curves are plotted in Figure C.3 in Appendix C. A selection of example light curves from some of the most interesting flares are shown in Figure 7.21.

The distribution of the new flare star candidates on the sky is shown in Figure 7.22 and can be compared to the WASP sky coverage in Figures 4.23, 4.24, 4.25 and 4.26. They appear to be evenly distributed across the sky which would support the hypothesis that the progenitor stars are nearby. This would negate any effects that could be caused by large galactic structure.

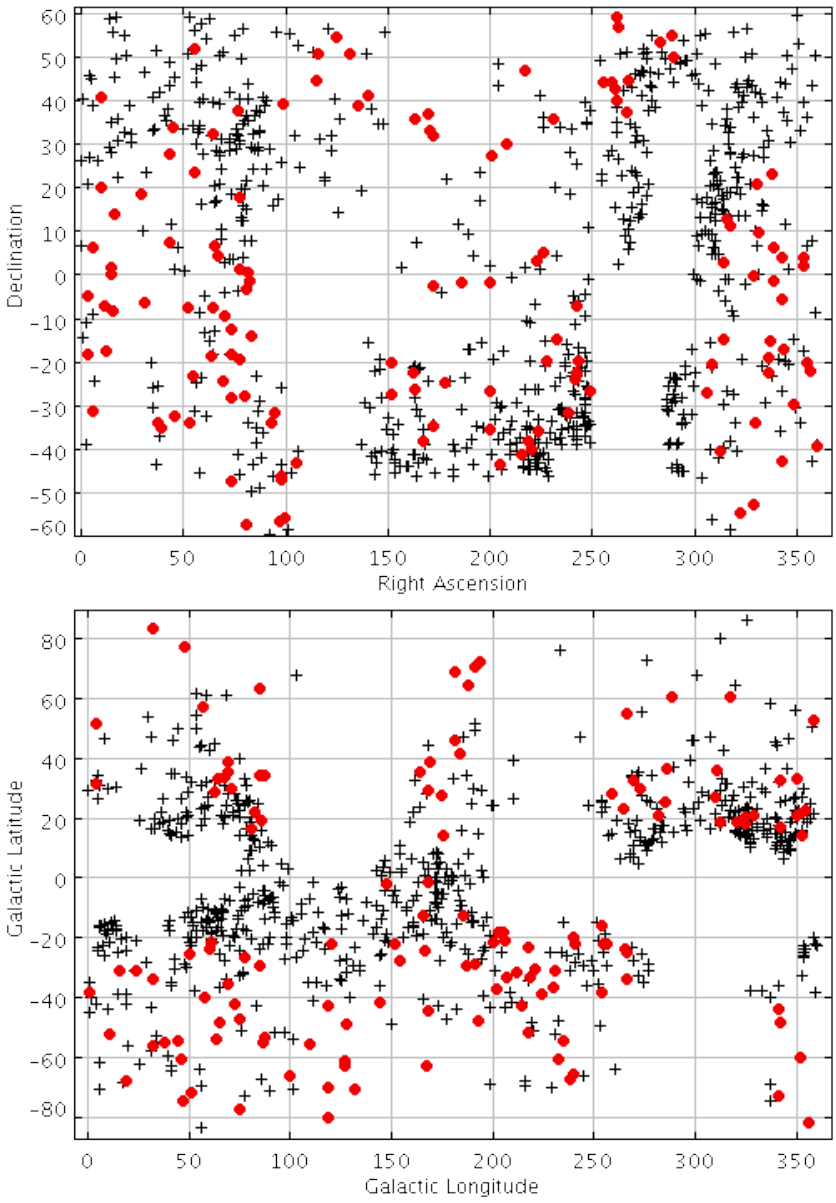

Figure 7.22: Plots of the sky distribution of flare star candidates in right ascension and declination and galactic coordinates. New flare star candidates are marked with red circles. All other detected transients are marked with black crosses.

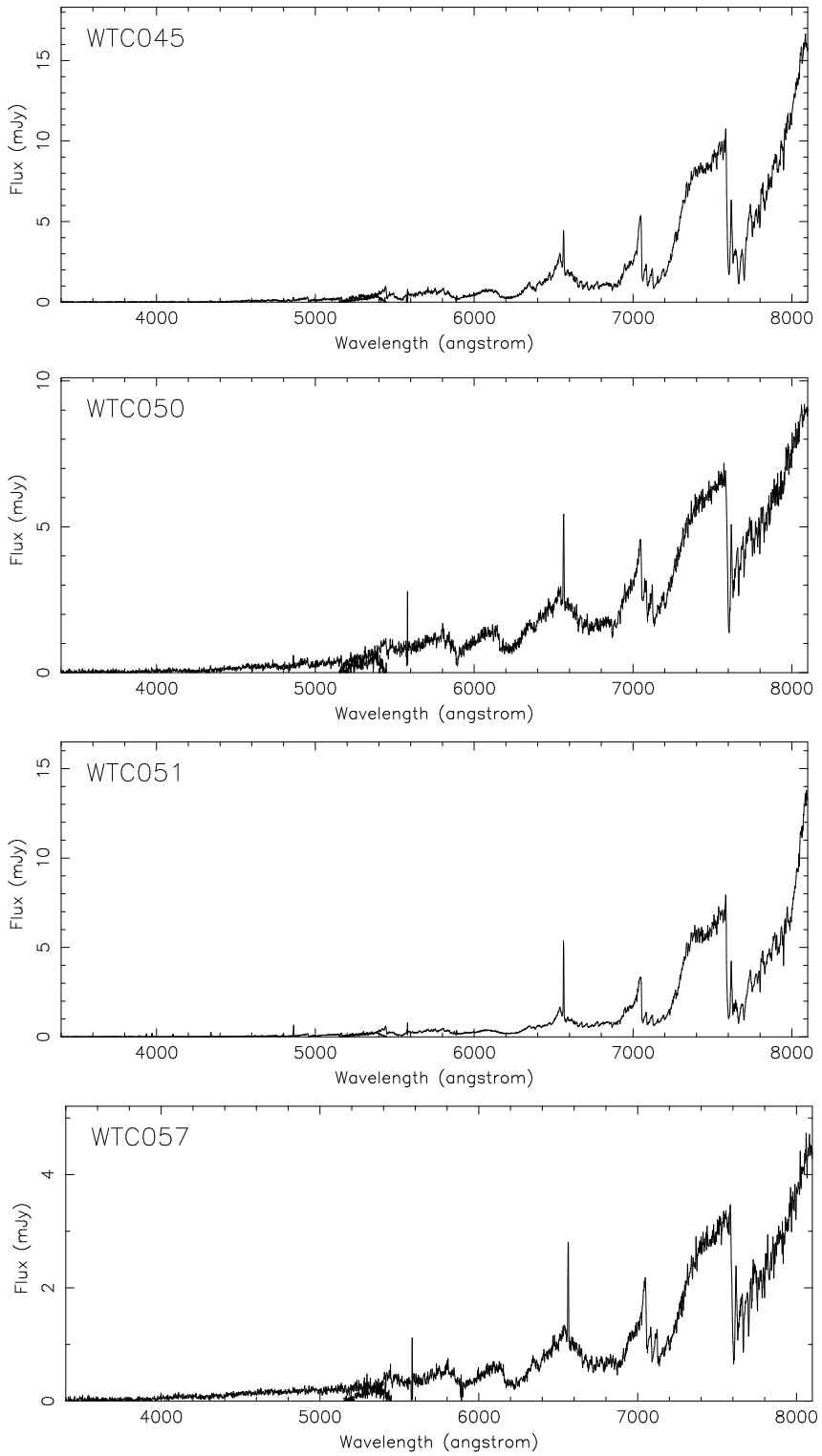

Figure 7.23: Spectra taken at the William Herschel Telescope of flare star candidates.

7.2.2 Spectra of candidate systems

Spectra were taken of flare star candidates identified by a prototype version of the untargeted search algorithm described in Section 4.2. Of the four systems observed WTC045, WTC050 and WTC057 were also independently identified by the final search algorithm. As described in Section 5.2, the spectra were taken using the ISIS instrument on the William Herschel Telescope in La Palma in September 2008. The gratings used were R316R and R300B with central wavelengths of 6450 and 4253 Å. The spectra are shown in Figure 7.23. The H alpha emission line and red spectra indicate an active M-star. This M-type classification can also be seen for all of the flare candidates in their position on the reduced proper motion colour plot (see Figure 5.1). This re-enforces the classification of these transients as flares.

The spectral types of the candidates were established by measuring the ratio of the depth of the Titanium oxide absorption feature between 7140Å and 7190Å to the average flux in the band 7450Å and 7550Å. This was then compared to recorded values to determine the spectral type [23]. The spectral type of WTC045 was found to be M6.5, WTC050 was M4, WTC051 was M7 and WTC057 was M5.

7.2.3 Properties of flare stars discovered

A histogram of the amplitudes of the flares detected by WASP is shown in Figure 7.24. The quiescent magnitudes used were from the NOMAD catalogue [178]. From this histogram it can be seen that WASP is detecting huge amplitude flares. The lack of smaller flares is due to a selection effect in the automated search algorithm. The algorithm is far more sensitive to large amplitude changes as otherwise the candidate could be rejected when cross-correlated with USNO-B (see Section 4.7).

Figure 7.25 shows a histogram of the flare durations as recorded by the WASP observatories. As we are unable to detect the star when it is not flaring this can only be a lower limit for the actual flare duration. What can be seen from this histogram is that again the sample of flare candidates is dominated by selection effects. The longest duration flare is 97 minutes. However, the majority are far shorter with 71% shorter than 20 minutes. Under normal conditions WASP has a cadence of about

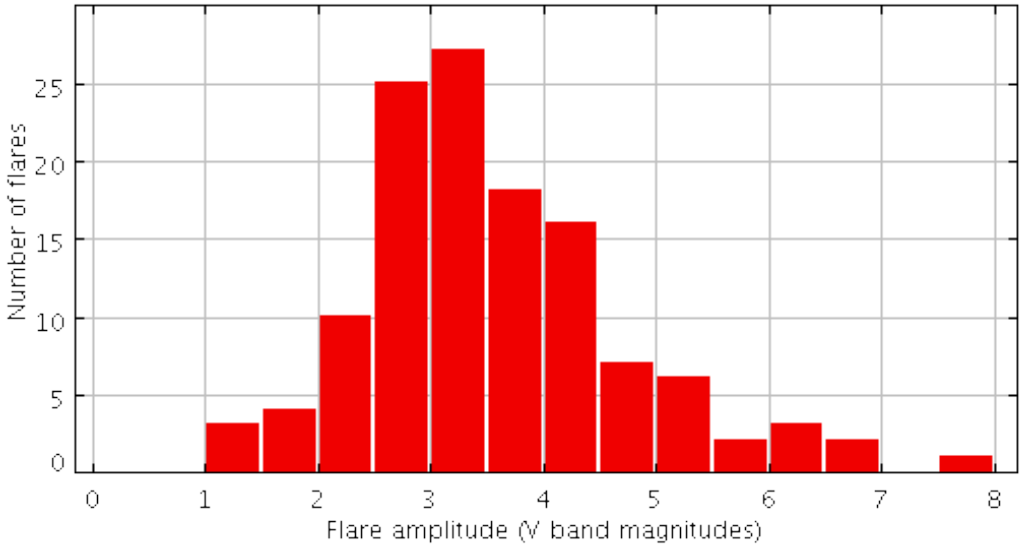

Figure 7.24: A histogram of the amplitudes of the observed flares (in an estimation of the V-band).

15 minutes (see Section 2.1) and, in order to be considered, WASP must detect it at least 3 times. This requires the flare to last at least 30 minutes (or 15 if pairs of observations are being taken). This indicates that most of the flares that were identified were only found by the search algorithm because of an unusually high cadence in the WASP data. This could have occurred if, for example, the other fields scheduled to be observed were too close to the moon.

7.2.4 Distances to flare stars

To estimate the distance to the flare stars discovered by WASP (and hence calculate the energy, see Section 7.2.5) it was necessary to use a model to predict the absolute magnitude of the star from its colours. The colour V-J was found from the corresponding sources in the 2MASS [147] and NOMAD [178] catalogues (if a NOMAD magnitude was not available an average of the USNO-B r2 and b2 magnitudes was used as an approximation). This was compared to the Baraffe model for low-mass stars [15] to find the absolute magnitude of the star in the J-band (M_J). The Baraffe model was chosen as flare stars are expected to be of late spectral type so it should be representative of the stars that WASP detected flares in. The relation for V-J

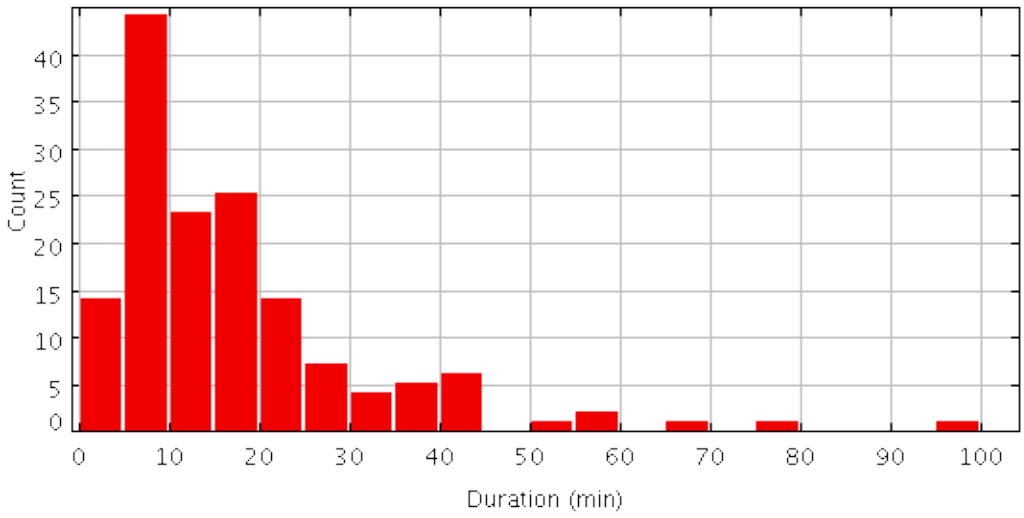

Figure 7.25: A histogram of the observed durations of candidate flares detected in the WASP data.

(see Figure 7.26) was chosen as the equation for finding M_J in any other colour was either degenerate (such as with H-K) or reliant on very accurate measurements of colour (such as with J-K). A correction was applied to the model to make it's magnitudes comparable to 2MASS magnitudes [30].

The specific model chosen (shown as a red line in Figure 7.26) was with solar metallicity, an initial helium mass fraction of 0.275 (average for the model) and an age of 2 Gyr. The effect of reducing the metallicity to [M/H]=-0.5 is shown in green on the plot (the line shows the relation for stars 2 Gyrs old). As can be seen in the plot, the change in metallicity has a comparatively minor effect on the curve with the difference typically far less than a magnitude in M_J. An increase in the initial helium mass fraction to 0.282 is shown in blue on the plot. This clearly has a far more significant effect, however, since most of the candidates have V-J values far larger than the most extreme values of this model it appears that for many (if not all) of the candidates considered this model is not correct. However, the effect of age presents more of a problem.

Models with solar metallicity and an initial helium mass fraction of 0.275 are shown in black. The black lines from top to bottom mark out the models for stars of ages 0.002 Gyr, 0.005 Gyr, 0.01 Gyr, 0.02 Gyr, 0.05 Gyr, 0.1 Gyr and 1 Gyr with

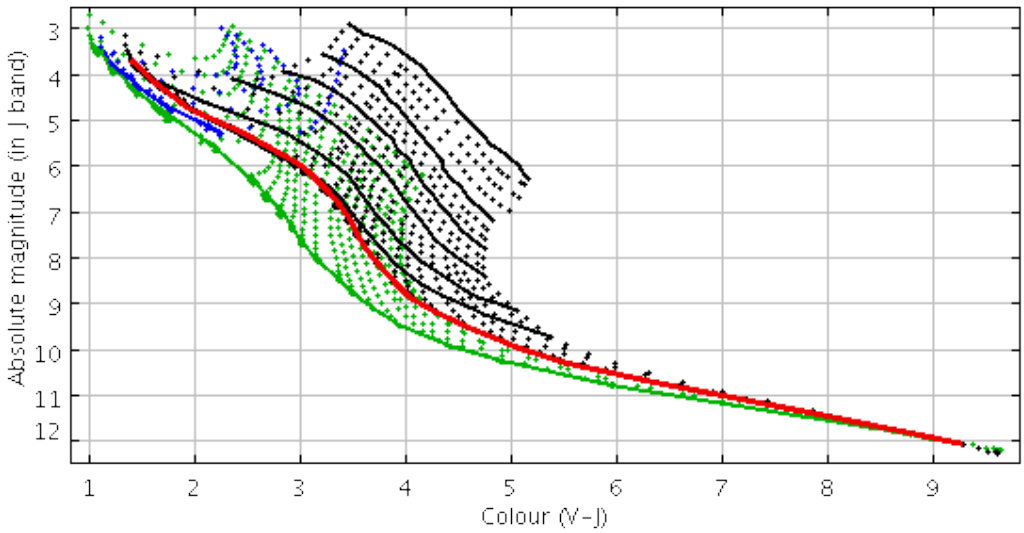

Figure 7.26: A plot of absolute magnitude against colour for the Baraffe model for low mass stars [15]. Stars with solar metallicity and an initial helium fraction of 0.275 are shown in black on the plot (with the red line marking out the model for stars 2 Gyrs old). Stars with metallicity of [M/H]=-0.5 are shown in green with the solid line marking out stars that are 2 Gyrs old. The models for stars with an initial helium mass fraction of 0.282 are shown in blue.

the red line marking the chosen age of 2 Gyr. After that the model remains almost static as the stars have reached the main sequence. The 2 Gyr age was chosen as it was representative of an M-star for the vast majority of its lifetime. Furthermore, from previous surveys for activity in M-dwarfs [145] it was found that young active systems on the main sequence would be of a similar age and activity would continue for 6-7 Gyr. If this estimate of age were to be incorrect, and the star were to actually be younger, the absolute magnitude would be brighter than estimated and hence the distance and energy values calculated below would be underestimating the real value.

From the V-J colour of the corresponding star it was then possible to use this model to calculate the expected absolute J-band magnitude (and also the effective temperature of the star). A test for this was to compare the spectral type from the spectra in Section 7.2.2 to the spectral type from the model. For WTC045 and WTC051 the spectra gave classifications of M6.5 and M7 whereas the model gave M7 for both. For WTC057 the spectra was of type M5 whereas the model was

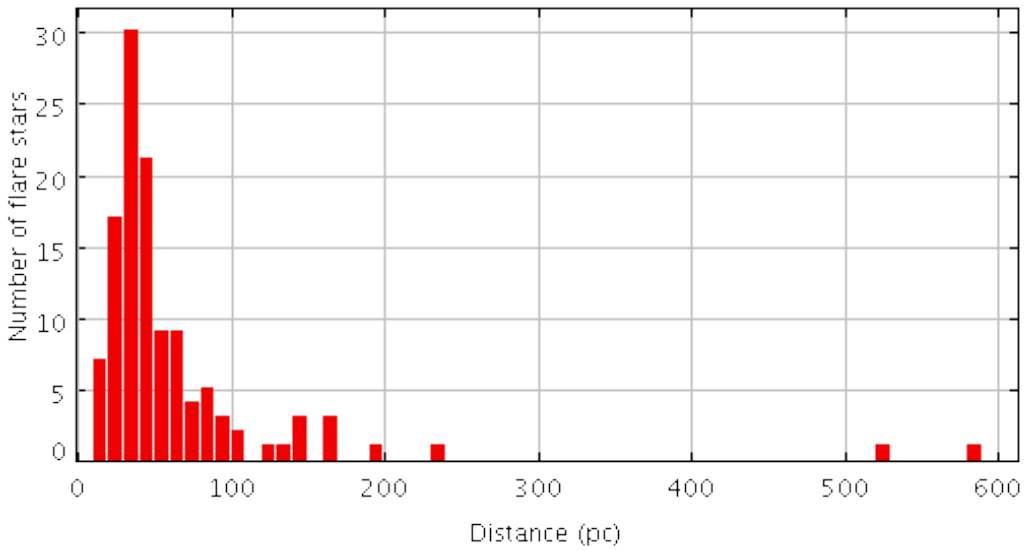

Figure 7.27: A histogram of the estimated distances to the WASP flare star candidates (not including the exceptionally energetic flare from WTC101 at 1956pc).

M4. Using the absolute magnitude (M_J) from the model and the apparent J-band magnitude from 2MASS (m_J) the distance (d) to the flare star could be estimated using the equation:

$$d = 10 \times 10^{\frac{m_J - M_J}{5}}$$

A histogram of these distance is shown in Figure 7.27. From this it can be seen that most flare stars are within 100 parsecs indicating that they are intrinsically very faint as would be expected from late type dwarf stars.

7.2.5 Energies of detected flares

Using these estimated distances and the flux measurements of the flare from the WASP data, it was possible to calculate a lower limit for the flare energy in the observed band. Since the WASP cameras are centered on the V-band this was used to make the estimate. More detail on the WASP passband can be found in Don Pollacco's paper on the WASP cameras [125].

The measured peak WASP flux in WASP flux units (f_{wasp}) corresponds to a peak observed magnitude (m_{wasp}) in an approximation of the V-band according to the formula:

$m_{wasp} = -2.5 \times log_{10}(\frac{f_{wasp}}{1{,}000{,}000})$

This in turn can be converted into a flux with units of erg cm^2 s^{-1} Å^{-1} using the formula:

$m_1 - m_2 = -2.5 \times log_{10}(\frac{f_1}{f_2})$

Where m_1 is m_{wasp} and m_2 is zero. f_2 is the absolute spectral irradience for a magnitude 0 star and, in the V-band, has a value of 3.64×10^{-9} erg cm^{-2}s^{-1}Å^{-1} [179]. f_1 is the required flux in units of erg cm^2 s^{-1} Å^{-1}. The peak power of the flare (P_{peak}) is then given by:

$P_{peak} = f_1 \times 4\pi d^2 \times \triangle\lambda$

Where, as before, d is distance but in units of centimeters instead of parsecs and $\triangle\lambda$ is the full width half maximum of the V-band which is 890Å[179].

Finally, the total energy of the flare in the V-band (E_V) can be calculated using the area under the observed light curve (A):

$E_V = \frac{P_{peak} \times A}{f_{wasp}}$

However, for some of the detected flares these calculations were not possible because the WASP pipeline had not been able to accurately establish a flux.

The estimated V-band energies plotted against the effective temperature from the Baraffe model are shown in Figure 7.28 and as a histogram in Figure 7.29. Other than WTC101 all of the candidate flares fall between effective temperatures of 2400K and 4000K suggesting that they are M type stars or young brown dwarfs. The flare energies range from 2.8×10^{32}erg to 9.5×10^{34}erg in the V-band alone indicating that WASP has identified the most energetic flares ever detected on UV Ceti stars. Some of the largest comparable flares include a 7 magnitude flare from an M4 star observed by Bond in 1976 releasing approximately 4×10^{35}erg in total across all bands [54]. The largest M-star flare observed by WASP is already a quarter of this in the V-band alone. A flare was observed on an M3 star which released 2.3×10^{34}erg in the V-band and even more than this in the U-band [115]. More recently, a flare with an optical amplitude of 6 magnitudes was seen on an M8 dwarf [151]. It was found to release 3×10^{32}erg in the V-band.

Even though WASP preferentially selects extreme flares, the sample still

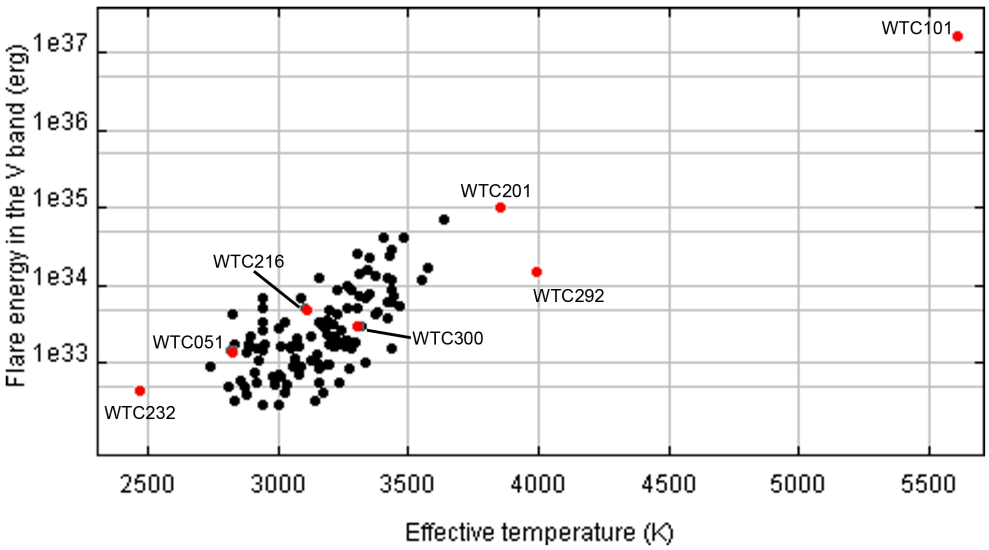

Figure 7.28: A scatter plot of the energy of the observed flare against the effective temperature of the progenitor star for the new flare candidates. Several of the most interesting flares are highlighted in red.

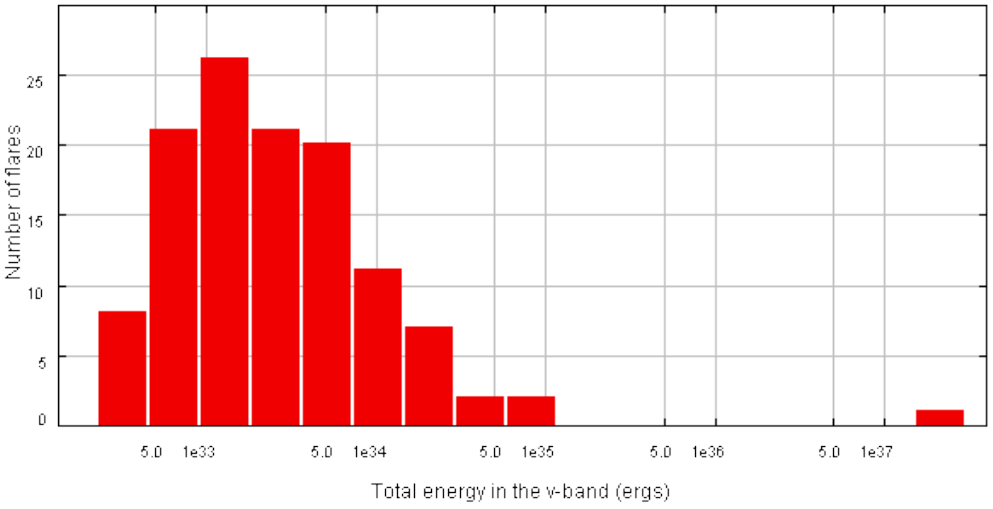

Figure 7.29: A histogram of the energies of the flares discovered by WASP.

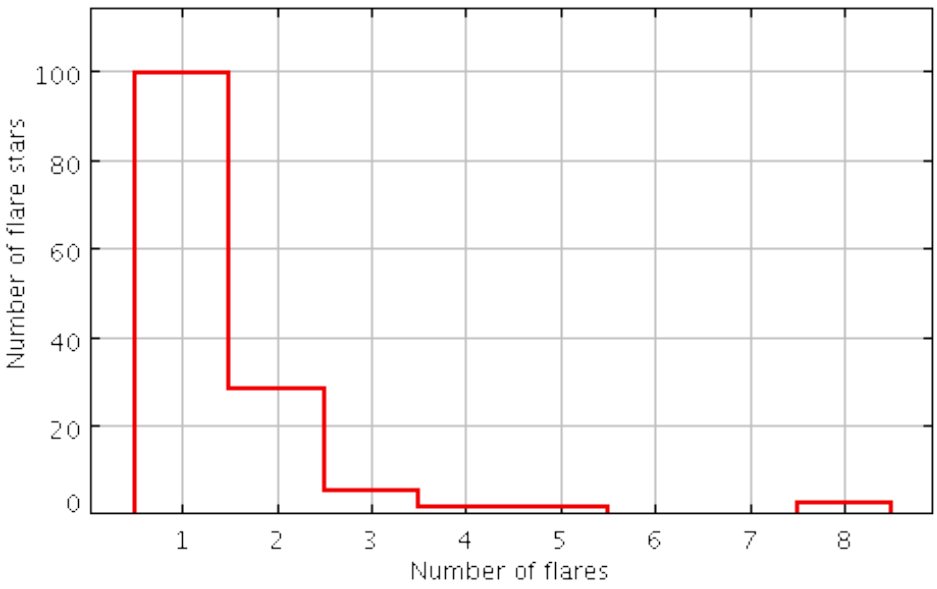

Figure 7.30: A histogram of the number of candidate flares observed on each flare star candidate.

indicates that across the whole sky these events must occur fairly regularly, especially since WASP is not ideally suited to detecting them because of their extremely short duration. Previous surveys have been biased against detecting these flares since they require long duration coverage of the sky with a high cadence. Most previous surveys have instead limited themselves to monitoring a small number of known flare stars [103].

7.2.6 Flare rates and frequency

It is difficult to make any statements on the rates of flares across the sky as the short durations (shown in Figure 7.25) means that most are only discovered if WASP is observing an area of sky with unusually high cadence. The fact that WASP detected any at all implies that, across the whole sky, they must be fairly common.

The frequency of high energy flares is indicated by the number of times more than one flare is detected on a flare star candidate. To test this the positions of the flare star candidates were searched again using the cone search algorithm (see Section 2.4.1). A search radius of 20 arcseconds was used with detections from the

2004 to 2008 seasons being considered. Flares were only counted as separate if they occurred on different nights. To improve the sensitivity of the search to extremely short duration flares, only a single detection was required to identify a flare.

Out of the 136 flare star candidates 37 showed more than one flare. A histogram of the number of flares observed on each candidate is shown in Figure 7.30. To test the number of these flares caused by chance alignments with spurious detections four sets of identical searches were carried out at offsets from the flare star positions of 2 arcminutes. These were found to have detections at 29, 26, 23 and 21 positions. If an average of 25 is taken, this would suggest that genuine repeat flares are seen on ∼12 of the flare star candidates.

7.2.7 Exceptional flares

Several of the flare star candidates have already been noted as low mass stars in other surveys and hence there are more accurate spectral types available. These include an M3 type for WTC216 [27], M3.5 type for WTC088 [134], M4 type for WTC127 [96], WTC222 [168] and WTC244 [85], M4.5 type for WTC314 [134] and M8 type for WTC051 [12] and WTC232 [35]. Furthermore, WTC216 was also identified as a T Tauri star. Some of the more unusual flares detected by WASP are discussed in more detail below.

WTC232: A cool M8 dwarf

WTC232 is the coolest flare star discovered by our survey with an estimated effective temperature of 2463K suggesting it is an M8 type star. This has been confirmed independently in the 2MU2 survey using 2MASS [35]. WTC232 showed the largest amplitude flare (7.65 magnitudes in the V-band) but this more reflects how faint the star is in quiescence. This can be seen in the estimated total energy of 4.17×10^{32}erg which, while still large, is one of the least energetic flares observed by WASP. Large flares have been seen on late M stars before such as a 6 magnitude flare in the UV (only 2.7 magnitudes in R) on an M9 star [137] and a 6 magnitude flare (in the optical) on an M8 star releasing 3×10^{32}erg in the V-band [151]. However, the flare

seen on WTC232 is clearly the largest flare ever seen on an M8 star.

WTC216: A large flare on a T Tauri star

WTC216 was independently identified as a T Tauri star in the Orion OB1 association [27]. The star was classified as M3 (compared to M5 by the Baraffe model) and the age of the cluster is $\sim 4-6$Myr. This is clearly far younger than the model assumed indicating a significantly brighter absolute magnitude and hence a far greater distance. The distance to the Orion OB1 association is 440pc (compared to 63pc by the model) which leads to a corrected flare energy estimate of 2.34×10^{35}erg. Young systems, such as this one, are often seen to be active especially if they are still being formed from an accretion disc so flare activity is to be expected. However, the flare observed by WASP is far more energetic than has been detected in the past and, with the corrected distance, is even more energetic than the other M-star flares observed.

WTC300: A flare on a young M-star

WTC300 was independently identified as a member of the Upper Sco OB association indicating an age of only 5 Myr [95]. A corresponding 2.67 magnitude flare was observed in the WASP data. As the star is still young, the Baraffe model will again underestimate the distance and hence the energy. The distance to the Upper Sco OB association is 145 ± 2 pc. This gives a corrected flare energy of 2.65×10^{34}erg, approximately an order of magnitude larger than if the star had been on the main sequence.

WTC201 and WTC292: Flares on M0 stars

The two hottest M-type stars in the sample are WTC201 and WTC292. With estimated effective temperatures of 3853K and 3992K respectively they are both classified as belonging to the spectral class M0 (it is possible that they could be lower mass stars which are pre-main sequence). Their flare amplitudes are 3.3 and

1.5 in the V-band with energies of 9.45×10^{34}erg and 1.41×10^{34}erg indicating that they are also some of the most energetic flares observed.

These flares are interesting as they represent the limit of what was found by WASP. None of these giant flares were found in earlier spectral types (with the exception of WTC101 which is discussed below) and few were found at these temperatures. Furthermore, the energies of these flares suggest that they are probably the largest flares ever seen on an M-dwarf.

It should be noted though that the durations of both of these flares are very short (9.3 and 4.5 minutes for WTC201 and WTC292 respectively). Under normal operation these flares would have been missed as they would not have had the required 3 observations. This suggests that large numbers of flares have been rejected by the search algorithm which means giant flares in late K-type stars or earlier could have been missed. However, as there is no evidence of a correlation between duration and temperature for later spectral types, it would be surprising not to see any longer duration outburst.

WTC101: A super flare on a G5 star?

WTC101 is a clear outlier in Figure 7.28 and corresponds to a G5 star from the Baraffe model with an estimated energy of $1.58 \pm 0.05 \times 10^{37}$erg. However, this estimation of the flare energy is based on the assumption that the normal contribution of flux from the star is insignificant. With an amplitude of 2.32 magnitudes this is no longer correct which suggests this may be an overestimate of the energy by $\sim$12 percent.

The corresponding object in 2MASS has j, h and k magnitudes of 14.81, 14.43 and 14.39 respectively. In USNO-B the object has a b2 magnitude of 16.4 and r2 magnitude of 15.4. These are both consistent with the spectral classification determined by the Baraffe model and there are no other nearby catalogued stars that could represent the source. This suggests one of three possibilities; the transient is a genuine super flare from a solar type star, the transient is real but unrelated to the G5 star or the transient is spurious.

If the flare is from a G5 star it would represent one of the largest flare of its type ever seen. The spectral type suggests that it could be a RS CVn type system (see Section 1.5.1) but while these systems can show large flares the 1.58×10^{37}erg seen from the V-band alone would still represent by far the largest flare ever observed [57]. The only comparable flare is a 2×10^{38}erg (in the V-band) flare seen on a G1 star in 1899 [143] which it has been speculated was caused by its interaction with a giant planet in close orbit [139]. Similarities can also be seen in the duration of the flares with the 1899 flare lasting between 17 and 367 minutes and WTC101 lasting 69 minutes. A flare like this might have significant implications for life on other planets. At a distance of 1 AU a flare of this type could cause glacial melting, temporary heating of the atmosphere and extensive depletion of the ozone layer [143]. This depletion of the ozone layer would in turn leave the surface of the planet open to ultraviolet irradiation which could cause global extinctions.

An alternative possibility is that the transient represents an unrelated object that is coincidently close to a G5 star on the sky. The separation between the centre of the transient detections and the position of the 2MASS star is 8 arcseconds. This is comparatively large for a genuine transient associated with an object although it is less than one pixel and is not as large as some confirmed associations (see Section 3.3 for a detailed analysis of WASP offsets from known star positions). The most obvious source of a short transient with no visible progenitor would be a gamma ray burst. As was discussed in Section 1.5.5, it is feasible for WASP to detect one of these. No corresponding GRB candidate was identified by Swift (or the InterPlanetary Network) but with Swift's limited sky coverage it could easily have been missed in the gamma rays. The problem that this presents is that, without gamma ray observations, confirming its nature is extremely difficult.

The final possibility is that the transient is not genuine and is caused by a fault in the WASP observations. The coverage for the night is very patchy making it difficult to establish the nature of the transient with any certainty and the detections are within 15 pixels of the edge of the CCD where problems can often occur. Furthermore, as can be seen from the raw images in Figure 7.31, it looks like there

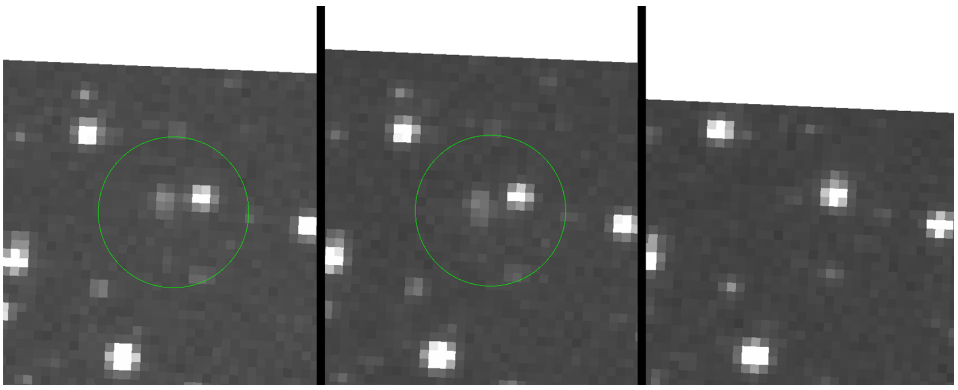

Figure 7.31: WASP images 226200612171918520, 226200612172026510 and 226200612172210060 of the flare candidate WTC101. The images were taken at the start of the flare, the end of the flare and shortly after the last WASP detection respectively.

might be slight movement of the centre of the detection. The candidate also appears slightly blurred, although this could be due to it being a particularly blue source. However, from the non-detection image the source does not appear to move in the way expected for an asteroid or a ghost image. The only other possibility is that an unusual edge effect has occurred. In most cases with spurious detections near the edge of a chip the candidate is not visible in the raw images so an effect such as this is without known president in the WASP data.

A spectrum of the corresponding 2MASS star could shed some light on the source of the transient as an active star would point towards a flare origin. If a supernova was found in deep observations at the position of the transient, the gamma ray burst possibility would be favoured. However, this transient was detected in 2006 making it unlikely that a supernova could be identified at this late stage. Alternatively, the detection of a corresponding host galaxy at the correct position could provide some evidence to suggest a GRB origin.

7.2.8 Discussion of flare star candidates

The flares found in the WASP survey are clearly some of the most energetic ever observed. One of the previous largest flares known in a normal UV Ceti system was Bond's 1976 flare with an estimated total energy of 4×10^{35}erg [54]. Several of the

flares discovered by WASP are comparable to this in the V-band alone. While RS CVn systems have been seen to have slightly larger flares than this, the spectral types of the WASP candidates suggest that these are, with the exception of WTC101, M-type stars or later.

The extreme flares were detected both in fully convective stars (later types than M3) and in stars with a radiative core. As with other activity surveys [145], no transition between these states can be seen. This indicates that the magnetic field being generated in convective stars must still be quite large and also suggests that stars with only a relatively small radiative core may already have their magnetic field generated by the convective layer alone since otherwise the transition should be visible. Only two M8 dwarfs were found to have flares and no stars of later type than these were identified. This suggests that there is an abrupt drop in activity after this which matches with the findings of other work in the field [145] [104]. The implication of this is that if brown dwarfs have extreme flares as is seen in M type stars, they must occur while the star is still very young and comparatively hot or extremely infrequently.

To further test this, cone searches (as described in Section 3.2) were carried out at the positions of 801 known L and T dwarfs from Chris Gelino's online archive [4]. 87 of the cone searches had a single detection within 20 arcseconds. Confirming the nature of these was difficult because of the lack of corroborating detections. However, four other sets of cone searches were carried out with 1 degree offsets from the brown dwarf positions to determine the number of matches by chance alignments. From these there were 66, 88, 72 and 64 matches with only one detection suggesting that, while 87 matches is fairly high, it is consistent with no genuine flare detections.

A further 72 of the cone searches had 2 or more detections within 20 arcseconds but all but one of these were established to be spurious (primarily ghost images or nearby bright stars). A two detection flare was found on SSSPM J0306-3648 which was classified as L0 from infrared observations but only M8 from the optical [94]. The fact that the only flare detected was on an M8/L0 star (one of the earliest type stars on the list) further reinforces the result that there appears to be

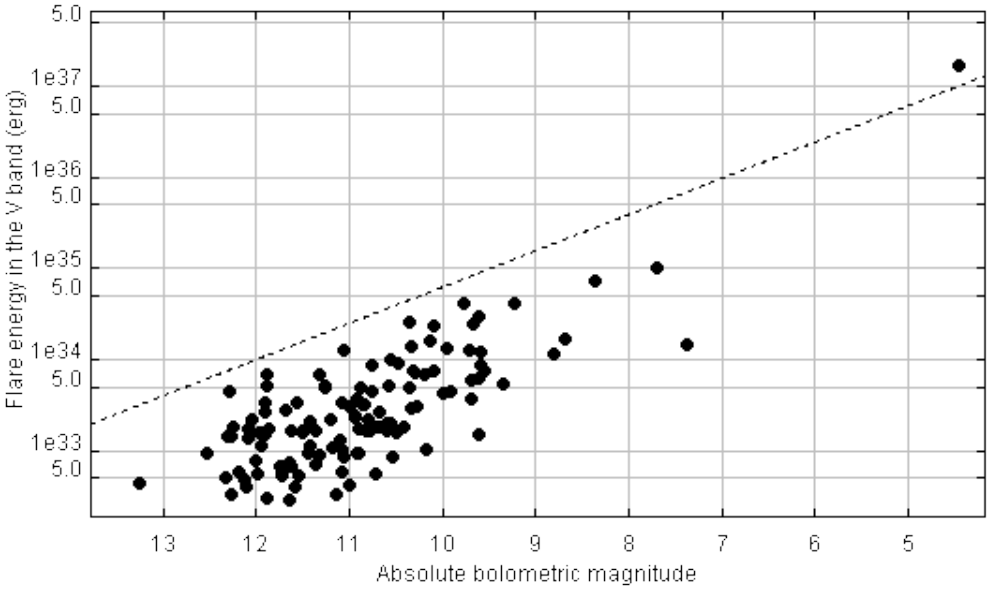

Figure 7.32: A scatter plot of the energy of the observed flare against the absolute bolometric magnitude of the progenitor star for the new flare candidates. A one to one relationship between luminosity and flare energy is shown as a dotted line.

a sharp drop in activity in stars of later spectral type than M8.

A scatter plot of the absolute bolometric magnitude (from the Baraffe model) against the total flare energy in the V-band is shown in Figure 7.32. It appears from this that the most energetic flares are only seen on the most luminous stars and the least energetic flares on the faintest. The dearth of less energetic flares on bright stars can be understood as a selection effect in the WASP data. Less energetic, and hence fainter, flares would only cause a relatively small change in brightness on the most luminous host stars. These would then be unlikely to pass the USNO-B comparison tests (see Section 4.7) so would be automatically rejected. On fainter stars the flares would make a bigger difference so would not be rejected. However, the lack of high energy flares on fainter stars does not appear to be caused by a selection effect so may represent a genuine relationship between the luminosity of the star and the maximum flare energy available.

Several unusual flares were also identified. WTC232 was found to be a cool M8 dwarf indicating that stars fairly close to the hydrogen burning limit can show huge flares. WTC101 also offers several intriguing possibilities including a huge flare

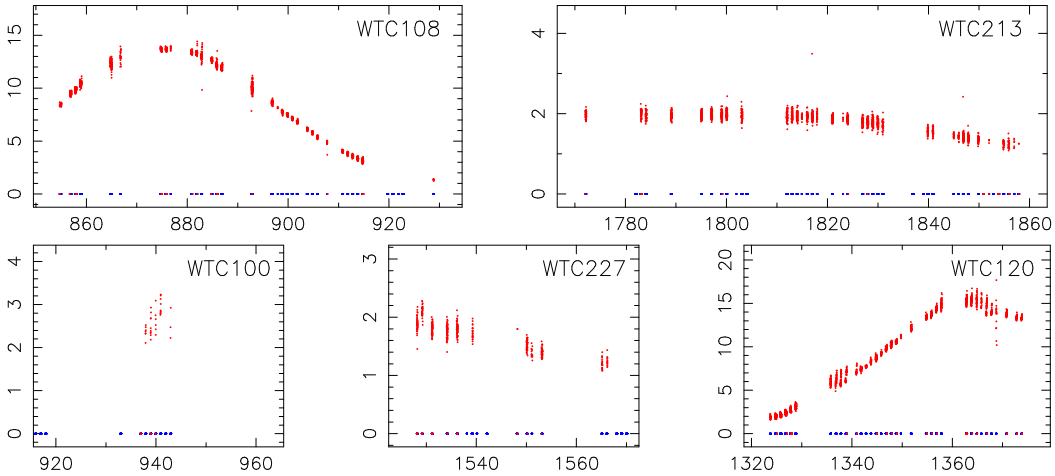

Figure 7.33: Example light curves of pulsating variable star candidates. Time in days after JD 2453005.5 is plotted on the x-axis. Flux is plotted on the y-axis in WASP flux units. Red dots mark detections and blue dots at zero flux mark observations.

on a G-type star and a detection of a gamma ray burst. Unfortunately a spurious source cannot be ruled out by the WASP data.

The fact that these extreme flares have been missed previously despite their seemingly high sky frequency emphasises the importance of high cadence surveys such as WASP and, in fact, suggests that even higher cadence wide-field surveys may be necessary to understand populations of short transients such as these.

7.3 Pulsating Variable Stars

The new candidate pulsating variable stars are listed in Table B.2 in Appendix B. 60 new pulsating variable stars were identified causing 88 clusters in the processed fields. From the light curves of these systems (see Figure C.2 in Appendix C or selected examples in Figure 7.33) it appears that they are mostly Miras or semi-regular variables with large amplitudes and periods of several months. This is not surprising as these types of variable stars are fairly common and their large amplitudes make them easy to identify as transients in the WASP data (see Section 1.6). Out of the 472 known pulsating variable stars 407 were Miras with most of the remainder being semi-regular variables.

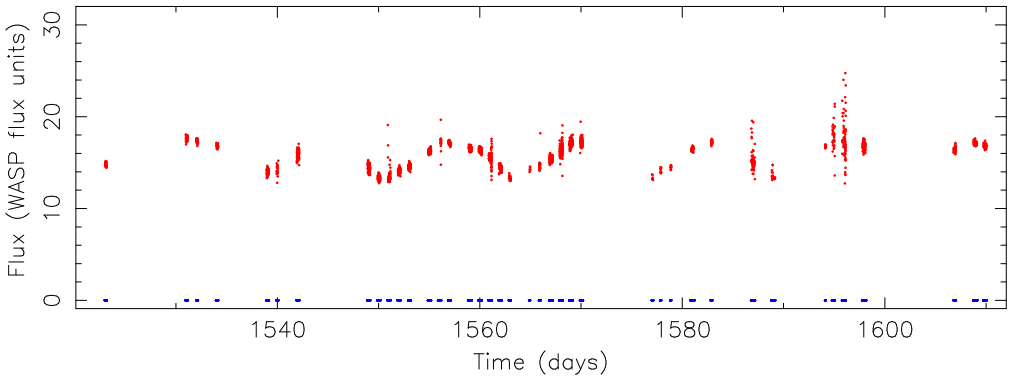

Figure 7.34: Light curve of known cephid variable star WY Sco. Time in days after JD 2453005.5 is plotted on the x-axis. Flux is plotted on the y-axis in WASP flux units. Red dots mark detections and blue dots at zero flux mark observations.

An interesting exception was WY Sco (a cephid variable) which was detected in the 2007 and 2008 WASP south data. A light curve for this system is shown in Figure 7.34. Systems with small amplitude oscillations such as this would normally be rejected by the USNO-B cross-correlation test described in Section 4.7 as, because of inaccuracies in USNO-B, the test is not very sensitive to small deviations in expected brightness. WY Sco appears to have passed the test because of unusually faint magnitudes in USNO-B.

7.3.1 Comparison to known populations

To establish whether the new pulsating variable star candidates represent a different population from known systems a scatter plot was made of their galactic coordinates. This is shown in Figure 7.35 with known systems detected by WASP marked as hollow circles and new pulsating variable star candidates marked as black diamonds. From this it can be seen that, although the WASP coverage is somewhat uneven (see Figure 4.22), there is no obvious difference in the distribution of the two populations.

Figure 7.36 shows the peak magnitudes of known Mira variable stars from the General Catalogue of Variable Stars [142] (in blue). This is compared to the known pulsating variables detected by WASP (in green) and the new candidate pulsating variables (in red). The new candidates have slightly fainter peak magnitudes than the known miras that were detected suggesting that, as expected, the known

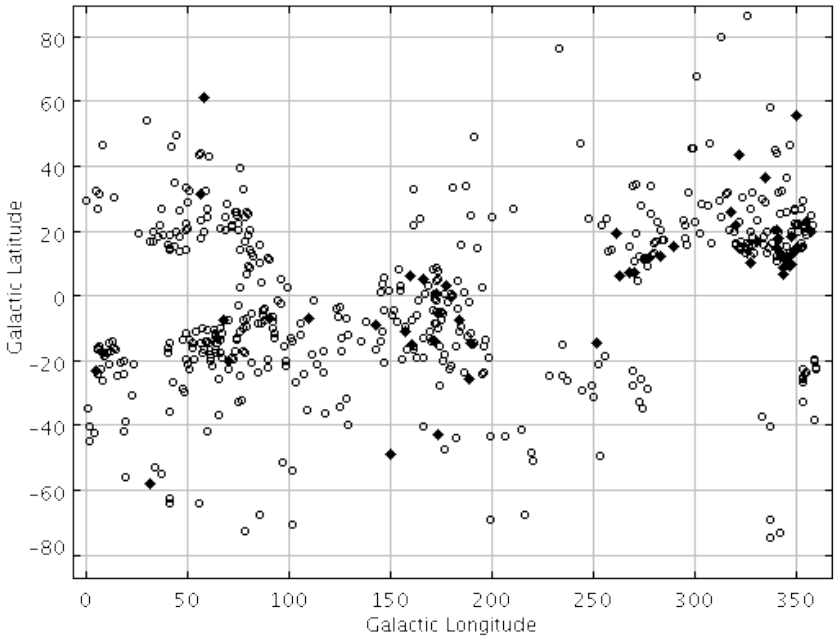

Figure 7.35: A scatter plot showing the galactic coordinates of known pulsating variable stars (marked with hollow circles) and new candidate pulsating variables (marked with black diamonds) that were identified in the WASP orphans database.

population is less complete at fainter magnitudes.

From these plots, the similarity of the light curves in Figure C.2 to known pulsating variables detected in WASP and their distribution on the reduced proper motion plot shown in Figure 5.1, it does not appear that WASP is sampling a different population.

7.3.2 Distance estimates to pulsating variable candidates

The pulsation period (P) of a Mira variable star is related to its mean absolute magnitude in the k-band (M_K) by the equation [45]:

$$M_K = -3.47 log P + 0.91$$

Using this and the recorded apparent magnitude in the k-band from the corresponding 2MASS object, it should be possible to estimate the distance to Mira variable stars detected by WASP. Figure 7.37 shows the estimated distances to the pulsating variable candidates detected by WASP using this method. The extremely large distances suggest that they could be used to probe the structure of the Galaxy

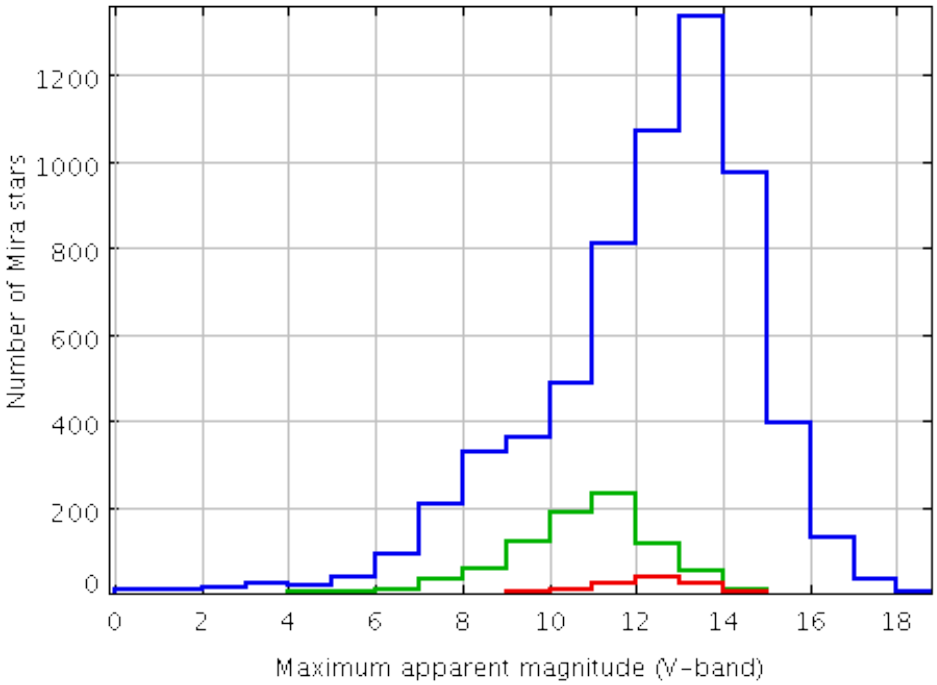

Figure 7.36: A histogram of the peak apparent magnitude of Mira variable stars. Known Miras from the General Catalogue of Variable Stars are shown in blue, known pulsating variables detected by WASP are in green and new candidate pulsating variables are in red.

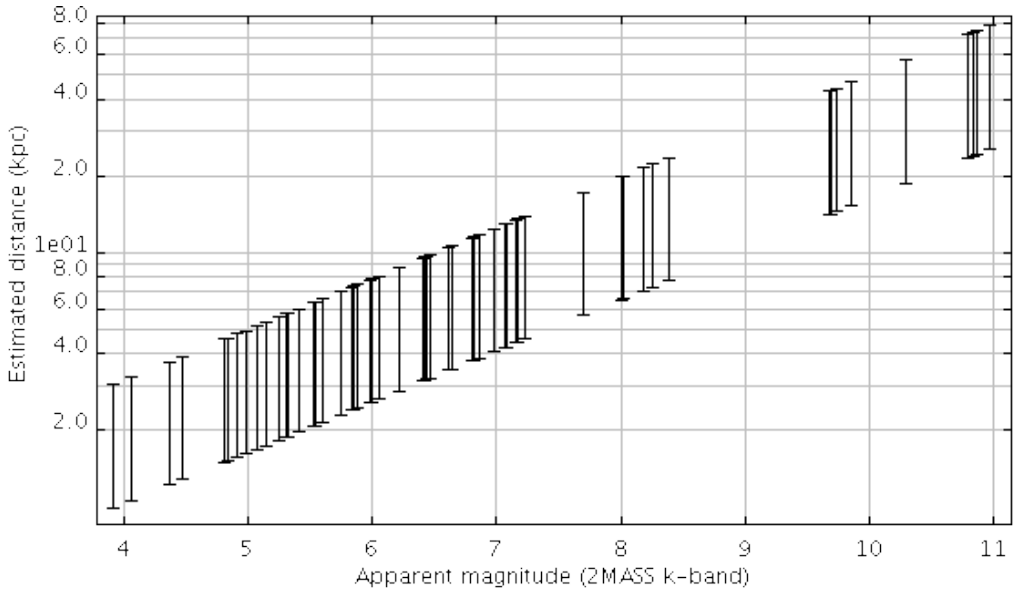

Figure 7.37: Estimated distances to pulsating variable star candidates for a given 2MASS k-band magnitude.

and, in particular, the halo. However, these distance come with several caveats. Firstly, due to the comparatively short duration of coverage it was not possible in most cases to calculate the period of oscillation. The range of values for the distance on Figure 7.37 represents a the range of typical periods for Miras from ∼100 days to ∼500 days. Secondly the apparent magnitude from 2MASS may not correspond to the mean so may be incorrect by up to several magnitudes. Thirdly, although most of the pulsating variable candidates are likely to be Miras the different types of known pulsating variables detected suggests that some may not be. Finally, the sample selected by WASP is likely to be incomplete and significantly effected by selection effects as WASP is insensitive to lower amplitude variables (see Section 1.6).

7.3.3 Rarer phenomena

An important consideration is whether any of the pulsating variable star candidates actually represent a long duration transient such as a supernova or nova. From the light curves (see Figure C.2) there are no strong candidates although in some cases,

such as WTC213, a declining supernova or slow nova can not be ruled out. Many, however, oscillate in brightness over multiple seasons indicating that their classification is fairly secure. Furthermore, all the candidates match relatively bright sources in 2MASS and USNO-B which would imply too small an amplitude of outburst to be a nova or supernova.

From the reduced proper motion scatter plot (Figure 5.1) two candidates in particular stand out from the other pulsating variables. WTC227 with a reduced proper motion of 0.9 and 2MASS J-K magnitude of 1.0 has a slowly declining light curve in Figure 7.33. However, its position in Figure 5.1 does contain other known pulsating variables. WTC100 appears more promising with a reduced proper motion of 6.3 and a 2MASS J-K magnitude of 0.7. It stands out noticeably from other known pulsating variables and its light curve in Figure 7.33 is ambiguous. It is possible that this system could be a CV displaying a normal outburst with a slow rise.

7.4 Novae

While none of the candidate transients were identified as probable novae it is possible that one of the cataclysmic variable or pulsating variable star candidates has been misclassified. This problem can be seen in Figure 7.38 where WASP light curves from two known novae (at the top) are plotted next to the two longest duration cataclysmic variable candidates. The light curves of the two new candidates appear similar to the known recurrent nova LMC 1971b. The amplitude of WTC150 (6.9 magnitudes) is a bit too small for a typical nova although, unusually for a super-outburst from a dwarf nova, there is no sign of a superhump period. However, an outburst of 8.6 magnitudes for WTC126 is consistent with a fast or recurrent nova. However, these light curves and amplitudes are also consistent with a dwarf nova superoutburst, specifically from a WZ Sge type system. Furthermore, a period of 88 minutes was found in the light curve of WTC126 suggesting that it is almost certainly a dwarf nova.

It is also possible that one of the pulsating variable star candidates could be a slower type of nova similar to V2467 Cyg shown in the top left of Figure 7.38. However, this seems unlikely as the candidates all have fairly bright optical counterparts implying quite a small amplitude if the host star has been correctly identified.

Overall, it seems that, while a detection of a nova can not be ruled out, it is unlikely that any new cases have been found in the data. The reason for this is likely to lie in the observing strategy. To avoid images becoming too overcrowded WASP has not been observing in the galactic plane. Unfortunately this is where the majority of novae are likely to be found. Unlike dwarf novae, these systems are sufficiently bright that discoveries tend to be at further distances. For high galactic latitudes there is a comparatively small volume of space that forms part of the galactic plane so the chances of a nova being found there is correspondingly reduced. However, as two known novae were identified, in the future a new nova may yet be found. It is also possible that, if further years are searched, novae from the halo or intergalactic novae could be found (see Section 1.5.3).

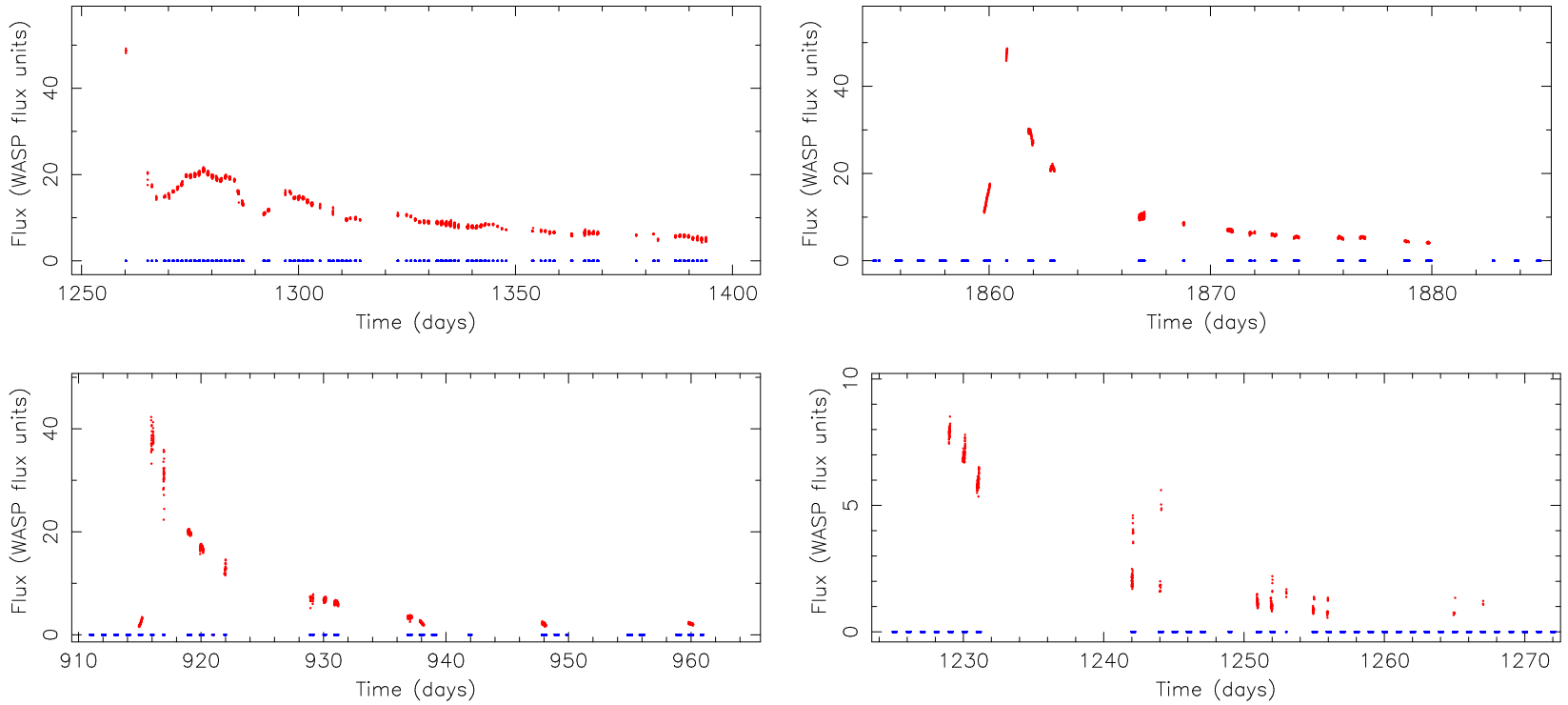

Figure 7.38: Light curves of two known novae detected by WASP and two candidate CVs with long duration outbursts. Time in days after JD 2453005.5 is plotted on the x-axis. Flux is plotted on the y-axis in WASP flux units. Blue points at zero flux mark the times of observations. Top right: Recurrent nova NOVA LMC 1971 b. top left: Slow nova V2467 Cyg. Bottom left: transient candidate WTC126. Bottom right: transient candidate WTC150.

7.5 Supernovae

From the candidates identified, it seems that WASP has not detected any previously unknown supernovae. This is not surprising as, from the targeted search for known supernovae (see Section 3.5), it was clear that WASP was often unable to distinguish them from their host galaxy. The only exception to this, SN2007od, occurred in a particularly faint galaxy. This problem, combined with the relatively shallow depth of the WASP cameras, means that WASP is only capable of identifying a small subset of the supernovae that occur. The initial shock breakout could be slightly brighter but this would still be difficult to distinguish from the host galaxy and, as described in Section 1.5.4, could be very short depending on the type of star [43].

As a known supernova was identified in the all-sky data it is possible that unknown supernovae may also be found in the unsearched all-sky data or indeed in any future data taken by WASP observatories. However, it must be acknowledged that, as discussed in Section 1.6, WASP is not well suited to identifying this type of transient compared to other surveys such as the Palomar Transient Factory.

7.6 Gamma Ray Bursts

There do not appear to be any strong gamma ray burst candidates in the WASP data. The optical light curve from a gamma ray burst could resemble a flare star. However, apart from WTC101 all of the flare star candidates are associated with M-type stars (see Section 7.2). While WTC101 is a possible gamma ray burst candidate it is also coincident with a G-star (which have been known to show flares with similar properties to WTC101 [54]). Furthermore, the WASP coverage on that night was patchy and the quality of the detections was relatively low meaning a non-physical source could not be ruled out.

Several of the short unclassified candidates do not have counterparts in USNO-B or 2MASS (specifically WTC081, WTC224, WTC265 and WTC294). However, two of these candidates are found very close to the edge of the CCD and it is not clear whether the transient would have been visible for a lot longer if it

had been in the centre of the image. In the other cases the images were corrupted so it was not possible to check for any issues. These problems suggest that these candidates may be caused by some error in the hardware or software rather than by genuine transient phenomena, such as gamma ray bursts.

Without strong candidates the question is whether it was reasonable to expect WASP to detect one. An expected number can be estimated from the sample of gamma ray bursts discovered by Swift. Swift has a sky coverage of 1.4 steradians [18] which implies that 11% of the sky is covered by it. From Figure 1.9 it can be seen that there are 5 gamma ray burst that are bright enough (15th magnitude or brighter) and last long enough enough at this magnitude (at least approximately 20 minutes) for WASP to detect and identify them. These were discovered between the 5th of April 2005 and the 24th of April 2009. Extrapolating from this implies that over the 1481 days there will have been approximately 44 gamma ray bursts across the whole sky that WASP could potentially identify. Each WASP camera has a sky coverage of 61 sq. degrees [33] and in 2008 867,432 pairs of images were taken. Combining the rate from Swift with the sky coverage of WASP gives an expected rate of 0.4 gamma ray burst a year. This expected rate does not account for any overlap in WASP fields or changes in the WASP cadence. In contrast, it also does not account for any orphan afterglows that would not be detectable in gamma rays so would be missed by Swift. However, it should give an indication of the number of gamma ray bursts that WASP could identify.

With three years of complete coverage and one further year with only five cameras it would be expected that WASP should identify 1.3 gamma ray bursts in the data that has been searched. While it is a little disappointing that no strong candidates were identified, the number is sufficiently small that it is not too surprising. What this does show though is the potential that WASP has for identifying optical counterparts of gamma ray bursts and, if further years are searched, it seems likely that a gamma ray burst could be detected.

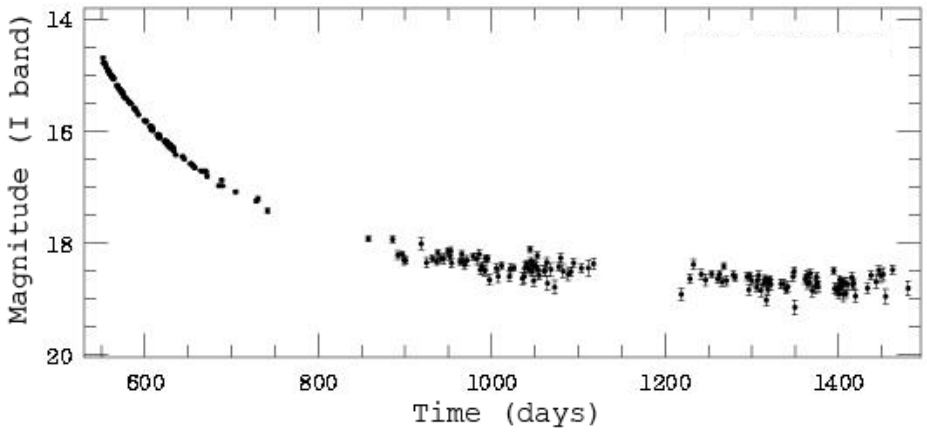

Figure 7.39: An example light curve of a microlensing candidate in data from the OGLE project [173].

7.7 Gravitational Microlensing

No strong microlensing candidates were identified. However, if the microlensing event could only be observed at maximum brightness it could resemble one of the unclassified one day transient candidates. A long duration microlensing event (such as the OGLE microlensing candidate shown in Figure 7.39) could resemble a variable star in the WASP data where only part of one cycle is seen. Furthermore, the light curve can appear even more complicated if the lensing object is part of a binary. Therefore a microlensing detection cannot be ruled out and should be considered as a candidate if the spectra of a source reveals no activity.

7.8 Tidal Disruption of a Star by a Supermassive Black Hole

As with supernovae, it does not appear that any tidal disruption events were identified by the WASP search. This is not surprising since, as was discussed in Section 1.5.9, these events are quite infrequent and may not occur at all in many galaxies. Even when they do occur the amplitude of the increase in brightness of the galaxy could be relatively small (especially in the case of red giant stars [153]). A solar

type star disrupted by a black hole of $10^6 - 10^7$ solar masses would peak at 10-60% of the luminosity of the bulge of the host galaxy in the V-band.

As was discussed in Sections 1.6 and 3.5 the WASP telescopes can struggle to identify supernovae if the host galaxy is comparatively bright. This equally applies to tidal disruption events implying that even if a sufficiently bright event occurred in our field-of-view WASP still may not be able to distinguish it from the galaxy. However, the possibility of detecting these in the WASP data in the future cannot be ruled out. As was seen in the case of the known supernova identified in the all-sky data (see Section 3.5.3), favourable circumstances such as fainter host galaxies can improve the chances of an event being detected. In particular this means that WASP may still be sensitive to lower mass black holes in dwarf galaxies.

Chapter 8

Conclusions

8.1 Summary of Results

In this thesis an untargeted search for transient candidates has been carried out using the Wide Angle Search for Planets (WASP) observatories. Unlike other wide-field surveys of this type, the WASP observations were taken with a high cadence allowing short time scale variations and outbursts to be identified. Overall, 44 new cataclysmic variable candidates, 144 new extreme flare candidates, 63 new pulsating variable star candidates and 57 transients of unknown type were found.

The sample of new cataclysmic variables (see Section 7.1) showed many similarities with the current population but also uncovered several selection effects in sky distribution (see Section 7.1.6) and duty cycle (see Section 7.1.4). However, as with many other surveys, we found no evidence of a large number of systems at short orbital periods as predicted by population models. Of particular note were two candidate WZ Sge type systems (WTC126 and WTC150) with one showing a period of 88 minutes. Another unusual candidate was WTC179 which, with a period of 540 minutes, was found to be eclipsing and is a strong candidate for follow up observations. Radial velocity measurements of this system could be used to establish the mass ratio and detailed observations of the eclipses could be used to measure the radius of the white dwarf. WTC068 was particularly unusual as the spectrum seemed to suggest an unusually cool white dwarf or, alternatively, a different type

of object that showed dwarf nova like outbursts. From known samples of CVs (see Section 3.4) there was extensive coverage of echo outbursts in 1RXS J0232-3718 and precursor outbursts in QZ Vir, AQ Eri and PU CMa. These precursor outbursts in particular are interesting as they are easily missed since they require relatively high cadence observations of the early outburst. While WASP has not discovered as many CVs as projects such as Catalina, the high cadence coverage has allowed the measurement of short duration variations such as pre-cursor outbursts and the superhump period.

The sample of flare stars discovered was particularly interesting as WASP found a large number of extremely energetic flares (see Section 7.2). These represent some of the largest flares ever observed (up to 10^{35}erg in the V-band) and, with the search algorithm's limitations in identifying such short transients, it implies that these events must occur relatively often across the whole sky. The lack of observed flares on stars of spectral type M9 or later suggests that extreme flares are either far rarer or do not occur at all on brown dwarfs. Several particularly interesting flares include one flare on an ultra-cool dwarf of spectral type M8 (WTC232) and an extremely energetic candidate flare (10^{37}erg in the V-band) on a G-type star (WTC101). These high energy flares have not been seen in other transient surveys because WASP's extremely high-cadence is essential for detecting these short duration events.

For nova, two known systems were identified as well as a new candidate (WTC150) if it is not a dwarf nova (see Section 7.4). For supernova, a known system was found in the all-sky data and the WASP detections even pre-dated its discovery (see Section 3.5). However, no new candidates were identified (see Section 7.5). A targeted search at the positions of known gamma ray burst was carried out (see Section 3.6) but no matches were found. The full untargeted search resulted in the candidate WTC101 where a gamma ray burst origin is one of the possible explanations for it (see Section 7.6). It is clearly feasible for WASP to detect these events and the high cadence makes it possible to gather multiple detections on outbursts.

Most of the 57 unclassified candidates are unlikely to represent any exotic phenomena. Instead it appears that many are single night outbursts from dwarf novae or long duration flares. Several also appear to be pulsating variable stars although there is insufficient coverage to be sure.

8.2 Future Work

There is still great scope for future work on this and similar projects. As is discussed in Section 7.1.8, observations of the sky over a longer baseline could be used to establish the properties of the predicted minimum period spike of cataclysmic variables which is key to understanding binary evolution. Despite the expected large numbers it is not currently known what outburst amplitude or frequency these systems have. Furthermore, if their accretion rate is sufficiently low, detections of outbursts might be the only effective way to identify them as their colours would look similar to detached binaries. A long baseline survey could place limits on the numbers of these systems and their accretion rates.

For flare stars a higher cadence survey or, alternatively, a modification to the search algorithm allowing candidates with only two detections to pass, could make it possible to estimate the rates of these highly energetic flares. The current system is not sensitive enough to transient events lasting less that ~ 15 minutes for this to be achieved. This is essential, not only for understanding the energies available for flares, but also for understanding the false positives that giant flares will cause in deeper optical searches for gamma ray bursts (such as with LSST).

The early detections of supernova 2007od suggests that WASP may in the future observe the initial stages of shock breakout in a supernova allowing for the properties of the progenitor to be established. One possible method to increase the survey area would be to apply a modified version of the search algorithm (see Section 4.11) to the all-sky data. This will pose problems with false positives, because the number of required detections will have to drop to two each night, but would dramatically increase the number of long duration (two or more nights)

transients, such as supernova, discovered.

For gamma ray bursts, it seems that a continuation of the search over other years has good prospects of optically detecting one of these phenomena. In Section 7.6 it was estimated that over a survey period of about 3 years a detectable gamma ray burst should occur in the WASP field-of-view.

A further improvement would be to adapt the search algorithm to work in real time. This would allow follow-up observations to happen immediately which would make it possible to gather more detailed information on outbursts and rule out false positives. This could be particularly useful for infrequent or single occurrence events such as gamma ray bursts, WZ Sge superoutbursts, nova and supernova.

Although it may seem that surveys such as WASP will rapidly be made obsolete by projects such as Pan-STARRS, PTF and, in the future, LSST (see Section 1.3), they do not operate in the same parameter space. While they observe far deeper (26th magnitude for Pan-STARRS and 27.5th for LSST), they do not offer the same continuous, high cadence coverage WASP does. Furthermore, they may not be as sensitive to the brightest examples of each transient class. For example, the LSST CCDS saturate at 16th magnitude which is the faintest that WASP can observe. Bright transients, such as those found by WASP, are the easiest to follow up and hence can lead to the greatest steps forward in understanding these phenomena.

Bibliography

[1] The american association of variable star observers. `www.aavso.org`.

[2] Asas website. `www.astrouw.edu.pl/asas/`.

[3] Harvard supernova list. `www.cfa.harvard.edu/iau/lists/Supernovae.html`.

[4] L and t dwarf list. `www.dwarfarchive.org`.

[5] Moa project website. `https://it019909.massey.ac.nz/moa/`.

[6] Wasp leicester website. `www.wasp.le.ac.uk`.

[7] Wasp website. `www.superwasp.org`.

[8] Abazajian, K. N., et al., 2009. The Seventh Data Release of the Sloan Digital Sky Survey. *ApJ*, 182:543–558.

[9] Akerlof, C. W., et al., 2003. The ROTSE-III Robotic Telescope System. *PASP*, 115:132–140.

[10] Alard, C., Terzan, A., and Guibert, J., 1996. Light curves and periods of Mira variables. *Astronomy and Astrophysics Supplement*, 120:275–282.

[11] Alcock, C., et al., 2000. The MACHO Project: Microlensing Results from 5.7 Years of Large Magellanic Cloud Observations. *ApJ*, 542:281–307.

[12] Allen, P. R., et al., 2007. A New Brown Dwarf Desert? A Scarcity of Wide Ultracool Binaries. *ApJ*, 133:971–978.

[13] Baade, W., 1938. The Absolute Photographic Magnitude of Supernovae. *ApJ*, 88:285–+.

[14] Bakos, G., et al., 2004. Wide-Field Millimagnitude Photometry with the HAT: A Tool for Extrasolar Planet Detection. *PASP*, 116:266–277.

[15] Baraffe, I., et al., 1998. Evolutionary models for solar metallicity low-mass stars: mass-magnitude relationships and color-magnitude diagrams. *A&A*, 337:403–412.

[16] Barbary, K., et al., 2009. Discovery of an Unusual Optical Transient with the Hubble Space Telescope. *ApJ*, 690:1358–1362.

[17] Barker, J. and Kolb, U., 2003. The minimum period problem in cataclysmic variables. *MNRAS*, 340:623–631.

[18] Barthelmy, S. D., et al., 2005. The Burst Alert Telescope (BAT) on the SWIFT Midex Mission. *Space Science Reviews*, 120:143–164.

[19] Beaulieu, J., et al., 2006. Discovery of a cool planet of 5.5 Earth masses through gravitational microlensing. *Nature*, 439:437–440.

[20] Becker, A. C., et al., 2004. The Deep Lens Survey Transient Search. I. Short Timescale and Astrometric Variability. *ApJ*, 611:418–433.

[21] Belczynski, K., et al., 2006. A Study of Compact Object Mergers as Short Gamma-Ray Burst Progenitors. *ApJ*, 648:1110–1116.

[22] Bertin, E. and Arnouts, S., 1996. SExtractor: Software for source extraction. *Astronomy and Astrophysics Supplement*, 117:393–404.

[23] Beuermann, K., 2006. Barnes-Evans relations for dwarfs with an application to the determination of distances to cataclysmic variables. *A&A*, 460:783–792.

[24] Bode, M. F., 2010. The outbursts of classical and recurrent novae. *Astronomische Nachrichten*, 331:160–+.

[25] Boella, G., et al., 1997. BeppoSAX, the wide band mission for X-ray astronomy. *Astronomy and Astrophysics Supplement*, 122:299–307.

[26] Botticella, M. T., et al., 2010. SN 2009kf : a UV bright type IIP supernova discovered with Pan-STARRS 1 and GALEX. *ArXiv e-prints*.

[27] Briceño, C., et al., 2005. The CIDA Variability Survey of Orion OB1. I. The Low-Mass Population of Ori OB1a and 1b. *ApJ*, 129:907–926.

[28] Burrows, D. N., et al. The Swift X-Ray Telescope: Status and Performance. *ArXiv e-prints*.

[29] Calzavara, A. J. and Matzner, C. D., 2004. Supernova properties from shock breakout X-rays. *MNRAS*, 351:694–706.

[30] Carpenter, J. M., 2001. Color Transformations for the 2MASS Second Incremental Data Release. *ApJ*, 121:2851–2871.

[31] Chevalier, R. A., 1982. The radio and X-ray emission from type II supernovae. *ApJ*, 259:302–310.

[32] Chevalier, R. A., 1998. Synchrotron Self-Absorption in Radio Supernovae. *ApJ*, 499:810–+.

[33] Christian, D. J., et al., 2005. Current status of the SuperWASP project. In F. Favata, G. A. J. Hussain, & B. Battrick, editor, *13th Cambridge Workshop on Cool Stars, Stellar Systems and the Sun*, volume 560 of *ESA Special Publication*, pp. 475–+.

[34] Clement, C. M., et al., 2001. Variable Stars in Galactic Globular Clusters. *ApJ*, 122:2587–2599.

[35] Cruz, K. L., et al., 2003. Meeting the Cool Neighbors. V. A 2MASS-Selected Sample of Ultracool Dwarfs. *ApJ*, 126:2421–2448.

[36] Cutri, R. M., et al., 2003. *2MASS All Sky Catalog of point sources.*

[37] Dalal, N., Griest, K., and Pruet, J., 2002. The Difficulty in Using Orphan Afterglows to Measure Gamma-Ray Burst Beaming. *ApJ*, 564:209–215.

[38] Darnley, M. J., et al., 2006. Classical novae from the POINT-AGAPE microlensing survey of M31 - II. Rate and statistical characteristics of the nova population. *MNRAS*, 369:257–271.

[39] Davies, S. R., 1990. An improved test for periodicity. *MNRAS*, 244:93–95.

[40] Djorgovski, S. G., et al., 2008. The Palomar-Quest digital synoptic sky survey. *Astronomische Nachrichten*, 329:263–+.

[41] Downes, R. A., et al., 2001. A Catalog and Atlas of Cataclysmic Variables: The Living Edition. *PASP*, 113:764–768.

[42] Drake, A. J., et al., 2009. First Results from the Catalina Real-Time Transient Survey. *ApJ*, 696:870–884.

[43] Ensman, L. and Burrows, A., 1992. Shock breakout in SN 1987A. *ApJ*, 393:742–755.

[44] Faulkner, J., 1971. Ultrashort-Period Binaries, Gravitational Radiation, and Mass Transfer. I. The Standard Model, with Applications to WZ Sagittae and Z Camelopardalis. *ApJ*, 170:L99+.

[45] Feast, M. W., 1996. The pulsation, temperatures and metallicities of Mira and semiregular variables in different stellar systems. *MNRAS*, 278:11–21.

[46] Galama, T. J., et al., 1998. An unusual supernova in the error box of the γ-ray burst of 25 April 1998. *Nature*, 395:670–672.

[47] Gänsicke, B. T., 2005. Observational population studies of cataclysmic variables - The golden era of surveys. In J.-M. Hameury & J.-P. Lasota, editor, *The Astrophysics of Cataclysmic Variables and Related Objects*, volume 330 of *Astronomical Society of the Pacific Conference Series*, pp. 3–+.

[48] Gänsicke, B. T., et al., 2009. SDSS unveils a population of intrinsically faint cataclysmic variables at the minimum orbital period. *MNRAS*, 397:2170–2188.

[49] Gehrels, N., Ramirez-Ruiz, E., and Fox, D. B., 2009. Gamma-Ray Bursts in the Swift Era. *Annual Reviews*, 47:567–617.

[50] Gezari, S., et al., 2008. UV/Optical Detections of Candidate Tidal Disruption Events by GALEX and CFHTLS. *ApJ*, 676:944–969.

[51] Ghez, A. M., et al., 1998. High Proper-Motion Stars in the Vicinity of Sagittarius A*: Evidence for a Supermassive Black Hole at the Center of Our Galaxy. *ApJ*, 509:678–686.

[52] Glass, I. S. and Evans, T. L., 1981. A period-luminosity relation for Mira variables in the Large Magellanic Cloud. *Nature*, 291:303–+.

[53] Granot, J., et al., 2002. Off-Axis Afterglow Emission from Jetted Gamma-Ray Bursts. *ApJ*, 570:L61–L64.

[54] Greenstein, J. L., 1977. Bond's flare star 2329-03. *PASP*, 89:304–308.

[55] Greiner, J. and Motch, C., 1995. A large amplitude flaring dMe star in the 1978 October 6B γ-ray burst error box. *A&A*, 294:177–182.

[56] Groot, P. J., et al., 2003. The Faint Sky Variability Survey - I. Goals and data reduction process. *MNRAS*, 339:427–434.

[57] Haisch, B., Strong, K. T., and Rodono, M., 1991. Flares on the sun and other stars. *Annual Reviews*, 29:275–324.

[58] Halpern, J. P., Gezari, S., and Komossa, S., 2004. Follow-Up Chandra Observations of Three Candidate Tidal Disruption Events. *ApJ*, 604:572–578.

[59] Hamuy, M., 2003. Review on the Observed and Physical Properties of Core Collapse Supernovae. *ArXiv Astrophysics e-prints*.

[60] Harrison, T. E., et al., 2004. An Astrometric Calibration of the $M_V - P_{orb}$ Relationship for Cataclysmic Variables based on Hubble Space Telescope Fine Guidance Sensor Parallaxes. *ApJ*, 127:460–468.

[61] Hartmann, L. and Kenyon, S. J., 1985. On the nature of FU Orionis objects. *ApJ*, 299:462–478.

[62] Hartmann, L. and Kenyon, S. J., 1996. The FU Orionis Phenomenon. *Annual Reviews*, 34:207–240.

[63] Hellier, C., 2001. *Cataclysmic Variable Stars How and Why They Vary*. Praxis Publishing Ltd.

[64] Herbig, G. H., 1977. Eruptive phenomena in early stellar evolution. *ApJ*, 217:693–715.

[65] Hillebrandt, W. and Niemeyer, J. C., 2000. Type IA Supernova Explosion Models. *Annual Reviews*, 38:191–230.

[66] Hjorth, J., et al., 2003. A very energetic supernova associated with the γ-ray burst of 29 March 2003. *Nature*, 423:847–850.

[67] Hodapp, K. W., et al., 2004. Design of the Pan-STARRS telescopes. *Astronomische Nachrichten*, 325:636–642.

[68] Høg, E., et al., 2000. The Tycho-2 catalogue of the 2.5 million brightest stars. *A&A*, 355:L27–L30.

[69] Howell, S. B., Nelson, L. A., and Rappaport, S., 2001. An Exploration of the Paradigm for the 2-3 Hour Period Gap in Cataclysmic Variables. *ApJ*, 550:897–918.

[70] Howell, S. B., Rappaport, S., and Politano, M., 1997. On the existence of low-luminosity cataclysmic variables beyond the orbital period minimum. *MNRAS*, 287:929–936.

[71] Howell, S. B., et al., 1996. Superoutburst Photometry of AL Comae Berenices. *ApJ*, 111:2367–+.

[72] Ivezic, Z., et al., 2008. LSST: from Science Drivers to Reference Design and Anticipated Data Products. *ArXiv e-prints*.

[73] Izzard, R. G., Ramirez-Ruiz, E., and Tout, C. A., 2004. Formation rates of core-collapse supernovae and gamma-ray bursts. *MNRAS*, 348:1215–1228.

[74] Jurić, M., et al., 2008. The Milky Way Tomography with SDSS. I. Stellar Number Density Distribution. *ApJ*, 673:864–914.

[75] Kaiser, N., et al., 2002. Pan-STARRS: A Large Synoptic Survey Telescope Array. In J. A. Tyson & S. Wolff, editor, *Society of Photo-Optical Instrumentation Engineers (SPIE) Conference Series*, volume 4836 of *Society of Photo-Optical Instrumentation Engineers (SPIE) Conference Series*, pp. 154–164.

[76] Kann, D. A., et al., 2007. The Afterglows of Swift-era Gamma-Ray Bursts. I. Comparing pre-Swift and Swift era Long/Soft (Type II) GRB Optical Afterglows. *ArXiv e-prints*.

[77] Kato, T., 1997. The 1993 Superoutburst of T Leonis: Early Appearance of Superhumps during a Precursor Outburst. *PASJ*, 49:583–587.

[78] Keller, S. C., et al., 2007. The SkyMapper Telescope and The Southern Sky Survey. *Publications of the Astronomical Society of Australia*, 24:1–12.

[79] Kinemuchi, K., et al., 2006. Analysis of RR Lyrae Stars in the Northern Sky Variability Survey. *ApJ*, 132:1202–1220.

[80] King, A. R., Schenker, K., and Hameury, J. M., 2002. Blunting the spike: the cataclysmic variable minimum period. *MNRAS*, 335:513–516.

[81] Klebesadel, R. W., Strong, I. B., and Olson, R. A., 1973. Observations of Gamma-Ray Bursts of Cosmic Origin. *ApJ*, 182:L85+.

[82] Kolb, U., 1993. A model for the intrinsic population of cataclysmic variables. *A&A*, 271:149–+.

[83] Kolb, U. and Baraffe, I., 1999. Brown dwarfs and the cataclysmic variable period minimum. *MNRAS*, 309:1034–1042.

[84] Kouveliotou, C., et al., 1993. Identification of two classes of gamma-ray bursts. *ApJ*, 413:L101–L104.

[85] Kowalski, A. F., et al., 2009. M Dwarfs in Sloan Digital Sky Survey Stripe 82: Photometric Light Curves and Flare Rate Analysis. *ApJ*, 138:633–648.

[86] Lacy, C. H., Moffett, T. J., and Evans, D. S., 1976. UV Ceti stars - Statistical analysis of observational data. *ApJ*, 30:85–96.

[87] Lasota, J. and Hameury, J., 1998. Disk instability models. In S. S. Holt & T. R. Kallman, editor, *American Institute of Physics Conference Series*, volume 431 of *American Institute of Physics Conference Series*, pp. 351–360.

[88] Lee, W. H. and Ramirez-Ruiz, E., 2007. The progenitors of short gamma-ray bursts. *New Journal of Physics*, 9:17–+.

[89] Lewis, J. R., et al., 1994. Optical Observations of Supernova 1993J from La-Palma - Part One - Days 2 TO 125. *MNRAS*, 266:L27+.

[90] Liller, W. and Mayer, B., 1987. The rate of nova production in the Galaxy. *PASP*, 99:606–609.

[91] Littlefair, S. P., et al., 2006. A Brown Dwarf Mass Donor in an Accreting Binary. *Science*, 314:1578–.

[92] Littlefair, S. P., et al., 2008. On the evolutionary status of short-period cataclysmic variables. *MNRAS*, 388:1582–1594.

[93] Lloyd Evans, T. and Menzies, J. W., 1973. Red Variables Stars in Metal Rich Globular Clusters. In *IAU Colloq. 21: Variable Stars in Globular Clusters and*

in Related Systems, volume 36 of *Astrophysics and Space Science Library*, pp. 151–+.

[94] Lodieu, N., et al., 2005. Spectroscopic classification of red high proper motion objects in the Southern Sky. *A&A*, 440:1061–1078.

[95] Lodieu, N., et al., 2007. New brown dwarfs in Upper Sco using UKIDSS Galactic Cluster Survey science verification data. *MNRAS*, 374:372–384.

[96] López-Santiago, J., et al., 2007. The stellar content of the XMM-Newton bright serendipitous survey. *A&A*, 463:165–174.

[97] LSST Science Collaborations, et al., 2009. LSST Science Book, Version 2.0. *ArXiv e-prints*.

[98] Magorrian, J. and Tremaine, S., 1999. Rates of tidal disruption of stars by massive central black holes. *MNRAS*, 309:447–460.

[99] Malesani, D., et al., 2004. SN 2003lw and GRB 031203: A Bright Supernova for a Faint Gamma-Ray Burst. *ApJ*, 609:L5–L8.

[100] Marsh, T. R., 1989. The extraction of highly distorted spectra. *PASP*, 101:1032–1037.

[101] Metzger, B. D., Piro, A. L., and Quataert, E., 2008. Time-dependent models of accretion discs formed from compact object mergers. *MNRAS*, 390:781–797.

[102] Modjaz, M., et al., 2009. From Shock Breakout to Peak and Beyond: Extensive Panchromatic Observations of the Type Ib Supernova 2008D Associated with Swift X-ray Transient 080109. *ApJ*, 702:226–248.

[103] Moffett, T. J., 1974. UV Ceti flare stars - Observational data. *ApJ*, 29:1–42.

[104] Mohanty, S. and Basri, G., 2003. Rotation and Activity in Mid-M to L Field Dwarfs. *ApJ*, 583:451–472.

[105] Monet, D. and et al., 1998. A catalogue of astrometric standards. *VizieR Online Data Catalog*, 1252:0–+.

[106] Monet, D. G., et al., 2003. The USNO-B Catalog. *ApJ*, 125:984–993.

[107] Morokuma, T., et al., 2008. The Subaru/XMM-Newton Deep Survey (SXDS). V. Optically Faint Variable Object Survey. *ApJ*, 676:163–183.

[108] Nakano, S., et al., 2007. V2467 Cygni = Nova Cygni 2007. *IAU Circ*, 8821:1–+.

[109] Osaki, Y., 1989. A model for the superoutburst phenomenon of SU Ursae Majoris stars. *PASJ*, 41:1005–1033.

[110] Osaki, Y., 1996. Dwarf-Nova Outbursts. *PASP*, 108:39–+.

[111] Paczynski, B., 1977. A model of accretion disks in close binaries. *ApJ*, 216:822–826.

[112] Paczynski, B., 1986. Gravitational microlensing by the galactic halo. *ApJ*, 304:1–5.

[113] Paczynski, B. and Schwarzenberg-Czerny, A., 1980. Disk accretion in U Geminorum. *Acta Astronomica*, 30:127–141.

[114] Paczynski, B. and Sienkiewicz, R., 1981. Gravitational radiation and the evolution of cataclysmic binaries. *ApJ*, 248:L27–L30.

[115] Pagano, I., et al., 1997. A major optical flare on the recently discovered X-ray active dMe star G 102-21. *A&A*, 318:467–471.

[116] Parker, E. N., 1955. Hydromagnetic Dynamo Models. *ApJ*, 122:293–+.

[117] Parley, N. R., et al., 2005. Serendipitous Asteroid Lightcurve Survey Using SuperWASP. *Earth Moon and Planets*, 97:261–268.

[118] Peterson, B. M. and Ferland, G. J., 1986. An accretion event in the Seyfert galaxy NGC 5548. *Nature*, 324:345–347.

[119] Pettersen, B. R., 1989. A review of stellar flares and their characteristics. *Colloquium on Solar and Stellar Flares*, 121:299–312.

[120] Pietsch, W., 2010. X-ray emission from optical novae in M 31. *Astronomische Nachrichten*, 331:187–+.

[121] Piran, T., 2005. The beaming factor and other open issues in GRB Jets. *Nuovo Cimento C Geophysics Space Physics C*, 28:373–+.

[122] Podsiadlowski, P., et al., 2004. The Rates of Hypernovae and Gamma-Ray Bursts: Implications for Their Progenitors. *ApJ*, 607:L17–L20.

[123] Pojmański, G., 2001. The All Sky Automated Survey (ASAS-3) System - Its Operation and Preliminary Data. In B. Paczynski, W.-P. Chen, & C. Lemme, editor, *IAU Colloq. 183: Small Telescope Astronomy on Global Scales*, volume 246 of *Astronomical Society of the Pacific Conference Series*, pp. 53–+.

[124] Polidan, R. S. and Holberg, J. B., 1987. Multiwavelength monitoring of the dwarf nova VW Hydri. IV - Voyager observations. *MNRAS*, 225:131–140.

[125] Pollacco, D. L., et al., 2006. The WASP Project and the SuperWASP Cameras. *PASP*, 118:1407–1418.

[126] Preston, G. W., et al., 1963. A Spectroscopic and Photoelectric Survey of the RV Tauri Stars. *ApJ*, 137:401–+.

[127] Pretorius, M. L., Knigge, C., and Kolb, U., 2007. The influence of selection effects on the observed cataclysmic variable population: modelling and application to the Palomar-Green sample. *MNRAS*, 374:1495–1505.

[128] Quimby, R. M., et al., 2009. Mysterious transients unmasked as the bright blue death throes of massive stars. *ArXiv e-prints*.

[129] Racusin, J. L., et al., 2008. Broadband observations of the naked-eye γ-ray burst GRB080319B. *Nature*, 455:183–188.

[130] Rappaport, S., Verbunt, F., and Joss, P. C., 1983. A new technique for calculations of binary stellar evolution, with application to magnetic braking. *ApJ*, 275:713–731.

[131] Rau, A., et al., 2009. Exploring the Optical Transient Sky with the Palomar Transient Factory. *PASP*, 121:1334–1351.

[132] Rees, M. J., 1988. Tidal disruption of stars by black holes of 10 to the 6th-10 to the 8th solar masses in nearby galaxies. *Nature*, 333:523–528.

[133] Renzini, A., et al., 1995. An ultraviolet flare at the centre of the elliptical galaxy NGC4552. *Nature*, 378:39–41.

[134] Riaz, B., Gizis, J. E., and Harvin, J., 2006. Identification of New M Dwarfs in the Solar Neighborhood. *ApJ*, 132:866–872.

[135] Ritter, H., 2008. Formation and Evolution of Cataclysmic Variables. *ArXiv e-prints*.

[136] Ritter, H. and Kolb, U., 2010. Cataclysmic Binaries, LMXBs, and related objects (Ritter+, 2010). *VizieR Online Data Catalog*, 1:2018–+.

[137] Rockenfeller, B., et al., 2006. Multiband photometric detection of a huge flare on the M9 dwarf 2MASSW J1707183+643933. *MNRAS*, 367:407–411.

[138] Rodríguez-Gil, P., et al., 2009. An evolved donor star in the long-period cataclysmic variable ¡ASTROBJ¿HS 0218+3229¡/ASTROBJ¿. *A&A*, 496:805–812.

[139] Rubenstein, E. P. and Schaefer, B. E., 2000. Are Superflares on Solar Analogues Caused by Extrasolar Planets? *ApJ*, 529:1031–1033.

[140] Rykoff, E. S., et al., 2005. A Search for Untriggered GRB Afterglows with ROTSE-III. *ApJ*, 631:1032–1038.

[141] Salim, S. and Gould, A., 2002. Classifying Luyten Stars Using an Optical-Infrared Reduced Proper-Motion Diagram. *ApJ*, 575:L83–L86.

[142] Samus, N. N., Durlevich, O. V., and et al., 2009. General Catalogue of Variable Stars (Samus+ 2007-2011). *VizieR Online Data Catalog*, 1:2025–+.

[143] Schaefer, B. E., King, J. R., and Deliyannis, C. P., 2000. Superflares on Ordinary Solar-Type Stars. *ApJ*, 529:1026–1030.

[144] Schawinski, K., et al., 2008. Supernova Shock Breakout from a Red Supergiant. *Science*, 321:223–226.

[145] Schmidt, S. J., et al., 2007. Activity and Kinematics of Ultracool Dwarfs, Including an Amazing Flare Observation. *ApJ*, 133:2258–2273.

[146] Shara, M. M., 2006. Tramp Classical Novae as Tracers of Intergalactic Stars. *ApJ*, 131:2980–2985.

[147] Skrutskie, M. F., et al., 2006. The Two Micron All Sky Survey (2MASS). *ApJ*, 131:1163–1183.

[148] Sokoloski, J. L., et al., 2006. An X-ray-emitting blast wave from the recurrent nova RS Ophiuchi. *Nature*, 442:276–278.

[149] Starrfield, S., Sparks, W. M., and Shaviv, G., 1988. A model for the 1987 outburst of the recurrent nova U Scorpii. *ApJ*, 325:L35–L38.

[150] Starrfield, S., et al., 1972. CNO Abundances and Hydrodynamic Models of the Nova Outburst. *ApJ*, 176:169–+.

[151] Stelzer, B., et al., 2006. Simultaneous optical and X-ray observations of a giant flare on the ultracool dwarf LP 412-31. *A&A*, 460:L35–L38.

[152] Sterken, C. and Jaschek, C., 2001. *Lightcurves of varaible stars; a pictoral atlas*. Cambridge University Press.

[153] Syer, D. and Ulmer, A., 1999. Tidal disruption rates of stars in observed galaxies. *MNRAS*, 306:35–42.

[154] Szkody, P., et al., 2009. Cataclysmic Variables from SDSS. VII. The Seventh Year (2006). *ApJ*, 137:4011–4019.

[155] Tanvir, N. R., et al., 2009. A γ-ray burst at a redshift of z˜8.2. *Nature*, 461:1254–1257.

[156] Thorstensen, J. R., 2003. Parallaxes and Distance Estimates for 14 Cataclysmic Variable Stars. *ApJ*, 126:3017–3029.

[157] Tobias, S. M., 2002. The solar dynamo. *Royal Society of London Philosophical Transactions Series A*, 360:2741–2756.

[158] Udalski, A., Kubiak, M., and Szymanski, M., 1997. Optical Gravitational Lensing Experiment. OGLE-2 – the Second Phase of the OGLE Project. *Acta Astronomica*, 47:319–344.

[159] Udalski, A., et al., 2000. The Optical Gravitational Lensing Experiment. Catalog of Microlensing Events in the Galactic Bulge. *Acta Astronomica*, 50:1–65.

[160] Ulmer, A., 1997. Evolution of Thick Accretion Disks Produced by Tidal Disruption Events. *ArXiv Astrophysics e-prints*.

[161] van der Woerd, H. and van Paradijs, J., 1987. Recurrence behavior of outbursts in VW HYI. *ASS*, 130:135–142.

[162] van der Woerd, H. and van Paradijs, J., 1987. Recurrence behavior of outbursts in VW HYI. *MNRAS*, 224:271–281.

[163] Vestrand, W. T., et al., 2002. The RAPTOR experiment: a system for monitoring the optical sky in real time. In R. I. Kibrick, editor, *Society of Photo-Optical Instrumentation Engineers (SPIE) Conference Series*, volume 4845 of *Society of Photo-Optical Instrumentation Engineers (SPIE) Conference Series*, pp. 126–136.

[164] Voges, W., et al., 1999. The ROSAT all-sky survey bright source catalogue. *A&A*, 349:389–405.

[165] Voges, W., et al., 2000. Rosat All-Sky Survey Faint Source Catalogue. *IAU Circ*, 7432:3–+.

[166] Warner, B., 1987. Absolute magnitudes of cataclysmic variables. *MNRAS*, 227:23–73.

[167] Warner, B., 1995. *Cataclysmic Variable Stars*. Cambridge University Press.

[168] West, A. A., et al., 2008. Constraining the Age-Activity Relation for Cool Stars: The Sloan Digital Sky Survey Data Release 5 Low-Mass Star Spectroscopic Sample. *ApJ*, 135:785–795.

[169] Wheatley, P., 2004. Optical Transient with WASP. *WASP Discussion Document*.

[170] Wheatley, P. J., Burleigh, M. R., and Watson, M. G., 2000. Observations of the extreme-ultraviolet transient REJ1255+266: a short outburst of a WZ Sge system? *MNRAS*, 317:343–347.

[171] Woosley, S. E. and Bloom, J. S., 2006. The Supernova Gamma-Ray Burst Connection. *Annual Reviews*, 44:507–556.

[172] Worden, S. P., et al., 1981. Flare Activity on T-Tauri Stars. *ApJ*, 244:520–+.

[173] Wozniak, P. R., et al., 2001. Difference Image Analysis of the OGLE-II Bulge Data. II. Microlensing Events. *Acta Astronomica*, 51:175–219.

[174] Woźniak, P. R., et al., 2004. Northern Sky Variability Survey: Public Data Release. *ApJ*, 127:2436–2449.

[175] Woźniak, P. R., et al., 2005. RAPTOR Observations of the Early Optical Afterglow from GRB 050319. *ApJ*, 627:L13–L16.

[176] Yaron, O., et al., 2005. An Extended Grid of Nova Models. II. The Parameter Space of Nova Outbursts. *ApJ*, 623:398–410.

[177] Young, T. R., Baron, E., and Branch, D., 1995. Light Curve Studies of SN 1993J and SN 1994I. *ApJ*, 449:L51+.

[178] Zacharias, N., et al., 2004. The Naval Observatory Merged Astrometric Dataset (NOMAD). In *Bulletin of the American Astronomical Society*, volume 36 of *Bulletin of the American Astronomical Society*, pp. 1418–+.

[179] Zombeck, M. V., 1990. *Handbook of space astronomy and astrophysics*.

Appendix A

Light Curves of Transients Identified by the Targeted Search

This appendix contains light curves of all dwarf nova outbursts of Ritter and Kolb cataclysmic variables detected between 2004 and 2008 (see Section 3.4) and candidate transient objects identified by the X-ray selected targeted search (see Section 3.7).

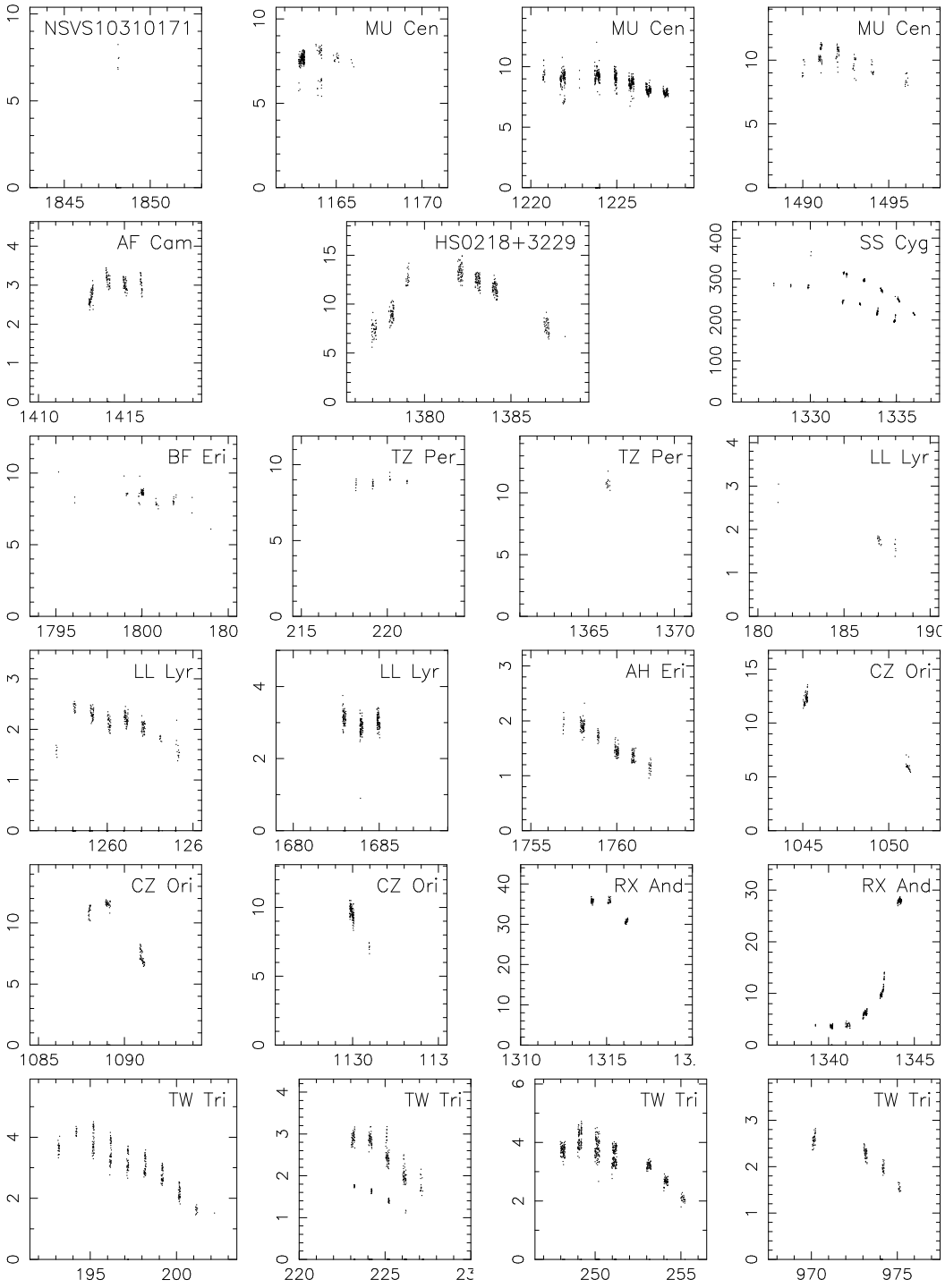

Figure A.1: Light curves of known CVs detected in WASP. Time in days after JD 2453005.5 is plotted on the x-axis. Flux is plotted on the y-axis in WASP flux units.

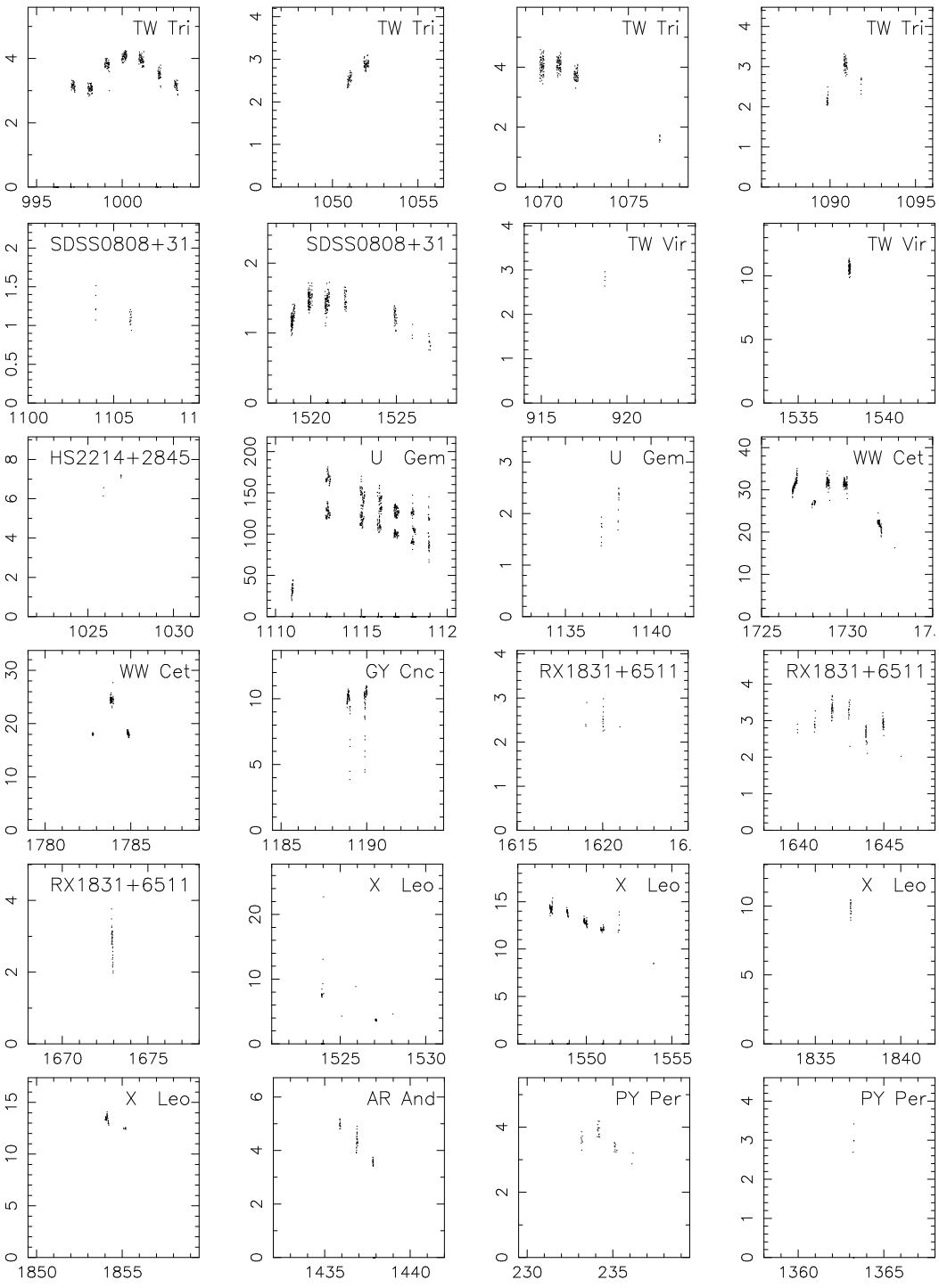

Figure A.1 ii (continued): Light curves of known CVs detected in WASP. Time in days after JD 2453005.5 is plotted on the x-axis. Flux is plotted on the y-axis in WASP flux units.

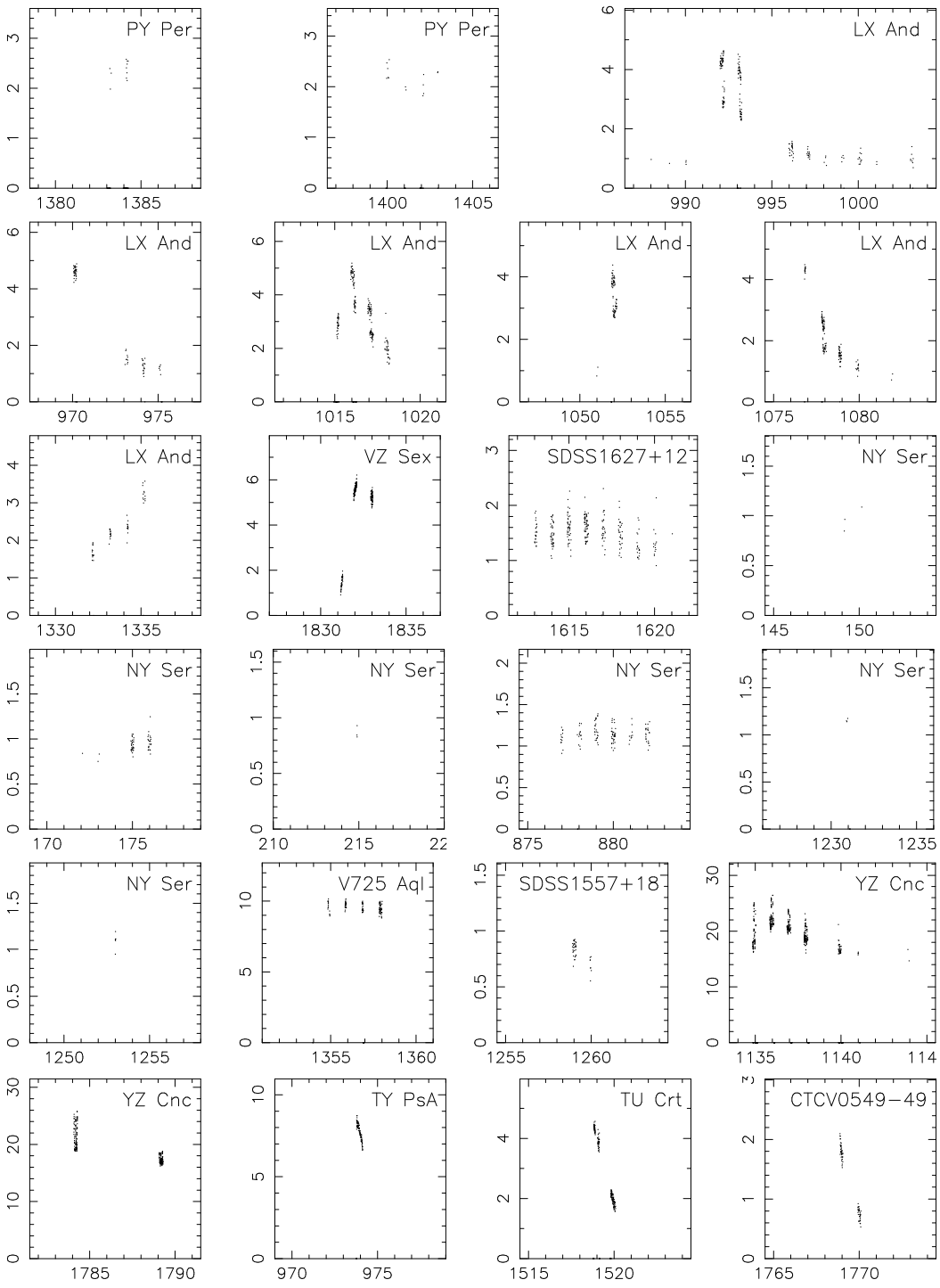

Figure A.1 iii (continued): Light curves of known CVs detected in WASP. Time in days after JD 2453005.5 is plotted on the x-axis. Flux is plotted on the y-axis in WASP flux units.

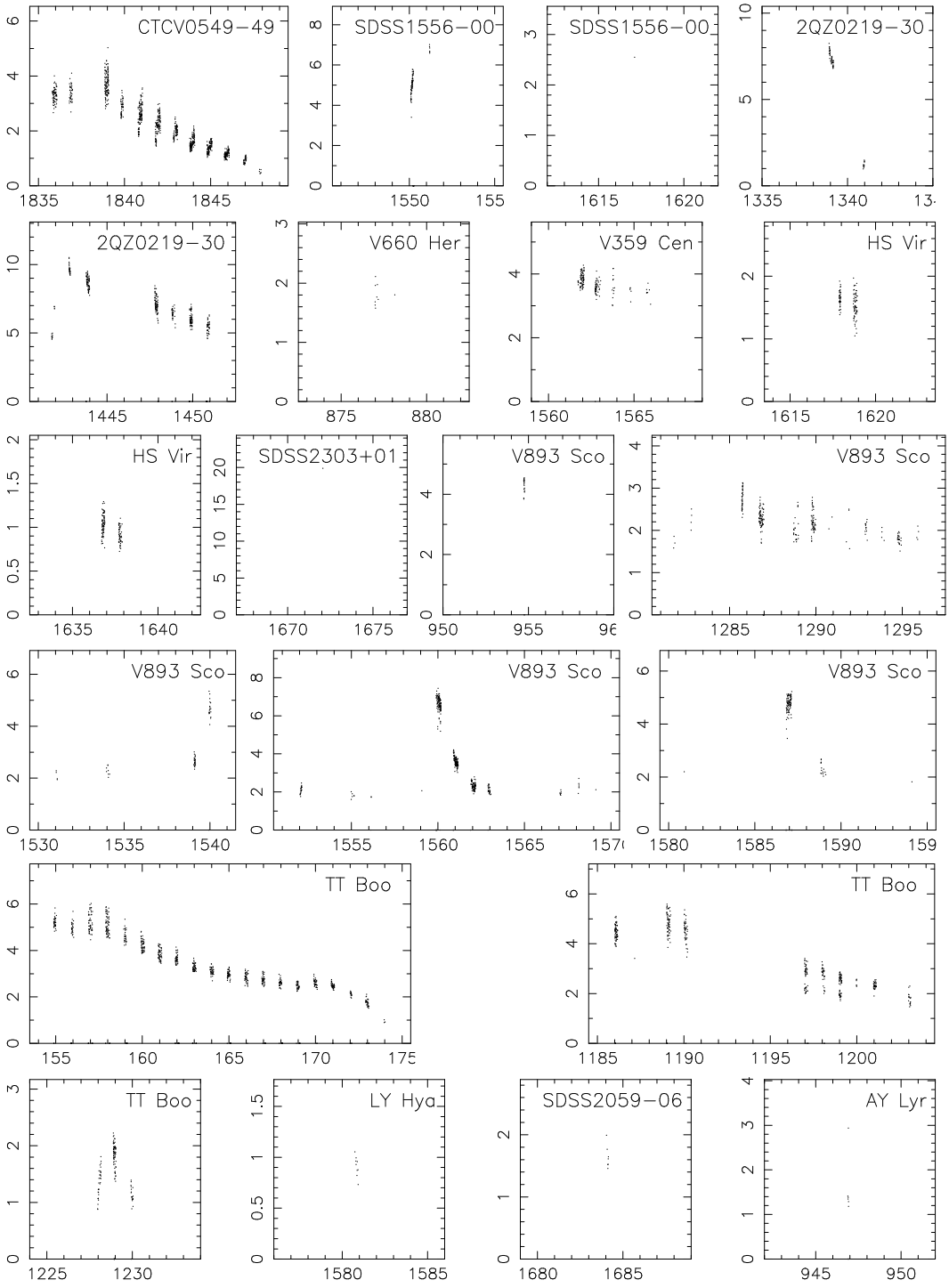

Figure A.1 iv (continued): Light curves of known CVs detected in WASP. Time in days after JD 2453005.5 is plotted on the x-axis. Flux is plotted on the y-axis in WASP flux units.

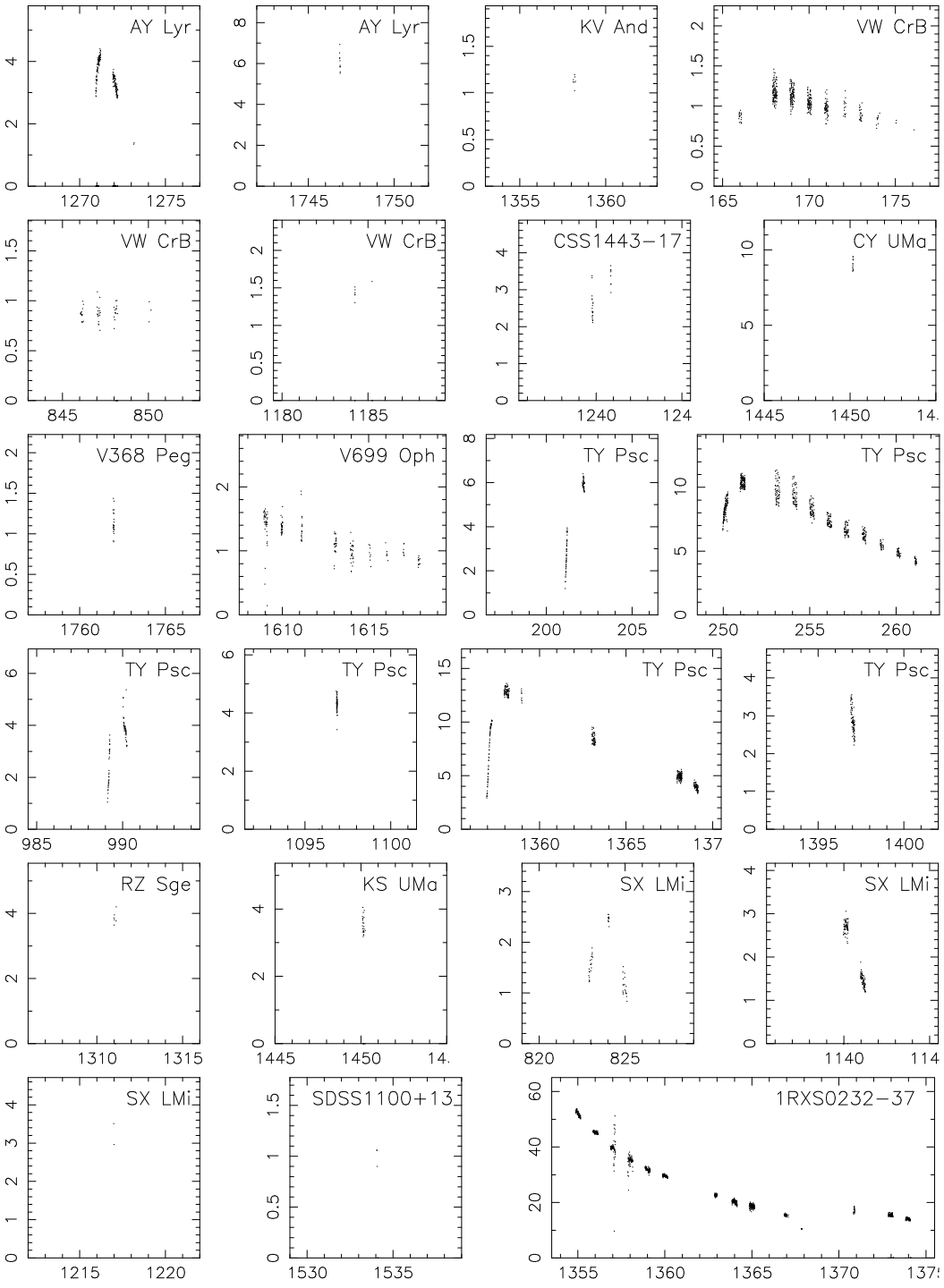

Figure A.1 v (continued): Light curves of known CVs detected in WASP. Time in days after JD 2453005.5 is plotted on the x-axis. Flux is plotted on the y-axis in WASP flux units.

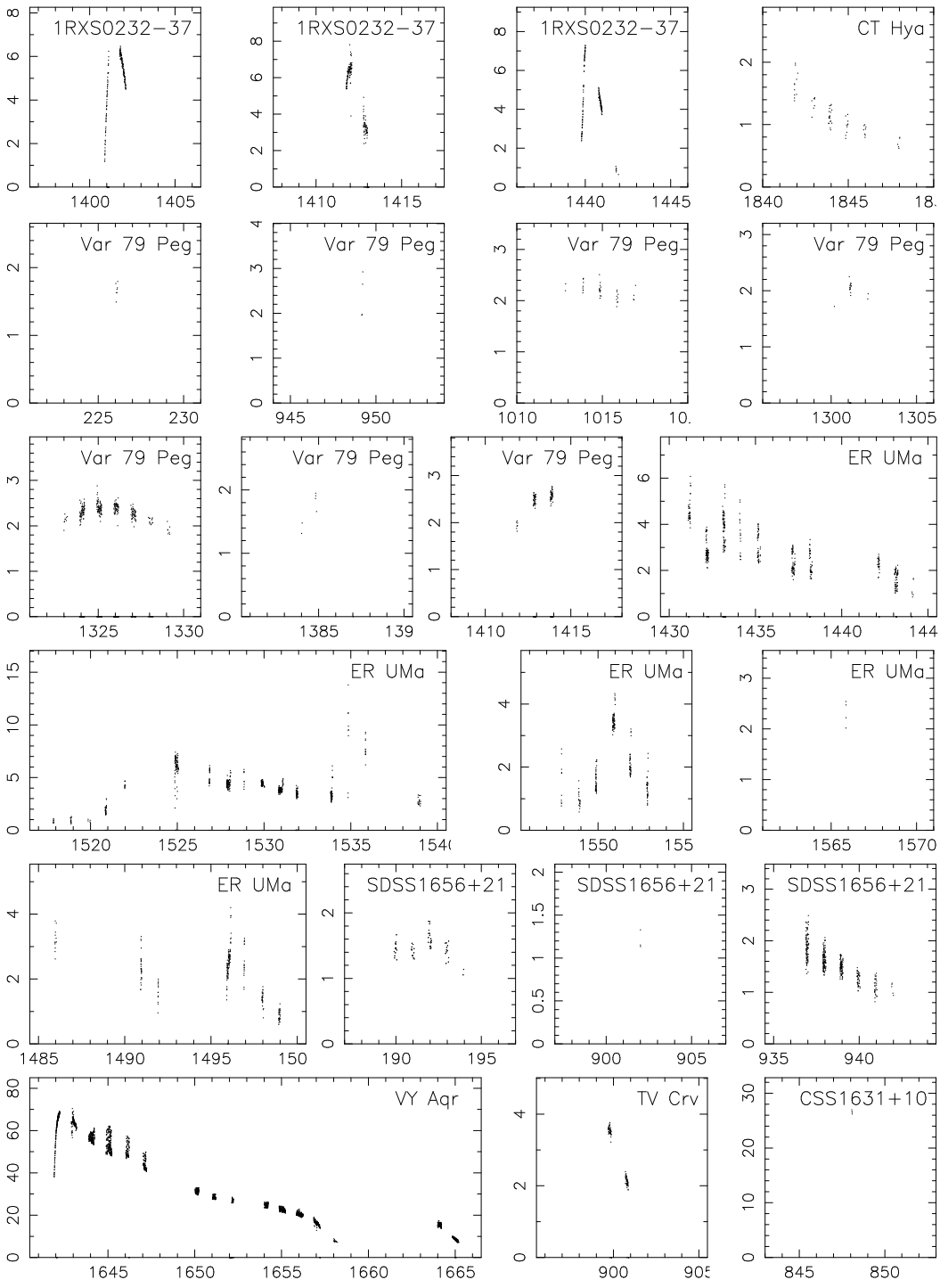

Figure A.1 vi (continued): Light curves of known CVs detected in WASP. Time in days after JD 2453005.5 is plotted on the x-axis. Flux is plotted on the y-axis in WASP flux units.

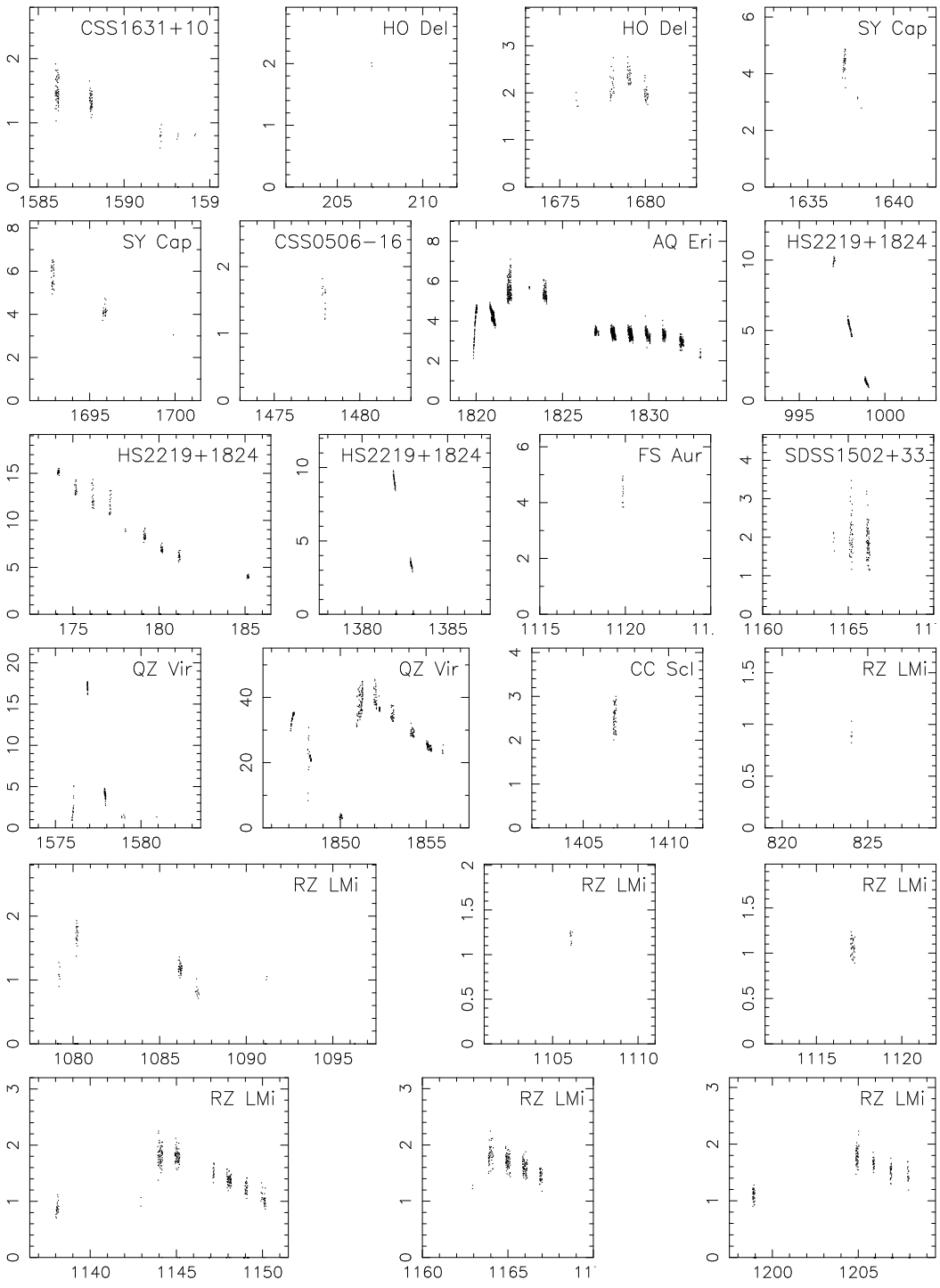

Figure A.1 vii (continued): Light curves of known CVs detected in WASP. Time in days after JD 2453005.5 is plotted on the x-axis. Flux is plotted on the y-axis in WASP flux units.

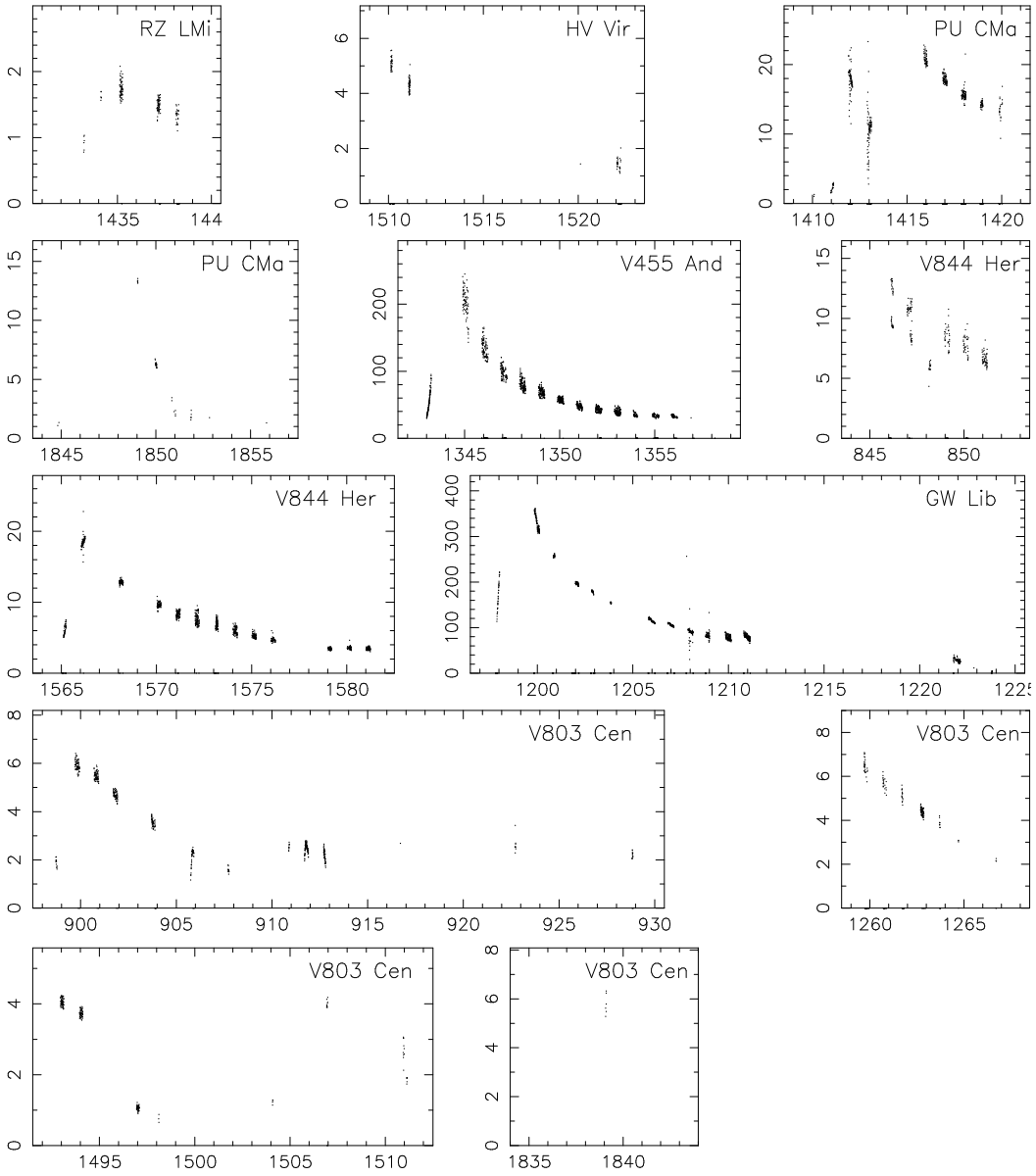

Figure A.1 viii (continued): Light curves of known CVs detected in WASP. Time in days after JD 2453005.5 is plotted on the x-axis. Flux is plotted on the y-axis in WASP flux units.

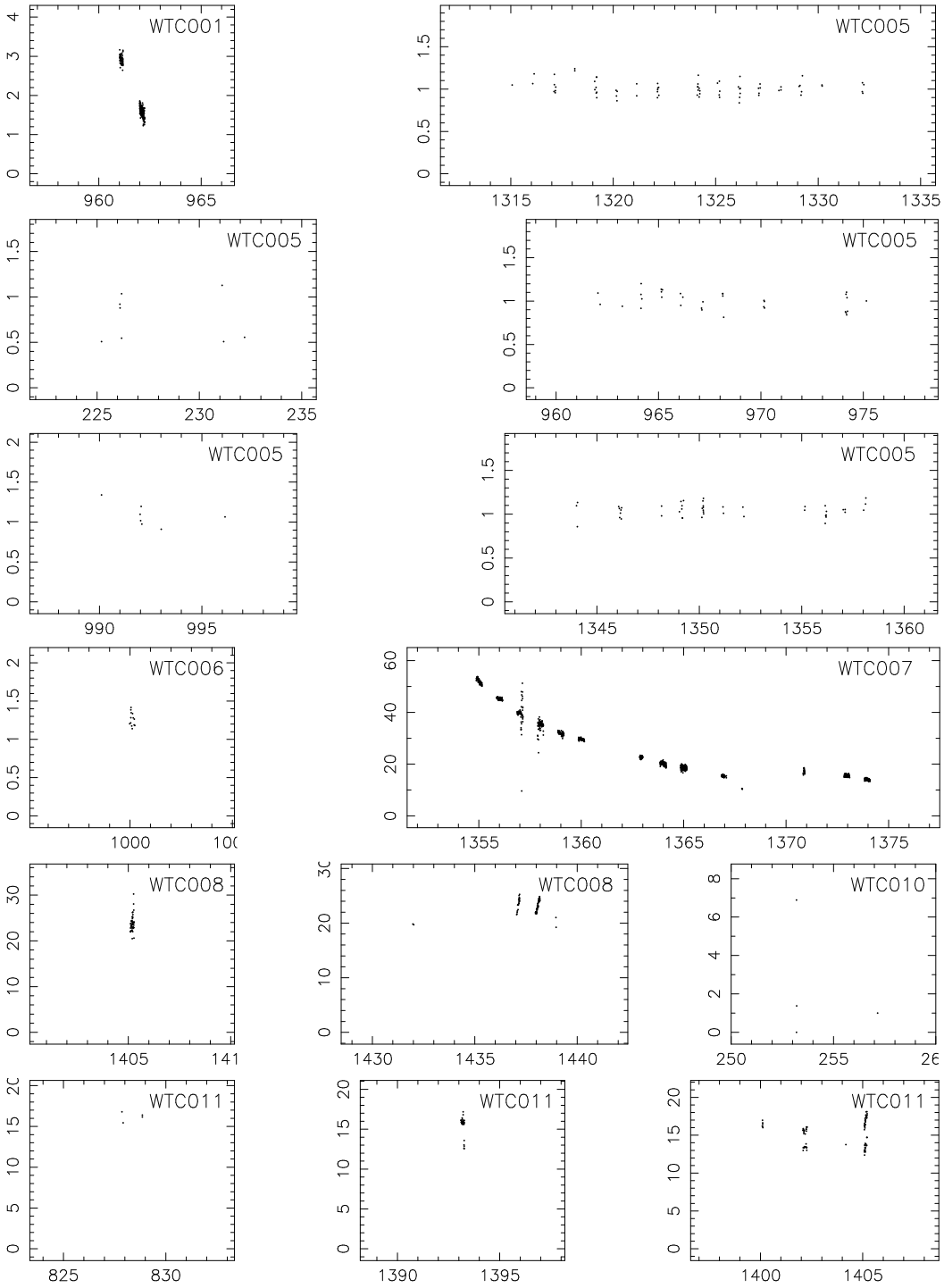

Figure A.2: Light curves of transient candidates found in the WASP data at the position of known X-ray sources. Time in days after JD 2453005.5 is plotted on the x-axis. Flux is plotted on the y-axis in WASP flux units.

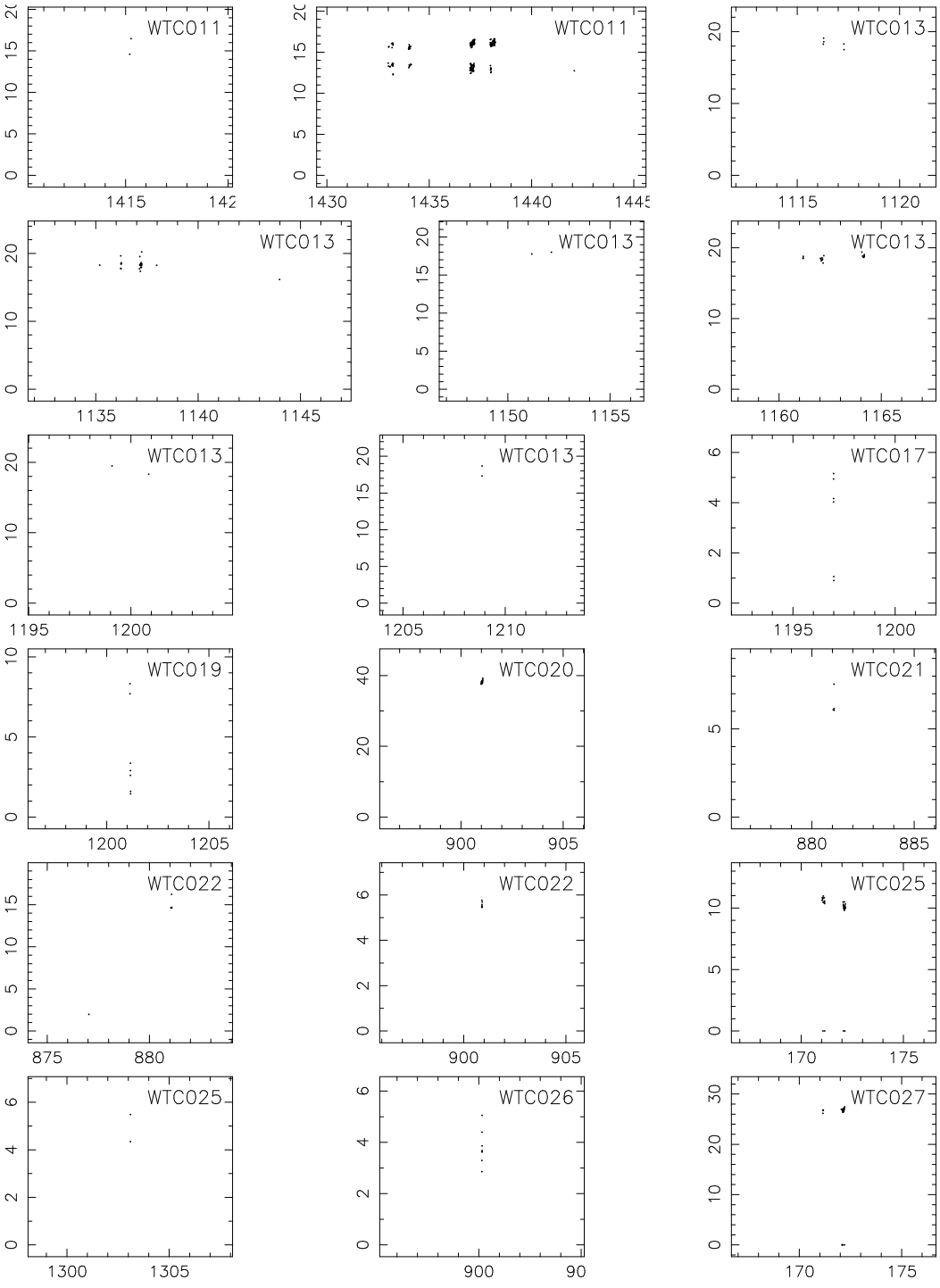

Figure A.2 continued: Light curves of transient candidates found in the WASP data at the position of known X-ray sources. Time in days after JD 2453005.5 is plotted on the x-axis. Flux is plotted on the y-axis in WASP flux units.

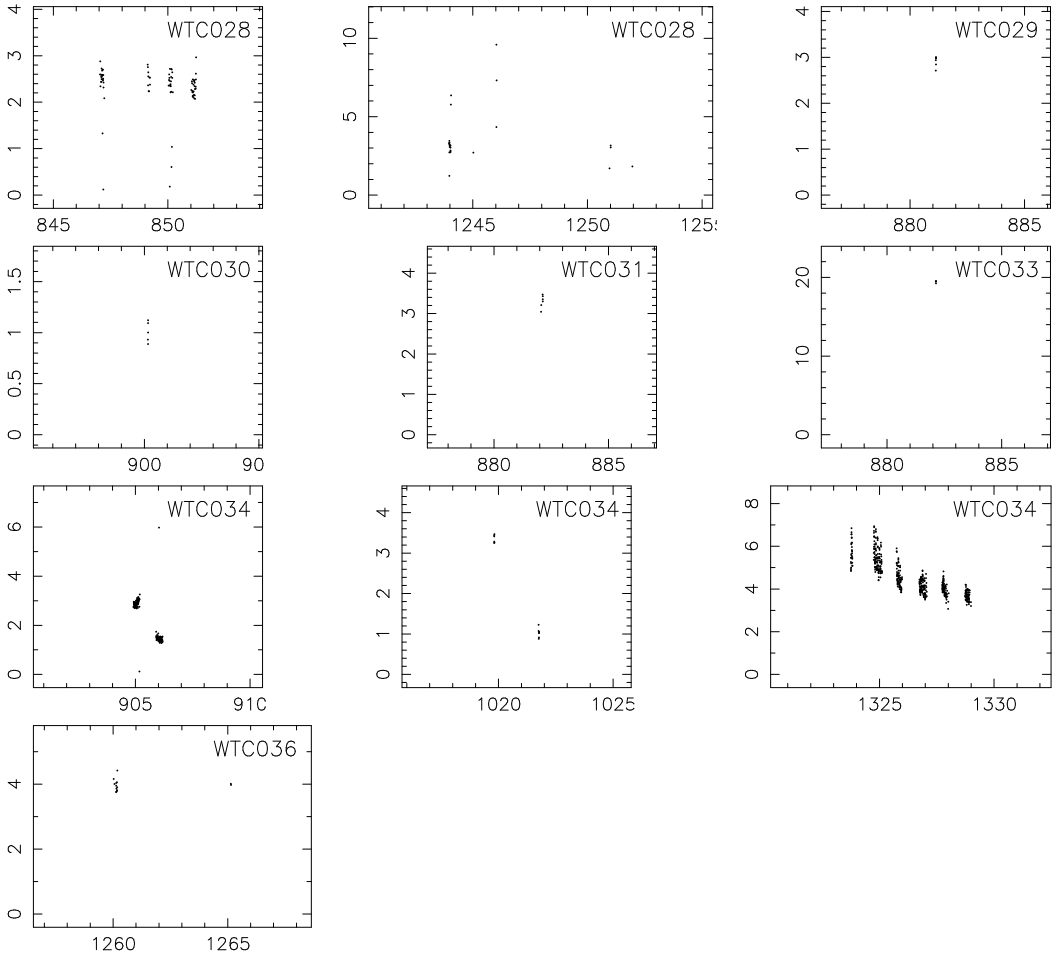

Figure A.2 continued: Light curves of transient candidates found in the WASP data at the position of known X-ray sources. Time in days after JD 2453005.5 is plotted on the x-axis. Flux is plotted on the y-axis in WASP flux units.

Appendix B

Transients Identified by the Untargeted Search

This appendix contain tables listing the WASP name, field, season of discovery, right ascension and declination of candidate transients discovered in Chapter 7. The candidates are divided into 4 tables, firstly cataclysmic variable stars (see Table B.1), next pulsating variable star candidates (see Table B.2), then flare star candidates (see Table B.3) and finally transient candidates where it was not possible to determine a classification (see Table B.4).

WASP name	WASP field	Season	Right Ascension	Declination	Period (min)	Magnitude	
						Quiescent	Outburst
WTC009	SW0517-4234_227	2006s	05 07 07.9	-41 46 27	83.4±0.1	19.2	12.8
WTC034	SW2112-2801_223	2007s	20 56 52.2	-30 14 39	108.9±0.1	15.6	12.5
WTC039*	SW0016+2410_142	2006n	00 13 47.6	+20 25 04		21.3	12.9
	SW0012+1734_146	2006n					
WTC041*	SW0045+3644_105	2004n	00 59 10.0	+34 38 33		21.0	12.8
WTC068*	SW2152+1042_147	2006n	21 39 12.7	+13 19 51		17.49	13.9
WTC090	SW2316+3126_103	2004n	23 05 46.2	+29 54 13		20.27	13.3
WTC095	SW2211+1035_146	2006n	21 58 15.2	+09 47 09		17.6	12.8
	SW2142+0827_143	2008n					
	SW2152+1042_147	2006n					
WTC102	SW0517-4234_227	2006s	05 11 37.9	-46 05 32		19.9	14.4
WTC103	SW0556-3537_222	2006s	05 41 18.9	-35 24 14		17.9	13.7
	SW0556-3537_222	2007s					
	SW0556-3533_222	2008s					
WTC109	SW1347-3523_221	2006s	13 59 15.2	-39 14 50	101.2±0.3	18.2	14.0
	SW1347-3523_221	2008s					
	SW1347-3523_221	2007s					
	SW1347-4234_227	2006s					
WTC111	SW1426-3537_222	2008s	14 31 45.1	-35 52 07		17.5	12.7
	SW1426-3537_222	2007s					
	SW1426-3537_222	2006s					

Table B.1: A table showing the candidate cataclysmic variable stars identified by the untargeted search algorithm. Candidates marked with a * were confirmed spectroscopically. Quiescent magnitudes were taken from the blue magnitudes of corresponding stars in USNO-B.

WASP name	WASP field	Season	Right Ascension	Declination	Period (min)	Magnitude	
						Quiescent	Outburst
WTC112	SW1426-3537_222	2006s	14 32 11.0	-35 12 43		16.3	13.9
WTC125	SW2229-2032_226	2006s	22 42 58.0	-19 45 51	136.3±0.3	19.1	13.7
WTC126	SW2301-3523_221	2006s	22 47 39.7	-36 22 53	87.7±0.1	20.7	10.6
WTC137	SW0524+5221_145	2007n	05 15 29.0	+56 05 34		18.3	13.5
WTC144	SW1339+4623_148	2007n	13 37 21.3	+48 01 19	80±0.1	20.7	13.6
WTC150	SW1720+3947_142	2007n	17 40 33.3	+41 47 53		19.7	12.3
WTC151	SW1835+5520_148 SW1833+4730_143	2007n 2007n	18 20 30.2	+51 44 45	134.6±0.1	19.7	13.3
WTC152	SW1824+5221_145	2007n	18 34 54.5	+54 48 26		20.3	13.9
WTC157	SW0017-2822_224	2007s	00 27 41.3	-24 39 45		18.6	14.3
WTC158	SW0212-2801_223	2007s	02 21 37.8	-26 19 51	90.5±0.4	20.0	14.0
WTC166	SW0402-3523_221	2007s	04 04 24.7	-32 42 12		19.8	14.1
WTC169	SW0556-3537_222	2007s	05 57 21.9	-36 30 57		20.3	13.4
WTC173	SW1000-2026_225 SW0929-2032_226 SW0929-2032_226	2008s 2008s 2007s	09 45 51.3	-19 43 58		17.4	14.0
WTC175	SW1002-3523_221	2007s	10 01 31.9	-33 02 35	131.2±0.2	16.1	13.1
WTC177	SW1002-4234_227	2007s	10 11 25.7	-40 24 35		19.9	12.6
WTC179	SW1044-2032_226	2007s	10 49 25.9	-21 47 36	539.7±0.6	17.6	13.3
WTC180	SW1117-4234_227	2007s	10 58 43.5	-43 32 33		19.1	14.5
WTC181	SW1230-2026_225	2007s	12 32 12.2	-24 07 53		20.1	14.4

Table B.1 continued: A table showing the candidate cataclysmic variable stars identified by the untargeted search algorithm. Quiescent magnitudes were taken from the blue magnitudes of corresponding stars in USNO-B.

WASP name	WASP field	Season	Right Ascension	Declination	Period (min)	Magnitude	
						Quiescent	Outburst
WTC182	SW1231-3523_221	2008s	12 45 07.3	-38 13 25	120.1±0.7	17.9	13.1
	SW1232-4234_227	2008s			119.9±0.1		
	SW1231-3523_221	2007s			119.0±1.3		
WTC198	SW1920-2801_223	2007s	19 06 21.6	-28 51 06	95.0±0.2	17.5	13.2
WTC204	SW2344-2032_226	2007s	23 33 59.9	-17 59 55		20.6	12.7
WTC257	SW0446-1858_228	2008s	04 49 02.7	-18 41 30		17.7	14.7
WTC282	SW1157-2801_223	2008s	12 02 57.1	-24 50 54		18.9	14.3
WTC287	SW1347-3523_221	2008s	13 45 18.7	-36 30 15		19.1	14.0
WTC311	SW2140-6557_227	2008s	21 12 12.9	-66 38 03		19.0	13.8
WTC313	SW2117-1814_227	2008s	21 32 03.1	-19 36 57	134.6±0.1	18.8	13.8
	SW2145-1859_228	2008s			134.5±0.1		
WTC322	SW1044-2032_226	2007s	10 57 50.0	-21 56 58	107.7±0.1	18.5	13.4

Table B.1 continued: A table showing the candidate cataclysmic variable stars identified by the untargeted search algorithm. Quiescent magnitudes were taken from the blue magnitudes of corresponding stars in USNO-B.

WASP name	WASP field	Season	Right Ascension	Declination
WTC073	SW0344+3944_105	2004n	03 51 57.9	+39 09 44
WTC074	SW0343+3126_102	2004n	03 52 36.5	+33 55 52
WTC075	SW0417+2326_104	2004n	04 31 20.7	+26 58 45
WTC076	SW0516+3126_103	2004n	05 05 26.5	+31 29 47
WTC077	SW0517+2326_104	2004n	05 24 28.0	+21 25 13
WTC078	SW0516+3126_103	2004n	05 26 32.9	+35 11 31
WTC079	SW0538+3135_143	2006n	05 48 07.9	+32 48 57
	SW0543+3126_102	2004n		
WTC080	SW0543+3126_102	2004n	05 49 05.0	+32 24 51
WTC082	SW1444+3944_105	2004n	15 04 55.2	+35 47 53
WTC086	SW2046+2445_105	2004n	20 30 46.5	+26 00 39
WTC087	SW2045+1628_102	2004n	20 44 10.2	+20 22 49
WTC089	SW2114+1628_103	2004n	21 22 03.6	+19 52 50
WTC099	SW0520+4007_142	2007n	05 27 47.7	+43 24 22
	SW0541+3924_148	2006n		
WTC100	SW1722+3000_144	2006n	17 28 55.4	+32 30 53
WTC104	SW0926-3537_222	2006s	09 09 23.2	-39 13 25
	SW0926-3537_222	2007s		
	SW0925-4259_228	2006s		
WTC105	SW0925-4259_228	2006s	09 29 20.4	-42 01 54
WTC106	SW1002-4234_227	2006s	10 13 20.7	-43 33 04
	SW1002-4234_227	2007s		
WTC108	SW1347-3523_221	2006s	13 57 30.3	-35 53 56
	SW1347-3523_221	2008s		
	SW1347-3523_221	2007s		
WTC110	SW1426-3537_222	2006s	14 11 30.2	-38 51 48
	SW1426-3537_222	2008s		
WTC113	SW1502-4234_227	2007s	15 15 33.1	-46 28 26
	SW1502-4234_227	2006s		
WTC114	SW1541-3537_222	2008s	15 36 45.6	-31 12 12
	SW1542-2801_223	2006s		
	SW1542-2801_223	2008s		
WTC115	SW1541-3537_222	2006s	15 47 28.7	-32 25 44
WTC116	SW1541-3537_222	2006s	15 52 22.4	-35 19 04
WTC117	SW1617-3523_221	2007s	16 09 39.8	-35 02 02
	SW1617-3523_221	2006s		

Table B.2: A table showing the candidate pulsating variable stars identified by the untargeted search algorithm.

WASP name	WASP field	Season	Right Ascension	Declination
WTC119	SW1617-3523_221	2006s	16 26 26.1	-34 35 55
WTC120	SW1920-2801_223	2006s	19 15 48.3	-29 46 31
	SW1920-2801_223	2007s		
WTC121	SW1918-3537_222	2006s	19 36 42.8	-34 33 28
	SW1954-3523_221	2006s		
WTC124	SW2229-2032_226	2006s	22 31 45.1	-23 32 46
	SW2229-2032_226	2007s		
WTC132	SW0233+4730_143	2007n	02 52 22.7	+48 39 52
WTC136	SW0524+5221_145	2007n	05 12 25.3	+49 12 02
WTC153	SW2138+4028_141	2007n	21 41 55.0	+42 45 07
WTC154	SW2335+5520_148	2007n	23 23 09.2	+52 50 13
WTC172	SW0925-4259_228	2007s	09 37 43.1	-43 22 51
WTC174	SW1002-2822_224	2008s	09 46 47.1	-28 41 18
	SW0927-2801_223	2008s		
	SW0927-2801_223	2007s		
WTC189	SW1502-3523_221	2008s	15 11 18.7	-39 04 00
	SW1502-3523_221	2007s		
	SW1502-4234_227	2007s		
	SW1502-4234_227	2008s		
WTC191	SW1617-3523_221	2008s	16 10 20.1	-35 45 11
	SW1617-3523_221	2007s		
WTC192	SW1615-2026_225	2007s	16 12 20.8	-19 49 54
	SW1615-2026_225	2008s		
WTC193	SW1617-2822_224	2008s	16 24 21.6	-32 01 56
	SW1617-2822_224	2007s		
	SW1617-3523_221	2008s		
	SW1617-3523_221	2007s		
WTC194	SW1617-2822_224	2007s	16 26 41.9	-29 57 19
WTC195	SW1617-3523_221	2007s	16 30 27.3	-35 15 31
WTC196	SW1617-3523_221	2008s	16 34 36.1	-38 49 03
	SW1617-3523_221	2007s		
WTC197	SW1617-3523_221	2007s	16 35 38.6	-34 54 02
WTC199	SW1954-3523_221	2007s	19 36 15.7	-34 31 10
	SW1954-3523_221	2008s		
WTC208	SW0148+0558_143	2008n	02 00 56.0	+09 45 33
	SW0146+1313_148	2008n		

Table B.2 continued: A table showing the candidate pulsating variable stars identified by the untargeted search algorithm.

WASP name	WASP field	Season	Right Ascension	Declination
WTC213	SW0520+1409_145	2008n	05 12 23.5	+12 50 32
WTC227	SW1441+0129_141	2008n	14 29 21.2	+01 27 11
WTC249	SW0316+0312_225	2008s	03 08 17.3	+05 50 18
WTC255	SW0447+0314_226	2008s	04 33 16.8	+07 40 53
WTC271	SW0637-4438_225	2008s	07 03 35.2	-40 47 46
WTC273	SW1040-4259_228	2008s	10 22 56.6	-44 11 38
WTC275	SW1040-4259_228	2008s	10 55 14.9	-46 42 28
WTC280	SW1117-4234_227	2008s	11 32 29.2	-45 57 03
WTC288	SW1345-1858_228	2008s	13 47 19.8	-17 53 54
WTC290	SW1429-2032_226	2008s	14 37 29.1	-20 19 42
WTC298	SW1617-2822_224	2008s	16 05 57.1	-27 47 32
WTC303	SW1617-2822_224	2008s	16 24 20.2	-28 37 03
WTC304	SW1617-3523_221	2008s	16 25 59.1	-37 25 37
WTC305	SW1617-2822_224	2008s	16 26 30.4	-29 07 31
WTC306	SW1617-1815_227	2008s	16 28 32.2	-19 59 40
WTC307	SW1617-3523_221	2008s	16 33 53.6	-33 56 14

Table B.2 continued: A table showing the candidate pulsating variable stars identified by the untargeted search algorithm.

WASP name	WASP field	Season	Right Ascension	Declination
WTC017	SW1317+2350_142	2007n	13 23 53.9	+26 51 19
WTC019	SW1420+4323_145	2007n	14 29 03.4	+46 45 35
WTC040	SW0044+2127_101	2004n	00 37 40.6	+19 43 39
WTC045	SW0212+1734_146	2006n	01 58 15.7	+18 07 13
WTC051	SW0244+2427_101	2004n	02 53 20.7	+27 13 37
WTC057	SW0342+2432_141	2006n	03 41 25.7	+23 15 34
WTC066	SW2052+0236_147	2006n	20 55 18.3	+02 37 40
WTC084	SW1744+3944_105	2004n	17 47 37.9	+36 52 22
WTC088	SW2115+0828_104	2004n	21 03 59.7	+12 18 56
WTC091	SW0238+3135_143	2006n	02 58 46.9	+33 24 14
WTC093	SW2211+1035_146	2006n	22 06 19.1	+09 34 07
WTC096	SW0618+3625_145	2006n	06 34 17.1	+39 00 12
	SW0641+3924_148	2006n		
WTC097	SW0018+3625_145	2006n	00 38 00.8	+40 26 21
WTC098	SW2221+2302_144	2006n	22 30 44.1	+22 45 46
WTC101	SW0444-2032_226	2006s	04 38 43.6	-24 43 39
WTC122	SW2030-2026_225	2006s	20 34 48.1	-20 44 39
WTC123	SW2229-2032_226	2006s	22 24 57.7	-22 49 45
WTC127	SW2300-2026_225	2006s	22 53 49.7	-17 21 31
WTC128	SW2302-2822_224	2006s	23 14 21.7	-30 13 23
WTC130	SW2340-4259_228	2006s	23 58 15.4	-39 35 33
	SW0017-4234_227	2006s		
WTC133	SW0324+5221_145	2007n	03 41 42.5	+51 44 50
WTC134	SW0414+3332_146	2007n	04 17 40.5	+31 57 33
WTC135	SW0514+3332_146	2007n	05 07 14.2	+37 30 40
WTC139	SW0918+3625_145	2007n	09 01 28.8	+38 32 58
WTC140	SW1038+3135_143	2007n	10 54 28.9	+35 16 38
WTC141	SW1118+3625_145	2007n	11 18 04.9	+36 41 55
WTC142	SW1122+3000_144	2007n	11 22 53.9	+32 41 26
WTC143	SW1138+3134_143	2007n	11 29 39.2	+31 39 45
WTC145	SW1341+3117_141	2007n	13 52 08.8	+29 53 16
WTC146	SW1518+3625_145	2007n	15 24 36.0	+35 25 53
WTC147	SW1633+4730_143	2007n	17 00 10.3	+43 50 28
WTC148	SW1728+4555_144	2007n	17 16 53.7	+43 45 52
WTC149	SW1720+3947_142	2007n	17 28 10.1	+39 39 38

Table B.3: A table showing the candidate flare stars identified by the untargeted search algorithm.

WASP name	WASP field	Season	Right Ascension	Declination
WTC156	SW0017-2822_224	2007s	00 21 18.0	-31 43 25
	SW0017-3523_221	2007s		
WTC160	SW0247-3523_221	2007s	02 30 26.4	-34 26 03
WTC161	SW0247-3523_221	2007s	02 37 51.0	-35 34 53
WTC162	SW0247-3523_221	2007s	03 02 28.0	-32 57 02
WTC163	SW0326-3537_222	2007s	03 32 08.3	-34 13 16
WTC164	SW0329-2032_226	2007s	03 39 38.3	-23 48 17
WTC167	SW0517-2822_224	2007s	05 19 25.9	-28 11 07
WTC170	SW0556-3537_222	2007s	06 10 41.2	-34 11 08
WTC171	SW0632-3523_221	2007s	06 19 03.6	-32 06 31
WTC176	SW1002-2822_224	2007s	10 07 59.4	-27 44 44
WTC178	SW1044-2032_226	2007s	10 48 19.8	-22 50 11
WTC183	SW1312-2801_223	2007s	13 19 19.6	-27 09 48
WTC185	SW1426-3537_222	2007s	14 35 25.8	-38 42 21
WTC186	SW1502-3523_221	2007s	14 54 04.1	-36 06 12
WTC187	SW1502-3523_221	2007s	14 54 49.1	-36 27 48
WTC188	SW1500-2026_225	2007s	15 10 11.5	-20 12 41
WTC190	SW1541-3537_222	2007s	15 53 43.9	-32 12 35
WTC200	SW2032-2822_224	2007s	20 24 07.4	-27 36 55
WTC201	SW2147-3523_221	2007s	22 00 22.6	-34 27 38
WTC202	SW2229-2032_226	2007s	22 23 43.0	-19 26 48
WTC203	SW2302-4234_227	2007s	22 50 26.8	-43 16 13
WTC205	SW2344-2032_226	2007s	23 38 42.6	-20 29 37
WTC206	SW2344-2032_226	2007s	23 48 03.0	-22 31 31
WTC207	SW0120+1409_145	2008n	01 04 28.3	+13 37 15
WTC209	SW0418+0759_144	2008n	04 19 53.5	+06 17 22
WTC210	SW0456-1016_147	2008n	04 53 27.5	-12 49 28
WTC211	SW0520+1409_145	2008n	05 09 26.2	+17 24 23
WTC212	SW0517+0028_142	2008n	05 10 08.3	+00 46 33
	SW0516+0312_225	2008s		
WTC214	SW0508-0745_146	2008n	05 22 10.7	-03 36 55
WTC215	SW0517+0028_142	2008n	05 27 44.2	+00 07 16
	SW0516+0312_225	2008s		
WTC216	SW0517-0028_142	2008n	05 31 12.0	-01 50 56
WTC218	SW0733+4730_143	2008n	07 40 34.7	+44 18 35

Table B.3 continued: A table showing the candidate flare stars identified by the untargeted search algorithm.

WASP name	WASP field	Season	Right Ascension	Declination
WTC219	SW0733+4730_143	2008n	07 44 45.0	+50 17 21
	SW0724+5221_145	2008n		
WTC220	SW0831+5229_145	2008n	08 20 54.8	+54 22 18
WTC221	SW0824+5221_145	2008n	08 44 12.6	+50 28 36
WTC222	SW0922+3920_142	2008n	09 22 09.3	+40 55 33
WTC225	SW1117-0028_142	2008n	11 29 31.1	-02 44 09
WTC226	SW1208-0745_146	2008n	12 22 48.8	-02 05 37
WTC228	SW1735+4020_141	2008n	17 25 08.5	+42 30 24
	SW1722+3937_142	2008n		
WTC229	SW1725+5456_148	2008n	17 29 05.1	+58 58 36
WTC230	SW1725+5456_148	2008n	17 29 44.9	+56 31 39
	SW1731+5229_145	2008n		
WTC231	SW1734+4719_143	2008n	17 50 12.9	+44 24 03
WTC232	SW1901+5318_143	2008n	18 52 16.5	+52 57 15
	SW1831+5229_145	2008n		
WTC233	SW1901+5318_143	2008n	19 15 40.7	+54 47 11
WTC234	SW1901+5318_143	2008n	19 20 26.6	+49 50 51
WTC235	SW2119+1342_145	2008n	21 08 26.2	+10 46 40
WTC236	SW2139+1610_148	2008n	22 02 15.0	+20 36 07
WTC237	SW2245-0345_223	2008s	22 50 33.6	-05 59 26
	SW2256-1017_147	2008n		
WTC238	SW2341+0129_141	2008n	23 32 43.8	+01 33 20
	SW2347+0314_226	2008s		
WTC239	SW0017-1814_227	2008s	00 13 48.6	-18 43 02
WTC240	SW0017-0452_224	2008s	00 14 33.9	-05 11 23
WTC241	SW0015+0312_225	2008s	00 22 47.6	+05 57 13
WTC242	SW0044-1138_222	2008s	00 45 59.0	-07 37 32
WTC243	SW0045-1858_228	2008s	00 48 21.1	-17 40 49
WTC244	SW0047+0313_226	2008s	00 58 47.8	+01 10 15
WTC245	SW0045-0345_223	2008s	00 58 59.9	-00 18 02
WTC246	SW0114-1205_221	2008s	01 03 21.0	-08 34 30
WTC247	SW0217-0453_224	2008s	02 05 04.3	-06 53 27
WTC248	SW0247+0314_226	2008s	02 51 54.6	+07 03 08
WTC250	SW0317-0453_224	2008s	03 28 20.0	-07 46 57
	SW0314-1206_221	2008s		
	SW0344-1137_222	2008s		

Table B.3 continued: A table showing the candidate flare stars identified by the untargeted search algorithm.

WASP name	WASP field	Season	Right Ascension	Declination
WTC252	SW0417-1814_227	2008s	04 14 22.1	-19 10 21
WTC253	SW0414-1205_221	2008s	04 17 18.1	-08 02 53
WTC254	SW0415+0312_225	2008s	04 28 10.8	+04 03 33
WTC256	SW0444-1137_222	2008s	04 40 05.6	-09 41 16
WTC258	SW0445-2842_226	2008s	04 53 37.7	-28 35 31
WTC259	SW0446-1858_228	2008s	04 54 48.8	-18 38 47
WTC260	SW0438-5053_228	2008s	04 54 53.1	-47 47 12
WTC261	SW0517-1814_227	2008s	05 09 11.5	-19 53 47
WTC262	SW0545-5926_222	2008s	05 22 21.0	-57 54 50
WTC263	SW0517-1814_227	2008s	05 32 26.4	-14 30 56
WTC266	SW0643-5954_221	2008s	06 30 00.6	-57 07 59
WTC267	SW0637-4438_225	2008s	06 30 57.4	-46 31 09
WTC268	SW0637-4438_225	2008s	06 33 00.5	-47 32 12
WTC269	SW0643-5954_221	2008s	06 37 36.2	-56 06 59
WTC270	SW0637-4438_225	2008s	07 02 36.6	-43 26 58
WTC272	SW1000-2026_225	2008s	10 06 03.6	-20 36 55
WTC274	SW1042-2801_223	2008s	10 52 00.8	-26 35 02
WTC277	SW1117-3523_221 SW1117-4234_227	2008s 2008s	11 09 49.9	-38 28 07
WTC279	SW1117-3523_221	2008s	11 30 18.9	-35 00 15
WTC281	SW1157-2801_223	2008s	11 50 27.9	-25 04 05
WTC283	SW1317-0453_224	2008s	13 19 56.3	-01 58 49
WTC284	SW1311-3537_222	2008s	13 21 09.7	-36 00 01
WTC286	SW1347-4234_227	2008s	13 40 01.6	-43 48 57
WTC289	SW1425-4259_228	2008s	14 21 55.2	-41 41 32
WTC292	SW1502-4234_227	2008s	14 42 51.5	-40 28 40
WTC293	SW1447+0314_226	2008s	14 52 42.6	+02 47 25
WTC295	SW1516+0312_225	2008s	15 05 37.2	+04 41 11
WTC296	SW1545-1859_228	2008s	15 31 08.0	-15 07 18
WTC299	SW1615-2026_225	2008s	16 06 51.9	-24 26 20
WTC300	SW1615-2026_225	2008s	16 08 46.1	-22 46 53
WTC301	SW1617-0453_224	2008s	16 10 19.9	-07 32 18
WTC302	SW1617-1815_227	2008s	16 13 06.4	-20 18 37
WTC308	SW1617-2822_224	2008s	16 34 35.0	-26 58 03
WTC309	SW2041-4441_226	2008s	20 48 56.9	-41 02 04
WTC310	SW2045-1858_228	2008s	20 55 08.7	-15 03 33

Table B.3 continued: A table showing the candidate flare stars identified by the untargeted search algorithm.

WASP name	WASP field	Season	Right Ascension	Declination
WTC312	SW2129-5240_224	2008s	21 30 09.3	-55 02 53
WTC314	SW2145-0345_223	2008s	21 55 17.4	-00 45 51
WTC315	SW2129-5240_224	2008s	21 56 56.9	-53 06 19
WTC316	SW2245-1858_228	2008s	22 29 17.7	-15 42 31
WTC317	SW2247+0314_226	2008s	22 33 16.0	+06 05 36
WTC318	SW2245-0345_223	2008s	22 35 26.7	-01 44 11
WTC319	SW2247+0314_226	2008s	22 51 24.5	+03 29 33
WTC320	SW2347+0314_226	2008s	23 31 52.2	+03 30 23

Table B.3 continued: A table showing the candidate flare stars identified by the untargeted search algorithm.

WASP name	WASP field	Season	Right Ascension	Declination
WTC028	SW1731+5229_145	2008n	17 48 27.8	+50 50 39
WTC064	SW0541+3924_148	2006n	05 38 07.5	+36 03 41
WTC072	SW0217+2326_104	2004n	02 06 28.8	+23 02 35
WTC081	SW1342+4642_105	2004n	13 37 25.1	+43 11 20
WTC083	SW1741+4024_101	2004n	17 27 57.9	+38 00 20
	SW1722+3937_142	2008n		
WTC085	SW1739+4723_102	2004n	18 02 22.6	+45 52 46
WTC092	SW0642+2432_141	2006n	06 32 12.9	+50 50 38
WTC094	SW0039+2836_143	2006n	00 56 18.6	+36 03 41
WTC107	SW1347-4234_227	2006s	13 41 48.3	+23 02 34
WTC118	SW1617-3523_221	2006s	16 09 48.8	+43 11 19
	SW1617-3523_221	2008s		
	SW1617-3523_221	2007s		
WTC129	SW2341-3537_222	2006s	23 28 28.8	+45 52 46
WTC131	SW0028+4554_144	2007n	00 16 49.7	+25 36 21
WTC138	SW0624+5221_145	2007n	06 21 49.6	+28 48 20
WTC155	SW2333+4730_143	2007n	23 57 13.4	-44 55 00
WTC159	SW0247-4234_227	2007s	02 28 14.4	-39 11 13
WTC165	SW0402-2822_224	2007s	03 43 09.4	-39 11 16
WTC168	SW0517-3523_221	2007s	05 25 58.3	-39 11 16
WTC184	SW1347-3523_221	2007s	14 00 40.9	-34 10 05
WTC217	SW0733+4730_143	2008n	07 34 42.7	+45 15 41
WTC223	SW0914+3332_146	2008n	09 29 12.7	+37 44 11
WTC224	SW0931+5229_145	2008n	09 54 52.3	+55 35 37
WTC251	SW0417-0452_224	2008s	03 59 58.8	-05 12 36
	SW0345-0345_223	2008s		
WTC264	SW0525-5006_227	2008s	05 32 36.5	-50 13 03
WTC265	SW0557-4439_226	2008s	06 15 33.3	-46 36 08
WTC276	SW1041-3537_222	2008s	10 56 39.2	-31 22 07
WTC278	SW1117-3523_221	2008s	11 28 15.2	-34 48 08
WTC285	SW1314-2032_226	2008s	13 24 40.1	-19 51 26
WTC291	SW1426-3537_222	2008s	14 39 15.5	-35 27 10
WTC294	SW1447+0314_226	2008s	14 57 44.1	+01 05 07
WTC297	SW1617-0453_224	2008s	16 03 03.3	-05 07 18
WTC321	SW2347+0314_226	2008s	23 38 34.0	+06 24 54

Table B.4: A table showing the candidate transients of uncertain type identified by the untargeted search algorithm.

WASP name	Amplitude (V-band)	Effective temp (K)	Distance (pc)	Peak power ($ergs^{-1}$)	Total energy (erg)
WTC017	4.75	2807	26	1.37×10^{30}	4.86×10^{32}
WTC019	3.25	3189	35	3.90×10^{30}	3.49×10^{33}
WTC040	3.09	3424	168	1.64×10^{31}	2.29×10^{34}
WTC051	6.02	2824	28	4.85×10^{30}	1.34×10^{33}
WTC084	3.85	2872	19	9.02×10^{29}	4.67×10^{32}
WTC088	2.65	3302	45	4.74×10^{30}	4.77×10^{33}
WTC091	3.72	3264	49	9.77×10^{30}	9.31×10^{33}
WTC093	3.55	2851	29	6.00×10^{29}	5.58×10^{32}
WTC096	3.94	3311	61	1.65×10^{31}	7.08×10^{33}
WTC097	2.75	3188	29	2.45×10^{30}	9.09×10^{32}
WTC098	3.83	3089	50	3.52×10^{30}	8.40×10^{32}
WTC101	2.32	5606	1956	4.93×10^{33}	1.58×10^{37}
WTC122	4.44	3344	148	3.28×10^{31}	1.54×10^{34}
WTC123	2.97	3637	233	6.29×10^{31}	6.85×10^{34}
WTC127	1.22	3169	26	5.26×10^{29}	3.92×10^{32}
WTC128	5.31	3158	72	2.11×10^{31}	1.22×10^{34}
WTC130	3.36	3044	31	1.72×10^{30}	1.47×10^{33}
	3.48	3044	31	1.93×10^{30}	1.61×10^{33}
WTC133	3.04	3153	36	2.54×10^{30}	3.22×10^{33}
WTC134	3.43	3304	64	9.80×10^{30}	2.41×10^{34}
WTC135	3.1	3058	14	1.48×10^{30}	8.85×10^{32}
WTC139	2.45	3432	87	9.65×10^{30}	5.97×10^{33}
WTC140	3.91	3081	26	3.61×10^{30}	1.55×10^{33}
WTC142	4.05	3263	40	1.32×10^{31}	4.88×10^{33}
WTC145	4.02	3168	82	6.94×10^{30}	2.89×10^{33}
WTC146	2.73	3211	55	2.77×10^{30}	1.58×10^{33}
WTC148	2.89	3432	145	1.45×10^{31}	1.45×10^{33}
WTC156	3.02	3418	89	1.48×10^{31}	3.55×10^{33}
	3.22	3418	89	1.78×10^{31}	5.69×10^{33}
WTC160	3.06	3023	37	1.14×10^{30}	3.84×10^{32}
WTC161	2.67	3441	60	1.27×10^{31}	7.05×10^{33}
WTC162	4.06	3183	28	7.92×10^{30}	2.30×10^{33}
WTC163	2.41	3216	40	2.14×10^{30}	2.05×10^{33}
WTC164	2.34	3153	52	1.34×10^{30}	5.43×10^{32}
WTC167	2.81	2942	23	5.40×10^{29}	2.81×10^{32}

Table B.5: A table listing the calculated properties of the candidate flare stars and the energies of the observed flares.

WASP name	Amplitude (V-band)	Effective temp (K)	Distance (pc)	Peak power ($ergs^{-1}$)	Total energy (erg)
WTC170	3.67	3484	194	4.54×10^{31}	3.93×10^{34}
WTC171	2.19	3185	45	1.43×10^{30}	2.20×10^{33}
WTC183	1.97	3234	37	1.60×10^{30}	5.31×10^{32}
WTC185	2.92	3011	23	9.30×10^{29}	6.31×10^{32}
WTC186	2.91	3011	17	9.21×10^{29}	1.59×10^{33}
WTC187	1.8	3550	66	1.31×10^{31}	1.09×10^{34}
WTC190	3.46	3195	38	4.92×10^{30}	4.58×10^{33}
WTC201	3.34	3853	522	2.06×10^{32}	9.45×10^{34}
WTC202	2.84	3152	40	2.09×10^{30}	9.68×10^{32}
WTC203	4.48	2895	47	1.86×10^{30}	2.11×10^{33}
WTC205	4.76	2882	33	2.21×10^{30}	1.66×10^{33}
WTC207	5.04	2829	39	2.05×10^{30}	3.09×10^{32}
WTC209	4.05	3027	43	2.92×10^{30}	3.13×10^{33}
WTC210	3.1	3146	50	2.57×10^{30}	1.26×10^{33}
WTC211	3.32	2985	19	1.15×10^{30}	5.17×10^{32}
WTC212	4.41	2998	33	3.38×10^{30}	2.63×10^{33}
WTC215	3.48	3437	168	2.59×10^{31}	1.14×10^{34}
	3.33	3437	168	2.26×10^{31}	8.25×10^{33}
WTC216	4.04	3105	64	4.75×10^{30}	4.82×10^{33}
WTC218	3.25	3349	103	1.12×10^{31}	7.24×10^{33}
WTC219	5.39	2943	38	5.86×10^{30}	4.94×10^{33}
	6.1	2943	38	1.13×10^{31}	6.55×10^{33}
WTC220	1.95	3469	106	8.22×10^{30}	5.24×10^{33}
WTC221	3.47	3209	62	5.43×10^{30}	3.04×10^{33}
WTC222	4.26	2813	28	9.01×10^{29}	1.37×10^{33}
WTC225	3.7	3334	66	1.54×10^{31}	6.44×10^{33}
WTC228	3.87	3223	47	8.54×10^{30}	4.19×10^{33}
	4.55	3223	47	1.60×10^{31}	8.19×10^{33}
WTC229	3.79	2984	46	1.75×10^{30}	4.97×10^{32}
WTC230	5.15	2880	36	3.12×10^{30}	1.28×10^{33}
WTC232	7.65	2463	29	1.94×10^{30}	4.17×10^{32}
WTC233	4.71	3350	95	4.40×10^{31}	2.18×10^{34}
WTC234	4.03	2919	36	1.44×10^{30}	1.48×10^{33}
WTC235	2.91	3292	35	5.58×10^{30}	1.75×10^{33}
WTC236	4.67	2908	16	2.43×10^{30}	7.32×10^{32}

Table B.5 continued: A table listing the calculated properties of the candidate flare stars and the energies of the observed flares.

WASP name	Amplitude (V-band)	Effective temp (K)	Distance (pc)	Peak power ($ergs^{-1}$)	Total energy (erg)
WTC237	3.33	3005	28	1.31×10^{30}	6.91×10^{32}
	3.38	3005	28	1.37×10^{30}	2.76×10^{32}
WTC238	3.88	3376	121	2.43×10^{31}	1.28×10^{34}
WTC239	2.96	3219	38	3.63×10^{30}	1.57×10^{33}
WTC240	4	3314	96	1.77×10^{31}	6.95×10^{33}
WTC241	2.78	2925	24	4.71×10^{29}	1.06×10^{33}
WTC242	5.7	2833	70	3.88×10^{30}	1.70×10^{33}
WTC244	2.64	3244	63	3.17×10^{30}	2.48×10^{33}
WTC245	2.62	3191	37	2.22×10^{30}	1.69×10^{33}
WTC246	2.97	3035	51	1.14×10^{30}	5.09×10^{32}
WTC248	3.55	2876	32	6.98×10^{29}	3.74×10^{32}
WTC250	4.14	2939	40	1.81×10^{30}	1.43×10^{33}
	4.37	2939	40	2.24×10^{30}	2.52×10^{33}
	4.39	2939	40	2.27×10^{30}	3.25×10^{33}
WTC252	3.03	3122	31	2.07×10^{30}	2.14×10^{33}
WTC253	3.12	3194	44	3.56×10^{30}	8.95×10^{32}
WTC254	3.08	3309	58	7.36×10^{30}	1.31×10^{34}
WTC256	1.95	3269	46	1.99×10^{30}	8.26×10^{32}
WTC258	3.85	3067	11	3.13×10^{30}	1.97×10^{33}
WTC259	2.36	3335	56	4.52×10^{30}	9.66×10^{32}
WTC260	4.31	3063	73	4.66×10^{30}	1.09×10^{33}
WTC261	2.6	3278	46	3.84×10^{30}	1.47×10^{33}
WTC262	5.18	3089	52	1.23×10^{31}	6.47×10^{33}
WTC263	2.22	3266	43	2.50×10^{30}	1.92×10^{33}
WTC266	4.8	3405	146	6.99×10^{31}	3.94×10^{34}
WTC267	3.17	3138	51	2.61×10^{30}	3.17×10^{32}
WTC268	6.54	2739	50	4.49×10^{30}	8.72×10^{32}
WTC269	3.25	3317	46	9.07×10^{30}	2.91×10^{33}
WTC272	2.8	3259	36	4.05×10^{30}	1.86×10^{33}
WTC277	2.84	3435	43	1.42×10^{31}	2.77×10^{34}
	2.83	3435	43	1.40×10^{31}	2.79×10^{34}
WTC283	2.25	3383	66	5.70×10^{30}	4.21×10^{33}
WTC284	4.55	2915	29	2.26×10^{30}	5.39×10^{32}
WTC286	3.59	3203	18	5.80×10^{30}	3.00×10^{33}
WTC289	2.51	3369	33	6.57×10^{30}	4.06×10^{33}

Table B.5 continued: A table listing the calculated properties of the candidate flare stars and the energies of the observed flares.

WASP name	Amplitude (V-band)	Effective temp (K)	Distance (pc)	Peak power ($ergs^{-1}$)	Total energy (erg)
WTC292	1.46	3992	132	5.66×10^{31}	1.41×10^{34}
WTC293	3.94	3079	41	3.66×10^{30}	6.79×10^{32}
WTC295	6.16	2822	81	5.50×10^{30}	4.18×10^{33}
WTC296	4.24	3572	582	1.40×10^{32}	1.60×10^{34}
WTC299	3.15	3416	46	1.64×10^{31}	1.18×10^{34}
WTC300	2.67	3307	47	5.00×10^{30}	2.79×10^{33}
WTC301	2.39	3128	36	1.19×10^{30}	1.01×10^{33}
WTC308	2.79	2980	21	6.74×10^{29}	6.27×10^{32}
WTC314	2.73	3157	24	1.96×10^{30}	7.95×10^{32}
WTC315	2.97	3238	71	4.12×10^{30}	1.75×10^{33}
WTC318	2.18	3256	32	2.25×10^{30}	1.57×10^{33}
WTC320	3.94	3106	67	4.36×10^{30}	4.57×10^{33}

Table B.5 continued: A table listing the calculated properties of the candidate flare stars and the energies of the observed flares.

Appendix C

Light Curves of Candidate Transients Identified by the Unargeted Search

This appendix contains light curves of the candidate dwarf novae, pulsating variables and flares discovered in the orphans data as described in Chapter 7. The data plotted is from the orphans database only (some of the pulsating variable star candidates have detections in the main WASP archive as well as in the orphans).

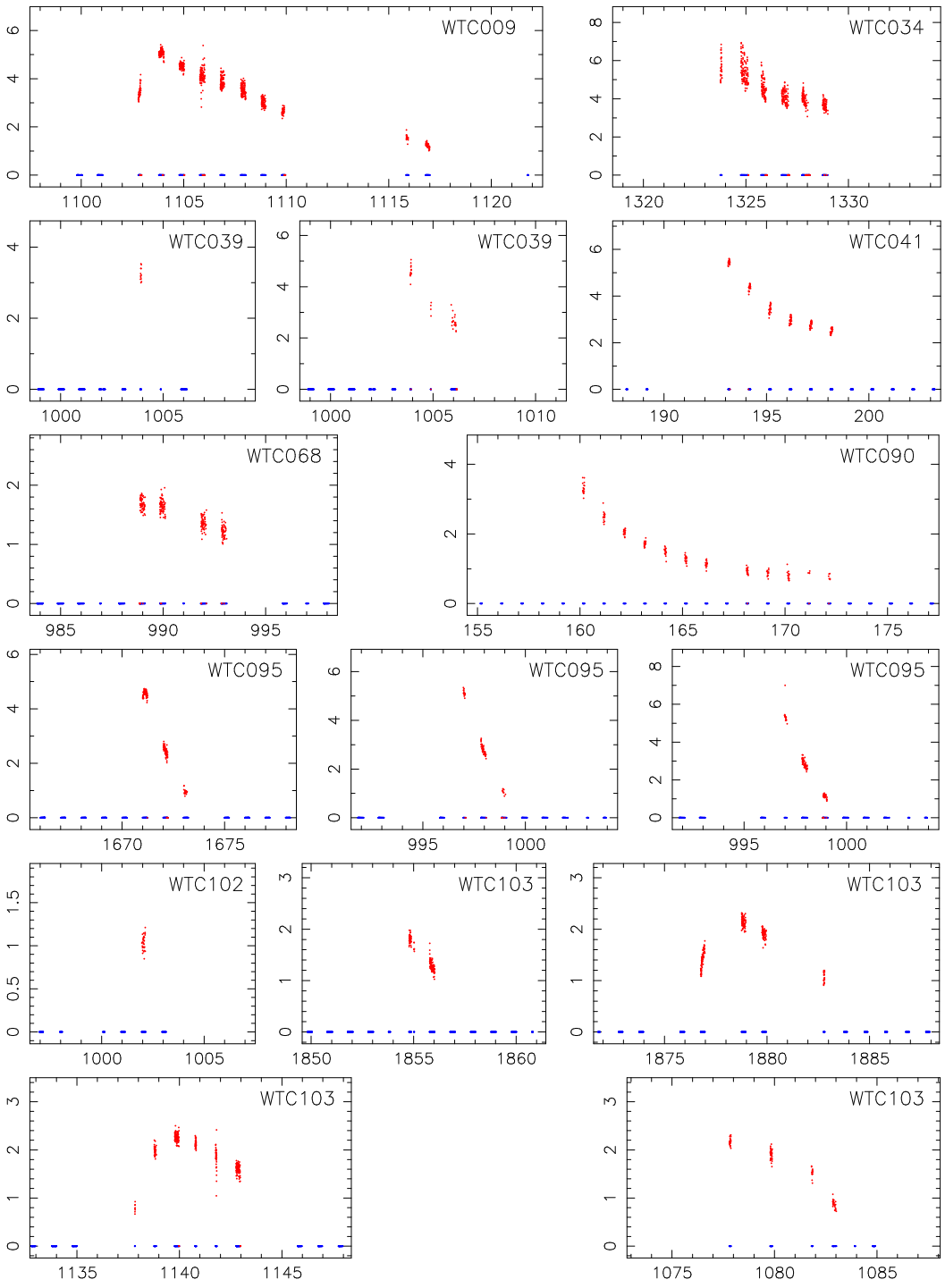

Figure C.1: Light curves of candidate CVs detected in WASP. Time in days after JD 2453005.5 is plotted on the x-axis. Flux is plotted on the y-axis in WASP flux units. Detections are marked with red dots and observations are marked with blue dots at zero flux.

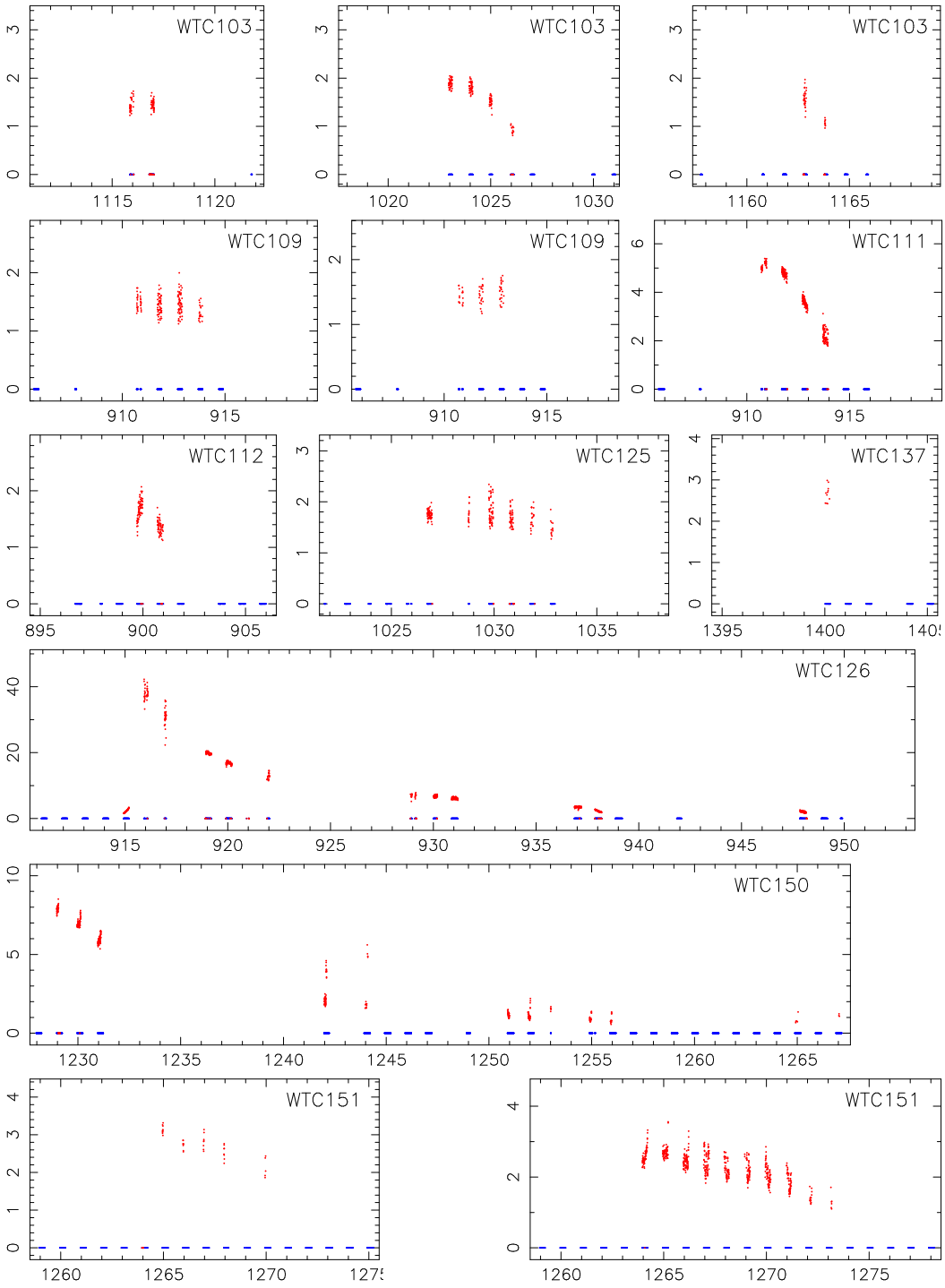

Figure C.1 continued: Light curves of candidate CVs detected in WASP. Time in days after JD 2453005.5 is plotted on the x-axis. Flux is plotted on the y-axis in WASP flux units. Detections are marked with red dots and observations are marked with blue dots at zero flux.

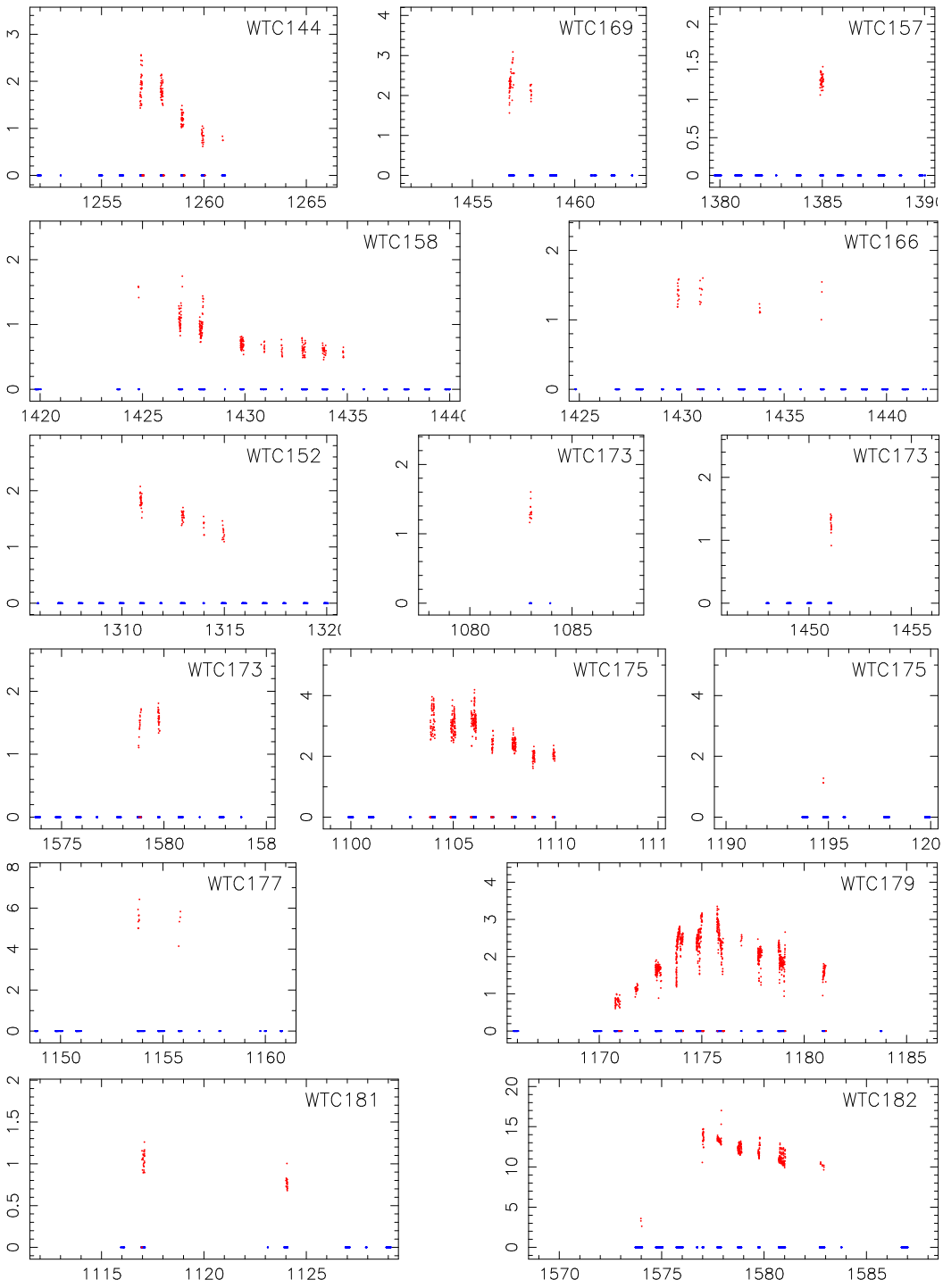

Figure C.1 continued: Light curves of candidate CVs detected in WASP. Time in days after JD 2453005.5 is plotted on the x-axis. Flux is plotted on the y-axis in WASP flux units. Detections are marked with red dots and observations are marked with blue dots at zero flux.

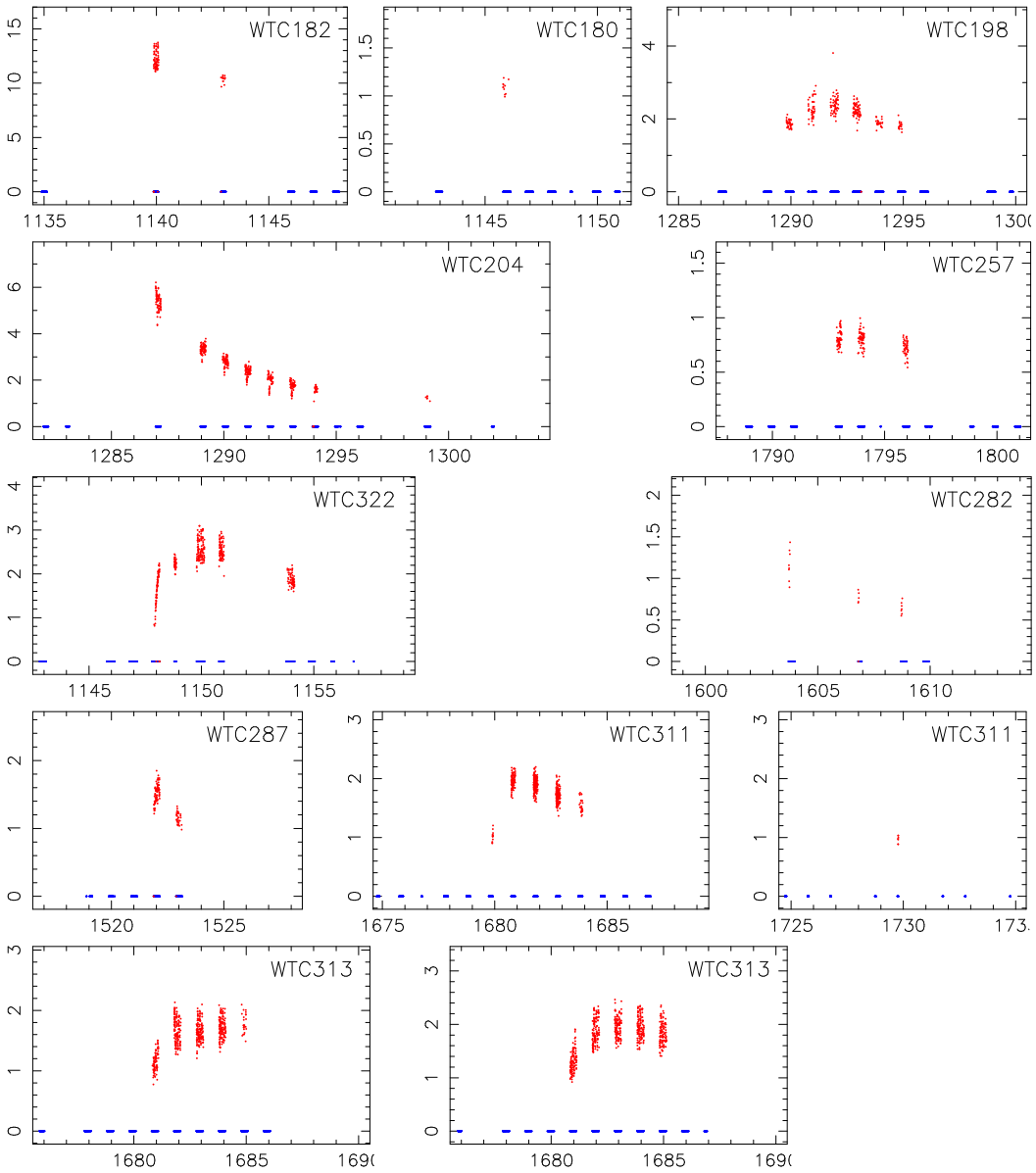

Figure C.1 continued: Light curves of candidate CVs detected in WASP. Time in days after JD 2453005.5 is plotted on the x-axis. Flux is plotted on the y-axis in WASP flux units. Detections are marked with red dots and observations are marked with blue dots at zero flux.

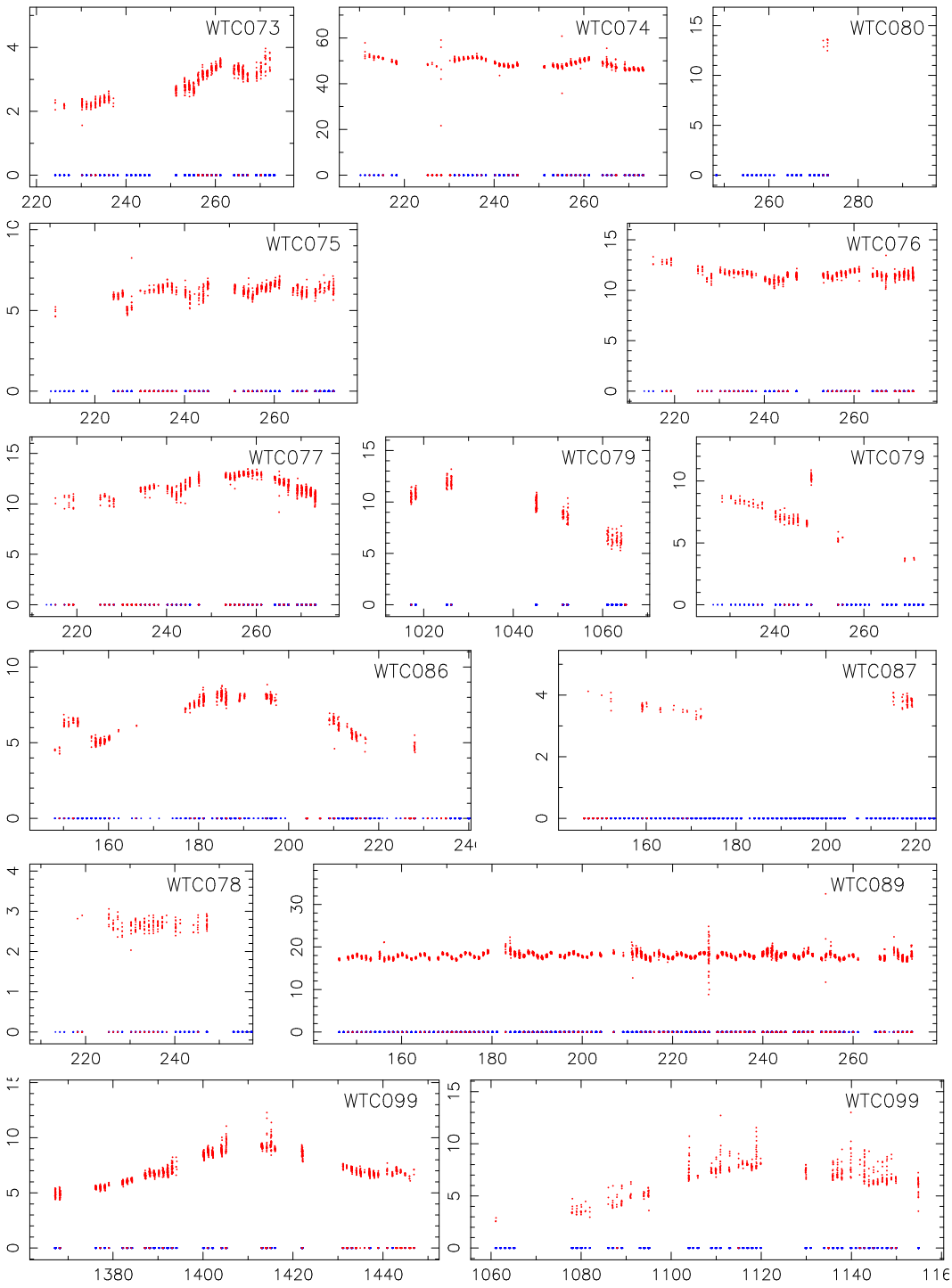

Figure C.2: Light curves of candidate pulsating variable stars detected in WASP. Time in days after JD 2453005.5 is plotted on the x-axis. Flux is plotted on the y-axis in WASP flux units.

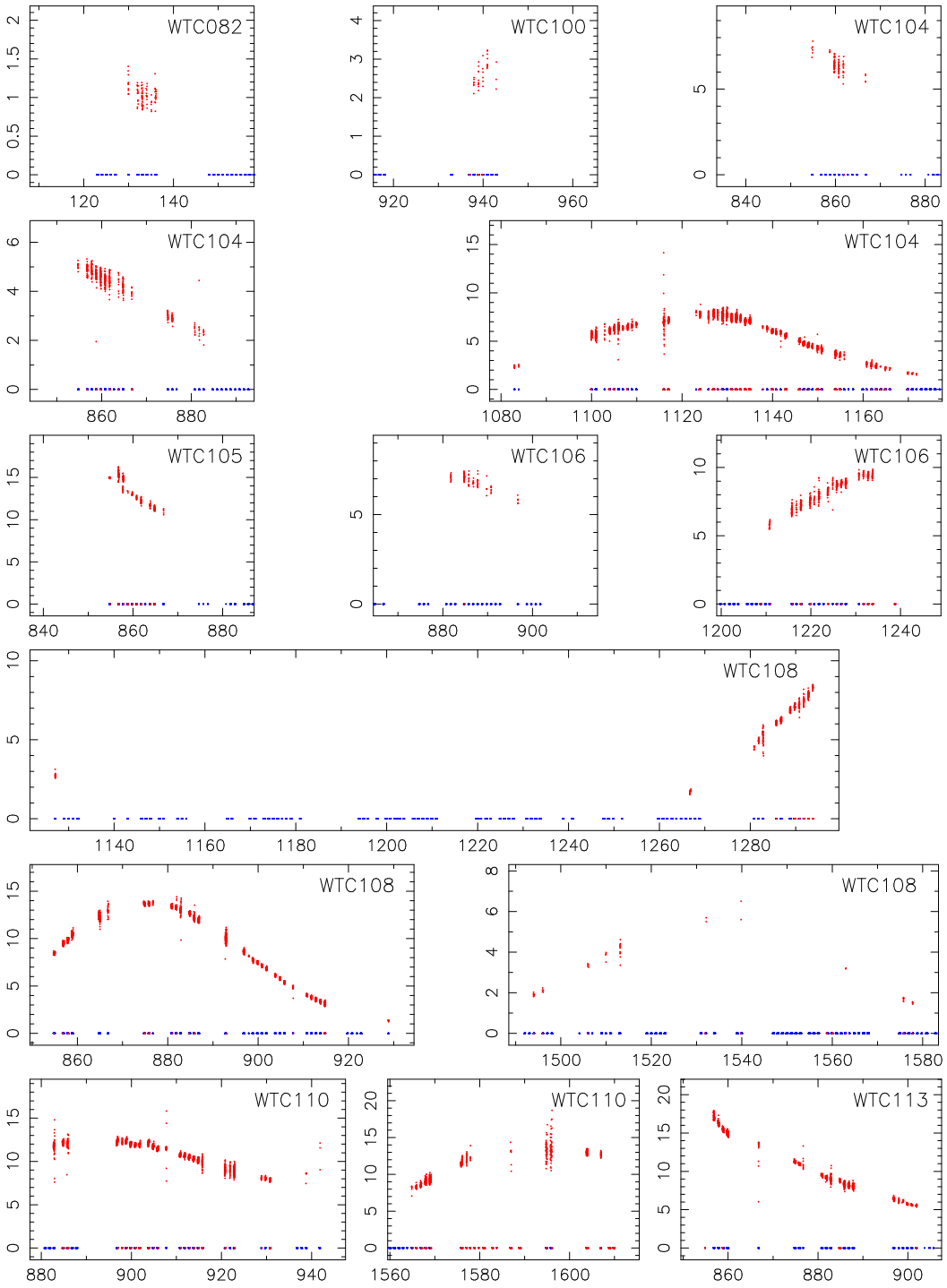

Figure C.2 continued: Light curves of candidate pulsating variable stars detected in WASP. Time in days after JD 2453005.5 is plotted on the x-axis. Flux is plotted on the y-axis in WASP flux units.

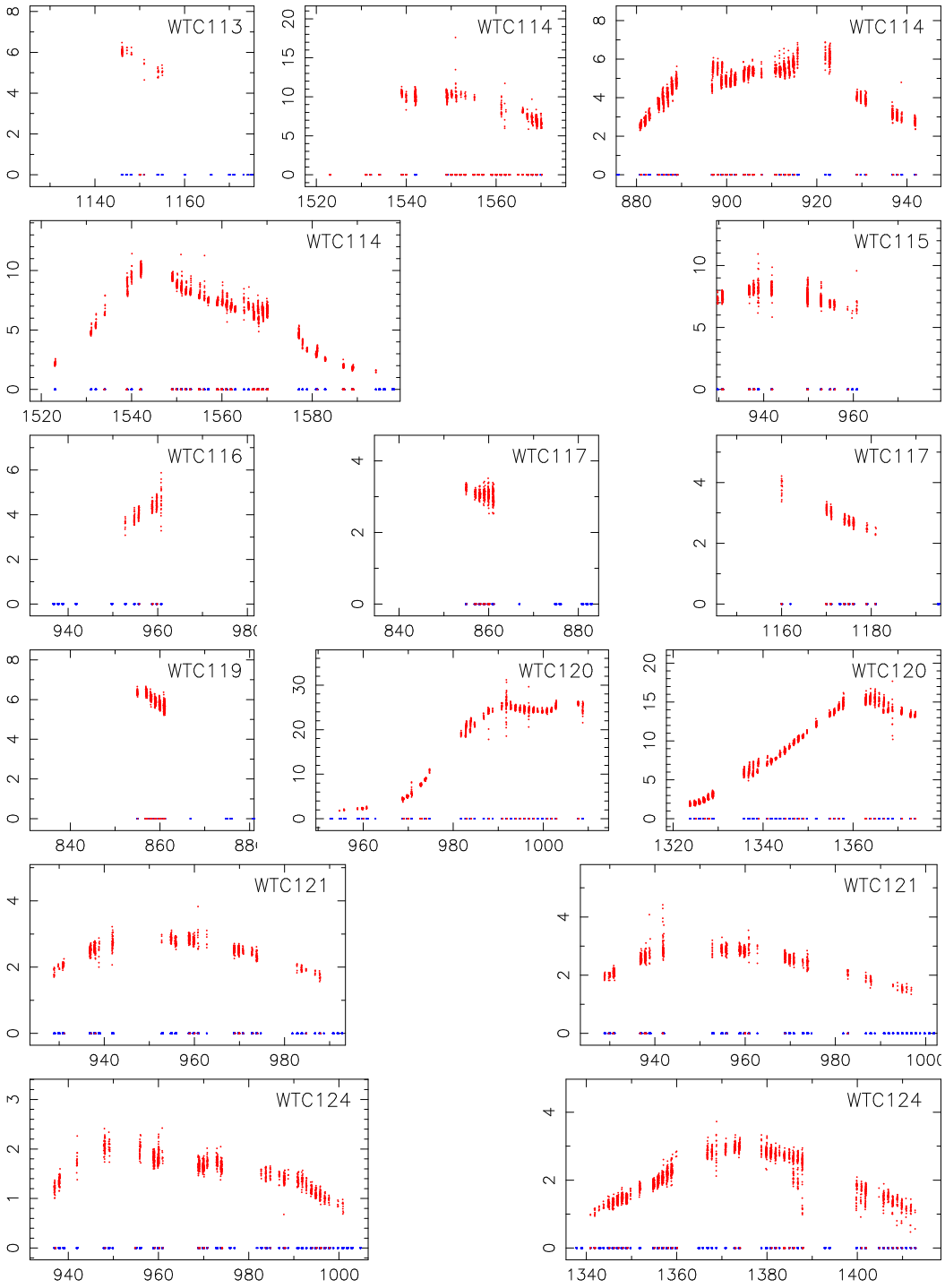

Figure C.2 continued: Light curves of candidate pulsating variable stars detected in WASP. Time in days after JD 2453005.5 is plotted on the x-axis. Flux is plotted on the y-axis in WASP flux units.

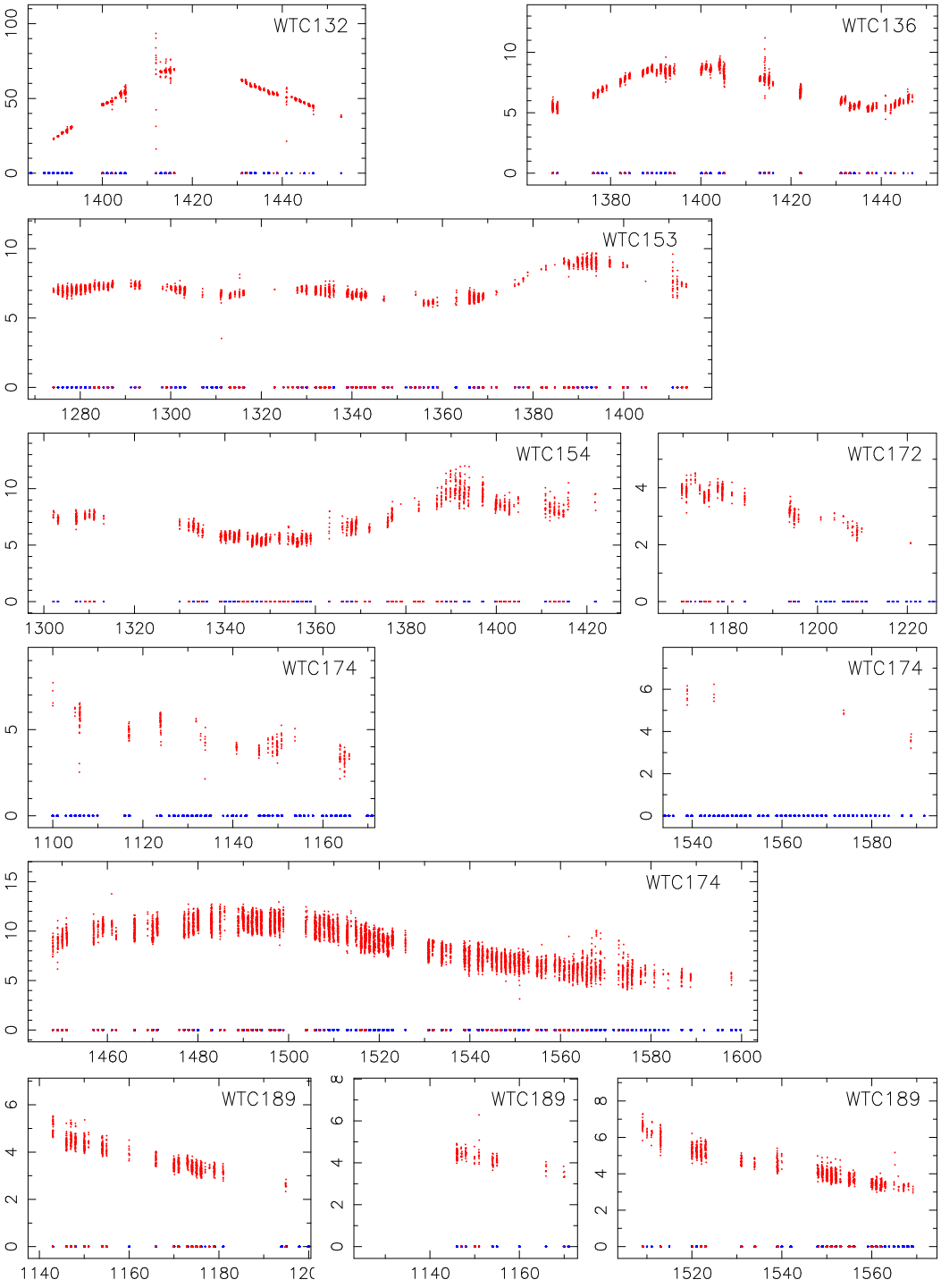

Figure C.2 continued: Light curves of candidate pulsating variable stars detected in WASP. Time in days after JD 2453005.5 is plotted on the x-axis. Flux is plotted on the y-axis in WASP flux units.

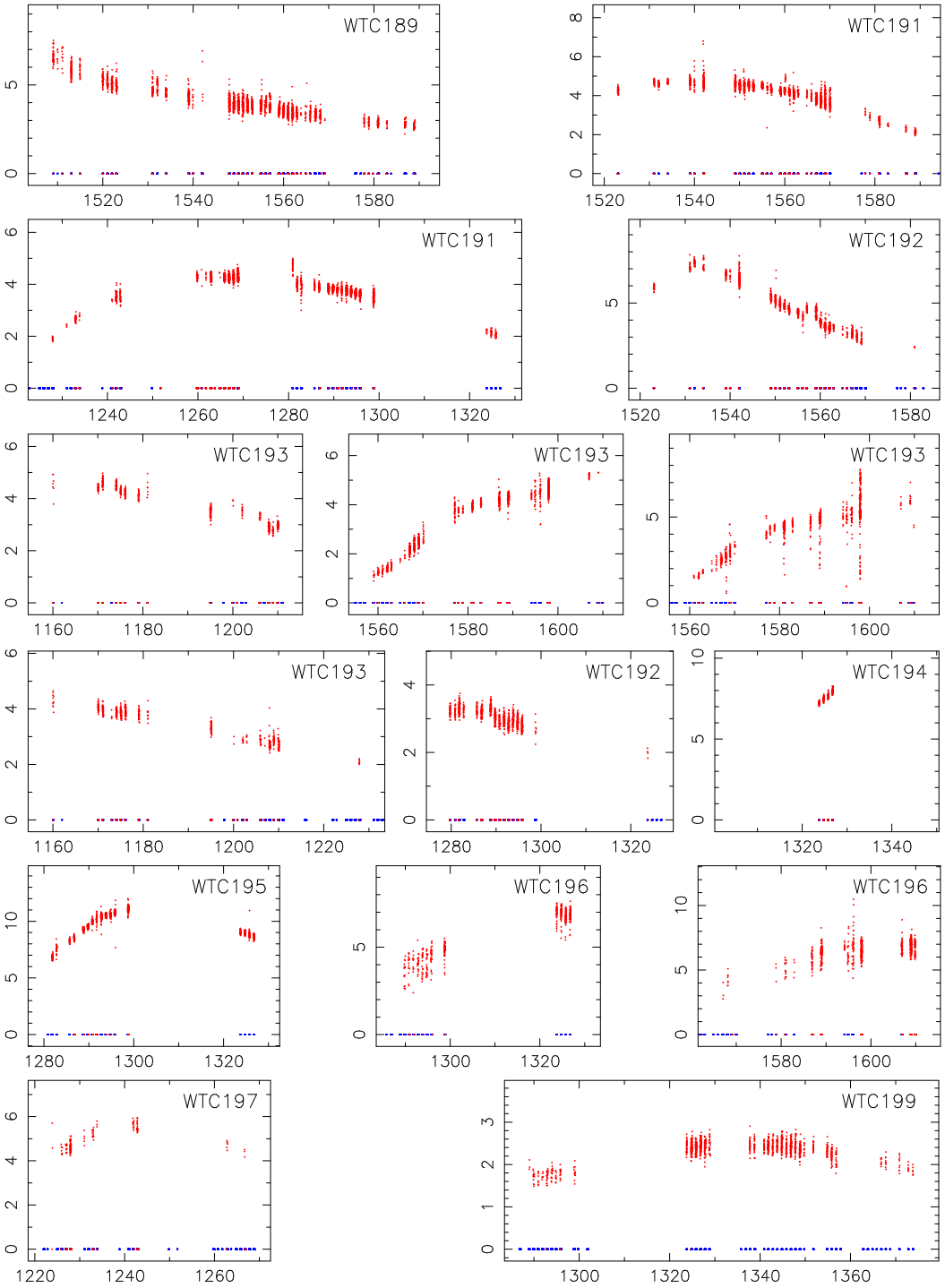

Figure C.2 continued: Light curves of candidate pulsating variable stars detected in WASP. Time in days after JD 2453005.5 is plotted on the x-axis. Flux is plotted on the y-axis in WASP flux units.

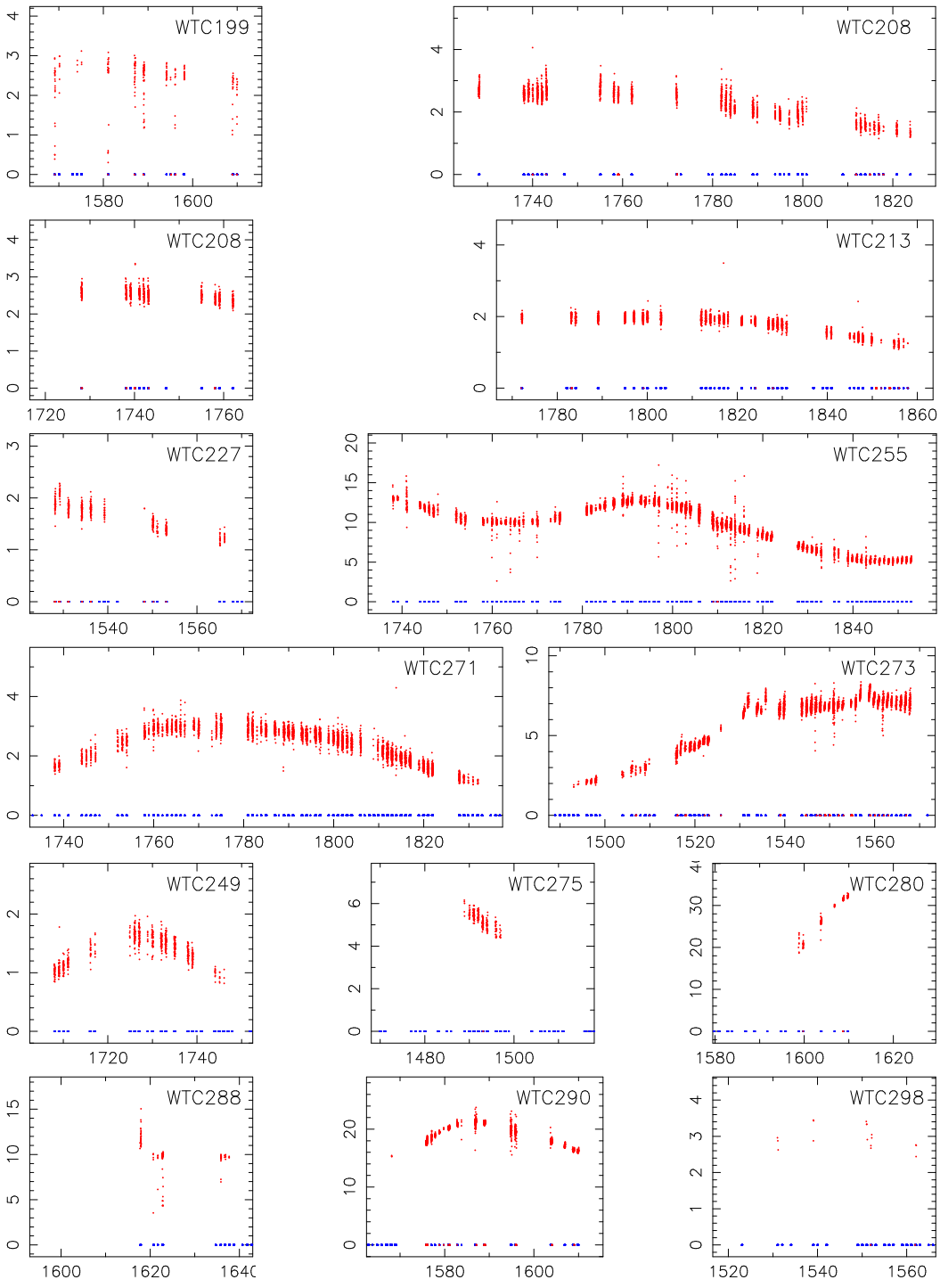

Figure C.2 continued: Light curves of candidate pulsating variable stars detected in WASP. Time in days after JD 2453005.5 is plotted on the x-axis. Flux is plotted on the y-axis in WASP flux units.

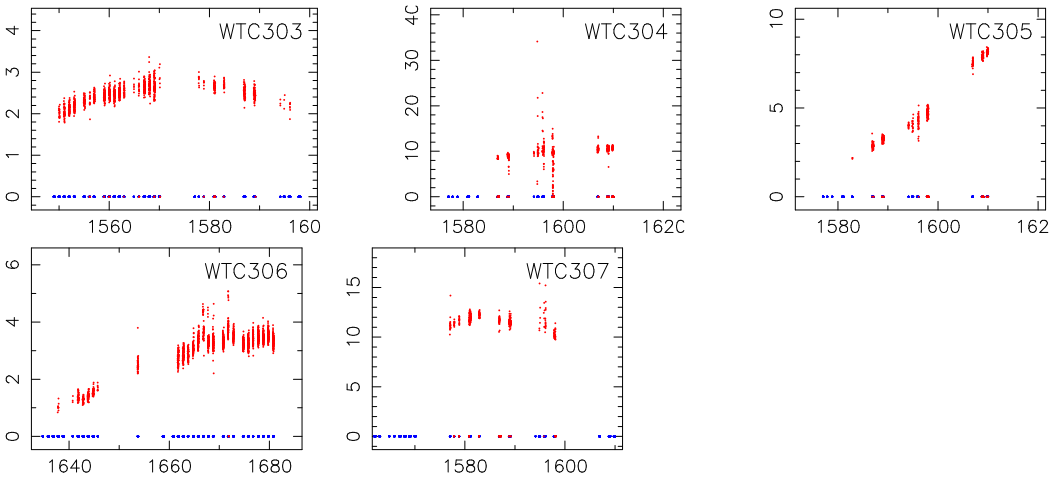

Figure C.2 continued: Light curves of candidate pulsating variable stars detected in WASP. Time in days after JD 2453005.5 is plotted on the x-axis. Flux is plotted on the y-axis in WASP flux units.

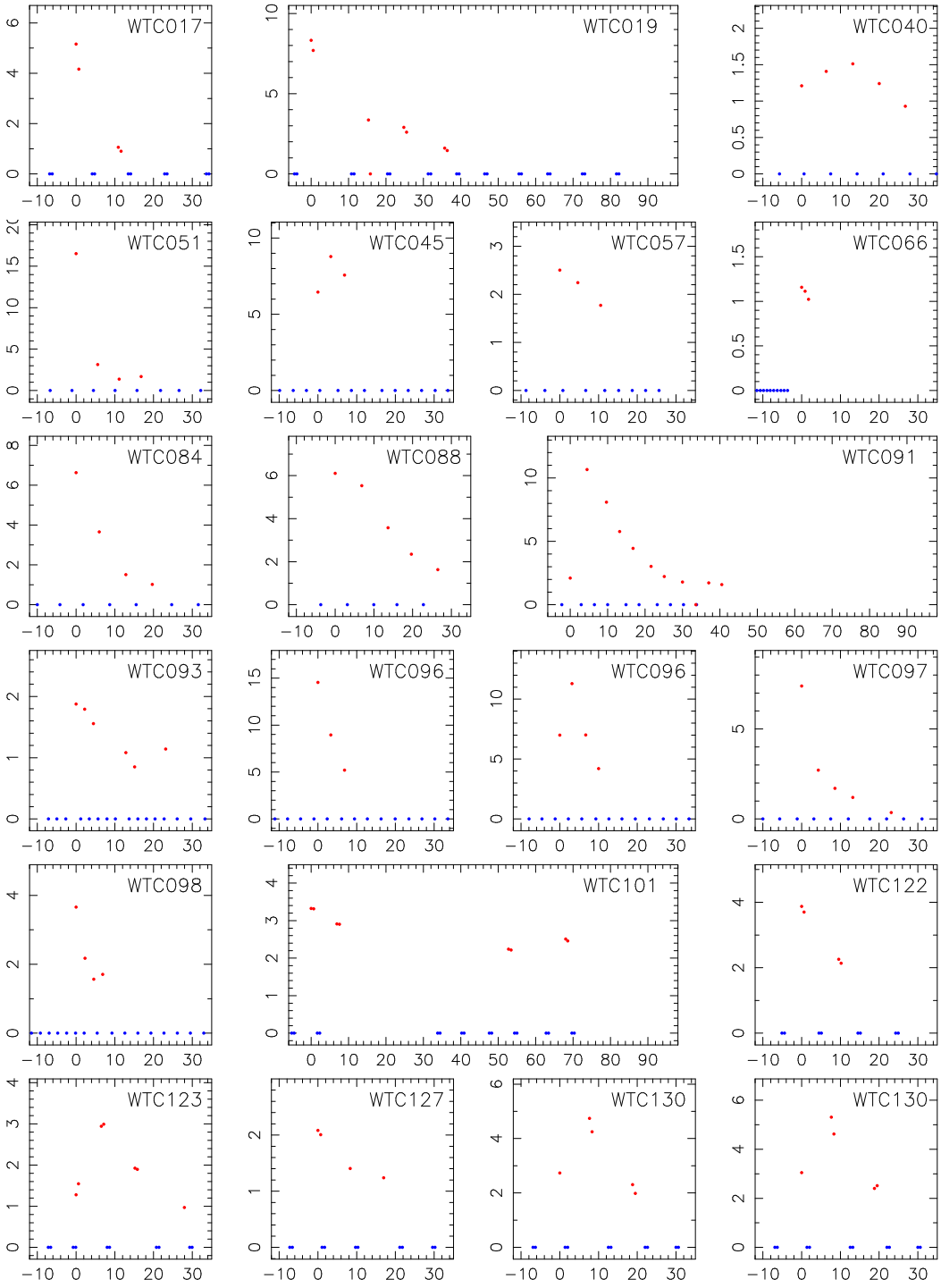

Figure C.3: Light curves of candidate flare stars detected in WASP. Time in minutes after first detection is plotted on the x-axis. Flux is plotted on the y-axis in WASP flux units. Detections are marked with red dots and observations are marked with blue dots at zero flux.

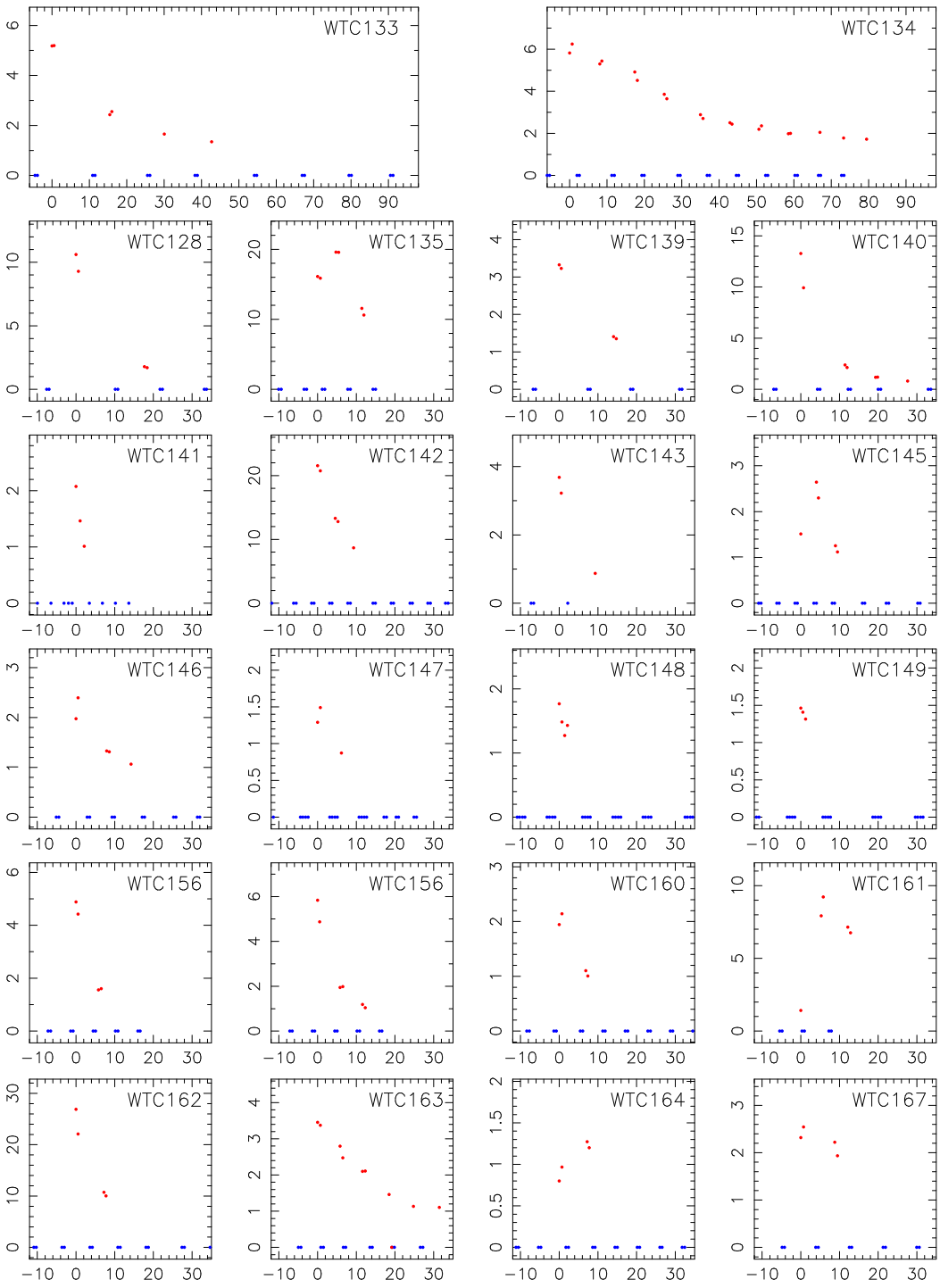

Figure C.3 continued: Light curves of candidate flare stars detected in WASP. Time in minutes after first detection is plotted on the x-axis. Flux is plotted on the y-axis in WASP flux units. Detections are marked with red dots and observations are marked with blue dots at zero flux.

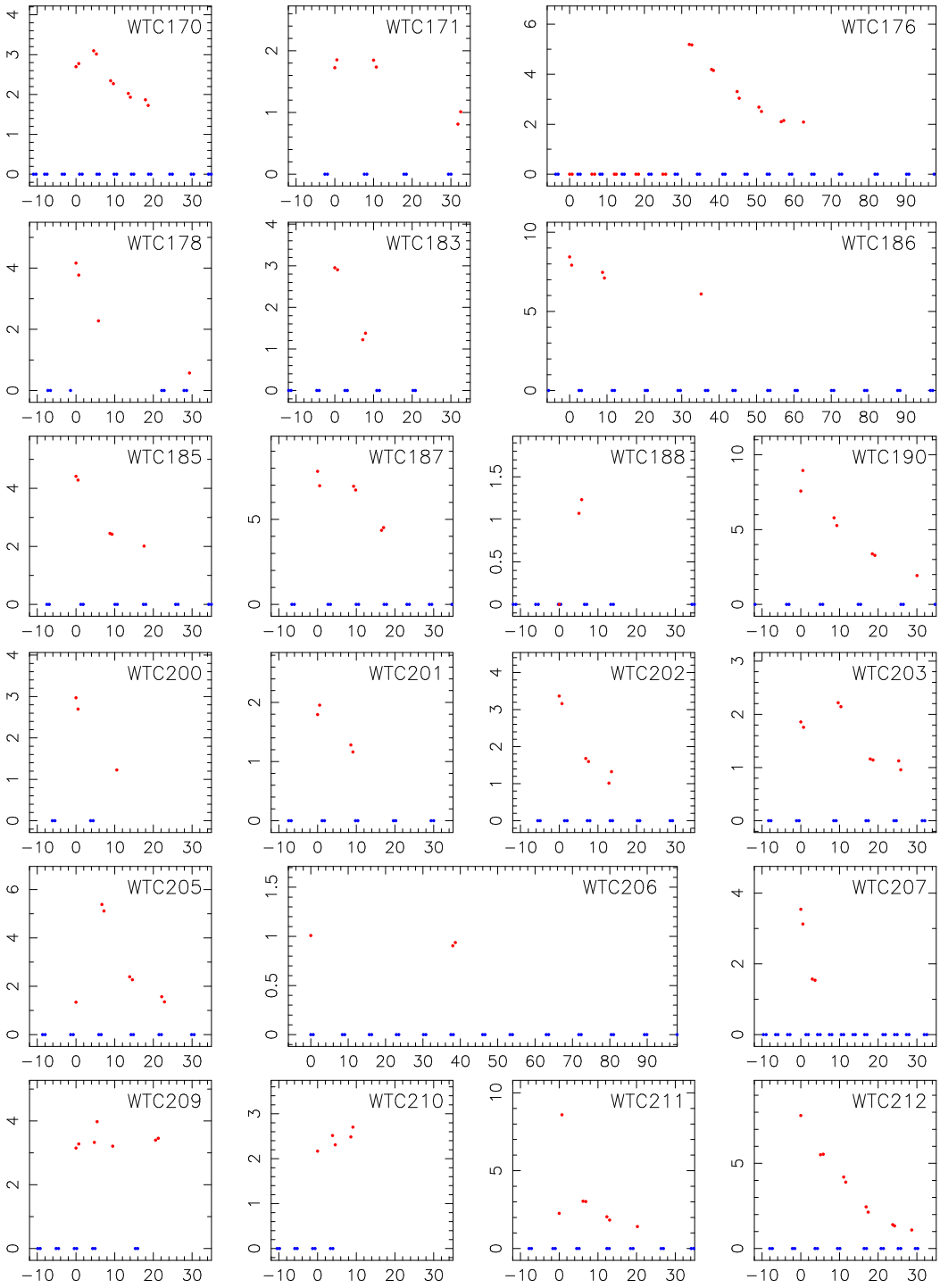

Figure C.3 continued: Light curves of candidate flare stars detected in WASP. Time in minutes after first detection is plotted on the x-axis. Flux is plotted on the y-axis in WASP flux units. Detections are marked with red dots and observations are marked with blue dots at zero flux.

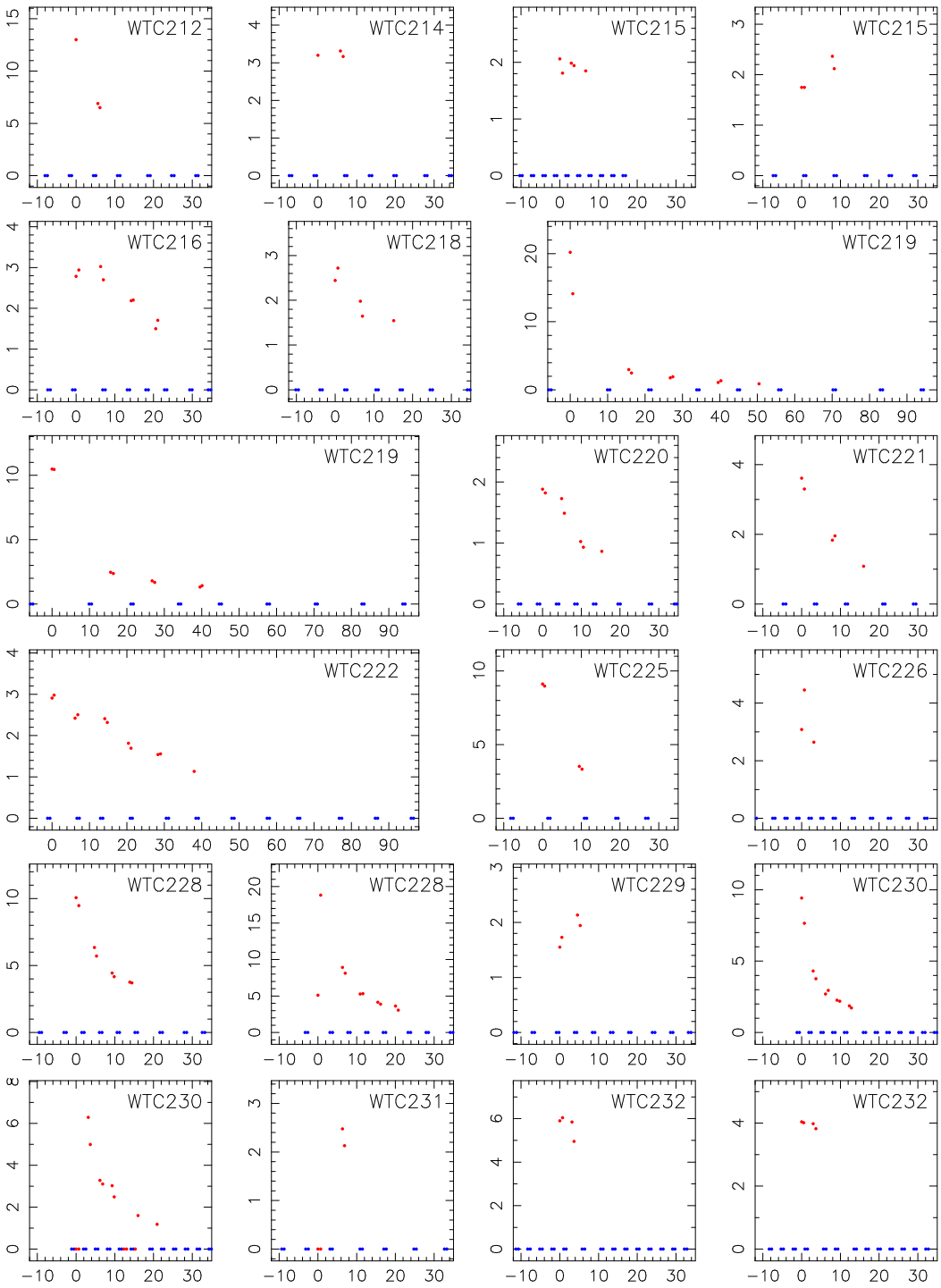

Figure C.3 continued: Light curves of candidate flare stars detected in WASP. Time in minutes after first detection is plotted on the x-axis. Flux is plotted on the y-axis in WASP flux units. Detections are marked with red dots and observations are marked with blue dots at zero flux.

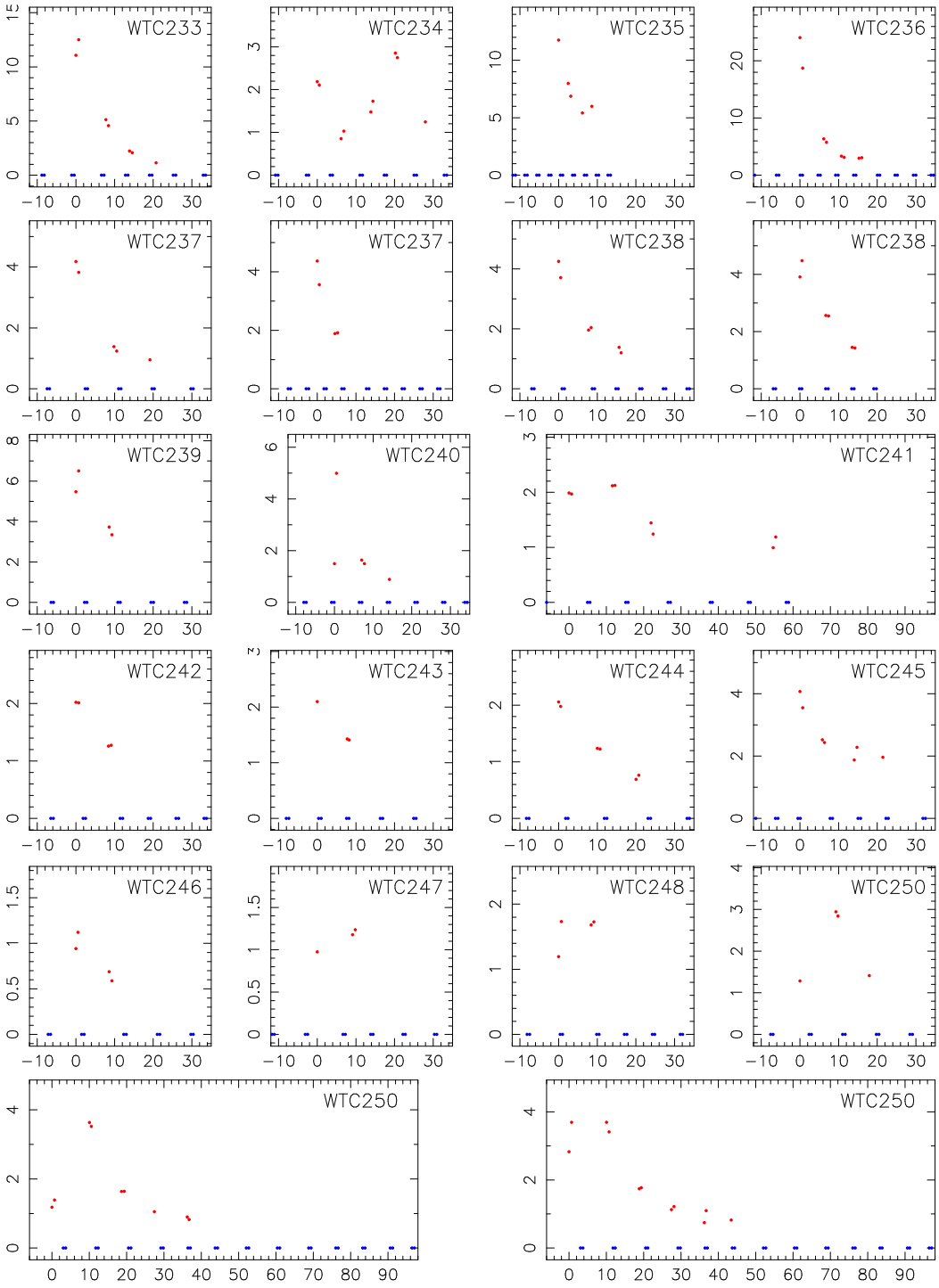

Figure C.3 continued: Light curves of candidate flare stars detected in WASP. Time in minutes after first detection is plotted on the x-axis. Flux is plotted on the y-axis in WASP flux units. Detections are marked with red dots and observations are marked with blue dots at zero flux.

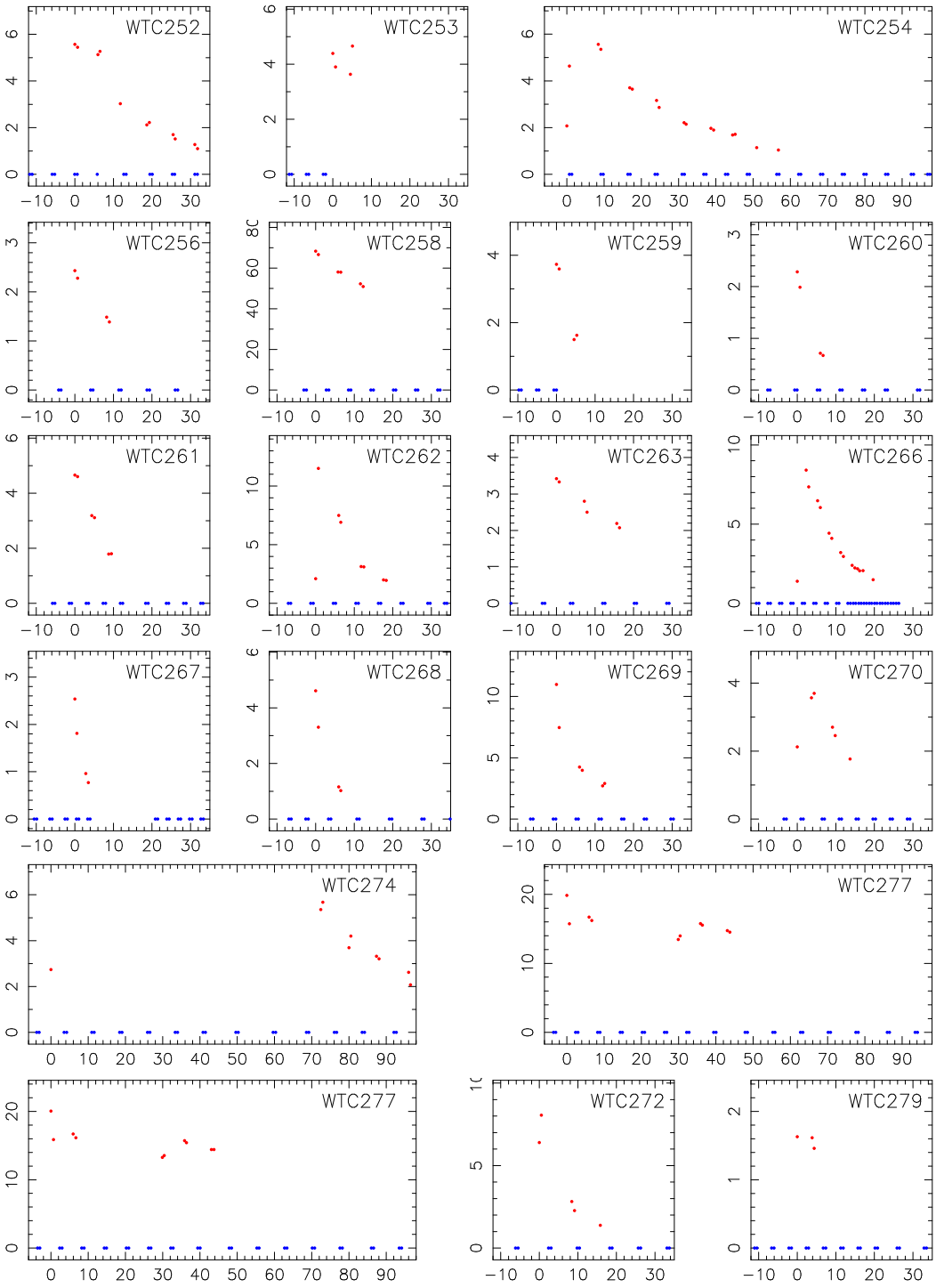

Figure C.3 continued: Light curves of candidate flare stars detected in WASP. Time in minutes after first detection is plotted on the x-axis. Flux is plotted on the y-axis in WASP flux units. Detections are marked with red dots and observations are marked with blue dots at zero flux.

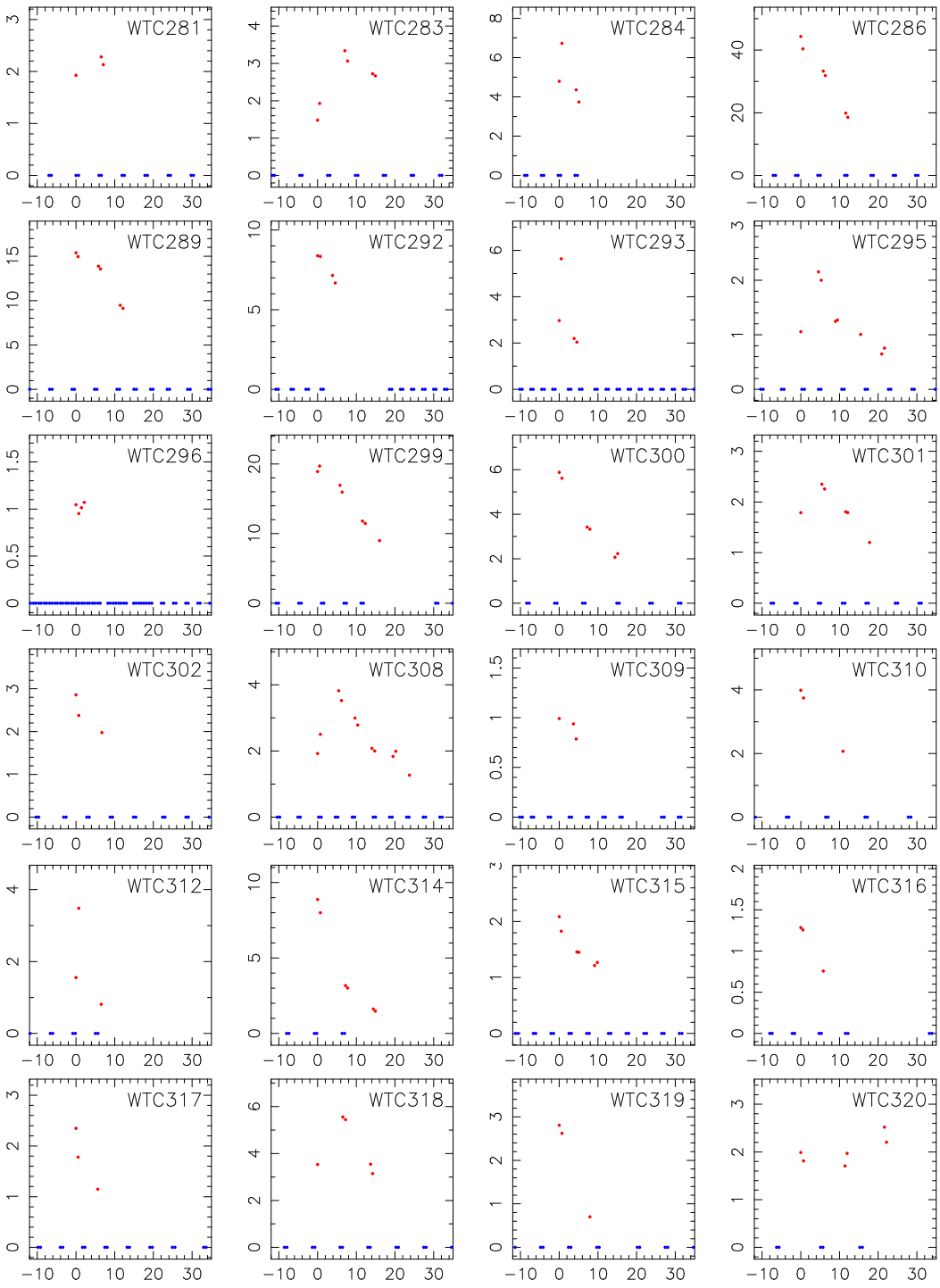

Figure C.3 continued: Light curves of candidate flare stars detected in WASP. Time in minutes after first detection is plotted on the x-axis. Flux is plotted on the y-axis in WASP flux units. Detections are marked with red dots and observations are marked with blue dots at zero flux.

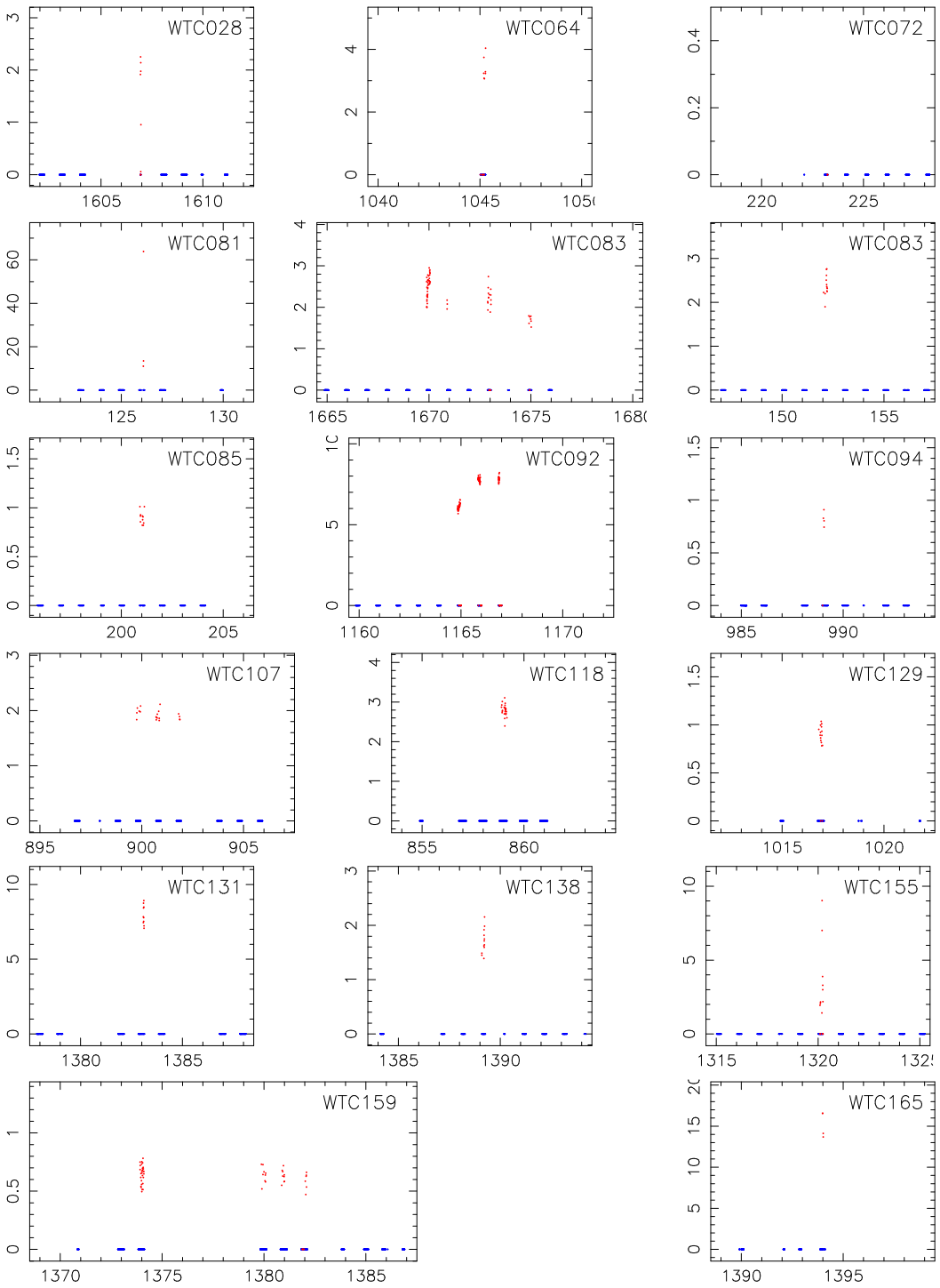

Figure C.4: Light curves of candidate transients of unknown type detected in WASP. Time in days after JD 2453005.5 is plotted on the x-axis. Flux is plotted on the y-axis in WASP flux units. Detections are marked with red dots and observations are marked with blue dots at zero flux.

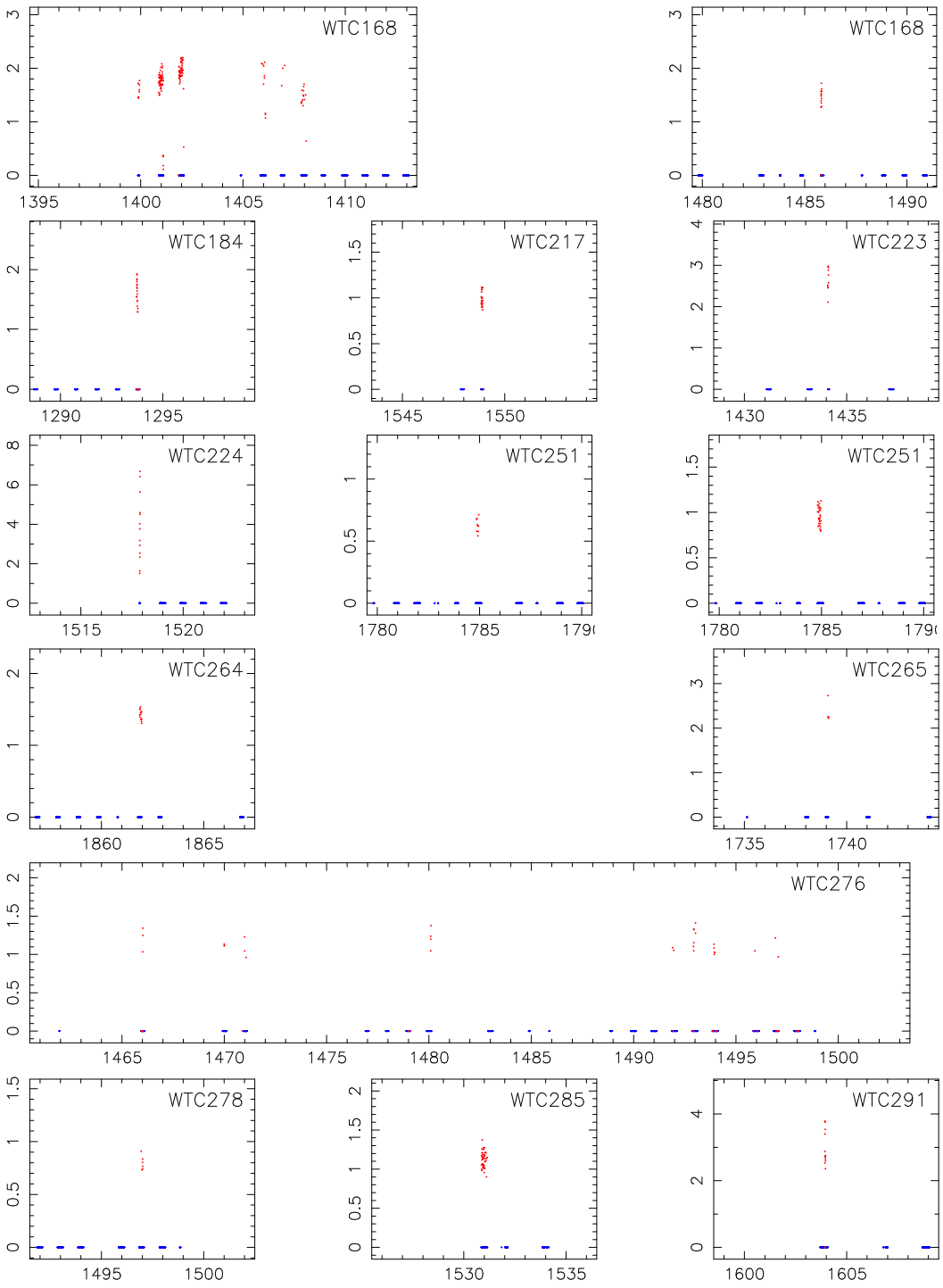

Figure C.4 continued: Light curves of candidate transients of unknown type detected in WASP. Time in days after JD 2453005.5 is plotted on the x-axis. Flux is plotted on the y-axis in WASP flux units. Detections are marked with red dots and observations are marked with blue dots at zero flux.

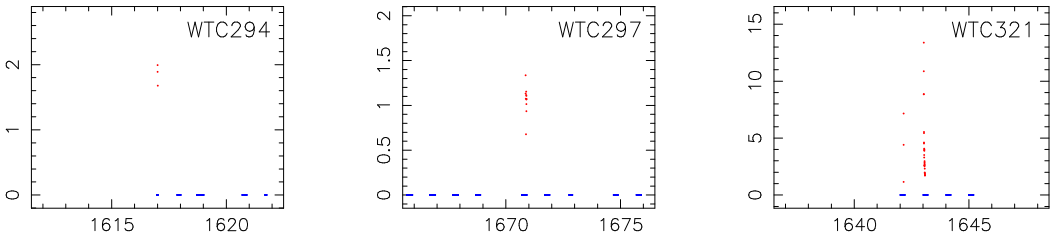

Figure C.4 continued: Light curves of candidate transients of unknown type detected in WASP. Time in days after JD 2453005.5 is plotted on the x-axis. Flux is plotted on the y-axis in WASP flux units. Detections are marked with red dots and observations are marked with blue dots at zero flux.

Appendix D

Candidate List

This appendix contains a complete list of all the candidate transients discovered in the WASP orphans database. For each candidate the source of the discovery is listed. Candidates discovered by the targeted search at the positions of ROSAT sources (see Section 3.7) and other X-ray or SDSS based targeted searches are listed as *Targeted*. Candidates discovered by the untargeted search algorithm (see Section 4.2) are listed as *Untargeted* or *Prototype* if they were discovered during the testing phase.

The candidates are classified as either CV, flare star or pulsating variable candidates. Where a classification is unclear they are listed as *uncertain*. The processes for determining a provisional classification is described in Section 5.1. In several cases the candidate was later found to be spurious but these are included in the list for completeness.

Identification	Right Ascension	Declination	Source	Type
WTC001	00 15 38.2	+26 36 57	Targeted	CV*
WTC002	00 20 50.5	-25 35 19	Targeted	Uncertain
WTC003	00 37 56.4	+40 25 20	Targeted	Flare
WTC004	00 38 58.4	+30 37 29	Targeted	Spurious
WTC005	01 26 16.7	+30 27 52	Targeted	Uncertain
WTC006	01 33 08.7	+38 32 18	Targeted	CV*
WTC007	02 32 38.1	-37 17 55	Targeted	CV
WTC008	04 25 37.5	+32 44 51	Targeted	Uncertain
WTC009	05 07 07.9	-41 46 28	Targeted	CV
	05 07 08.0	-41 46 28	Untargeted	
WTC010	05 10 20.1	+27 14 03	Targeted	Uncertain
WTC011	07 04 01.6	+37 35 14	Targeted	Uncertain
WTC012	08 39 22.9	+18 04 34	Targeted	Uncertain
WTC013	10 59 38.3	+20 58 20	Targeted	Uncertain
WTC014	12 11 16.9	+21 15 50	Targeted	Uncertain
WTC015	12 36 03.7	+18 28 44	Targeted	Uncertain
WTC016	13 09 56.2	+21 57 03	Targeted	Uncertain
WTC017	13 23 53.9	+26 51 20	Targeted	Flare*
	13 23 53.9	+26 51 20	Untargeted	
WTC018	13 30 03.6	+25 05 44	Targeted	Uncertain
WTC019	14 29 03.4	+46 45 38	Targeted	Flare*
	14 29 03.5	+46 45 36	Untargeted	
WTC020	14 33 00.4	+17 04 23	Targeted	Uncertain
WTC021	15 08 04.6	+39 58 54	Targeted	Flare
WTC022	15 10 17.8	+33 22 04	Targeted	Uncertain
WTC023	15 10 48.9	+42 48 16	Targeted	Uncertain
WTC024	15 49 59.9	+36 59 18	Targeted	Uncertain
WTC025	17 15 28.1	+54 25 09	Targeted	Uncertain
WTC026	17 35 30.2	+34 32 13	Targeted	Flare
WTC027	17 42 42.7	+21 37 31	Targeted	Uncertain
WTC028	17 48 27.9	+50 50 40	Targeted	CV*
	17 48 27.8	+50 50 39	Untargeted	
WTC029	17 55 04.3	+24 00 43	Targeted	Flare
WTC030	17 55 30.8	+54 11 25	Targeted	Flare
WTC031	18 02 05.2	+39 34 49	Targeted	Flare
WTC032	18 04 01.8	+54 10 14	Targeted	Spurious

Table D.1: A list of all the transient candidates discovered in the WASP orphans database. Each row includes an identification number, a right ascension, a declination, the search where the candidate was found and a provisional classification. Candidates marked with a * were confirmed spectroscopically.

Identification	Right Ascension	Declination	Source	Type
WTC033	18 10 06.0	+34 29 55	Targeted	Uncertain
WTC034	20 56 52.2	-30 14 39	Targeted	CV
	20 56 52.2	-30 14 40	Untargeted	
WTC035	21 52 45.7	-30 27 15	Targeted	Uncertain
WTC036	22 15 30.8	-28 32 03	Targeted	Uncertain
WTC037	22 42 45.0	+29 43 00	Targeted	Spurious
WTC038	00 07 29.2	+34 37 14	Prototype	Flare
WTC039	00 13 47.0	+20 25 11	Prototype	CV*
	00 13 47.5	+20 25 08	Untargeted	
WTC040	00 37 40.6	+19 43 39	Untargeted	Flare*
	00 37 40.9	+19 43 48	Prototype	
WTC041	00 59 09.3	+34 38 31	Prototype	CV*
	00 59 10.1	+34 38 33	Untargeted	
WTC042	01 35 27.1	+21 43 50	Prototype	Flare
WTC043	01 38 26.1	+27 28 06	Prototype	Uncertain
WTC044	01 41 35.3	+42 18 47	Prototype	Uncertain
WTC045	01 58 15.8	+18 07 14	Untargeted	Flare*
	01 58 16.1	+18 07 09	Prototype	
WTC046	02 00 30.5	+22 35 27	Prototype	Uncertain
WTC047	02 06 34.4	+20 57 08	Prototype	Uncertain
WTC048	02 27 54.4	+59 43 10	Prototype	CV*
WTC049	02 31 38.1	+25 10 17	Prototype	Uncertain
WTC050	02 36 20.7	+22 23 01	Prototype	Flare*
WTC051	02 53 20.5	+27 13 42	Prototype	Flare
	02 53 20.7	+27 13 37	Untargeted	
WTC052	02 57 27.3	+11 18 10	Prototype	Pulsating Variable
WTC053	02 59 32.3	+20 56 21	Prototype	Uncertain
WTC054	03 00 56.1	+31 34 35	Prototype	Uncertain
WTC055	03 21 19.3	+29 43 35	Prototype	Uncertain
WTC056	03 38 51.4	+27 31 49	Prototype	Uncertain
WTC057	03 41 25.8	+23 15 34	Untargeted	Flare*
	03 41 26.3	+23 15 45	Prototype	
WTC058	03 48 32.7	+32 16 42	Prototype	Pulsating Variable*
WTC059	03 54 46.6	+29 28 00	Prototype	Uncertain
WTC060	04 05 26.5	+29 38 11	Prototype	Uncertain
WTC061	04 32 38.4	+23 58 26	Prototype	Pulsating Variable*

Table D.1 continued: A list of all the transient candidates discovered in the WASP orphans database. Each row includes an identification number, a right ascension, a declination, the search where the candidate was found and a provisional classification. Candidates marked with a * were confirmed spectroscopically.

Identification	Right Ascension	Declination	Source	Type
WTC062	05 01 08.8	+31 24 27	Prototype	Uncertain
WTC063	05 22 48.1	+35 54 53	Prototype	Pulsating Variable
WTC064	05 38 07.5	+36 03 41	Untargeted	Uncertain
	05 38 08.3	+36 03 37	Prototype	
WTC065	19 12 35.8	+50 34 31	Prototype	CV*
WTC066	20 55 18.3	+02 37 40	Untargeted	Flare*
	20 55 19.2	+02 37 44	Prototype	
WTC067	21 26 28.3	+21 53 19	Prototype	Uncertain
WTC068	21 39 12.7	+13 19 52	Untargeted	CV*
	21 39 13.1	+13 19 47	Prototype	
WTC069	22 09 35.9	+23 01 53	Prototype	Uncertain
WTC070	23 28 42.4	+33 21 51	Prototype	Uncertain
WTC071	23 58 11.5	+40 07 02	Prototype	Spurious
WTC072	02 06 28.9	+23 02 34	Untargeted	Uncertain
WTC073	03 51 57.9	+39 09 44	Untargeted	Pulsating Variable
WTC074	03 52 36.5	+33 55 53	Untargeted	Pulsating Variable
WTC075	04 31 20.8	+26 58 45	Untargeted	Pulsating Variable
WTC076	05 05 26.5	+31 29 47	Untargeted	Pulsating Variable
WTC077	05 24 28.0	+21 25 14	Untargeted	Pulsating Variable
WTC078	05 26 32.9	+35 11 32	Untargeted	Pulsating Variable
WTC079	05 48 07.9	+32 48 59	Untargeted	Pulsating Variable
WTC080	05 49 05.0	+32 24 51	Untargeted	Pulsating Variable
WTC081	13 37 25.1	+43 11 20	Untargeted	Uncertain
WTC082	15 04 55.3	+35 47 53	Untargeted	Pulsating Variable
WTC083	17 27 58.0	+38 00 20	Untargeted	Uncertain
WTC084	17 47 37.9	+36 52 22	Untargeted	Flare
WTC085	18 02 22.6	+45 52 46	Untargeted	Uncertain
WTC086	20 30 46.5	+26 00 40	Untargeted	Pulsating Variable
WTC087	20 44 10.3	+20 22 49	Untargeted	Pulsating Variable
WTC088	21 03 59.7	+12 18 57	Untargeted	Flare
WTC089	21 22 03.6	+19 52 50	Untargeted	Pulsating Variable
WTC090	23 05 46.2	+29 54 14	Untargeted	CV
WTC091	02 58 47.0	+33 24 15	Untargeted	Flare
WTC092	06 32 12.9	+25 36 22	Untargeted	Uncertain
WTC093	22 06 19.2	+09 34 08	Untargeted	Flare
WTC094	00 56 18.7	+28 48 21	Untargeted	Uncertain

Table D.1 continued: A list of all the transient candidates discovered in the WASP orphans database. Each row includes an identification number, a right ascension, a declination, the search where the candidate was found and a provisional classification. Candidates marked with a * were confirmed spectroscopically.

Identification	Right Ascension	Declination	Source	Type
WTC095	21 58 15.2	+09 47 10	Untargeted	CV
WTC096	06 34 17.2	+39 00 13	Untargeted	Flare
WTC097	00 38 00.9	+40 26 22	Untargeted	Flare
WTC098	22 30 44.1	+22 45 47	Untargeted	Flare
WTC099	05 27 47.7	+43 24 24	Untargeted	Pulsating Variable
WTC100	17 28 55.4	+32 30 54	Untargeted	Pulsating Variable
WTC101	04 38 43.6	-24 43 40	Untargeted	Flare
WTC102	05 11 37.9	-46 05 33	Untargeted	CV
WTC103	05 41 18.9	-35 24 15	Untargeted	CV
WTC104	09 09 23.0	-39 13 40	Untargeted	Pulsating Variable
WTC105	09 29 20.5	-42 01 54	Untargeted	Pulsating Variable
WTC106	10 13 20.8	-43 33 04	Untargeted	Pulsating Variable
WTC107	13 41 48.3	-44 55 01	Untargeted	Uncertain
WTC108	13 57 30.4	-35 53 56	Untargeted	Pulsating Variable
WTC109	13 59 15.3	-39 14 50	Untargeted	CV
WTC110	14 11 30.2	-38 51 49	Untargeted	Pulsating Variable
WTC111	14 31 44.9	-35 52 09	Untargeted	CV
WTC112	14 32 11.0	-35 12 43	Untargeted	CV
WTC113	15 15 33.1	-46 28 28	Untargeted	Pulsating Variable
WTC114	15 36 45.9	-31 12 19	Untargeted	Pulsating Variable
WTC115	15 47 28.7	-32 25 44	Untargeted	Pulsating Variable
WTC116	15 52 22.5	-35 19 05	Untargeted	Pulsating Variable
WTC117	16 09 39.9	-35 02 03	Untargeted	Pulsating Variable
WTC118	16 09 48.8	-39 11 13	Untargeted	Uncertain
WTC119	16 26 26.1	-34 35 56	Untargeted	Pulsating Variable
WTC120	19 15 48.4	-29 46 31	Untargeted	Pulsating Variable
WTC121	19 36 42.8	-34 33 29	Untargeted	Pulsating Variable
WTC122	20 34 48.1	-20 44 39	Untargeted	Flare
WTC123	22 24 57.7	-22 49 45	Untargeted	Flare
WTC124	22 31 45.1	-23 32 46	Untargeted	Pulsating Variable
WTC125	22 42 58.1	-19 45 51	Untargeted	CV
WTC126	22 47 39.7	-36 22 54	Untargeted	CV
WTC127	22 53 49.8	-17 21 32	Untargeted	Flare
WTC128	23 14 21.7	-30 13 23	Untargeted	Flare
WTC129	23 28 28.8	-34 10 06	Untargeted	Uncertain
WTC130	23 58 15.4	-39 35 34	Untargeted	Flare

Table D.1 continued: A list of all the transient candidates discovered in the WASP orphans database. Each row includes an identification number, a right ascension, a declination, the search where the candidate was found and a provisional classification. Candidates marked with a * were confirmed spectroscopically.

Identification	Right Ascension	Declination	Source	Type
WTC131	00 16 49.7	+45 15 42	Untargeted	Uncertain
WTC132	02 52 22.8	+48 39 52	Untargeted	Pulsating Variable
WTC133	03 41 42.5	+51 44 50	Untargeted	Flare
WTC134	04 17 40.5	+31 57 34	Untargeted	Flare
WTC135	05 07 14.2	+37 30 41	Untargeted	Flare
WTC136	05 12 25.4	+49 12 02	Untargeted	Pulsating Variable
WTC137	05 15 29.0	+56 05 34	Untargeted	CV
WTC138	06 21 49.6	+55 20 50	Untargeted	Uncertain
WTC139	09 01 28.9	+38 32 59	Untargeted	Flare
WTC140	10 54 28.9	+35 16 39	Untargeted	Flare
WTC141	11 18 04.9	+36 41 56	Untargeted	Flare
WTC142	11 22 54.0	+32 41 26	Untargeted	Flare
WTC143	11 29 39.3	+31 39 45	Untargeted	Flare
WTC144	13 37 21.3	+48 01 20	Untargeted	CV
WTC145	13 52 08.8	+29 53 17	Untargeted	Flare
WTC146	15 24 36.1	+35 25 54	Untargeted	Flare
WTC147	17 00 10.3	+43 50 28	Untargeted	Flare
WTC148	17 16 53.8	+43 45 52	Untargeted	Flare
WTC149	17 28 10.2	+39 39 39	Untargeted	Flare
WTC150	17 40 33.4	+41 47 54	Untargeted	CV
WTC151	18 20 30.2	+51 44 46	Untargeted	CV
WTC152	18 34 54.6	+54 48 26	Untargeted	CV
WTC153	21 41 55.1	+42 45 07	Untargeted	Pulsating Variable
WTC154	23 23 09.3	+52 50 13	Untargeted	Pulsating Variable
WTC155	23 57 13.4	+50 04 05	Untargeted	Uncertain
WTC156	00 21 18.1	-31 43 26	Untargeted	Flare
WTC157	00 27 41.3	-24 39 45	Untargeted	CV
WTC158	02 21 37.9	-26 19 51	Untargeted	CV
WTC159	02 28 14.4	-44 05 53	Untargeted	Uncertain
WTC160	02 30 26.5	-34 26 03	Untargeted	Flare
WTC161	02 37 51.0	-35 34 53	Untargeted	Flare
WTC162	03 02 28.0	-32 57 03	Untargeted	Flare
WTC163	03 32 08.3	-34 13 16	Untargeted	Flare
WTC164	03 39 38.4	-23 48 17	Untargeted	Flare
WTC165	03 43 09.5	-31 44 59	Untargeted	Uncertain
WTC166	04 04 24.7	-32 42 12	Untargeted	CV

Table D.1 continued: A list of all the transient candidates discovered in the WASP orphans database. Each row includes an identification number, a right ascension, a declination, the search where the candidate was found and a provisional classification. Candidates marked with a * were confirmed spectroscopically.

Identification	Right Ascension	Declination	Source	Type
WTC167	05 19 25.9	-28 11 07	Untargeted	Flare
WTC168	05 25 58.3	-34 27 27	Untargeted	Uncertain
WTC169	05 57 21.9	-36 30 58	Untargeted	CV
WTC170	06 10 41.2	-34 11 08	Untargeted	Flare
WTC171	06 19 03.7	-32 06 32	Untargeted	Flare
WTC172	09 37 43.1	-43 22 51	Untargeted	Pulsating Variable
WTC173	09 45 51.0	-19 44 01	Untargeted	CV
WTC174	09 46 47.2	-28 41 18	Untargeted	Pulsating Variable
WTC175	10 01 31.9	-33 02 36	Untargeted	CV
WTC176	10 07 59.5	-27 44 44	Untargeted	Flare
WTC177	10 11 25.7	-40 24 36	Untargeted	CV
WTC178	10 48 19.9	-22 50 11	Untargeted	Flare
WTC179	10 49 25.9	-21 47 36	Untargeted	CV
WTC180	10 58 43.5	-43 32 34	Untargeted	CV
WTC181	12 32 12.2	-24 07 53	Untargeted	CV
WTC182	12 45 07.3	-38 13 27	Untargeted	CV
WTC183	13 19 19.7	-27 09 48	Untargeted	Flare
WTC184	14 00 41.0	-33 48 56	Untargeted	Uncertain
WTC185	14 35 25.9	-38 42 21	Untargeted	Flare
WTC186	14 54 04.2	-36 06 12	Untargeted	Flare
WTC187	14 54 49.2	-36 27 49	Untargeted	Flare
WTC188	15 10 11.5	-20 12 41	Untargeted	Flare
WTC189	15 11 18.8	-39 04 03	Untargeted	Pulsating Variable
WTC190	15 53 43.9	-32 12 35	Untargeted	Flare
WTC191	16 10 20.3	-35 45 11	Untargeted	Pulsating Variable
WTC192	16 12 20.9	-19 49 55	Untargeted	Pulsating Variable
WTC193	16 24 21.7	-32 02 01	Untargeted	Pulsating Variable
WTC194	16 26 41.9	-29 57 19	Untargeted	Pulsating Variable
WTC195	16 30 27.4	-35 15 31	Untargeted	Pulsating Variable
WTC196	16 34 36.2	-38 49 03	Untargeted	Pulsating Variable
WTC197	16 35 38.6	-34 54 02	Untargeted	Pulsating Variable
WTC198	19 06 21.7	-28 51 06	Untargeted	CV
WTC199	19 36 15.7	-34 31 10	Untargeted	Pulsating Variable
WTC200	20 24 07.5	-27 36 56	Untargeted	Flare
WTC201	22 00 22.6	-34 27 38	Untargeted	Flare
WTC202	22 23 43.0	-19 26 49	Untargeted	Flare

Table D.1 continued: A list of all the transient candidates discovered in the WASP orphans database. Each row includes an identification number, a right ascension, a declination, the search where the candidate was found and a provisional classification. Candidates marked with a * were confirmed spectroscopically.

Identification	Right Ascension	Declination	Source	Type
WTC203	22 50 26.9	-43 16 14	Untargeted	Flare
WTC204	23 34 00.0	-17 59 55	Untargeted	CV
WTC205	23 38 42.6	-20 29 38	Untargeted	Flare
WTC206	23 48 03.1	-22 31 32	Untargeted	Flare
WTC207	01 04 28.3	+13 37 16	Untargeted	Flare
WTC208	02 00 55.9	+09 45 36	Untargeted	Pulsating Variable
WTC209	04 19 53.6	+06 17 22	Untargeted	Flare
WTC210	04 53 27.5	-12 49 28	Untargeted	Flare
WTC211	05 09 26.2	+17 24 24	Untargeted	Flare
WTC212	05 10 08.4	+00 46 34	Untargeted	Flare
WTC213	05 12 23.6	+12 50 33	Untargeted	Pulsating Variable
WTC214	05 22 10.7	-03 36 55	Untargeted	Flare
WTC215	05 27 44.2	+00 07 16	Untargeted	Flare
WTC216	05 31 12.1	-01 50 56	Untargeted	Flare
WTC217	07 34 42.7	+50 42 29	Untargeted	Uncertain
WTC218	07 40 34.8	+44 18 36	Untargeted	Flare
WTC219	07 44 45.0	+50 17 21	Untargeted	Flare
WTC220	08 20 54.8	+54 22 19	Untargeted	Flare
WTC221	08 44 12.6	+50 28 37	Untargeted	Flare
WTC222	09 22 09.3	+40 55 33	Untargeted	Flare
WTC223	09 29 12.8	+37 44 11	Untargeted	Uncertain
WTC224	09 54 52.3	+55 35 37	Untargeted	Uncertain
WTC225	11 29 31.1	-02 44 10	Untargeted	Flare
WTC226	12 22 48.8	-02 05 37	Untargeted	Flare
WTC227	14 29 21.2	+01 27 11	Untargeted	Pulsating Variable
WTC228	17 25 08.6	+42 30 25	Untargeted	Flare
WTC229	17 29 05.1	+58 58 37	Untargeted	Flare
WTC230	17 29 45.0	+56 31 39	Untargeted	Flare
WTC231	17 50 13.0	+44 24 04	Untargeted	Flare
WTC232	18 52 16.6	+52 57 15	Untargeted	Flare
WTC233	19 15 40.7	+54 47 11	Untargeted	Flare
WTC234	19 20 26.7	+49 50 51	Untargeted	Flare
WTC235	21 08 26.2	+10 46 40	Untargeted	Flare
WTC236	22 02 15.0	+20 36 07	Untargeted	Flare
WTC237	22 50 34.2	-05 59 30	Untargeted	Flare
WTC238	23 32 43.8	+01 33 21	Untargeted	Flare

Table D.1 continued: A list of all the transient candidates discovered in the WASP orphans database. Each row includes an identification number, a right ascension, a declination, the search where the candidate was found and a provisional classification. Candidates marked with a * were confirmed spectroscopically.

Identification	Right Ascension	Declination	Source	Type
WTC239	00 13 48.6	-18 43 03	Untargeted	Flare
WTC240	00 14 34.0	-05 11 23	Untargeted	Flare
WTC241	00 22 47.6	+05 57 13	Untargeted	Flare
WTC242	00 45 59.0	-07 37 33	Untargeted	Flare
WTC243	00 48 21.1	-17 40 49	Untargeted	Flare
WTC244	00 58 47.8	+01 10 16	Untargeted	Flare
WTC245	00 58 59.9	-00 18 02	Untargeted	Flare
WTC246	01 03 21.1	-08 34 30	Untargeted	Flare
WTC247	02 05 04.4	-06 53 28	Untargeted	Flare
WTC248	02 51 54.7	+07 03 09	Untargeted	Flare
WTC249	03 08 17.3	+05 50 18	Untargeted	Pulsating Variable
WTC250	03 28 20.0	-07 47 01	Untargeted	Flare
WTC251	03 59 58.9	-05 12 36	Untargeted	Uncertain
WTC252	04 14 22.1	-19 10 22	Untargeted	Flare
WTC253	04 17 18.2	-08 02 53	Untargeted	Flare
WTC254	04 28 10.8	+04 03 34	Untargeted	Flare
WTC255	04 33 16.9	+07 40 54	Untargeted	Pulsating Variable
WTC256	04 40 05.7	-09 41 17	Untargeted	Flare
WTC257	04 49 02.7	-18 41 30	Untargeted	CV
WTC258	04 53 37.7	-28 35 31	Untargeted	Flare
WTC259	04 54 48.8	-18 38 48	Untargeted	Flare
WTC260	04 54 53.1	-47 47 12	Untargeted	Flare
WTC261	05 09 11.5	-19 53 47	Untargeted	Flare
WTC262	05 22 21.0	-57 54 51	Untargeted	Flare
WTC263	05 32 26.4	-14 30 56	Untargeted	Flare
WTC264	05 32 36.6	-50 13 03	Untargeted	Uncertain
WTC265	06 15 33.3	-46 36 09	Untargeted	Uncertain
WTC266	06 30 00.6	-57 07 59	Untargeted	Flare
WTC267	06 30 57.5	-46 31 10	Untargeted	Flare
WTC268	06 33 00.6	-47 32 12	Untargeted	Flare
WTC269	06 37 36.3	-56 06 59	Untargeted	Flare
WTC270	07 02 36.7	-43 26 58	Untargeted	Flare
WTC271	07 03 35.3	-40 47 46	Untargeted	Pulsating Variable
WTC272	10 06 03.6	-20 36 55	Untargeted	Flare
WTC273	10 22 56.7	-44 11 39	Untargeted	Pulsating Variable
WTC274	10 52 00.9	-26 35 02	Untargeted	Flare

Table D.1 continued: A list of all the transient candidates discovered in the WASP orphans database. Each row includes an identification number, a right ascension, a declination, the search where the candidate was found and a provisional classification. Candidates marked with a * were confirmed spectroscopically.

Identification	Right Ascension	Declination	Source	Type
WTC275	10 55 14.9	-46 42 28	Untargeted	Pulsating Variable
WTC276	10 56 39.2	-31 22 07	Untargeted	Uncertain
WTC277	11 09 49.9	-38 28 07	Untargeted	Flare
WTC278	11 28 15.3	-34 48 08	Untargeted	Uncertain
WTC279	11 30 18.9	-35 00 15	Untargeted	Flare
WTC280	11 32 29.3	-45 57 03	Untargeted	Pulsating Variable
WTC281	11 50 28.0	-25 04 05	Untargeted	Flare
WTC282	12 02 57.1	-24 50 55	Untargeted	CV
WTC283	13 19 56.3	-01 58 49	Untargeted	Flare
WTC284	13 21 09.7	-36 00 01	Untargeted	Flare
WTC285	13 24 40.1	-19 51 26	Untargeted	Uncertain
WTC286	13 40 01.6	-43 48 57	Untargeted	Flare
WTC287	13 45 18.7	-36 30 16	Untargeted	CV
WTC288	13 47 19.8	-17 53 55	Untargeted	Pulsating Variable
WTC289	14 21 55.2	-41 41 33	Untargeted	Flare
WTC290	14 37 29.2	-20 19 42	Untargeted	Pulsating Variable
WTC291	14 39 15.5	-35 27 10	Untargeted	Uncertain
WTC292	14 42 51.5	-40 28 40	Untargeted	Flare
WTC293	14 52 42.6	+02 47 25	Untargeted	Flare
WTC294	14 57 44.1	+01 05 08	Untargeted	Uncertain
WTC295	15 05 37.2	+04 41 11	Untargeted	Flare
WTC296	15 31 08.1	-15 07 18	Untargeted	Flare
WTC297	16 03 03.3	-05 07 18	Untargeted	Uncertain
WTC298	16 05 57.2	-27 47 33	Untargeted	Pulsating Variable
WTC299	16 06 52.0	-24 26 20	Untargeted	Flare
WTC300	16 08 46.2	-22 46 53	Untargeted	Flare
WTC301	16 10 20.0	-07 32 19	Untargeted	Flare
WTC302	16 13 06.4	-20 18 37	Untargeted	Flare
WTC303	16 24 20.2	-28 37 04	Untargeted	Pulsating Variable
WTC304	16 25 59.2	-37 25 37	Untargeted	Pulsating Variable
WTC305	16 26 30.5	-29 07 31	Untargeted	Pulsating Variable
WTC306	16 28 32.2	-19 59 41	Untargeted	Pulsating Variable
WTC307	16 33 53.6	-33 56 15	Untargeted	Pulsating Variable
WTC308	16 34 35.1	-26 58 03	Untargeted	Flare
WTC309	20 48 56.9	-41 02 05	Untargeted	Flare
WTC310	20 55 08.8	-15 03 34	Untargeted	Flare

Table D.1 continued: A list of all the transient candidates discovered in the WASP orphans database. Each row includes an identification number, a right ascension, a declination, the search where the candidate was found and a provisional classification. Candidates marked with a * were confirmed spectroscopically.

Identification	Right Ascension	Declination	Source	Type
WTC311	21 12 12.9	-66 38 03	Untargeted	CV
WTC312	21 30 09.3	-55 02 54	Untargeted	Flare
WTC313	21 32 03.2	-19 36 58	Untargeted	CV
WTC314	21 55 17.5	-00 45 52	Untargeted	Flare
WTC315	21 56 57.0	-53 06 19	Untargeted	Flare
WTC316	22 29 17.8	-15 42 31	Untargeted	Flare
WTC317	22 33 16.0	+06 05 37	Untargeted	Flare
WTC318	22 35 26.7	-01 44 11	Untargeted	Flare
WTC319	22 51 24.5	+03 29 34	Untargeted	Flare
WTC320	23 31 52.3	+03 30 24	Untargeted	Flare
WTC321	23 38 34.1	+06 24 54	Untargeted	Uncertain
WTC322	10 57 50.0	-21 56 58	Untargeted	CV

Table D.1 continued: A list of all the transient candidates discovered in the WASP orphans database. Each row includes an identification number, a right ascension, a declination, the search where the candidate was found and a provisional classification. Candidates marked with a * were confirmed spectroscopically.